Alma Mater Studiorum - Università di Bologna

DOTTORATO DI RICERCA IN

FISICA

Ciclo 35

Settore Concorsuale: 02/B2 - FISICA TEORICA DELLA MATERIA

Settore Scientifico Disciplinare: FIS/03 - FISICA DELLA MATERIA

EXCITONIC PROPERTIES OF TRANSITION METAL OXIDE PEROVSKITES AND
WORKFLOW AUTOMATIZATION OF GW SCHEMES

Presentata da: Lorenzo Varrassi

Coordinatore Dottorato

Michele Cicoli

Supervisore

Cesare Franchini

Esame finale anno 2023

Abstract

The Many-Body-Perturbation Theory (MBPT) approach is among the most successful theoretical frameworks for the study of excited state properties. It represents the current state-of-the-art approach for the calculation of accurate electronic structures beyond the known limits of Density Functional Theory and allows to describe the excitonic interactions, which play a fundamental role in the optical response of insulators and semiconductors.

The first part of the thesis focuses on the study of the quasiparticle, optical and excitonic properties of *bulk* Transition Metal Oxide (TMO) perovskites using a G_0W_0+Bethe Salpeter Equation (BSE) approach. TMO perovskites are an extensively studied class of materials with interesting physical and chemical properties and promising technological applications. A representative set of 14 compounds has been selected, including 3d ($SrTiO_3$, $LaScO_3$, $LaTiO_3$, $LaVO_3$, $LaCrO_3$, $LaMnO_3$, $LaFeO_3$ and $SrMnO_3$), 4d ($SrZrO_3$, $SrTcO_3$ and Ca_2RuO_4) and 5d ($SrHfO_3$, $KTaO_3$ and $NaOsO_3$) perovskites. An approximation of the BSE scheme, based on an analytic diagonal expression for the inverse dielectric function $\epsilon^{-1}_{\mathbf{G},\mathbf{G}}$, is used to compute the exciton binding energies and is carefully bench-marked against the standard BSE results. In 2019 an important breakthrough has been achieved with the synthesis of ultrathin $SrTiO_3$ films down to the monolayer limit. This allows us to explore how the quasiparticle and optical properties of $SrTiO_3$ evolve from the bulk to the two-dimensional limit. The electronic structure is computed with G_0W_0 approach: we prove that the inclusion of the off-diagonal self-energy terms is required to avoid non-physical band dispersions. The excitonic properties are investigated beyond the optical limit by calculating the energy loss function at finite momentum.

Lastly a study of the under pressure optical response of the topological nodal line semimetal ZrSiS is presented, in conjunction with the experimental results from the group of Prof. Dr. Kuntscher of the Augsburg University.

The second part of the thesis discusses the implementation of a workflow to automate G_0W_0 and BSE calculations with the VASP software. The workflow adopts a convergence scheme based on an explicit basis-extrapolation approach [J. Klimeš *et al.*, Phys. Rev.B 90, 075125 (2014)] which allows to reduce the number of intermediate calculations required to reach convergence and to explicit estimate the error associated to the basis-set truncation. These developments open the way for performing High-Throughput screening calculations using the G_0W_0 schemes within the VASP ab-initio software.

Contents

Chapter 1

Introduction

This thesis focuses on the optical response of condensed matter systems, both in the bulk and two-dimensional structures, with a particular attention on their excitonic properties. Excitons are correlated electron–hole excitation states that can be modeled as electrically neutral quasiparticles. Intuitively, they can be created during an absorption process, from the (screened) interaction between an electron excited into the conduction band and the corresponding electron hole in the valence band. Electron-hole pairs were first conceived and introduced by Frenkel in 1931 [1, 2]. The Wannier-Mott model, describing large-radius weakly bound excitons, was first proposed in 1937 [3, 4] and subsequently observed in 1951 in copper oxide by Gross and Karryev [5]. Excitonic effects profoundly alter and dominate the low-energy region of optical and loss spectra in semiconductors and insulators [6], and have an important role in many technological applications such as photocatalysis or photovoltaics. Many-Body Perturbation Theory (MBPT) is the state-of-the-art ab-initio formalism for predicting spectroscopic responses and excitonic properties in the condensed matter field. The MBPT approach is founded on the concept of quasiparticle, introduced by Landau [7, 8, 9, 10] : in this approximation the excited states of the many-body system are described as weakly interacting particles with renormalized masses and weak effective interactions associated to electric screening effects. Nowadays the so-called GW approximation, first proposed by Hedin in 1965 [11], is the standard and most used approach to characterize quasiparticle energies and orbitals. It's interesting to note that the seminal Density Functional Theory (DFT) papers were published in the same years [12, 13]; However, while DFT quickly become one of the most important and widespread formalism in the field of computational science, we have to wait until 1980s [14, 15, 16] for the first GW applications. The GW scheme is implemented in many ab-initio codes, such as VASP [17, 18], Yambo [19, 20], Abinit [21], WEST [22] and BerkeleyGW [23]. The success of the method can be ascribed to the very good agreement with experimental data for what regards band-structures and in particular band-gaps [24, 25, 26, 27], one of the most notorious deficiencies of DFT.

The excitonic properties are determined through the solution of the Bethe-Salpeter Equation (BSE), which takes into account the electron-hole coupling. In order to obtain a reliable estimation of the optical gap and of the interband transitions, an accurate evaluation of the

QP energies is essential; in this sense a GW bandstructure is typically employed as a starting point. The theoretical GW and BSE formalisms are introduced and discussed in chapters 3, 4.

The GW method presents however different important drawbacks. First of all, the computational complexity of the most common implementations scales as $O(N^4)$ with N equal to the number of electrons [28, 29], which makes calculations an order of magnitude more computationally expensive than the DFT counterparts. For non-self consistent GW calculations, the starting point dependence can strongly influence the accuracy of the final results [30]. Furthermore, the convergence of the QP energies requires a complex procedure with several hindrances. On the one hand, the inter-dependence of several computational parameters represents a critical point, which has been documented to cause unreliable results if not accurately controlled. On the other hand, the self-energy and polarizability expressions display a slow convergence with respect of the basis set dimension, absent in DFT or Hartree-Fock formalisms, which can lead to underconverged energies.

In this regard, several authors [31, 28, 32] recently proposed procedures to handle the numerical convergences in a systemic and efficient way, without incurring in the most common pitfalls. Among them, Klimeš and coworkers [33] developed an alternative scheme based on an extrapolation to the infinite-basis-set limit. The scheme is founded on a formal derivation of the asymptotic behavior of quasiparticle energies, and is outlined in chapter 5. It has been validated on molecules [34] and bulk solids [35, 36] and has been employed by Ergönenc and coworkers [37] to accurately estimate the band gap of a dataset formed by fourteen Transition Metal Oxide (TMO) perovskites. Chapter 6 follows and broadens the work of Ergönenc *et al.* and describes an in-depth study of the optical and excitonic properties of the dataset using the G_0W_0+BSE approach. The electron-hole coupling coefficients are analysed to determine the origin of the main features of the spectra and to investigate how transitions between the band manifolds determine the dominating contributions.

Recently an important breakthrough has been achieved by Ji *et al.* through the first synthesis o freestanding 2D perovskites $SrTiO_3$ and $BiFeO_3$ films with thicknesses reaching the monolayer limit [38]. Their work proves that TMO perovskites films can be realized with thicknesses below the critical limit previously proposed as necessary for crystalline order stability [39]. Chapter 7 thus extends the study of $SrTiO_3$ quasiparticle and excitonic properties, already discussed in the bulk dataset, to the monolayer limit. $SrTiO_3$ possesses a prototypical role between the TMO perovskites: it's one of the most studied compounds and its conducting, magnetic and optical properties has been widely investigated [40, 41, 42, 43, 44].

Chapter 8 presents a computational and experimental study of the optical response of ZrSiS under pressure. This material can be considered as a paradigmatic example of topological nodal line semimetal [45, 46]. The electronic structure of this class of materials exhibits a peculiar diamond-shaped line of Dirac nodes and linear dispersing bands close to Fermi level. The optical conductivity is determined through the G_0W_0+BSE approach and is compared

with the in-plane and out-of-plane optical experimental response at ambient pressure and high quasi-hydrostatic pressure. The work was carried out in collaboration with the groups of Prof. Dr. Kuntscher of the Augsburg University and Prof. Kuneš of the Technische Universität Wien.

Lastly, chapter 5 discusses the implementation of the extrapolation scheme derived by Klimeš *et al.* [33] as an automatized workflow (i.e. without need of manual user control) for High-Throughput G_0W_0 calculations. The workflow is based on the AiiDA platform [47, 48] and the AiiDA-VASP plugin and aims to prepare, submit and perform error handling of the G_0W_0 calculations in VASP with minimal user intervention. This work was realized in collaboration with the THEOS-MARVEL Group (where I spent a visiting period of three months) and with the main AiiDA-VASP plugin developers (E. Flage-Larsen, A. Togo, J. Chico and B. Zhu).

Chapter 2

Density Functional theory

1 Kohn-Hohenberg theorems

The Density Functional Theory (DFT) is one of the most popular formalisms in the field of condensed matter physics, frequently adopted to investigate the ground stated electronic, magnetic and structural properties of solids and molecules. The foundations of the theory are the two *Kohn-Hohenberg* theorems [12], that we present below[1].

Theorem 1 *For any system of interacting particles in a given external potential $v_{ext}(\boldsymbol{r})$, the potential itself is determined uniquely (within an additive constant) by the ground state particle density $n_0(\boldsymbol{r})$.*

The first theorem asserts the existence of the injective map $v_{ext} \rightarrow n_0$ [51, p. 10][52, p. 232]. If we restrict to the densities determined by a given v_{ext} the map can be inverted: the ground state density n_0 therefore becomes the fundamental variable of the formalism and, at the same time, v_{ext} becomes a unique functional of n_0.

This implies that **(i)** the many-body wavefunctions of the system are determined by n_0 and thus **(ii)** the expectation values of all operators ultimately depend on the density:

$$\psi(\mathbf{r}_1, \mathbf{r}_2, .., \mathbf{r}_N) = \psi[n_0(\mathbf{r})] \quad \implies \quad \left\langle \hat{O} \right\rangle = \langle \psi[n_0(\mathbf{r})] | \hat{O} | \psi[n_0(\mathbf{r})] \rangle$$

The energy can hence be written **(iii)** as a functional of n_0 $E = E[n_0(\mathbf{r})]$. It can be proved that the energy expression can be expanded as:

$$E[n_0(\mathbf{r})] = \left\langle \hat{T}[n_0(\mathbf{r})] \right\rangle + \langle v_{ext}[n_0(\mathbf{r})] \rangle + \langle V_{ee}[n_0(\mathbf{r})] \rangle \tag{2.1}$$

---

[1]The theorems will be presented without proof, which can be found in most computational physics books. [6, 49, 50, 51, 52]

where $\hat{T}$ is the kinetic energy and $\hat{V}_{ee}$ the term associated to the electron-electron interaction. This equation can be reorganized by defining the so called *Hohenberg-Kohn* functional F_{HK}:

$$F_{HK}[n_0(\mathbf{r})] \stackrel{\text{def}}{=} \left\langle \hat{T}[n_0(\mathbf{r})] \right\rangle + \langle V_{ee}[n_0(\mathbf{r})] \rangle \rightarrow \quad E[n_0(\mathbf{r})] = F_{HK}[n_0(\mathbf{r})] + \int d\mathbf{r} v_{ext}(\mathbf{r}) n_0(\mathbf{r}) \quad (2.2)$$

Theorem 2 *Let $v_{ext}(\boldsymbol{r})$ be the external potential of a specific system with exact ground state density $n_0(\boldsymbol{r})$. The exact ground state energy of the system is the global minimum value of the functional $E[n(\boldsymbol{r})]$, and the density that minimizes the functional is $n_0(\boldsymbol{r})$.*

The second theorem defines a variational principle: if F_{HK} is known the exact ground state density can be determined by minimizing the total energy of the system with respect to variation of the density $n(\mathbf{r})$. However, the analytical expression of F_{HK} is in general not known, and thus approximations must be introduced.

2 Kohn-Sham Equations

The popularity of Density Functional Theory has been largely associated to the approach pioneered by Kohn and Sham [13]. Their formulation is based on the assumption that for each ground state density of the interacting system n_0 there exists an *auxiliary independent-particle system* with the same density n_0^{KS}, i.e. $n_0^{KS}(\mathbf{r}) = n_0(\mathbf{r})$. The non-interacting density can be therefore expanded in terms of single particle wavefunctions:

$$n_0 = n_0^{KS}(\mathbf{r}) = \sum_{\sigma} \sum_{i:particles} \left| \psi_{i,\sigma}^{KS} \right|^2$$

This is referred as *non-interacting V-representability*, and we will assume its validity. The Kohn-Hohenberg theorems moreover state that the two systems are associated to the *same* external potential v_{ext}.

Now the ground state energy functional can be rewritten through the single-particle states:

$$E[n] = T_{ip}[n] + \int d\mathbf{r} v_{ext}(\mathbf{r}) n(\mathbf{r}) + E_H[n] + E_{xc}[n]$$

$$T_{ip}[n] = -\frac{1}{2} \sum_{\sigma} \sum_{i=1}^{N} \left\langle \psi_{i,\sigma}^{KS} \middle| \nabla^2 \middle| \psi_{i,\sigma}^{KS} \right\rangle = \frac{1}{2} \sum_{\sigma} \sum_{i=1}^{N} |\nabla \psi_{i,\sigma}^{KS}|^2 \quad (2.3)$$

$$E_H[n] = \frac{1}{2} \int d\mathbf{r} d\mathbf{r}' \frac{n(\mathbf{r}) n(\mathbf{r}')}{|\mathbf{r} - \mathbf{r}'|}$$

T_{ip} is the independent-particle kinetic energy and E_H is the Hartree Energy.; the exchange-correlation functional E_{xc} contains all many-body effects of exchange and correlation, and

can be formally defined as:

$$E_{xc}[n] \stackrel{\text{def}}{=} F_{HK}[n] - (T_{ip}[n] + E_H[n]) = \left\langle \hat{T} \right\rangle - T_{ip}[n] + \langle V_{ee} \rangle - E_H[n] \tag{2.4}$$

E_{xc} is a functional of the density since all the variables on the right-hand side are functional of it; moreover, it's a universal functional in the same sense of F_{HK}.
Finally the auxiliary hamiltonian can be written:

$$\left[-\frac{1}{2} \nabla^2 + v_{ext}(\mathbf{r}) + V_H(\mathbf{r}) + V_{xc}(\mathbf{r}) \right] \psi_i^{KS}(\mathbf{r}) = \epsilon_i^{KS} \psi_i^{KS}(\mathbf{r}) \tag{2.5}$$

with V_{xc} determined by the functional derivative of exchange-correlation term $V_{xc} \stackrel{\text{def}}{=} \delta E_{xc}/\delta n(\mathbf{r})$.

2.1 Exchange and correlation functionals

The formalism discussed above does not provide any explicit form of the exchange-correlation functional: we have to resort to approximations.
The simplest one available is the *Local Density Approximation* (LDA), where E_{xc} is considered only *locally* dependent on the charge density, and it's determined from the homogeneous electron gas exchange-correlation energy density ϵ_{xc}^{HEG}:

$$E_{xc}^{LDA}[n] \stackrel{\text{def}}{=} \int d\mathbf{r} n(\mathbf{r}) \epsilon_{xc}^{HEG}(n) \tag{2.6}$$

A refinement of the LDA is the so-called *Generalized Gradient approximation* (GGA), where E_{xc} is assumed dependent on n and also on $\nabla n(\mathbf{r})$ (functionals of this type are called *semilocal*):

$$E_{xc}^{GGA}[n] \stackrel{\text{def}}{=} \int d\mathbf{r} f\left(n(\mathbf{r}), \nabla n(\mathbf{r}) \right) \tag{2.7}$$

The most popular GGAs are *PBE* (proposed in 1996 by *Perdew, Burke and Ernzenhof* [53]) and *BLYP* (the combination of Becke's 1988 exchange functional [54] with the 1988 correlation functional by *Lee, Yang and Parr* [55]).

3 DFT implementation in VASP

The solution of the Kohn-Sham equation requires the expansion of the wavefunction over a basis-set. One of the most common choices is the plane-wave (PW) basis set, which is adopted by both codes used in this work (VASP [18, 17] and Yambo [19, 20]). This basis set allows to expand a generic wavefunction ψ for a material with translationally symmetry as:

$$\psi_{n\mathbf{k}}(\mathbf{r}) = u_{n\mathbf{k}}(\mathbf{r})e^{i\mathbf{k}\cdot\mathbf{r}} = \frac{1}{\sqrt{\Omega}}\sum_{\mathbf{G}}C_{n\mathbf{k}}(\mathbf{G})e^{i(\mathbf{k}+\mathbf{G})\cdot\mathbf{r}} \tag{2.8}$$

$\mathbf{k}$ is restricted to the first Brillouin Zone (BZ), $\mathbf{G}$ is a reciprocal lattice vector and Ω is the volume of the unit cell.

The numerical implementation of the expansion over the basis set can include only a finite number of basis vectors; therefore a cutoff (represented by the `ENCUT` flag in VASP) is imposed on the energy:

$$\psi_{n\mathbf{k}}(\mathbf{r}) = \frac{1}{\sqrt{\Omega}}\sum_{\mathbf{G}}^{\frac{1}{2}|\mathbf{k}+\mathbf{G}|^2 < ENCUT}C_{n\mathbf{k}}(\mathbf{G})e^{i(\mathbf{k}+\mathbf{G})\cdot\mathbf{r}} \tag{2.9}$$

Furthermore, integrals over the Brillouin Zone in reciprocal space are reduced to a weighted sum over a finite set of points (called *k-point grid* or *k-point mesh*):

$$\frac{1}{\Omega_{BZ}}\int_{\Omega_{BZ}}d\mathbf{k}f(\mathbf{k}) \simeq \sum_{\mathbf{k}}\omega_{\mathbf{k}}f(\mathbf{k})$$

The Projector Augmented-Wave method (PAW)

In order to reduce the computational cost associated with the solution of the Schrödinger equation many ab-initio codes (including VASP) adopt the *pseudopotential* approximation. First of all, the electrons of the systems are partitioned in the *valence* and *core* groups. The electrons belonging to the atoms' inner shells do not contribute significantly to the chemical properties and bounds of the compounds, which are essentially determined by the outermost (*valence*) electrons. The fundamental idea is hence to neglect the explicit treatment of core electrons and introduce an *effective potential* (the *pseudopotential*) to approximate the potential felt by valence electrons [56, 57, 58].

The VASP software [18, 17] implements the *Projector Augmented Wave Method* (*PAW*) [59], a generalization of the augmented wave methods [60] and the pseudopotential methods [58]. Let's start by defining a core region with radius r_c (called *augmentation region*) around each

atom. Two different wavefunctions are taken into account: the *all electron* wavefunctions $|\psi_{n\mathbf{k}}\rangle$ and *pseudized* $\left|\tilde{\psi}_{n\mathbf{k}}^{p}\right\rangle$ ones. The pseudized wavefunctions are identical (by construction) the all-electron one outside the sphere r_c and represents only a simplified approximation to true orbitals inside. Both wavefunctions are expanded over a basis of partial waves inside the augmentation region:

$$|\psi^e\rangle = \begin{cases} \sum_i c_i \,|\phi_i^e\rangle & r < r_c \\ |\psi^e\rangle & r \geq r_c \end{cases} \qquad \left|\tilde{\psi}^p\right\rangle = \begin{cases} \sum_i c_i \left|\tilde{\phi}_i^p\right\rangle & r < r_c \\ |\psi^e\rangle & r \geq r_c \end{cases} \tag{2.10}$$

The relation between $|\psi_{n\mathbf{k}}\rangle$ and $\left|\tilde{\psi}_{n\mathbf{k}}^{p}\right\rangle$ is given by the expression:

$$|\psi^e\rangle = \left|\tilde{\psi}^p\right\rangle + \sum_i \left[|\phi_i^e\rangle - \left|\tilde{\phi}_i^p\right\rangle \right] \left\langle \tilde{p}_i \middle| \tilde{\psi}^p \right\rangle \tag{2.11}$$

where $c_i = \left\langle \tilde{p}_i \middle| \tilde{\psi}^p \right\rangle$ are called projectors functions. The pseudo partial waves are determined by the equation:

$$\left[-\frac{\hbar^2}{2m}\nabla^2 + \tilde{v}_{eff} + \sum_{i,j} \left|\tilde{\phi}_i^p\right\rangle D_{ij} \left\langle \tilde{\phi}_i^p\right| \right] \left|\tilde{\phi}_i^p\right\rangle = \epsilon_i \left[1 + \sum_{i,j} \left|\tilde{\phi}_i^p\right\rangle D_{ij} \left\langle \tilde{\phi}_i^p\right| \right] \left|\tilde{\phi}_i^p\right\rangle \tag{2.12}$$

with $Q_{ij} = \left\langle \phi_i^e \middle| \phi_j^e \right\rangle - \left\langle \tilde{\phi}_i^p \middle| \tilde{\phi}_j^p \right\rangle$, $D_{ij} = \left\langle \phi_j^e \middle| \frac{\hbar^2}{2m}\nabla^2 + v_{eff} \middle| \phi_j^e \right\rangle - \left\langle \tilde{\phi}_j^p \middle| \frac{\hbar^2}{2m}\nabla^2 + v_{eff} \middle| \tilde{\phi}_j^p \right\rangle$.

Chapter 3

The GW Approximation

1 Interacting and non-interacting Green functions

For a system composed by N electrons the hole and electron propagators $G^<$, $G^>$ can be defined:

$$G^<(\mathbf{r}_1, t_1, \mathbf{r}_2, t_2) \overset{\text{def}}{=} +i \left\langle \psi_0^N \middle| \hat{\psi}^\dagger(\mathbf{r}_2, t_2) \hat{\psi}(\mathbf{r}_1, t_1) \middle| \psi_0^N \right\rangle \tag{3.1}$$

$$G^>(\mathbf{r}_1, t_1, \mathbf{r}_2, t_2) \overset{\text{def}}{=} -i \left\langle \psi_0^N \middle| \hat{\psi}(\mathbf{r}_1, t_1) \hat{\psi}^\dagger(\mathbf{r}_2, t_2) \middle| \psi_0^N \right\rangle \tag{3.2}$$

where $\hat{\psi}^\dagger(\mathbf{r}_2, t_2)$ and $\hat{\psi}(\mathbf{r}_1, t_1)$ are the creation and annihilation field operators in the Heisenberg picture, $\left| \psi_0^N \right\rangle$ is the ground-state wavefunction of the interacting system. We note that the equation 3.1 is valid also for a non-interacting system: in that case the expectation value is evaluated using the non-interacting ground state wavefunction.

This definition also offers a direct qualitative interpretation: $\hat{\psi}^\dagger(\mathbf{r}_2, t_2) \left| \psi_0^N \right\rangle$ adds an electron to the ground state at time t_2 and position $\mathbf{r}_2$; this $(N+1)$ state propagates from t_2 to t_1 under the action of the interacting hamiltonian (comprised in the Heisenberg picture of the operators). The Green function is equal to the overlap between the propagated state and the $(N+1)$ state obtained by creating an electron at $(\mathbf{r}_1, t_1)$: in this sense G represents the transition amplitude associated to the propagation of the test electron from $(\mathbf{r}_2, t_2)$ to $(\mathbf{r}_1, t_1)$. The two Green functions can be combined in the one-particle *casual* or *time-ordered* Green function is defined as:

$$G(\mathbf{r}_1, t_1, \mathbf{r}_2, t_2) \overset{\text{def}}{=} -i \left\langle \psi_0^N \middle| \hat{T} \left[\hat{\psi}(\mathbf{r}_1, t_1) \hat{\psi}^\dagger(\mathbf{r}_2, t_2) \right] \middle| \psi_0^N \right\rangle \tag{3.3}$$

$$= G^<(\mathbf{r}_1, t_1, \mathbf{r}_2, t_2)\theta(t_2 - t_1) + G^>(\mathbf{r}_1, t_1, \mathbf{r}_2, t_2)\theta(t_1 - t_2)$$

where $\hat{T}$ is the time-ordering operator defined as:

$$\hat{T}\left[\hat{\psi}(\mathbf{r}_1, t_1)\hat{\psi}^\dagger(\mathbf{r}'_2, t_2)\right] \overset{\text{def}}{=} \hat{\psi}(\mathbf{r}_1, t_1)\hat{\psi}^\dagger(\mathbf{r}_2, t_2)\theta(t_1 - t_2) - \hat{\psi}^\dagger(\mathbf{r}_2, t_2)\hat{\psi}(\mathbf{r}_1, t_1)\theta(t_1 - t_1)$$

Moreover, by considering the definitions of the field operators

$$\hat{\psi}(\mathbf{r}, t) \overset{\text{def}}{=} \frac{1}{\sqrt{\Omega}} \sum_\alpha \phi_\alpha(\mathbf{r})\hat{c}_\alpha(t) \qquad \hat{\psi}^\dagger(\mathbf{r}, t) \overset{\text{def}}{=} \frac{1}{\sqrt{\Omega}} \sum_\alpha \phi_\alpha(\mathbf{r})\hat{c}_\alpha^\dagger(t)$$

the Green function can be ri-expressed in terms of creation and annihilation operators:

$$G(\mathbf{r}_1, t_1, \mathbf{r}_2, t_2) = -i \sum_{\alpha_1, \alpha_2} \phi_{\alpha_1}(\mathbf{r}_1)\phi_{\alpha_2}(\mathbf{r}_2) \left\langle \psi_0^N \middle| \hat{T}\left[\hat{c}_{\alpha_1}(t_1)\hat{c}_{\alpha_2}^\dagger(t_2)\right] \middle| \psi_0^N \right\rangle \tag{3.4}$$

Fourier transforms of the Green functions

In the following sections we will often manipulate the Fourier transform of the Green functions, which we briefly elaborate. It's possible to define [7, p. 62] the Fourier transforms with respect to space variables $\mathbf{r}_1, \mathbf{r}_2$ and time variables as:

$$G(\mathbf{r}_1, t_1, \mathbf{r}_2, t_2) = \frac{1}{\Omega} \sum_{\mathbf{k}_1, \mathbf{k}_2} G(\mathbf{k}_1, t_1, \mathbf{k}_2, t_2)e^{i\mathbf{k}_1 \cdot \mathbf{r}_1}e^{-i\mathbf{k}_2 \cdot \mathbf{r}_2} \tag{3.5}$$

$$G(\mathbf{k}_1, t_1, \mathbf{k}_2, t_2) = \frac{1}{2\pi} \iint d\omega_1 d\omega_2 G(\mathbf{k}_1, \omega_1, \mathbf{k}_2, \omega_2)e^{-i\omega_1 t_1}e^{i\omega_2 t_2} \tag{3.6}$$

If the Hamiltonian is translationally invariant, it can be proved that $G(\mathbf{r}_1, t_1, \mathbf{r}_2, t_2)$ depends only on the $\mathbf{r}_1 - \mathbf{r}_2$: $G(\mathbf{r}_1, t_1, \mathbf{r}_2, t_2) = G(\mathbf{r}_1 - \mathbf{r}_2, t_1, t_2)$; this in turn implies that the Green Function [7, p. 124] becomes diagonal in $\mathbf{k}_1, \mathbf{k}_2$: $G(\mathbf{k}_1, t_1, \mathbf{k}_2, t_2) = \delta_{\mathbf{k}_1, \mathbf{k}_2}G(\mathbf{k}_1, t_1, t_2)$.
A similar argument can be made if the Hamiltonian is time-independent: in this case G holds $G(\mathbf{k}_1, t_1, \mathbf{k}_2, t_2) = G(\mathbf{k}_1, \mathbf{k}_2, t_1 - t_2)$ and it becomes diagonal in the frequencies ω_1, ω_2:

$$G(\mathbf{k}, t - t') = \frac{1}{2\pi} \int d\omega G(\mathbf{k}, \omega)e^{-i\omega(t - t')} \tag{3.7}$$

In the following discussion we'll assume a time-independent and translationally invariant hamiltonian.

1.1 Lehmann representation of the Green function

Let's start the completeness relation of the Fock space (where $\left|\psi_m^N\right\rangle$ denotes the *m-th* eigenstate of a system with N particles):

$$\hat{1} = |vac\rangle\langle vac| + \sum_{m\geq 0}\left|\psi_m^1\right\rangle\left\langle\psi_m^1\right| + .. + \sum_{m\geq 0}\left|\psi_m^N\right\rangle\left\langle\psi_m^N\right| + ..$$

and insert it into the Green function definition

$$G^<(\mathbf{k}, t_1 - t_2) = +i\sum_{m\geq 0}|\left\langle\psi_m^{N-1}\right|\hat{c}_\mathbf{k}^\dagger\left|\psi_0^N\right\rangle|^2 e^{+\frac{i}{\hbar}\left[E_m^{(N-1)} - E_0^{(N)}\right](t_1 - t_2)}$$

$$G^>(\mathbf{k}, t_1 - t_2) = -i\sum_{m\geq 0}|\left\langle\psi_m^{N+1}\right|\hat{c}_\mathbf{k}^\dagger\left|\psi_0^N\right\rangle|^2 e^{-\frac{i}{\hbar}\left[E_m^{(N+1)} - E_0^{(N)}\right](t_1 - t_2)}$$

where we have used the fact that scalar products between wavefunctions with a different number of particles are equal to zero. From the integral representation of the step function the so-called *Lehmann representation* of the Green function is obtained:

$$G(\mathbf{k}, \omega) = \lim_{\eta\to 0^+}\sum_{m\geq 0}\frac{|\left\langle\psi_m^{N+1}\right|\hat{c}_\mathbf{k}^\dagger\left|\psi_0^N\right\rangle|^2}{\omega - \frac{1}{\hbar}\left(E_m^{(N+1)} - E_0^{(N)}\right) + i\eta} + \sum_{m\geq 0}\frac{|\left\langle\psi_m^{N-1}\right|\hat{c}_\mathbf{k}\left|\psi_0^N\right\rangle|^2}{\omega + \frac{1}{\hbar}\left(E_m^{(N-1)} - E_0^{(N)}\right) - i\eta}$$
(3.8)

$$G(\mathbf{r}_1, \mathbf{r}_2, \omega) = \lim_{\eta\to 0^+}\sum_{m\geq 0}\frac{\Psi_m^{N+1}(\mathbf{r}_1)\Psi_m^{N+1*}(\mathbf{r}_2)}{\omega - \frac{1}{\hbar}\left(E_m^{(N+1)} - E_0^{(N)}\right) + i\eta} + \sum_{m\geq 0}\frac{\Psi_m^{N-1}(\mathbf{r}_1)\Psi_m^{N-1*}(\mathbf{r}_2)}{\omega + \frac{1}{\hbar}\left(E_m^{(N-1)} - E_0^{(N)}\right) - i\eta}$$
(3.9)

where $\Psi_m^M(\mathbf{r})$ is defined as $\Psi_m^M(\mathbf{r}) = \left\langle\psi_m^M\right|\hat{\psi}^\dagger(\mathbf{r})\left|\psi_0^N\right\rangle$. To obtain eq. 3.12 the Fourier transform formula and the definition of field operator using a plane-wave basis set have been employed. From these expressions we note that the interacting Green function has poles at the exact excitation energies, defined as the addition or removal energies and involving the *exact* eigenvalues of the N and $N + 1$ system.

Through the definition of the two *spectral functions* A_+, A_- the Green function $G(\mathbf{k}, \omega)$ can

be reformulated as:

$$A_+(\mathbf{k}, \omega) \overset{\text{def}}{=} \sum_{m \geq 0} |\langle \psi_m^{N+1} | \hat{c}_{\mathbf{k}}^\dagger | \psi_0^N \rangle|^2 \delta\left[\omega - \frac{1}{\hbar}\left(E_m^{(N+1)} - E_0^{(N)}\right)\right] \tag{3.10}$$

$$A_-(\mathbf{k}, \omega) \overset{\text{def}}{=} \sum_{m \geq 0} |\langle \psi_m^{N-1} | \hat{c}_{\mathbf{k}} | \psi_0^N \rangle|^2 \delta\left[\omega + \frac{1}{\hbar}\left(E_m^{(N-1)} - E_0^{(N)}\right)\right] \tag{3.11}$$

$$G(\mathbf{k}, \omega) = \lim_{\eta \to 0^+} \int_{-\infty}^{+\infty} d\omega' \left[\frac{A_+(\mathbf{k}, \omega)}{\omega - \omega' + i\eta} + \frac{A_-(\mathbf{k}, \omega)}{\omega + \omega' - i\eta}\right] \tag{3.12}$$

The A_- and A_+ functions are real, positive and equal to zero for $\omega < 0$. Their sum $A(\mathbf{k}, \omega) \overset{\text{def}}{=} A_+(\mathbf{k}, \omega) + A_-(\mathbf{k}, \omega)$ satisfies the *sum rule*:

$$\int_0^\infty d\omega A(\mathbf{k}, \omega) = 1 \tag{3.13}$$

Due to the two properties above, $A(\mathbf{k}, \omega)$ can be formally interpreted *as a probability density*. It's possible to derive a similar expression for the non-interacting Green function G_0 [61]:

$$G_0(\mathbf{k}, t - t') = -ie^{-iE(\mathbf{k})(t-t')/\hbar} \left[\theta(t - t')\theta(k - k_F) - \theta(t' - t)\theta(k_F - k)\right] \tag{3.14}$$

$$\Downarrow$$

$$G_0(\mathbf{k}, \omega) = \lim_{\eta \to 0^+} \frac{\theta(k - k_F)}{\omega - \frac{1}{\hbar}E(\mathbf{k}) + i\eta} + \frac{\theta(k_F - k)}{\omega - \frac{1}{\hbar}E(\mathbf{k}) - i\eta} \tag{3.15}$$

The spectral functions for a non-interacting G_0 are therefore [62, p. 175]:

$$A_+(\mathbf{k}, \omega) = \theta(k - k_F)\delta\left(\omega - \frac{1}{\hbar}E(\mathbf{k})\right) \tag{3.16}$$

$$A_-(\mathbf{k}, \omega) = \theta(k_F - k)\delta\left(\omega - \frac{1}{\hbar}E(\mathbf{k})\right)$$

2 The Dyson equation and the Quasiparticle concept

In the previous sections we have studied several relevant properties of the interacting Green function; but, given that the interacting ground state $|\psi_0^N\rangle$ is not known, we haven't yet determined a way to calculate it.

The *Dyson equation* connects the unknown interacting Green function to the *non-interacting*

one [61]:

$$G(\mathbf{r}_1, \mathbf{r}_2, \omega) = G_0(\mathbf{r}_1, \mathbf{r}_2, \omega) + \iint d\mathbf{r}_3 d\mathbf{r}_4 G_0(\mathbf{r}_1, \mathbf{r}_3, \omega) \Sigma(\mathbf{r}_3, \mathbf{r}_4, \omega) G_0(\mathbf{r}_4, \mathbf{r}_2, \omega) \qquad (3.17)$$

Although the expression in momentum and frequency space is more common:

$$G(\mathbf{k}, \omega) = G_0(\mathbf{k}, \omega) + G_0(\mathbf{k}, \omega) \Sigma(\mathbf{k}, \omega) G(\mathbf{k}, \omega) \qquad (3.18)$$

It can be solved with respect to the interacting G:

$$G(\mathbf{k}, \omega) = \frac{G_0(\mathbf{k}, \omega)}{G_0(\mathbf{k}, \omega) - \Sigma(\mathbf{k}, \omega)} \qquad (3.19)$$

which can be written explicitly by substituting the known G_0 expression:

$$G(\mathbf{k}, \omega) = \frac{1}{\hbar\omega - E_{\mathbf{k}} + i\eta - \Sigma(\mathbf{k}, \omega)} \qquad (3.20)$$

associated to a spectral function [63, 64]:

$$A(\mathbf{k}, \omega) \propto \frac{|Im\Sigma(\mathbf{k}, \omega)|}{[\hbar\omega - E_{\mathbf{k}} - Re\Sigma(\mathbf{k}, \omega)]^2 + [Im\Sigma(\mathbf{k}, \omega)]^2} \qquad (3.21)$$

We can now discuss the *Quasiparticle concept* and start from the following question: *under which conditions we can consider the additional state as a separate particle that propagates in the system?*. In other words, the physical intuition behind this idea is to approximate the interacting system with a weakly interacting description composed by particles with different properties (for example different effective masses).
In order to describe the system in an (almost) free particle way, it should be possible to approximate G as:

$$G(\mathbf{k}, t) \approx -iZ_{\mathbf{k}} e^{-i\tilde{E}(\mathbf{k})t/\hbar} e^{-\Gamma_{\mathbf{k}} t} + G_{incoherent}(\mathbf{k}, t) \qquad (3.22)$$

where $e^{-\Gamma_{\mathbf{k}} t}$ indicates that this approximation holds only for a finite time interval ($\hat{c}_{\mathbf{k}}^{\dagger} \psi_0^N$ is not an eigenstate of the interacting system).
The question can be restated in terms of spectral functions. In the previous section we have seen that the non-interacting spectral functions (eq. 3.16) are proportional to Dirac delta; to preserve an expression like 3.22 therefore $A(\mathbf{k}, \omega)$ must be similar to the non-interacting one

(see also Figure 3.1):

$$A(\mathbf{k}, \omega) \approx Z_{\mathbf{k}} \frac{\Gamma_{\mathbf{k}}}{(\hbar\omega - E_{\mathbf{k}} - \Delta E_{\mathbf{k}})^2 + \Gamma_{\mathbf{k}}^2} \; + \; A_{incoherent}(\mathbf{k}, \omega) \qquad (3.23)$$

where $Z_{\mathbf{k}}$ is the renormalization factor and the energies $E(\mathbf{k}) - \Delta E(\mathbf{k})$ are renormalized with respect to the non-interacting ones; the width of peak $\Gamma_{\mathbf{k}}$ is equal to the inverse lifetime of the quasiparticle.

Let's compare it with equation 3.21: if the imaginary part of the self energy $Im\Sigma(\mathbf{k}, \omega)$ is much smaller than the other terms at the denominator the spectral function will possess a dominant peak at $E(\mathbf{k}) + Re\Sigma(\mathbf{k}, \omega)$ (with a broadening equal to $\Gamma_{\mathbf{k}} = Im\Sigma(\mathbf{k}, \omega)$).
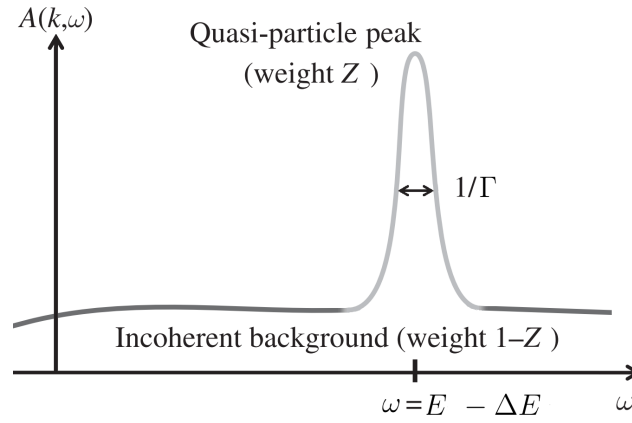

Figure 3.1: Qualitative picture of the spectral function: recognize the peak over an incoherent background.

18

3 The Hedin equations

In a seminal paper published in 1965 [11] Lars Hedin determined a set of five coupled integral equations which represents the starting point for the calculation of the self-energy and the interacting Green function:

$$G(1,2) = G_0(1,2) + \int d(3,4)G_0(1,3)\Sigma(3,4)G(4,2) \tag{3.24}$$

$$\Sigma(1,2) = i \int d(3,4)G(1,3)\Gamma(3,2,4)W(4,1^+) \tag{3.25}$$

$$W(1,2) = v(1,2) + \int d(3,4)v(1,3)P(3,4)W(4,2) \tag{3.26}$$

$$P(1,2) = -i \int d(3,4)G(1,3)G(4,1^+)\Gamma(3,4,2) \tag{3.27}$$

$$\Gamma(1,2,3) = \delta(1,2)\delta(1,3) + \int d(4,5,6,7)\frac{\delta\Sigma(1,2)}{\delta G(4,5)}G(4,6)G(7,5)\Gamma(6,7,3) \tag{3.28}$$

where we used the notation $1 = (\mathbf{r}_1,\sigma_1,t_1), 1^+ = (\mathbf{r}_1,\sigma_1,t_1 + \delta)$ with δ positive infinitesimal. The physical quantities involved in the Hedin equations are:

1. The self-energy Σ and the interacting Green function G, connected by the Dyson equation 3.24 already cited in the previous section.

2. The effective screened interaction W, which includes the screening of the bare Coulomb potential v present in a polarizable system. The connection between W and bare v is provided by the inverse dielectric function $W = \epsilon^{-1}v$.

3. The irreducible polarizability P, which can be defined as the variation of the density δn upon a small perturbation of the total potential δv_{tot} [6]:

$$P(1,2) \overset{\text{def}}{=} -i\frac{\delta G(1,1^+)}{\delta v_{tot}(2)} = \frac{\delta n(1)}{\delta v_{tot}(2)}$$

4. the vertex function Γ

$$\Gamma(1,2,3) = \frac{\delta G^{-1}(1,2)}{\delta v_{tot}(3)}$$

which accounts for two-particle effects in the polarizability P.

This set of equations is *exact* and must be solved self-consistently; however they are not tractable for any system of interest, and thus a simplification is required. The most used, the *GW approximation*, assumes:

$$\Gamma(1,2,3) = \delta(1,2)\delta(1,3) \tag{3.29}$$

which in turn implies:

$$G(1,2) = G_0(1,2) + \int d(3,4)G_0(1,3)\Sigma(3,4)G(4,2) \tag{3.30}$$

$$\Sigma(1,2) = iG(1,2)W(1^+,2) \tag{3.31}$$

$$W(1,2) = v(1,2) + \int d(3,4)v(1,3)P(3,4)W(4,2) \tag{3.32}$$

$$P(1,2) = -iG(1,2)G(2,1^+) \tag{3.33}$$

$$\Gamma(1,2,3) = \delta(1,2)\delta(1,3) \tag{3.34}$$

In this approximation the GW self-energy can be written as a convolution in frequency space:

$$\Sigma_{GW}(\mathbf{r}_1,\mathbf{r}_2,\omega_1) = \frac{i}{2\pi}\int d\omega_2 e^{i\omega_2 0^+}G(\mathbf{r}_1,\mathbf{r}_2,\omega_1+\omega_2)W(\mathbf{r}_1,\mathbf{r}_2,\omega_2) \tag{3.35}$$

and that the polarizability term in eq. 3.33 is formally equal to the RPA expression [65, p. 618][66, p. 41] and results in turn in an explicit expression equal to the independent-particle polarizability χ^0:

$$P_{\mathbf{q}}^{GW}(\mathbf{G}_1,\mathbf{G}_2,\omega) = \frac{1}{\Omega}\sum_{n,m}\sum_{\mathbf{k}}(f_{n\mathbf{k}} - f_{m\mathbf{k}-\mathbf{q}}) \tag{3.36}$$

$$\frac{\langle n,\mathbf{k}|\mathbf{q}+\mathbf{G}_1|m,\mathbf{k}-\mathbf{q}\rangle\,\langle m,\mathbf{k}-\mathbf{q}|-(\mathbf{q}+\mathbf{G}_2)|n,\mathbf{k}\rangle}{\omega + E_{m,\mathbf{k}-\mathbf{q}} - E_{n,\mathbf{k}} + i\eta sgn(E_{m,\mathbf{k}-\mathbf{q}} - E_{n,\mathbf{k}})} = \chi_{\mathbf{q}}^0(\mathbf{G}_1,\mathbf{G}_2,\omega)$$

4   The Quasiparticle equation

We start from the equation of motion for the one-particle Green function

$$\left[i\hbar\frac{\partial}{\partial t_1} + \frac{\hbar}{2m_e}\nabla_{\mathbf{r}_1}^2 - V_{ion}(\mathbf{r}_1)\right]G(1,2) - \int d3\Sigma(1,3)G(3,2) = \delta(1-2) \tag{3.37}$$

where we have used the compact notation $1 = \mathbf{r}_1, t_1$ and $\int d1 = \int d\mathbf{r}_1 \int dt_1$; the notation 1^+ is equal to $\lim_{\eta \to 0} \mathbf{r}_1, t_1 - i\eta$ and v is the Coulomb potential $v(1-2) = e^2 |\mathbf{r}_1 - \mathbf{r}_2|^{-1} \delta(t_1 - t_2)$. This expression can be derived [67] from the equation of motion of the field operator in the Heisenberg picture:

$$i\frac{\partial}{\partial t}\hat{\psi} = \{\hat{\psi}, \hat{H}\}$$

From the equation of motion the so-called *Quasiparticle equation* can be determined:

$$\left[-\frac{\hbar^2}{2m}\nabla^2 + v_{ext}(\mathbf{r}) + \frac{1}{2}\int d\mathbf{r}' \frac{n(\mathbf{r}')}{|\mathbf{r} - \mathbf{r}'|} \right] \Psi_m(\mathbf{r}) + \int d\mathbf{r}'\Sigma\left(\mathbf{r}, \mathbf{r}', \frac{\epsilon_m}{\hbar}\right) \Psi_m(\mathbf{r}') = \epsilon_m \Psi_m(\mathbf{r}) \quad (3.38)$$

The equation is non-linear in the energies (it requires a self-consistent solution) and possesses a structure similar to the Kohn-Sham equation. This analogy can provide a physical insight into the self-energy: Σ is the so-called *irreducible self-energy*, a non-local, non-hermitian and frequency dependent operator which implicitly contains all many-body exchange and correlation interactions.

5 GW Technical implementations

5.1 Calculation of χ and Σ from the spectral representation in VASP

The calculation of the RPA polarizability within the spectral method starts by calculating the spectral representation of the polarizability [68, 69]:

$$\chi_{\mathbf{q}}^{S}(\mathbf{G}_1, \mathbf{G}_2, \omega') = \frac{1}{\Omega} \sum_{n,m} \sum_{\mathbf{k}} \delta(\omega' - (E_{n\mathbf{k}} - E_{m\mathbf{k}-\mathbf{q}})) sgn(\omega')(f_{n\mathbf{k}} - f_{m\mathbf{k}-\mathbf{q}}) \qquad (3.39)$$

$$\langle n, \mathbf{k} | \mathbf{q} + \mathbf{G}_1 | m, \mathbf{k} - \mathbf{q} \rangle \, \langle m, \mathbf{k} - \mathbf{q} | -(\mathbf{q} + \mathbf{G}_2) | n, \mathbf{k} \rangle$$

where the notation $\langle u | \mathbf{G} | o \rangle \equiv \langle u | e^{i\mathbf{G} \circ \mathbf{r}} | o \rangle$ is used. The spectral function is evaluated for ω' defined on the same grid used for ω (formally $\{\omega_i\} = \{\omega_j'\}$).

The presence of $\delta(\omega' - (E_{n\mathbf{k}} - E_{m\mathbf{k}-\mathbf{q}}))$ implies that contributions from states $n, \mathbf{k}$ and $m, \mathbf{k} - \mathbf{q}$ is non-zero only for frequencies $\omega' = E_{n\mathbf{k}} - E_{m\mathbf{k}-\mathbf{q}}$. The polarization is calculated on a discrete grid, and Shishkin *et al.* [68] (as implemented in VASP) approximates the δ with a triangular function which is non-zero only for frequencies closest to $E_{n\mathbf{k}} - E_{m\mathbf{k}-\mathbf{q}}$, i.e. $\omega_i < E_{n\mathbf{k}} - E_{m\mathbf{k}-\mathbf{q}} < \omega_{i+1}$. This introduces a significant speedup with respect to the standard independent particle polarizability

$$\chi_{\mathbf{q}}^{0}(\mathbf{G}_1, \mathbf{G}_2, \omega) = \frac{1}{\Omega} \sum_{n,m} \sum_{\mathbf{k}} (f_{n\mathbf{k}} - f_{m\mathbf{k}-\mathbf{q}}) \qquad (3.40)$$

$$\frac{\langle n, \mathbf{k} | \mathbf{q} + \mathbf{G}_1 | m, \mathbf{k} - \mathbf{q} \rangle \, \langle m, \mathbf{k} - \mathbf{q} | -(\mathbf{q} + \mathbf{G}_2) | n, \mathbf{k} \rangle}{\omega + E_{m,\mathbf{k}-\mathbf{q}} - E_{n,\mathbf{k}} + i\eta sgn(E_{m,\mathbf{k}-\mathbf{q}} - E_{n,\mathbf{k}})}$$

because $\chi_{\mathbf{q}}^{0}$ inherently exhibits a linear scaling with respect to the number of frequencies (i.e. each sum term $n\mathbf{k}$, $m\mathbf{k} - \mathbf{q}$ contributes to all frequencies), while the cost for the evaluation of χ^{S} is twice that required for static calculation (the term $n\mathbf{k}$, $m\mathbf{k} - \mathbf{q}$ contributes *only* to two frequencies ω_i, ω_{i+1}).

The spectral function is related to the polarizability by $\chi_{\mathbf{q}}^{S}(\mathbf{G}_1, \mathbf{G}_2, \omega) = \pi^{-1} Im[\chi_{\mathbf{q}}^{0}(\mathbf{G}_1, \mathbf{G}_2, \omega)]$. The Hilbert (or Kramers-Kronig) transform can be applied to retrieve the polarizability:

$$\chi_{\mathbf{q}}^{0}(\mathbf{G}_1, \mathbf{G}_2, \omega) = \int_{0}^{\infty} d\omega' \chi_{\mathbf{q}}^{S}(\mathbf{G}_1, \mathbf{G}_2, \omega') \left(\frac{1}{\omega + \omega' + i\eta} - \frac{1}{\omega - \omega' + i\eta} \right) \qquad (3.41)$$

Where we stress than ω and ω' are evaluated using the same discrete frequency grid. The Transform can be expressed as a summation over the frequency grid $\{\omega_j\}$ as $\sum_{\omega_j'} t(\omega_i, \omega_j') \chi_{\mathbf{q}}^{S}(\mathbf{G}_1, \mathbf{G}_2, \omega_j')$ with weights $t(\omega_i, \omega_j')$ (see Shishkin *et al.* [68] for more details).

Let's briefly outline now the procedure used for the evaluation of the self energy diagonal elements, which follows a similar blueprint:

$$\langle n\mathbf{k}|\Sigma(\omega)|n\mathbf{k}\rangle = \frac{1}{\Omega}\frac{i}{2\pi}\sum_{\mathbf{q}}\sum_{\mathbf{G}_1,\mathbf{G}_2}\sum_{m:all}\int d\omega' W_{\mathbf{q}}(\mathbf{G}_1,\mathbf{G}_2,\omega')\times \tag{3.42}$$

$$\langle n,\mathbf{k}|\mathbf{q}+\mathbf{G}_1|m,\mathbf{k}-\mathbf{q}\rangle\,\langle m,\mathbf{k}-\mathbf{q}|-(\mathbf{q}+\mathbf{G}_2)|n,\mathbf{k}\rangle\times$$

$$\left[\frac{1}{\omega_{m,\mathbf{k}-\mathbf{q}}+\omega'+i\eta sgn(E_{n,\mathbf{k}-\mathbf{q}}-\mu)}+\frac{1}{\omega_{m,\mathbf{k}-\mathbf{q}}-\omega'+i\eta sgn(E_{n,\mathbf{k}-\mathbf{q}}-\mu)}\right]$$

with the notation $\omega_{m,\mathbf{k}-\mathbf{q}}=\omega-E_{m,\mathbf{k}-\mathbf{q}}$.

$\langle \mathbf{k}|\Sigma(\omega)|n\mathbf{k}\rangle$ can be evaluated in three different steps [68]. The first step performs the Hilbert Transform of $W_{\mathbf{q}}$:

$$C_{\mathbf{q}}^{\pm}(\mathbf{G}_1,\mathbf{G}_2,\omega_{n,\mathbf{k}}) = \frac{i}{2\pi}\int_0^{\infty}d\omega' W_{\mathbf{q}}(\mathbf{G}_1,\mathbf{G}_2,\omega')\left(\frac{1}{\omega_{m,\mathbf{k}-\mathbf{q}}+\omega'\pm i\eta}+\frac{1}{\omega_{m,\mathbf{k}-\mathbf{q}}-\omega'\pm i\eta}\right) \tag{3.43}$$

To reduce the computational time an approximation is introduced: $C_{\mathbf{q}}^{\pm}(\mathbf{G}_1,\mathbf{G}_2,\omega_{n,\mathbf{k}})$ is evaluated on the same frequency grid of ω, which means dropping the dependence of ω on the eigenvalues $E_{n\mathbf{k}}$. This implies that for a single $\mathbf{q}$ the Hilbert transform of $W_{\mathbf{q}}$ is evaluated once for each points of the frequency grid; the dependence of ω on $E_{n\mathbf{k}}$ would require a complete recalculation over the entire $\{\omega_i\}$ grid for each $E_{n\mathbf{k}}$.

The second step consists in the contraction over the $\mathbf{G}_1,\mathbf{G}_2$ indexes:

$$S_{n\mathbf{k},m\mathbf{k}-\mathbf{q}}^{\pm}(\omega) = \frac{1}{\Omega}\sum_{\mathbf{G}_1,\mathbf{G}_2}C_{\mathbf{q}}^{\pm}(\mathbf{G}_1,\mathbf{G}_2,\omega)\,\langle n,\mathbf{k}|\mathbf{q}+\mathbf{G}_2|m,\mathbf{k}-\mathbf{q}\rangle\,\langle m,\mathbf{k}-\mathbf{q}|-(\mathbf{q}+\mathbf{G}_2)|n,\mathbf{k}\rangle \tag{3.44}$$

The variables $S_{n\mathbf{k},m\mathbf{k}-\mathbf{q}}^{\pm}$ are called *screened two-electron integrals*. In the third step the expectation value of the self-energy operator can be calculated directly from these screened two-electron integrals:

$$\langle n\mathbf{k}|\Sigma(\omega=E_{n\mathbf{k}})|n\mathbf{k}\rangle = \sum_m\sum_{\mathbf{q}}sgn(E_{n\mathbf{k}}-E_{n\mathbf{k}-\mathbf{q}})S_{n\mathbf{k},m\mathbf{k}-\mathbf{q}}^{sign}(|E_{n\mathbf{k}}-E_{m\mathbf{k}-\mathbf{q}}|) \tag{3.45}$$

where we used the notation $sign = sgn(E_{n\mathbf{k}}-\mu)sgn(E_{n\mathbf{k}}-E_{m\mathbf{k}-\mathbf{q}})$.
Both $C_{\mathbf{q}}^{\pm}(\mathbf{G}_1,\mathbf{G}_2,\omega)$ and the screened two-electron integrals are evaluated on the same frequency grid $\{\omega_i\}$. However in order to calculate $\langle n\mathbf{k}|\Sigma(E_{n\mathbf{k}})|n\mathbf{k}\rangle$ the values of $S_{n\mathbf{k},m\mathbf{k}-\mathbf{q}}^{\pm}$ evaluated at $|E_{n\mathbf{k}}-E_{m\mathbf{k}-\mathbf{q}}|$ need to be computed. A linear interpolation of $S_{n\mathbf{k},m\mathbf{k}-\mathbf{q}}^{\pm}$ between the two closest frequency points $\omega_i<|E_{n\mathbf{k}}-E_{m\mathbf{k}-\mathbf{q}}|<\omega_{i+1}$ is hence performed.

This is turn means that, similarly to χ^S, the contribution of the terms $n\mathbf{k}$, $m\mathbf{k} - \mathbf{q}$ to the sum of $\langle n\mathbf{k}|\Sigma(\omega = E_{n\mathbf{k}})|n\mathbf{k}\rangle$ depends only on the two frequencies $\omega_i < |E_{n\mathbf{k}} - E_{m\mathbf{k}-\mathbf{q}}| < \omega_{i+1}$: Again this implies that the computational cost is basically independent of the frequency grid dimension and twice that of a static calculation. The downside of this approach is that the response function must be allocated in memory for all frequencies $\{\omega_i\}$, which significantly increases the memory requirements.

5.2 G_0W_0 and the solution of the quasiparticle equation

The standard numerical implementation of G_0W_0 method relies on the Quasiparticle Equation (eq. 3.38) and exploits different approximations:

1. The interacting Green function in the self-energy $\Sigma = GW$ is approximated by the non-interacting one; both the Green Function and the screened potentials are calculated from the one-particle states and eigenvalues: $\Sigma \approx G_0W_0$.

2. The single-particle orbitals are not updated and kept at starting point level (which is typically a DFT calculation): $\psi^{GW} \approx \psi^{KS}$.

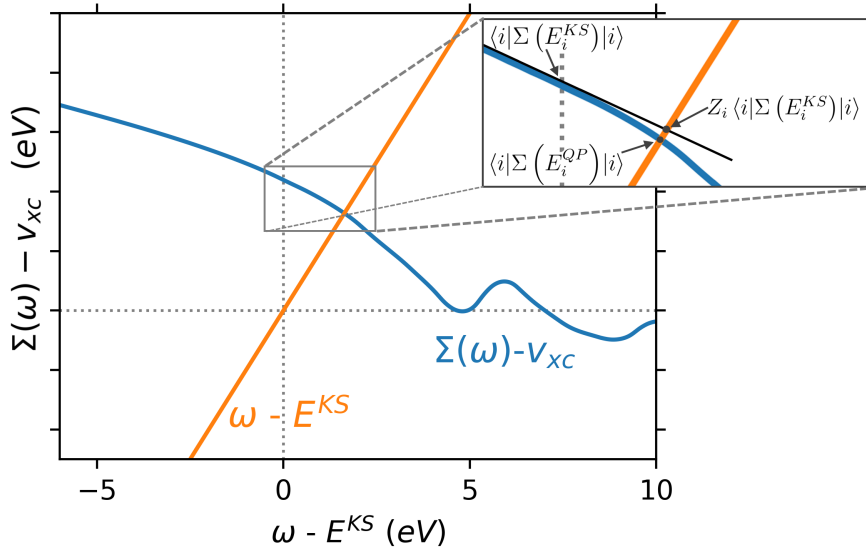**Figure 3.2:** Graphical representation of the solution of the Quasiparticle approximation. The orange line represents $\omega - E_{KS}$, the blue line is proportional to the self-energy and the black line the linear approximation of the self-energy. The intersection between orange and blue lines represent the solution of the QPE, while the intersection between orange and blue line is the solution of the linearized equation.

3. The updated eigenvalues are determined by solving the Quasiparticle Equation (QPE):

$$E_i^{QP} = Re\left[\langle \psi_i^{KS} | T + V_{ext} + V_H + \Sigma(E_i^{QP}) | \psi_i^{KS} \rangle \right] \qquad (3.46)$$

The self-energy term is in general complex; however $Im[\Sigma]$ is typically small for frequencies around E_i^{QP} in the quasiparticle approximation and thus can be neglected [30].

4. The QPE in eq. 3.46 must be solved self-consistently (Σ depends on E_i^{QP}). From the expansion at first order of the self-energy around $E_{n\mathbf{k}}^{KS}$ the update equation can be obtained:

$$\Sigma(\mathbf{r}, \mathbf{r}', E_i^{QP}) = \Sigma(\mathbf{r}, \mathbf{r}', E_i^{KS}) + \left(E_i^{QP} - E_i^{KS} \right) \frac{\partial \Sigma(\mathbf{r}, \mathbf{r}', \omega)}{\partial \omega}\bigg|_{E_i^{KS}} + O\left((E_i^{QP} - E_i^{KS})^2 \right)$$

$$(3.47)$$

which can be used to reach a closed expression for E_i^{QP}:

$$E_i^{QP} - E_i^{KS} = Z_i \langle \psi_i^{KS} | \Sigma(E_i^{KS}) - V_{xc} | \psi_i^{KS} \rangle \qquad (3.48)$$

where Z_i is the renormalization factor, and measures how much spectral weight the quasiparticle peak carries:

$$Z_i = \left[1 - \frac{\partial \Sigma(\mathbf{r}, \mathbf{r}', \omega)}{\partial \omega}\bigg|_{\omega = E_i^{KS}} \right]^{-1} \qquad (3.49)$$

The graphical solution to eq. 3.48 is illustrated in Figure 3.2.

5.3 GW with the inclusion of off-diagonal terms: fully self-consistent GW in VASP

The G_0W_0 schemes discussed until now iterate only the eigenvalues and keep the single-particle orbitals fixed at DFT level; in order to iterate also the orbitals the off-diagonal self-energy terms $\langle i | \Sigma(\omega) | j \rangle$ must be included in the calculation. The scheme employed in VASP, often labeled `QSGW`, is a variation of the method introduced by van Schilfgaarde *et al.* [70, 71]:

1. We start from a mean-field (typically DFT) starting point $\{E_i^{(0)}, \left| \psi_i^{(0)} \right\rangle\}$; from these starting wavefunctions the scheme determines the *full* self energy matrix (beyond the di-

agonal approximation) in the mean-field orbital basis $\left\langle \psi_i^{(0)} \middle| \Sigma(\omega) \middle| \psi_j^{(0)} \right\rangle$. From the self-energy operator $\tilde{\Sigma}(\omega) = \sum_{ij} \left| \psi_i^{(0)} \right\rangle \left\langle \psi_i^{(0)} \middle| \Sigma(\omega) \middle| \psi_j^{(0)} \right\rangle \left\langle \psi_j^{(0)} \right|$ a *non-linear one-electron* Schrödinger equation is constructed:

$$\left[T + v_{ext} + V_h + \tilde{\Sigma}(E_i^{(1)}) \right] \left| \psi_i^{(1)} \right\rangle = E_i^{(1)} \left| \psi_i^{(1)} \right\rangle \tag{3.50}$$

2. (1°approximation) To avoid a non-linear problem, the self-energy is linearized around $E_i^{(0)}$:

$$\Sigma(E_i^{(1)}) = \Sigma(E_i^{(0)}) + \frac{\partial \Sigma(E_i^{(0)})}{\partial E_i^{(0)}} (E_i^{(1)} - E_i^{(0)}) \tag{3.51}$$

By rearranging the terms a generalized linear (but non Hermitian) problem is obtained:

$$\underbrace{\left[h_0 + \tilde{\Sigma}(E_i^{(0)}) - \xi(E_i^{(0)}) E_i^{(0)} \right]}_{H(E_i^{(0)})} \left| \psi_i^{(1)} \right\rangle = E_i^{(1)} \underbrace{\left[1 - \xi(E_i^{(0)}) \right]}_{S(E_i^{(0)})} \left| \psi_i^{(1)} \right\rangle \tag{3.52}$$

with the notations $\xi(E_i^{(0)}) = \frac{\partial \tilde{\Sigma}(E_i^{(0)})}{\partial E_i^{(0)}}$ and $S(E_i^{(0)}) = 1 - \xi(E_i^{(0)})$ (called overlap matrix).

3. (2° approximation) The GW self-energy is non Hermitian [72]: this implies that the eigenvalues of eq. 3.52 are complex, the eigenstates are not guaranteed to be orthogonal and one should distinguish between left and right eigenvectors. To recover a Hermitian expression for the self energy operator, $\tilde{\Sigma}$ is approximated by

$$\langle i | \tilde{\Sigma}^{herm} | j \rangle = \frac{1}{2} \left[Re[\left\langle \psi_i^{(0)} \middle| \Sigma(E_i^{(0)}) \middle| \psi_j^{(0)} \right\rangle] + Re[\left\langle \psi_j^{(0)} \middle| \Sigma(E_j^{(0)}) \middle| \psi_i^{(0)} \right\rangle] \right] \tag{3.53}$$

where $Re()$ indicates the Hermitian part. The overlap matrix is approximated in an similar way.

This approximation was justified by van Schilfgaarde *et al.* [70] as the expression which determines a static hamiltonian H_0 *as close as possible* to the dynamical hamiltonian $H(\omega) = T + v_{ext} + V_h + \tilde{\Sigma}(\omega)$, in the sense that minimizes the difference $\Delta V(\omega) = H(\omega) - H_0$. Furthermore, Shishkin *et al.* [73] attests that this expression provides band gaps with an accuracy of 1% of those associated with the right-hand eigenvectors of the linearized non-Hermitian problem plus a successive reorthogonalization of the eigenstates.

4. The generalized hermitian problem is finally solved:

$$S^{herm^{-1/2}} H^{herm} S^{herm^{-1/2}} U = U\Lambda \qquad (3.54)$$

where U is a unitary matrix and Λ is the diagonal matrix composed by the eigenvalues. The new orbitals are determined by rotating the old wavefunctions through the U matrix $\psi_i^{(1)} = \sum_j U_{ji} \psi_j^{(0)}$.

The inclusion of non-diagonal Σ elements allows QSGW to achieve independence from the starting point, one of the most problematic aspects of perturbative diagonal G_0W_0. The advantage is particularly evident for materials where the DFT description (one of the most common starting points) is particularly flawed, such as small-gap semiconductors for which DFT predicts a metallic behaviour. In these cases diagonal G_0W_0 results are strongly affected by the metallic starting point, while QSGW strongly improves the description of the electronic structure [72]. Other typical examples are very large gap semiconductors such as diamond, MgO, CaO [74]: DFT strongly underestimates the experimental band gap (which in turn causes an underestimation of G_0W_0 results) while QSGW reaches a better agreement with experimental data.

Besides these outlier cases, it's however well documented in literature [74, 75, 76, 77, 78, 79] that iterating QSGW beyond the one-shot approach (and hence beyond G_0W_0 with the inclusion of the off-diagonal elements) produces a systematic overestimation of the experimental gap. This effect can be explained by looking at the screening term W, usually calculated in the RPA approximation. On the one hand the polarizability, and thus the screening is roughly inversely proportional to the band gap; hence a DFT starting point causes an overestimation of the screening. On the other hand, the neglect of electron-hole interaction in the RPA screened potential introduces an underestimation of the screening [73, 80]. The accuracy of the G_0W_0 approximation stems therefore from a cancellation of these two opposite errors [81, 82, 83]. Self-consistency (including recalculating W at each iteration) does not exploit this error cancellation, and the resulting underscreening causes an overestimation of the experimental gaps. In this sense, van Schilfgaarde and coworkers found that by empirically rescaling W by ~ 0.8 factor results were consistently improved [84, 85]. It has been argued that introducing the vertex corrections in the self-consistence calculation [73, 86] restores an accurate agreement with experimental data.

Beyond the gap, QSGW is able to provide a correct description of wavefunction orbital characters for materials wrongly characterized by DFT. For example, Bruneval et $al.$ [75] found that for Silicon or Argon the overlap between LDA and QSGW orbitals $\langle \psi^{LDA} | \psi^{QSGW} \rangle$ is greater than 99.9% for valence states at k-points with strong symmetry constraints such as Γ; however also for such classical materials the overlap is lowered for conduction states outside high symmetry k-points (up to $\sim 95\%$). Recently, Salas-Illanes et $al.$ [74] discussed how for the ionic materials LiF and MgO the QSGW clearly modifies the electronic charge density

27

(with respect to LDA densities) in the vicinity of the ions.

For materials where the orbitals character characterization by DFT is qualitatively wrong (such as in topological insulators [87, 88, 89] and materials with strong p-d hybridization [90, 91, 92, 93]), the inclusion of the off-diagonal Σ elements has proved able to restore the correct description. Significant changes of the band curvature due to the introduction of off-diagonal elements have also been noted for bulk GaAs and Argon [74]; in particular the LDA picture of Argon (wrongly) predicts an indirect bandgap, while QSGW describes a direct one.

5.4 Calculation of χ and Σ from Plasmon Pole model

An efficient way to calculate the integral over frequencies in the self energy expression is to approximate the frequency dependence of ϵ^{-1} and $W_{\mathbf{q}}$ with a single pole function [20, 94, 30, 95]. The approximation is called Plasmon Pole Model (PPM): two main variants exist (the Godby-Needs PPM [96, 97] and Hybertsen-Louie one [98]), though other versions have been developed (such as the Linder-Horsch [99] and Engel-Farid [100] PPMs).
Godby-Needs and Hybertsen-Louie PPMs define ϵ^{-1} as:

$$
\begin{aligned}
Im[\epsilon^{-1}_{\mathbf{G}_1,\mathbf{G}_2}] &= 1 - \frac{A_{\mathbf{G}_1,\mathbf{G}_2}(\mathbf{q})\bar{\omega}^2_{\mathbf{G}_1,\mathbf{G}_2}(\mathbf{q})}{\omega^2 - \bar{\omega}^2_{\mathbf{G}_1,\mathbf{G}_2}(\mathbf{q})} \\
Re[\epsilon^{-1}_{\mathbf{G}_1,\mathbf{G}_2}] &= A_{\mathbf{G}_1,\mathbf{G}_2}(\mathbf{q})\left[\delta(\omega - \bar{\omega}_{\mathbf{G}_1,\mathbf{G}_2}(\mathbf{q})) - \delta(\omega + \bar{\omega}_{\mathbf{G}_1,\mathbf{G}_2}(\mathbf{q}))\right]
\end{aligned}
\tag{3.55}
$$

where the second expression is computed by the Kramers-Kronig transform. $A_{\mathbf{G}_1,\mathbf{G}_2}(\mathbf{q})$ and $\omega_{\mathbf{G}_1,\mathbf{G}_2}(\mathbf{q})$ are parameters of the model and represent respectively the plasmon frequency and the effective peak amplitude. They can be determined by enforcing specific constraints:

1. Godby-Needs PPM reproduces exactly ϵ^{-1} at $\omega = 0$ and at the plasmon frequency $\omega = i\omega_p$.

2. The Hybertsen-Louie PPM imposes a generalized f-sum rule.

The great advantage of PPMs is that the self-energy integral over the frequencies is greatly simplified and can be performed analytically [101]:

$$
\langle n\mathbf{k}|\Sigma(\omega)|n\mathbf{k}\rangle \propto \sum_m \sum_{\mathbf{q}} \sum_{\mathbf{G}_1,\mathbf{G}_2} \frac{\bar{\omega}_{\mathbf{G}_1,\mathbf{G}_2}(\mathbf{q})v(\mathbf{q},\mathbf{G}_1,\mathbf{G}_2)\rho_{nm}(\mathbf{k},\mathbf{q},\mathbf{G}_1)\rho^*_{nm}(\mathbf{k},\mathbf{q},\mathbf{G}_2)}{\omega - E_{m,\mathbf{k}-\mathbf{q}} + (\bar{\omega}_{\mathbf{G}_1,\mathbf{G}_2}(\mathbf{q}) - i\eta)sgn(\mu - E_{m,\mathbf{k}-\mathbf{q}})}
\tag{3.56}
$$
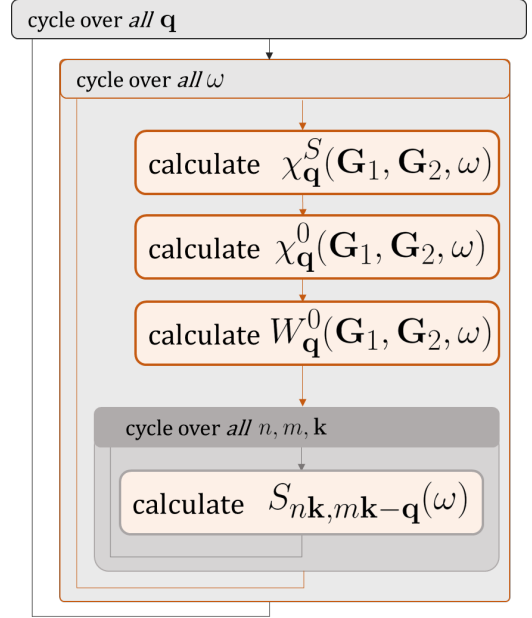
with $v(\mathbf{q},\mathbf{G}_1,\mathbf{G}_2) = 4\pi/|\mathbf{q}+\mathbf{G}_1||\mathbf{q}+\mathbf{G}_2|$ and $\rho_{nm}(\mathbf{k},\mathbf{q},\mathbf{G}) = \langle n,\mathbf{k}|\mathbf{q}+\mathbf{G}|m,\mathbf{k}-\mathbf{q}\rangle$.

The Plasmon Pole Approximation (in the Godby-Needs version) was employed in calculations using the Yambo software [19, 20] for the SrTiO$_3$ monolayer.

5.5 Implementation details: checkpointing feature for G_0W_0 runs in VASP

The application of G_0W_0 schemes notoriously requires large computational resources. These calculations would benefit from a checkpointing logic which supports a stop-resume behavior: such feature would allow the user to split a single G_0W_0 run in multiple, smaller, calculations. This would in turn help managing lengthy runs on cluster with small wall-time limits or modest resources and offer the possibility of creating mid-run backups.

The last public version of VASP (version 6.3.1) does not however currently support such feature; we therefore implemented it for the spectral method in the G_0W_0 scheme (`ALGO = EVGW0 ; NELMGW = 1` flags). This feature was employed during the convergence studies of monolayer $SrTiO_3$ (see chapter 7).

Figure 3.3: Example implementation of a simple Workchain class, which receives a single input argument (the geometric structure of a materials) and returns its energy. The workchain executes two methods sequentially.

We will briefly outline here the strategy used. The spectral method discussed in section 5.1 is implemented through a series of cycles (see Fig. 3.3). The outer level cycle loops over all $\mathbf{q}$ in the Irreducible Brillouin Zone. Before this cycle the main variables (the screened two-electron integrals and the response function) one plus several support variables are initialized to zero. For each $\mathbf{q}$ the screened potential at that $\mathbf{q}$ (for all frequencies and $\mathbf{G}$ vectors) is calculated; then all contributions deriving from that $W_{\mathbf{q}}$ are accumulated into the screened two-electron integral variable. In other words each iteration of the $\mathbf{q}$ cycle determines the contributions to $S_{n\mathbf{k},m\mathbf{k}-\mathbf{q}}(\omega)$ for all $n, m, \mathbf{k}, \omega$ at that fixed $\mathbf{q}$.

Saving at each cycle $W_{\mathbf{q}}(\mathbf{G}_1, \mathbf{G}_2, \omega)$ was considered not efficient: for large cells saving $W_{\mathbf{q}}$ for all frequencies would require an exceedingly large storage due to the sizable dimension of the $\mathbf{G}$ basis set. For example, a *single* $W_{\mathbf{q}}$ for the $SrTiO_3$ monolayer discussed in chapter 7 would require around $\sim$ 88 GB of storage in the production setup (a vacuum size of 40 Å, 96 frequency points and a cutoff of 325 eV).

The solution we adopted involves saving to disk, *at the end of each $\mathbf{q}$ iteration*, the screened two-electron integral variable. The great advantage of this approach is that $S_{n\mathbf{k},m\mathbf{k}-\mathbf{q}}$ requires a smaller storage dimension because $\mathbf{G}_1, \mathbf{G}_2$ are already contracted and are not indexes of S. The implementation of the checkpointing feature required different steps; the first was the

addition of INCAR flags to control the feature, which we document below:

1. The flags `LKCHI` and `LKTOTCHI` allow to run the outer q-point cycle over a selection of the IBZ **q**-points; the indexes of the selected **q**-points should be passed as an array to `LKTOTCHI`. The introduction of these flags have been developed in collaboration with PhD. Pietro Maria Forcella of the University of L'Aquila.

2. The flags `LCHI_READ` and `LCHI_WRITE` activate the possibility of respectively reading and writing on disk the screened two electron integrals.

If activated this feature initializes the screened two-electron variable (before the **q** cycle) by loading it from disk and distributing it to all MPI-tasks and $S_{n\mathbf{k},m\mathbf{k}-\mathbf{q}}$ is saved to disk at the end of each **q** cycle.

The current method currently does not support GW schemes with the inclusion of off-diagonal self-energy term (the scheme is defined as `ALGO=QPGW` in VASP and discussed in section 5.3). In a QSGW run a supplementary variable is calculated during the **q** cycle (in addition to $W_{\mathbf{q}}$ and the screened two-electron integrals):

$$\sum_{\mathbf{G}_1,\mathbf{G}_2} C_{\mathbf{q}}^{\pm}(\mathbf{G}_1,\mathbf{G}_2,\omega) \langle n,\mathbf{k}|e^{i(\mathbf{q}+\mathbf{G}_1)\cdot\mathbf{r}}|m,\mathbf{k}-\mathbf{q}\rangle \langle m,\mathbf{k}-\mathbf{q}| \, e^{-i(\mathbf{q}+\mathbf{G}_2)\cdot\mathbf{r}}$$

This expression is subsequently used to construct the hamiltonian. This variable must be first collected and correctly merged from all MPI threads then saved to disk; after a restart, VASP should re-load it and redistribute correctly to all MPI threads. Implementation is currently in progress: support of the checkpointing for QSGW is presently only preliminary and still requires extensive testing.

Chapter 4

The Bethe-Salpeter Equation

It's well documented in literature that excitonic effects should be taken into account in order to reproduce the optical properties of semiconductors [6]. In order to describe the electron-hole interaction we start by the definition of the *two-particle* Green function:

$$G(1,2,3,4) = (-i)^2 \left\langle \psi_0^N \middle| \hat{T} \left[\psi(1)\psi(2)\psi^\dagger(3)\psi^\dagger(4) \right] \middle| \psi_0^N \right\rangle \tag{4.1}$$

from the two-particle Green function the *4-particle reducible polarizability* can be defined:

$$L(1,2,3,4) = L_0(1,2,3,4) - G(1,2,3,4) \tag{4.2}$$

where the uncorrelated part associated to the independent particle polarizability $L_0(1,2,3,4) = iG(1,3)G(4,2)$ has been subtracted from the Green function. L describes the independent (without interaction) propagation of two particles. We note that by setting $3 = 1$, $4 = 2$ L^0 describes the (non-interacting) propagation of an electron-hole pair: this corresponds to the expression introduced in eq. 3.33.

The reducible polarizability satisfies a Dyson-like equation [65, 102], the famous Bethe-Salpeter Equation (BSE):

$$L(1,2,1',2') = L(1,2,1',2') + \int d(3,4,3',4') L_0(1,2,3',4') K(3,4,3',4') L(3',4',1',2') \tag{4.3}$$

The kernel $K(3,4,3',4')$ describes the effective interaction between the two particles, and can be written as:

$$K(3,4,3',4') = \delta(3,4)\delta(3',4')v(3,3') + i\frac{\delta\Sigma_{xc}(3,3')}{\delta G(4,4')} \tag{4.4}$$

Up to now we have not specified the functional form of Σ_{xc}; however to solve explicitly the equation a choice must be taken:

1. If the non-local and dynamic $\Sigma_{xc}(3,3')$ is approximated with the (local and non-dynamic) Kohn-Sham exchange-correlation potential $\Sigma_{xc}(3,3') \approx \delta(3,3')v_{xc}(3)$ and the non-interacting Kohn-Sham Green function G_0^{KS} is used the linear response screening equation of Time-Dependent DFT (the Casida equation) is reached. One of the main advantages of this approach is the lower computational cost: the two-particle equation is reduced to a single particle one [103].

2. By approximating $\Sigma_{xc}(3,3')$ with the non-local (but still non-dynamic) Fock exchange the linear response time-dependent Hartree-Fock [104] is obtained.

3. From the GW self-energy $\Sigma_{xc} = iG(1,2)W(1,2)$ the derivative can be written as:

$$\frac{\delta\Sigma^{GW}(3,3')}{\delta G(4,4')} = i\delta(3,4)\delta(3',4')W(3,3') + G(3,4)\frac{\delta W(3,4)}{\delta G(4',3')} \qquad (4.5)$$

At this point a *first approximation* is introduced: the second term in eq. 4.5 is neglected. This term contains the derivative $\delta W/\delta G$, which describes the variation of the screening potential with respect to G [105, 106]. The approximation is physically motivated by the fact that, while the first term in eq. 4.5 is first order in W, the second one contains only higher orders in W:

$$\frac{\delta W(3,4)}{\delta G(4',3')} \propto [W(3,4)W(4',3') + W(1,4')W(4,3')]G(4',4) \qquad (4.6)$$

This result can be proven [63, chap. 18] by starting from the inversion relation:

$$\frac{\delta W}{\delta G} = W\frac{\delta W^{-1}}{\delta G}W$$

(determined by deriving both terms of $WW^{-1} = 1$). The Dyson equation for W is the starting point for evaluating $\delta W^{-1}/\delta G$:

$$W(1,1') = v(1,1') + \int d(3,4)v(1,3)P(3,4)W(4,1')$$

approximate $P \approx P_0$ and use $\int d2G(1,2)G^{-1}(2,1') = \int d2G^{-1}(1,2)G(2,1') = \delta(1,1')$ for:

$$W^{-1}(1,1') = v(1,1') + G(1,1')G(1',1)$$

(this can be proven by multiplying both sides by $G_0^{-1}G^{-1}$ with indexes chosen in order to isolate L_0). The derivative is therefore equal to:

$$\frac{\delta W^{-1}(1,1')}{\delta G(2,2')} = [\delta(1,2)\delta(1',2)G(1'1) + G(1,1')\delta(1,2')\delta(1',2)]$$

The approximation has been tested and validated for bulk silicon [107]. The following kernel is therefore obtained:

$$K(3,4,3',4') = \delta(3,4)\delta(3',4')v(3,3') - \delta(3,3')\delta(4,4')W(3,4) \tag{4.7}$$

The two terms are respectively called exchange and direct term.
At this point _a second approximation_ is typically introduced. Due to the presence of W in eq. 4.7, the BSE is frequency dependent; however, similarly to the COHSEX approximation in the GW approach, this frequency dependence is neglected. The static approximation is equivalent to consider the interaction between the two particles (electron and hole) instantaneous as $W(1,2) = W(\mathbf{r}_1, \mathbf{r}_2)\delta(t_1 - t_2)$.

In this section the Bethe-Salpeter equation has been derived starting from the two-particle Green function. We note that other starting points are possible, such as including vertex corrections in the self energy; for more details see Onida _et al._ [65].

1 Solution of the BSE: diagonalization of an effective two particle Hamiltonian

The most common approach to solve the Bethe-Salpeter equation involves mapping the equation onto an effective two-particle hamiltonian which can be diagonalized with standard algebra techniques.
The first step is expanding L and L_0 over a basis set composed by products of single particle

orbitals $\psi_n(\mathbf{r})$ called *transition space*:

$$L(1, 2, 1', 2') = \sum_{n_1 n_2} \sum_{n_1' n_2'} L_{n_1 n_2}^{n_1' n_2'} \psi_{n_1}^*(\mathbf{r}_1)\psi_{n_2}(\mathbf{r}_2)\psi_{n_{1'}}(\mathbf{r}_{1'})\psi_{n_{2'}}^*(\mathbf{r}_{2'}) \tag{4.8}$$

$$L_{n_1 n_2}^{n_1' n_2'} = \left\langle \psi_{n_1}^*(\mathbf{r}_1)\psi_{n_2}(\mathbf{r}_2) \middle| L(1, 2, 1', 2') \middle| \psi_{n_{1'}}^*(\mathbf{r}_{1'})\psi_{n_{2'}}(\mathbf{r}_{2'}) \right\rangle \tag{4.9}$$

where n_i is a compact notation for band and k-point indexes. The advantage of this formulation is that L_0 (here written in frequency domain in its Lehmann representation):

$$L_0(1, 2, 1', 2', \omega) = \sum_{n_1 n_2} (f_{n_2} - f_{n_1}) \frac{\psi_{n_1}(\mathbf{r}_1)\psi_{n_2}^*(\mathbf{r}_2)\psi_{n_1}^*(\mathbf{r}_{1'})\psi_{n_2}(\mathbf{r}_{2'})}{E_{n_2} - E_{n_1} - \omega - i\eta}$$

is diagonal in transition space:

$$L_{0 n_1 n_2}^{n_1' n_2'} = (f_{n_2} - f_{n_1}) \frac{\delta_{n_1, n_{1'}} \delta_{n_2, n_{2'}}}{E_{n_2} - E_{n_1} - \omega - i\eta} \tag{4.10}$$

The Bethe-Salpeter eq. 4.3 can be rewritten for the matrix elements:

$$L_{n_1 n_2}^{n_1' n_2'} = L_{0 n_1 n_2}^{n_1' n_2'} + L_{0 n_1 n_2}^{n_3 n_4} K_{n_3 n_4}^{n_5 n_6} L_{n_5 n_6}^{n_1' n_2'} \tag{4.11}$$

this Dyson-like equation can be rewritten as (see Onida *et al.* [65] for a complete derivation):

$$L = [1 - L_0 K]^{-1} L_0 = L_0^{-1} \left[L_0^{-1} - L_0 K\right]^{-1} L_0 = \left[L_0^{-1} - L_0 K\right]^{-1} \tag{4.12}$$

In order to determine the polarizability L an inversion of an (effective) two-particle hamiltonian must be therefore performed:

$$L_{n_1 n_2}^{n_1' n_2'} = \left[H^{2p} - I\omega\right]^{-1}{}_{n_1 n_2}^{n_1' n_2'} \left(f_{n_{1'}} - f_{n_{2'}}\right) \tag{4.13}$$

$$H^{2p}{}_{n_1 n_2}^{n_1' n_2'} \stackrel{\text{def}}{=} \left(E_{n_2} - E_{n_1}\right) \delta_{n_1, n_{1'}} \delta_{n_2, n_{2'}} + \left(f_{n_1} - f_{n_2}\right) K_{n_1 n_2}^{n_1' n_2'} \tag{4.14}$$

where the kernel elements $K^{n_{1'}n_{2'}}_{n_1 n_2} = 2v^{n_{1'}n_{2'}}_{n_1 n_2} - W^{n_{1'}n_{2'}}_{n_1 n_2}$ are defined as:

$$v^{n_2 n_{2'}}_{n_1 n_{1'}} = \left\langle \psi_{n_1}(\mathbf{r})\psi^*_{n_{1'}}(\mathbf{r}) \middle| v(\mathbf{r},\mathbf{r}') \middle| \psi^*_{n_{2'}}(\mathbf{r}')\psi_{n_2}(\mathbf{r}') \right\rangle \tag{4.15}$$

$$= \int d\mathbf{r} d\mathbf{r}' \psi^*_{n_1}(\mathbf{r})\psi_{n_{1'}}(\mathbf{r})v(|\mathbf{r}-\mathbf{r}'|)\psi^*_{n_{2'}}(\mathbf{r}')\psi_{n_2}(\mathbf{r}')$$

$$W^{n_{1'}n_{2'}}_{n_1 n_2} = \left\langle \psi_{n_2}(\mathbf{r})\psi^*_{n_2'}(\mathbf{r}) \middle| W(\mathbf{r},\mathbf{r}') \middle| \psi^*_{n_{1'}}(\mathbf{r}')\psi_{n_1}(\mathbf{r}') \right\rangle \tag{4.16}$$

$$= \int d\mathbf{r} d\mathbf{r}' \psi^*_{n_2}(\mathbf{r})\psi_{n_{2'}}(\mathbf{r})W(\mathbf{r},\mathbf{r}')\psi^*_{n_{1'}}(\mathbf{r}')\psi_{n_1}(\mathbf{r}')$$

$$\tag{4.17}$$

Most ab-initio codes avoid a direct inversion of $[H^{2p} - I\omega]$, which would be computationally prohibitive, and employ its spectral representation [108]:

$$L = \sum_{\lambda_1,\lambda_2} \frac{|\lambda_1\rangle S^{-1}_{\lambda_1\lambda_2} \langle\lambda_2|}{E^{\lambda_1} - \omega - i\eta} \tag{4.18}$$

$$L^{n_{1'}n_{2'}}_{n_1 n_2} = \left[H^{2p} - I\omega\right]^{-1 n_{1'}n_{2'}}_{n_1 n_2} = \sum_{\lambda_1,\lambda_2} \frac{A^{\lambda_1}_{n_1 n_2} S^{-1}_{\lambda_1\lambda_2} A^{\lambda_2*}_{n_{1'}n_{2'}}}{E^{\lambda_1} - \omega - i\eta} \tag{4.19}$$

where $|\lambda\rangle$ and E^λ are the eigenvectors and eigenvalues of H^{2p}, while $A^\lambda_{n_1 n_2}$ are the coupling coefficients of the BSE eigenvectors over the transition space basis $|\lambda\rangle = \sum_{n_1 n_2} A^\lambda_{n_1 n_2} |n_1\rangle |n_2\rangle$. $S_{\lambda\lambda'}$ is the overlap matrix defined as $S_{\lambda_1\lambda_2} \overset{\text{def}}{=} \sum_{n_1 n_2} A^{\lambda_1}_{n_1 n_2} A^{\lambda_2}_{n_1 n_2}$. The effective eigenvalue equation can be written for $|\lambda\rangle$ and $A^{n_1 n_2}_\lambda$:

$$H^{2p} |\lambda\rangle = E_\lambda |\lambda\rangle \tag{4.20}$$

$$\sum_{n_{1'}n_{2'}} H^{2p\,n_{1'}n_{2'}}_{n_1 n_2} A^\lambda_{n_{1'}n_{2'}} = E^\lambda A^\lambda_{n_1 n_2} \tag{4.21}$$

This expression is also valid for a generic non-hermitian matrix; however, if H^{2p} is non-Hermitian its eigenvectors are in general not orthogonal and thus $S_{\lambda\lambda'}$ differs from the identity.

Once obtained an explicit procedure to calculate L, the dielectric function $\epsilon_M(\mathbf{q},\omega)$ can be determined from the contraction of the 2-particle polarizability [65, 109]:

$$\chi(1,2) = -iL(1,2,1^+,2^+) \Rightarrow \epsilon_M(\mathbf{q},\omega) = 1 - v(\mathbf{q}) \int d\mathbf{r}_1 d\mathbf{r}_2 e^{i\mathbf{q}\cdot(\mathbf{r}_1-\mathbf{r}_2)} L(\mathbf{r}_1,\mathbf{r}_1,\mathbf{r}_2,\mathbf{r}_2,\omega) \tag{4.22}$$

By exploiting the expansion over the transition space basis (eq. 4.8) and the spectral representation of its matrix elements (eq. 4.18) can be reached:

$$\epsilon_M^{BSE}(\mathbf{q}, \omega) = 1 - v(\mathbf{q}) \sum_{n_1 n_2} \sum_{n_1' n_2'} L_{n_1 n_2}^{n_1' n_2'} \langle n_2 | e^{i\mathbf{q}\mathbf{r}} | n_1 \rangle \langle n_1' | e^{-i\mathbf{q}\mathbf{r}} | n_2' \rangle$$

$$= 1 - v(\mathbf{q}) \sum_{\lambda_1 \lambda_2} \frac{S_{\lambda_1 \lambda_2}^{-1}}{E^\lambda - \omega - i\eta} \left[\sum_{n_1 n_2} \langle n_2 | e^{i\mathbf{q}\mathbf{r}} | n_1 \rangle A_{n_1 n_2}^{\lambda_1} \right] \times$$

$$\left[\sum_{n_1' n_2'} \langle n_1' | e^{-i\mathbf{q}\mathbf{r}} | n_2' \rangle A_{n_1' n_2'}^{\lambda_2 *} \right] \qquad (4.23)$$

2 Structure of the excitonic hamiltonian and the Tamm-Dancoff approximation

In this section we discuss explicitly the structure of the effective excitonic hamiltonian in the optical limit (transferred momenta $\mathbf{q} \to 0$); For a more detailed treatment we refer to the books of Bechstedt [63] or Martin, Reining and Ceperley [6]. We consider gapped systems at zero temperature with conservation of single-particle spin.

In a non-metal a T=0 K, due to the occupation factors $(f_{n_1} - f_{n_2})$ in H^{2p} (eq. 4.13) only interband transitions provide non-zero matrix elements to the hamiltonian. In light of this we slightly change the notation: instead of n_1, n_2, n_1', n_2' we use v_1, v_2 for the valence bands and c_1, c_2 for the unoccupied bands; the k-point index is dropped for simplicity (in the optical limit all transitions involved conserve momentum).

H^{2p} has a block matrix structure, as visible in eq. 4.24:

$$H^{2p} = \begin{bmatrix} H^{2p \, v_2 c_2}_{v_1 c_1} & H^{2p \, c_2 v_2}_{v_1 c_1} \\ H^{2p \, v_2 c_2}_{c_1 v_1} & H^{2p \, c_2 v_2}_{c_1 v_1} \end{bmatrix} \qquad = \begin{bmatrix} H^{resonant} & K^{coupling} \\ -\left(K^{coupling}\right)^* & -\left(H^{resonant}\right)^* \end{bmatrix} \qquad (4.24)$$

The resonant term $H^{2p \, v_2 c_2}_{v_1 c_1}$ is equal to :

$$H^{2p \, resonant} = H^{2p \, v_2 c_2}_{v_1 c_1} = (E_{c_1} - E_{v_1}) \delta_{c_1, c_2} \delta_{v_1, v_2} + 2 v_{v_1 c_1}^{v_2 c_2} - W_{v_1 c_1}^{v_2 c_2} \qquad (4.25)$$

and contains only transition corresponding to direct excitations $(v_1 \to c_1, v_2 \to c_2)$. The so called antiresonant term $H^{2p \, c_2 v_2}_{c_1 v_1}$ is equivalent to

$$H^{2p \, antiresonant} = H^{2p \, c_2 v_2}_{c_1 v_1} = -\left(H^{2p \, v_2 c_2}_{v_1 v_1}\right)^* = -\left(H^{resonant}\right)^* \qquad (4.26)$$
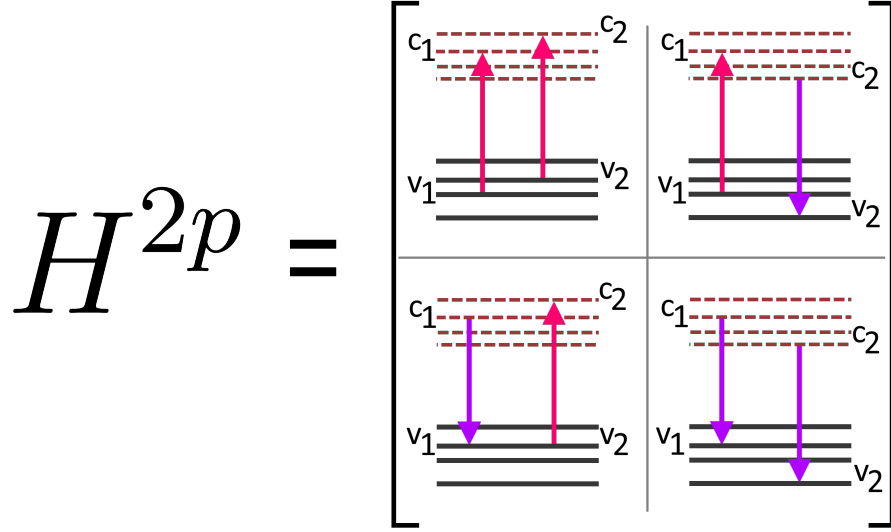
Figure 4.1: Graphical representation of the various components of the effective two-particle hamiltonian matrix elements.

and contains only de-excitation transitions.

The kernel elements of the resonant block are equal to $2v_{v_1c_1}^{v_2c_2} - W_{v_1c_1}^{v_2c_2}$ and are defined as:

$$v_{v_1c_1}^{v_2c_2} = \int d\mathbf{r}_1 d\mathbf{r}_2 \psi_{v_1}^*(\mathbf{r}_1)\psi_{c_1}(\mathbf{r}_1)v(|\mathbf{r}_1 - \mathbf{r}_2|)\psi_{c_2}^*(\mathbf{r}_2)\psi_{v_2}(\mathbf{r}_2) \tag{4.27}$$

$$= 2\sum_{\mathbf{G}_1,\mathbf{G}_2} v(\mathbf{G}_1) \langle v_1|e^{\mathbf{G}_1\mathbf{r}}|c_1\rangle \langle c_2|e^{-\mathbf{G}_2\mathbf{r}}|v_2\rangle$$

$$W_{v_1c_1}^{v_2c_2} = \int d\mathbf{r}_1 d\mathbf{r}_2 \psi_{c_1}^*(\mathbf{r}_1)\psi_{c_2}(\mathbf{r}_1)W(\mathbf{r}_1,\mathbf{r}_2)\psi_{v_2}^*(\mathbf{r}_2')\psi_{v_1}(\mathbf{r}_2) \tag{4.28}$$

$$= 2\sum_{\mathbf{G}_1,\mathbf{G}_2} W(\mathbf{G}_1,\mathbf{G}_2) \langle v_1|e^{\mathbf{G}_1\mathbf{r}}|c_2\rangle \langle v_2|e^{-\mathbf{G}_2\mathbf{r}}|v_1\rangle$$

$$\tag{4.29}$$

The resonant term is thus composed by three different contributions:

1. $(E_{c_1} - E_{v_1})\delta_{c_1,c_2}\delta_{v_1,v_2}$ contains the difference between the valence and conduction band energies; represents the independent particle transitions. If we neglect the following kernel terms and retain only this term, we recover the Independent Particle Approximation.

2. The second term $v_{v_1c_1}^{v_2c_2}$ includes the unscreened interaction; it stems from the variation of the Hartree potential, but it's called *exchange term* because the indexes are connected in an exchange-like manner [65]. The term provides a positive contribution and leads

to a blueshift in the transition energies.

3. The third term $W_{v_1 c_1}^{v_2 c_2}$ includes the screened potential and is labeled as the *direct* term (even if it originates from the variation of the exchange-correlation potential). It represents an *attractive interaction*, and thus causes a redshift of the transition energies.

To get physical insights into the components of the resonant block we can follow the suggestion of Martin *et al.* [6] and consider a BSE matrix formed by a single valence and conduction bands (a two-level system). In this case the kernel terms reduce to:

$$v_{vv}^{cc} = \int d\mathbf{r}_1 d\mathbf{r}_2 \rho_{vc}^*(\mathbf{r}_1) v(\mathbf{r}_1 - \mathbf{r}_2) \rho_{vc}(\mathbf{r}_2) \tag{4.30}$$

$$W_{vv}^{cc} = \int d\mathbf{r}_1 d\mathbf{r}_2 \rho_{vv}^*(\mathbf{r}_1) W(\mathbf{r}_1, \mathbf{r}_2) \rho_{cc}(\mathbf{r}_2) \tag{4.31}$$

with $\rho_{vc} = \psi_v^*(\mathbf{r}) \psi_c(\mathbf{r})$. We can see that v_{vv}^{cc} describes an interaction between two dipoles, while W_{vv}^{cc} is an interaction between the charge densities of an electron and a hole.

The Tamm-Dancoff approximation

The off-diagonal terms mix excitations and de-excitations, that is transitions with positive and negative energies. Neglecting these terms makes the BSE matrix Hermitian (and of half-size) - this approximation is called the *Tamm-Dancoff approximation* [109, 110]. It has been successfully tested and validated for bulk semiconductors and insulators [108], but it's considered less justified for finite systems [111].

Inside the Tamm-Dancoff approximation H^{2p} is hermitian, which implies that the excitonic states becomes orthogonal $S_{\lambda_1, \lambda_2} = \delta_{\lambda_1, \lambda_2}$. The macroscopic dielectric function $\epsilon_M(\mathbf{q}, \omega)$ in eq. 4.23 reduces to:

$$\epsilon_M^{BSE-TD}(\mathbf{q}, \omega) = 1 - v(\mathbf{q}) \sum_\lambda \frac{\left| \sum_{v,c} \sum_{\mathbf{k}} \langle v\mathbf{k} - \mathbf{q} | e^{-i\mathbf{q}\mathbf{r}} | c\mathbf{k} \rangle A_\lambda^{(v\mathbf{k})(c\mathbf{k})} \right|^2}{E^\lambda - \omega - i\eta} \tag{4.32}$$

It's instructive to compare this expression with $\epsilon(\mathbf{q}, \omega)$ in the Independent Particle Approximation (IPA):

$$\epsilon_M^{IPA}(\mathbf{q}, \omega) = 1 - v(\mathbf{q}) \sum_{v,c} \sum_{\mathbf{k}} \frac{\left| \langle v\mathbf{k} - \mathbf{q} | e^{-i\mathbf{q}\mathbf{r}} | c\mathbf{k} \rangle \right|^2}{(E_{c\mathbf{k}-\mathbf{q}} - E_{v\mathbf{k}}) - \omega - i\eta} \tag{4.33}$$

ϵ_M is defined as a sum of Lorentzian peaks $((E_{c\mathbf{k}} - E_{v\mathbf{k+q}}) - \omega - i\eta)^{-1}$ with broadening defined by η in both expressions[1]. In the IPA approximation each independent particle transition $E_{c\mathbf{k-q}} - E_{v\mathbf{k}}$ provides its Lorentzian contribution to ϵ_M^{IPA}, with amplitude equal to the square module of the transition dipole moment $|\langle v\mathbf{k} - \mathbf{q}|e^{-i\mathbf{qr}}|c\mathbf{k}\rangle|^2$.

The contributing Lorentzians in ϵ_M^{BSE-TD} are instead defined at the BSE exciton eigenvalues, and their amplitudes (commonly defined in literature as oscillator strengths) are proportional to $\left| \sum_{v,c} \sum_{\mathbf{k}} \langle v\mathbf{k} - \mathbf{q}|e^{-i\mathbf{qr}}|c\mathbf{k}\rangle A_\lambda^{(v\mathbf{k})(c\mathbf{k})} \right|^2$. This term can be interpreted as a mix of independent particle transitions with weights equal to the coupling coefficients A_n^λ; because A_n^λ are in general complex variables, constructive or destructive superposition effects can be found and have been discussed in literature [112, 113].

---

[1]The broadening is controlled by the `CSHIFT` flag in VASP. The default value, which is adopter for all calculations discussed in this thesis, is equal to 0.1 eV.

Chapter 5

Development of an AiiDA workflow for the G_0W_0 extrapolation method

The fast advancements in computational power and the maturation of ab-initio codes have opened the possibility of creating large databases of electronic and thermodynamic properties through automated procedures. These databases can be screened in search of novel materials with desiderable properties or utilized as training set for machine learning-derived approaches [114, 115, 116]. In fact in the last decades the computational High-Throughput approach (HT) has emerged, following the previous example of experimental HT ones, and large repositories like Materials Project [117], AFLOW [118, 119] or Materials Cloud [120] have been developed.

One of the essential elements of any HT project is the so-called Workflow Management System (WMS). A *workflow* can be defined as the sequence of different operations (ab-initio calculations or data manipulation), with some degree of interdependence; the role of the WMS is to automatize and streamline the preparation, submission and management of these simulations and their eventual parallelization.

Another crucial point in the computational science field is data reproducibility, which allows the validations of data and ensures reliable and reusable data in accordance with the FAIR principles [121] (*Findable, Accessible, Interoperable, Reusable*).
In order to guarantee reproducibility it should be possible to trace back all steps that led to data creation: a WMS should therefore not only store the data generated by also preserve the connections between results of different ab-initio calculations. The so-called *provenance* of the data produced should be therefore accurately documented, in order to guarantee reproducibility. This is especially true for results requiring complex chains of interconnected calculations, such as Quasiparticle and optical properties. In particular, the provenance should be handled by the WMS in order to comply with two different constraints:

- *Scalability*: given the large dimension of databases created in HPC (High-Performance Computing) environments, the provenance manager should be suitably robust in order

to handle and query efficiently sizable databases.

- *Complexity and flexibility*: material science workflows often require the implementation of multi-step and interdependent procedures, such as error-correcting and convergence sub-routines. The WMS should hence be able to handle and document dynamic workflows (a workflow is labeled as *dynamic* if it allows for changes at runtime level, such as inserting additional steps or logical branches depending on intermediate results). Most WMS however uses *static* markup languages (such as XML [122] or the Common Workflow Language[16]) which deny the possibility of any run-time logic.

The Workflow Management System employed in this work is AiiDA [47, 48], a robust open-source framework successfully deployed in High-Throughput [123, 124, 125, 126, 127, 128] and computational studies [129, 124].

As discussed in section 3, the state-of-the-art approach for accurately reproducing and predicting bandstructures is the many-body GW scheme. This method significantly outperforms DFT for what regards the description of excited state properties and represents an effective starting point for the calculation of excitonic and optical properties. The GW approach however possesses two main drawbacks with respect to standard DFT, namely:

1. The demanding computational cost and poor scaling with respect to system size: the standard implementation scales with the fourth power of the basis set dimension and the second power of the k-point mesh dimension, with a large prefactor.

2. The large number of numerical parameters which should be controlled, which requires a reliable procedure to assess convergence and avoid erroneous results.

Due to these complications the application of GW schemes to advanced materials was typically possible only for very experienced users, capable of accurately tuning the parallelization parameters and able to avoid convergence errors.

The ever-increasing availability of computational power in HPC center together with the introduction of low-scaling GW schemes [29, 130, 131] and optimized approximations [132, 133, 134, 135, 136], has made it possible to apply the High Throughput (HT) approach to GW schemes for the first time [137, 28, 31, 32, 35]. The High-Throughput implementation of GW methods requires however reliable and standardized convergence procedures; in this regard several schemes to systematize the convergence of the GW numerical parameters have been proposed in recent years [28, 31, 32, 35]. The present chapter describes an alternative scheme, introduced by Klimeš *et al.* [33] and Ellinger *et al.* [35, 36] and documents its development as a workflow in the AiiDA-VASP framework. The AiiDA-VASP plugin did not originally support post-DFT algorithms; hence an extension of the plugin to include GW/BSE support has been developed in parallel and it's discussed in section 4.

The workchain is fully available online and we plan to include it in a future release of the

AiiDA-VASP official plugin[1].

1   The AiiDA framework

The AiiDA WMS is composed by two main subsystems: the engine (that controls the execution, storage and communication with the clusters) and the user interface libraries. These libraries allow the user to write workflows in the standard Python language, without the need of additional markup languages.

The compatibility with ab-initio codes is ensured via plugins that can be downloaded and installed separately[2]; the AiiDA-VASP plugin is used thorough this work [141].

Structure of an AiiDA workflow

The `Workchain` class is the central component of workflow development in AiiDA. Each workflow is structured in different steps, each associated with a specific class method. These methods can leverage the standard scientific Python libraries, such as *numpy* or *scipy* to process data. In order to prevent data loss, progresses are saved in a checkpoint to the database by the engine after each step. This allows to continue the workflow from the last checkpoint in case of failures.

The main information of a workflow are encoded in a particular method, labeled `define()`, which acts effectively as a process specification. The method declares the workchain inputs and outputs (including information about their types and whether they

```
class Workchain_example(Workchain):
define():
  spec.input(structure, type=StructureData)
  spec.output(energy,   type=Float)

  spec.outline(
      cls.prepare_parameters(),
      cls.submit_calculation(),
      )


def prepare_parameters(self):
  [..]
def submit_calculation(self):
  [..]
```

Figure 5.1: Example implementation of a simple Workchain class, which receives a single input argument (the geometric structure of a materials) and returns its energy. The workchain executes two methods sequentially.

are required or optional) using the `spec.input` and `spec.output` keywords. The mandatory `spec.outline()` method encodes the internal logic of the workflow, i.e. the sequence of class methods composing the workchain and the order of execution. Each method called inside `outline()` represents a step that will be executed sequentially by the AiiDA engine. Conditional constructs (including `while` and `if/else` statements) can be included inside `outline()` to introduce flow control. As a simple example, the workchain in Figure 5.1

---

[1]The workflow as well as a patch for the extension of AiiDA-VASP can be found in `https://github.com/lorenzovarro/GW-VASP-workflow`.

[2]Others important plugins are AiiDA-Quantum Espresso [138], AiIDA-Yambo [139] and AiIDA-Abinit [140].

executes only two class methods: it starts by calling `prepare_parameters()` and after its execution continues with `submit_calculations()`.

The AiiDA workchains are self-documenting by design, in the sense that through an inspection of the `define()` method a user can understand the workflow's interface, main logic and eventual exit modes.

Variables returned by or passed to the workchains possess specific types defined by the AiiDA libraries. These types extend the standard Python types (`Float`, `Dict`, `Int`) or encompass material-science related data (`KpointsData`, `BandsData`, `StructureData`). These types include additional information about the data stored, such as the software that created them, creation and last modification times, a label and a unique identifier.

AiiDA-VASP main workflow

The AiiDA-VASP plugin provides an interface between AiiDA and VASP, and allows AiiDA to run, control and inspect VASP simulations. The plugin defines a special workflow, called `VaspWorkChain`, which performs the low level interactions with the VASP executable: it automatically constructs the input files from the parameters passed (`INCAR`, `POSCAR`, etc.), inspects the calculation for any problems (i.e. unfinished or crashed runs) and calls the correct parsers after the execution. In this sense it acts as an abstraction layer, allowing the user to manipulate AiiDA variables such as `KpointsData` and `StructureData` (instead of employing the specific KPOINTS or POSCAR syntaxes). All user workchains, including the G_0W_0 workchains described in this chapter, call `VaspWorkChain` as main entry point for executing VASP calculations.

2 Convergence procedures

2.1 Importance of Convergence

The essential parameters which must be converged in the GW schemes are:

- Number of bands included in the self energy expression 3.35 N_b^Σ.

- Number of bands included in the calculation of the response function 3.36 N_b^χ.

- Energy cutoff of the plane wave basis set E_{cut}.

- Energy cutoff of the plane wave basis used for the response function E_{cut}^χ, which defines the number of $\mathbf{G}$ vectors included in the response function $\chi_{\mathbf{q}}^0(\mathbf{G}_1, \mathbf{G}_2, \omega)$ and inverse dielectric matrix $\epsilon_{\mathbf{q}}^{-1}(\mathbf{G}_1, \mathbf{G}_2, \omega)$.

- The k-point mesh.

Note that VASP assumes $N_b^\Sigma = N_b^\chi$, and we will maintain this assumption for the following discussion. Moreover, to avoid ambiguities, we remark that the E_{cut}^χ cutoff does *not* control the expansion of the wavefunctions inside the transitions matrix elements $\langle n\mathbf{k}|e^{-i(\mathbf{q}+\mathbf{G})\circ\mathbf{r}}|m\mathbf{k}+\mathbf{q}\rangle$; the energy cutoff on the dipole elements is still controlled by E_{cut}.

In VASP syntax $N^\Sigma = N^\chi$ corresponds to the `NBANDS` flag, E_{cut}^χ to `ENCUTGW` and E_{cut} to `ENCUT`[3].

All schemes discussed in this chapter rely on the premise that the convergence of the energy cutoffs and of the total number of bands N_b^Σ are coupled together and that they are decoupled from the k-point mesh. In this context it means that, for example, the converged N_b^Σ value depends on the employed E_{cut}^χ and E_{cut} parameters (and vice-versa).

A first insight on the physical explanation behind the premise can be found by inspecting the static limit of the standard GW self-energy [142, 143]:

$$\Sigma^{COH}(\mathbf{r},\mathbf{r}') = \frac{1}{2}\delta(\mathbf{r}-\mathbf{r}')\left[W(\mathbf{r},\mathbf{r}',\omega=0)-v(\mathbf{r}-\mathbf{r}')\right]$$

$$= \frac{1}{2}\left[\sum_{n\mathbf{k}}\psi_{n\mathbf{k}}(\mathbf{r})\psi_{n\mathbf{k}}^*(\mathbf{r}')\right]\left[W(\mathbf{r},\mathbf{r}',\omega=0)-v(\mathbf{r}-\mathbf{r}')\right] \qquad (5.1)$$

where we have applied the completeness relation for the eigenvector basis. The terms inside the summation can be identified with virtual transitions caused by the charge fluctuations induced by a quasiparticle [142].

The expectation value of the static Coulomb Hole operator can be written in reciprocal space as:

$$\langle n\mathbf{k}|\Sigma^{COH}|n\mathbf{k}\rangle = \frac{1}{2}\sum_{m\mathbf{q}}\sum_{\mathbf{G}_1\mathbf{G}_2}M_{\mathbf{k},\mathbf{q}}^{mn}(\mathbf{G}_1)M_{\mathbf{k},\mathbf{q}}^{mn*}(\mathbf{G}_2)\left[\left(\epsilon_{\mathbf{G}_1,\mathbf{G}_2}^{-1}(\mathbf{q},0)-\delta_{\mathbf{G}_1,\mathbf{G}_2}\right)v(\mathbf{q}+\mathbf{G}_1)\right] \quad (5.2)$$

with $M_{\mathbf{k},\mathbf{q}}^{mn}(\mathbf{G}) = \langle n\mathbf{k}|e^{i(\mathbf{q}+\mathbf{G})\circ\mathbf{r}}|m\mathbf{k}-\mathbf{q}\rangle$. A reduced cutoff on $\mathbf{G}_1,\mathbf{G}_2$ will damp and thus prevent contributions from high energy unoccupied bands in Σ^{COH} sum; for this reason, undervalued cutoffs will cause a false convergence with the respect to the number of unoccupied bands [145, 146, 143, 135]. The coupled variables must therefore be considered simultaneously and a multidimensional parameter space must be explored in the convergence scheme. This topic will be discussed in details later in the chapter.

Another crucial point which should be handled by convergence schemes is the particularly slow convergence with respect to the number of bands included in the self energy contri-

---

[3]in VASP version 6.3 and later releases an additional cutoff flag is introduced, `ENCUTGWSOFT`, which allows to truncate the Coulomb kernel (inside the ϵ^{-1} calculation routines) slowly between the energy specified by ENCUTGWSOFT and ENCUTGW using a cosine window function. To maintain consistency with previous version we use `ENCUTGWSOFT=ENCUTGW`.

butions [142, 143, 147, 148, 30, 149, 150, 151]. This aspect becomes particularly critical when localized d orbitals have an important role in the physics of the compound, such as MgO, ZnO [149, 143, 152] or transition metal oxides perovskites [144, 145, 153]. These materials might require up to thousands of bands to obtain well-converged results. This numerical constraint is one of the reasons behind the comparatively limited number of many-body study of large systems [135, 154, 29, 155, 156, 157, 158] or $4d$ and $5d$ magnetic perovskites [144, 159, 160, 161, 162, 163, 164, 165]. This behavior becomes even more problematic in applications where absolute energies (and not just transitions between valence and conduction bands) should be accurately estimated (such as interfaces studies, molecular electronics or photovoltaic applications) [166].

The computational expense associated to this convergence over empty bands has led to the development of alternative GW formulations that avoid the summation over unoccupied states, such as the ones based on optimal basis sets [131] or on the Steinheimer equation [130].

An insight into the cause of this behavior can be found by looking again at the COH operator (eq. 5.2): the matrix elements $M_{\mathbf{k},\mathbf{q}}^{mn}(\mathbf{G})$ exhibit a slow decay with respect to energy difference between n and m bands, which implies that even virtual transitions to high energy bands may provide non-negligible contributions to the summation [142].

Moreover studies in the quantum chemistry community [167, 168, 169] have related the slow convergence of the RPA correlation energy (defined as $E_c^{RPA} = \int d\omega Tr\left[ln\left(1 - \chi^0(i\omega)v\right) + \chi^0(i\omega)v\right])$ to the electron-electron cusp in the many-electron wavefunction [170, 171]. The RPA correlation energy is closely related to GW methods, as these usually employ the RPA response function.

Figure 5.2: Representation of the conventional method convergence for the QP gap with respect to the number of bands and cutoff. Adapted from [144].

Two different convergence schemes will be discussed in this section: the *conventional* one, which can be considered as the standard and most common procedure [28], and the *basis-set extrapolation* of Klimeš *et al.* and Ellinger *et al.*, which is the one implemented in the AiiDA workflow.

2.2 Conventional method

The so-called *conventional* method (illustrated in fig. 5.2) attempts to converge the QP bandgap by an *iterative* approach:

- E_g is calculated as a function of the bands number N_b for a fixed energy cutoff value E_{cut}^1; the *converged* number of bands at that cutoff is labeled as $N_b(E_{cut}^1)$.
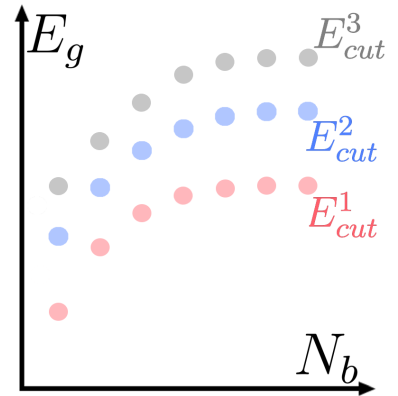
- The cutoff value must also be optimized; however due to the $E_{cut} - N_b$ coupling the converged N_b values for different cutoffs may be in principle different (i.e. $N_b(E_{cut}^1) \neq N_b(E_{cut}^2)$). Therefore the bands convergence at fixed E_{cut}^1 is *repeated* for different cutoff values E_{cut}^2, E_{cut}^3.

- The convergence in the $E_{cut} - N_b$ space is performed on a low-density k-points mesh. Due to the decoupling of the k-mesh from the $E_{cut} - N_b$ parameters, it can be assumed that the convergence performed at low-density k-point mesh holds also on more dense k-point meshes.
  Conversely, the k-points convergence is performed adopting under-converged (and less computationally expensive) E_{cut} and N_b.

- A final GW calculation is performed with the optimized parameters.

This procedure can achieve satisfactorily converged QP gaps with error below 100 meV [144]. Moreover, extrapolations to the infinite-basis-set limit based on different fitting schemes have been applied in literature [153, 172, 173, 28] *on top this convergence procedure* to further reduce the error.
There are however two main downsides:

1. On the one hand this scheme requires a comparatively large number of GW calculations in order to explore the two dimensional $E_{cut} - N_b$ parameter space.

2. On the other hand it lacks a rigorous mathematical foundation [144, 33]: to the best of our knowledge there is no analytic proof that guarantees that this approach yields correct converged properties. Its validity is based on a heuristic argument, in the sense that is based on extensive tests and comparison with experimental data.

2.3 Basis extrapolation method

The main results of the scheme derived by Klimeš *et al.* [33] is that, under the hypothesis of *complete basis*, the leading order error (due to truncation of the bands summation) on the QP energy of a ψ_m state close to the Fermi energy scales asymptotically with the inverse of the plane waves number:

$$\Delta E_m \propto \frac{1}{G_{cut}^3} \sum_{\mathbf{g}} \rho_m(\mathbf{g}) \rho(-\mathbf{g}) \propto \frac{1}{N_b} \sum_{\mathbf{g}} \rho_m(\mathbf{g}) \rho(-\mathbf{g}) \tag{5.3}$$

where $\mathbf{g} = \mathbf{G}_1 - \mathbf{G}_2$ (with $\mathbf{G}_1, \mathbf{G}_2$ reciprocal lattice vectors of the cell of volume Ω), ρ is the total density component in reciprocal space, ρ_m the density of the m orbital ψ_m and G_{cut} is the reciprocal vector cutoff associated to E_{cut}. Their derivation assumes a *complete basis set* for a given energy cutoff E_{cut}, meaning that the total number of (occupied plus unoccupied) orbitals included is determined by the E_{cut} choice, and *corresponds to all orbitals that the*

plane-wave basis set allows to calculate.

The protocol is illustrated in Figure 5.3 and can be summarized as:

- A set of three G_0W_0 calculations with different cutoffs $E_{cut}^1, E_{cut}^2, E_{cut}^3$ is performed. These simulations should satisfy two constraints: on the one hand the complete orbital basis for a given cutoff must be taken into account, which translates to setting N_b (NBANDS) equal the maximum number of plane waves (labeled respectively N_b^1, N_b^2 and N_b^3)[4]. On the other hand E_{cut}^χ should be set to a fixed ratio[5] of the corresponding cutoff E_{cut} (in order to avoid false convergences [33]).
  This scheme, similarly to the conventional one, takes advantage of the decoupling between N_b, E_{cut} and the number of k-points employed: the three calculations are hence performed on a low k-point density mesh (labeled n_k).

- The asymptotic limit of the gap with respect to the bands number $E_g^\infty(n_k, N_b^\infty)$ is determined by fitting a $1/N_b + offset$ curve to the results and extrapolating to $N_b \to \infty$ limits.

- The cutoffs employed by Klimeš *et al.* are chosen as the $1\times, 1.25\times, 1.587\times$ the maximum energy provided in the pseudo-potential (which correspond to an increase of the total number of bands of respectively $1.4\times$ and $2\times$). Ellinger *et al.* [35] introduced and tested a variant of this protocol with lower cutoffs ($0.75\times, 1\times, 1.25\times$ the maximum energy provided in the pseudo-potential).

- A single G_0W_0 calculation on a dense k-point mesh (labeled N_k) is performed using the E_{cut}^1 cutoff. The extrapolated correction computed on n_k is then added to account for the band convergence correction:

$$E_g^\infty(N_k, N_b^\infty) = E_g(N_k, N_b^1) + \underbrace{\left[E_g^\infty(n_k, N_b^\infty) - E_g(n_k, N_b^1)\right]}_{correction} \quad (5.4)$$

Validation and alternatives

This scheme has been extensively tested and validated on bulk solids (including challenging materials such as transition metal oxide perovskites) by Ellinger *et al.* [35, 36] and Ergönenc *et al.* [144]. Ellinger and coworkers applied the extrapolation scheme to a set of 70 binary compounds; Ergönenc *et al.* applied the scheme to the same dataset studied in chapter 6 and compared the extrapolated results to experimental data and values obtained with the

---

[4]The precise value is printed out by VASP in the OUTCAR file of the corresponding ground state calculation.

[5]VASP automatically sets E_{cut}^χ equal to 2/3 of E_{cut}; Ellinger and coworkers [35, 36] tested a version of the workflow where E_{cut}^χ is equal to $1/2 E_{cut}$. It's essential however to keep the value constant along the workflow.
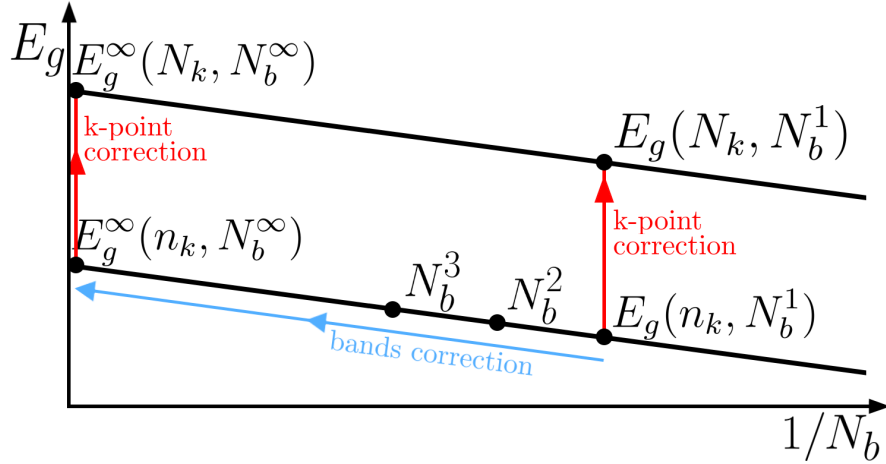
Figure 5.3: Adapted from [144]. Schematic representation of the basis-set extrapolation as defined in equation 5.4.

conventional method. The Mean Absolute Error (MAE) with respect to the experimental data obtained by the extrapolation method is 0.20 eV, versus a MAE of 0.25 eV for the non-extrapolated conventional method.

Maggio *et al.* [34] adopted the scheme to study a set of 100 closed shell molecules (the so called GW100 set) and compared the results with data obtained from local basis set codes (including extrapolation with respect to the local basis). VASP extrapolated HOMOs are in excellent agreement with local basis set data, with a mean absolute error of less than 60 meV. Analogous results for the GW100 set were obtained by Govoni and Galli [174].

The protocol introduced by Klimeš *et al.* represents a complementary approach to convergence accelerators based on the resolution of identity [175] or on effective energy denominator techniques [133, 132]. The cited methods allow to reduce the number of empty states with respect to standard GW while retaining a very similar accuracy; a conventional convergence study is still required in order to avoid false convergences (and to explore the $E_{cut} - N_b$ coupling), but the convergence curves with respect to the band number are strongly accelerated. Klimeš' scheme instead explicitly estimates the error due to truncation of high energy plane wave components in the response function, and extrapolates the results to the infinite basis set limit.

Furthermore, the assumption of a complete basis set **(i)** averts completely the risk of false convergences and **(ii)** adopts a clear relation between E_{cut} and N_b: this in turn avoids the need of optimizing E_{cut} and N_b separately and of exploring the 2-dimensional parameter space. The scheme therefore enables a more streamlined procedure and allows to reduce the total number of calculations required for convergence. These are the main advantages of the basis extrapolation method.

Derivation of equation 5.3 and further considerations

In this section a review of the main steps needed to prove eq. 5.3 will be given as described by Klimeš *et al.* [33]; the derivation allows to further explain and illustrate the properties of the $E_{cut} - N_b$ convergence discussed above.

Let's start by approximating the screened interaction W to second order $W = v + v\chi_0 v$, which implies $\Sigma = GW \approx G_0 v + G_0 v\chi_0 v$. The first order $G_0 v$ is the Fock exchange part and the second term represents the correlation part.

The second order term $v\chi_0 v$ can be written *for large* $\mathbf{G}$ (implying $|\mathbf{q} + \mathbf{G}|^2 \approx \mathbf{G}^2$) as:

$$v\chi_0 v(\mathbf{G}_1, \mathbf{G}_2) = \frac{2}{\Omega}\frac{4\pi}{\mathbf{G}_1^2}\frac{4\pi}{\mathbf{G}_2^2}\sum_{o:occ}\sum_{u:unocc}\frac{\langle o|-\mathbf{G}_1|u\rangle\,\langle u|\mathbf{G}_2|o\rangle}{w + (E_o - E_u) + i\eta} - \frac{\langle u|-\mathbf{G}_1|o\rangle\,\langle o|\mathbf{G}_2|u\rangle}{w - (E_u - E_o) - i\eta} \quad (5.5)$$

$\langle u|\mathbf{G}_2|o\rangle$ is a compact notation for the overlap density term $\langle u|\mathbf{G}|o\rangle \equiv \langle u|e^{i\mathbf{G}\circ\mathbf{r}}|o\rangle$, where the o index spans the occupied states and u the unoccupied ones.

We initially assume that the orthonormal orbital basis is complete (all infinite unoccupied states are included), thus u spans *all* empty orbitals.

The self energy contribution to the QP energy is obtained from eq. 3.35:

$$\langle m|\Sigma(\omega)|m\rangle \propto \frac{1}{\Omega}\sum_{\mathbf{q}}\sum_{\mathbf{G}_1,\mathbf{G}_2}\sum_{n:all}\int d\omega' W_{\mathbf{q}}(\mathbf{G}_1, \mathbf{G}_2, \omega')\times \quad (5.6)$$

$$\frac{\langle m,\mathbf{k}|\mathbf{q} + \mathbf{G}_1|n,\mathbf{k} - \mathbf{q}\rangle\,\langle n,\mathbf{k} - \mathbf{q}|-(\mathbf{q} + \mathbf{G}_2)|m,\mathbf{k}\rangle}{\omega - \omega' - E_{n,\mathbf{k}-\mathbf{q}} + i\eta\,sgn(E_{n,\mathbf{k}-\mathbf{q}} - \mu)}$$

where η is a positive infinitesimal and sgn is the sign function.

Let's focus on the correlation part developed at second order by substituting $W_{2\text{order}} \approx v\chi_0 v$. The $\int d\omega'$ integral can be calculated using the standard contour integration technique by closing the contour in the lower half of the complex plane (including only the set of poles with negative η). The first set of contributing poles derives from the denominator of the non-interacting Green function, which provides poles at $\omega' = \omega' - E_{n,\mathbf{k}-\mathbf{q}} - i\eta$ for n belonging to all *occupied* states (the empty states have a positive $i\eta sgn(E_{n,\mathbf{k}-\mathbf{q}} - \mu) = i\eta$, which locate them in the upper plane). The related contribution contains:

$$\sum_{n:occ}\langle m,\mathbf{k}|\mathbf{q} + \mathbf{G}_1|n,\mathbf{k} - \mathbf{q}\rangle\,\langle n,\mathbf{k} - \mathbf{q}|-(\mathbf{q} + \mathbf{G}_2)|m,\mathbf{k}\rangle \quad (5.7)$$

Let's introduce now two assumptions: **(1)** since we are interested in the asymptotic limit, we assume large $\mathbf{G}$ reciprocal lattice vectors and **(2)** we study only the QP corrections for the

m states close to the Fermi energy. Under these two hypothesis it holds (see Appendix A):

$$\langle n \sim occ.|\mathbf{G}|m \sim E_F\rangle \approx 0 \tag{5.8}$$

Where the $\mathbf{k}$ and $\mathbf{q}$ indexes have been suppressed for brevity; therefore this contribution at large $\mathbf{G}$ is negligible.

The second contribution comes instead from the poles of $W_{2\text{order}}$ located at the *transition* energies $\omega' = E_u - E_o - i\eta$ and reads as:

$$\langle m|\Sigma^{COH}(\omega = E_m)|m\rangle \propto \frac{1}{\Omega^2} \sum_{\mathbf{G}_1,\mathbf{G}_2} \frac{4\pi}{\mathbf{G}_1^2} \frac{4\pi}{\mathbf{G}_2^2} \sum_{n:all} \langle m|\mathbf{G}_1|n\rangle \langle n|-\mathbf{G}_2|m\rangle \tag{5.9}$$

$$\sum_{o:occ} \sum_{u:unocc} \frac{\langle o|-\mathbf{G}_1|u\rangle \langle u|\mathbf{G}_2|o\rangle}{E_m + (E_o - E_u) - E_n}$$

The COH labels derives from Klimeš *et al.*

Let's now study the terms inside the $\sum_{\mathbf{G}_1,\mathbf{G}_2}$ sum of eq. 5.9, and introduce a new approximation **(3)** by allowing the u index to range over *all* states instead of only the empty ones:

$$\langle m|\Sigma^{COH}|m\rangle (\mathbf{G}_1,\mathbf{G}_2) \propto \frac{1}{\Omega^2} \frac{4\pi}{\mathbf{G}_1^2} \frac{4\pi}{\mathbf{G}_2^2} \sum_{o:occ} \sum_{n,u:all} \langle m|\mathbf{G}_1|n\rangle \langle n|-\mathbf{G}_2|m\rangle \times \tag{5.10}$$

$$\frac{\langle o|-\mathbf{G}_1|u\rangle \langle u|\mathbf{G}_2|o\rangle}{E_m + (E_o - E_u) - E_n}$$

At this point two other key approximations are introduced: **(4)** the high energy *empty* states can be approximated with plane waves as $\psi_u(\mathbf{r}) \approx \Omega^{-1/2}e^{i\mathbf{G}_u\cdot\mathbf{r}}$ and energy $E_u \approx \mathbf{G}_u^2/2$ (the intuition is that at high energies the kinetic term is the dominant contribution to the Hamiltonian) and **(5)** the expansions over plane waves of the *occupied* Bloch orbitals below the Fermi energy have predominantly components at small $\mathbf{G}$ vectors. The first consequence of these approximations is that

$$\langle m|\mathbf{G}_1|n\rangle \langle n|-\mathbf{G}_2|m\rangle >> 0 \quad \text{only if } \mathbf{G}_n \approx -\mathbf{G}_1 \text{ and } \mathbf{G}_n \approx -\mathbf{G}_2 \tag{5.11}$$
$$\langle o|-\mathbf{G}_1|u\rangle \langle u|\mathbf{G}_2|o\rangle >> 0 \quad \text{only if } \mathbf{G}_u \approx -\mathbf{G}_1 \text{ and } \mathbf{G}_u \approx -\mathbf{G}_2$$

where we remind that we have previously assumed that m runs over states close to the Fermi energy. Since the only terms contributing significantly to the sum are the ones defined by

eq. 5.11, a further simplification is possible in the denominator:

$$E_m + E_o - (E_u - E_n) \approx E_m + E_o - \frac{1}{2}\left(\mathbf{G}_1^2 + \mathbf{G}_2^2\right) \overset{E_u,E_n >> E_o,E_m}{\approx} -\frac{1}{2}\left(\mathbf{G}_1^2 + \mathbf{G}_2^2\right) \tag{5.12}$$

thus:

$$\langle m|\Sigma^{COH}|m\rangle\,(\mathbf{G}_1,\mathbf{G}_2) \propto \frac{1}{\Omega^2}\frac{1}{\mathbf{G}_1^2}\frac{1}{\mathbf{G}_1^2}\frac{(4\pi)^2}{\mathbf{G}_1^2 + \mathbf{G}_2^2}$$
$$\sum_{o:occ}\sum_{n,u:all} \langle m|\mathbf{G}_1|n\rangle\,\langle n|-\mathbf{G}_2|m\rangle\,\langle o|-\mathbf{G}_1|u\rangle\,\langle u|\mathbf{G}_2|o\rangle \tag{5.13}$$

Now let's use the resolution of identity $\sum_u |u\rangle\langle u| = \hat{1}$ with respect to indexes n, u:

$$\langle m|\Sigma^{COH}|m\rangle\,(\mathbf{G}_1,\mathbf{G}_2) \propto \frac{1}{\Omega^2}\frac{1}{\mathbf{G}_1^2}\frac{1}{\mathbf{G}_1^2}\frac{(4\pi)^2}{\mathbf{G}_1^2 + \mathbf{G}_2^2}\sum_{o:occ} \langle m|\mathbf{G}_1 - \mathbf{G}_2|m\rangle\,\langle o|\mathbf{G}_2 - \mathbf{G}_1|o\rangle \tag{5.14}$$

$\langle o|\mathbf{G}|o\rangle$ is the Fourier component of the charge density of the ψ_o occupied state $\langle o|\mathbf{G}|o\rangle = \Omega^{-1}\int d\mathbf{r}\,\psi_o^*(\mathbf{r})\psi_o(\mathbf{r})e^{i\mathbf{G}\cdot\mathbf{r}} = \rho_o(\mathbf{G})$. The Fourier component of the *total* charge density is therefore $\rho(\mathbf{G}) = \sum_{o:occ}\rho_o(\mathbf{G})$, which implies:

$$\langle m|\Sigma^{COH}|m\rangle\,(\mathbf{G}_1,\mathbf{G}_2) \propto \frac{1}{\mathbf{G}_1^2}\frac{1}{\mathbf{G}_1^2}\frac{(4\pi)^2}{\mathbf{G}_1^2 + \mathbf{G}_2^2}\rho_m(\mathbf{G}_1 - \mathbf{G}_2)\rho(\mathbf{G}_2 - \mathbf{G}_1) \tag{5.15}$$

The error committed by introducing a cutoff G_{cut} can be estimated as:

$$\Delta E_m = \sum_{|\mathbf{G}_1| > G_{cut}}\sum_{|\mathbf{G}_2| > G_{cut}} \langle m|\Sigma^{COH}|m\rangle\,(\mathbf{G}_1,\mathbf{G}_2) \tag{5.16}$$

By performing a change of variables ($\mathbf{g} = \mathbf{G}_1 - \mathbf{G}_2$, $\mathbf{G}_c = (\mathbf{G}_1 + \mathbf{G}_2)/2$) and considering $\mathbf{G}_c >> \mathbf{g}$ (consequence of assumption (1)) we obtain:

$$\Delta E_m \propto (4\pi)^2\sum_{\mathbf{g}}\rho_m(\mathbf{g})\rho(-\mathbf{g})\sum_{|\mathbf{G}_c| > G_{cut}}\frac{1}{\mathbf{G}_c^6} \tag{5.17}$$

By summing up the terms $|\mathbf{G}_c| > G_{cut}$ we find:

$$\Delta E_m \propto \frac{1}{G_{cut}^3} \sum_{\mathbf{g}} \rho_m(\mathbf{g})\rho(-\mathbf{g}) \tag{5.18}$$

There are two different ways to introduce a cutoff on $\mathbf{G}_1, \mathbf{G}_2$: The first is to define a cutoff G_{cut}^χ on the response function χ_0 and the screened interaction $W(\mathbf{G}_1, \mathbf{G}_2, \omega')$. The second one is introduced by limiting the number of empty states: due to approximation (**4**) limiting the indexes u,n is equivalent to imposing a cutoff G_{cut}^b on the $\mathbf{G}_u, \mathbf{G}_v$ vectors, and due to the constraint elucidated in eq. 5.11 a restriction on $\mathbf{G}_u, \mathbf{G}_v$ imposes a restriction on the non-negligible $\mathbf{G}_1, \mathbf{G}_2$ term. The final cutoff is therefore determined as:

$$G_{cut} = min\left(G_{cut}^b, G_{cut}^\chi\right) \tag{5.19}$$

This proof offers an alternative explanation to the $E_{cut} - N_b$ coupling and to the false convergence behaviors discussed before. In fact *only the lower cutoff between G_{cut}^b, G_{cut}^χ determines the final effective value, and hence keeping fixed the lower one and further increasing the other one leaves G_{cut} unchanged.*
Moreover, *we note that the adoption of a complete band basis implies $G_{cut}^b = G_{cut}^\chi$: the assumption is therefore required to avoid false convergences.* By assuming $G_{cut}^b = G_{cut}^\chi$ we can retrieve the main result:

$$\Delta E_m \propto \frac{1}{G_{cut}^3} \sum_{\mathbf{g}} \rho_m(\mathbf{g})\rho(-\mathbf{g}) \propto \frac{1}{N_b} \sum_{\mathbf{g}} \rho_m(\mathbf{g})\rho(-\mathbf{g}) \tag{5.20}$$

where N_b can be also calculated as the number of plane waves in the cutoff sphere with radius G_{cut}.

Lastly, this result provides another insight on the reason behind the slow convergence with respect to the number of band: eq. 5.8 establishes that large $\mathbf{G}_1, \mathbf{G}_2$ do *not* contribute directly to the occupied density (that is $\rho_o(\mathbf{G}_1) = \langle o|\mathbf{G}_1|o\rangle \sim 0$). Eq. 5.20 tells us that they compare only as differences, i.e. they are folded back in to wave-vectors $\mathbf{g}$ with small norms ($|\mathbf{g}| \approx 0$), and $\rho_o(\mathbf{g} \approx 0) = \langle o|\mathbf{g} \approx 0|o\rangle$ are in general *not negligible*.

3 G_0W_0 Convergence workflow

In order to discuss the workflow structure we first briefly revise the different steps needed to run a successful G_0W_0 calculation in VASP:

1. As discussed in section 5.2, G_0W_0 is a perturbative approach which requires single-particle wavefunctions and energies as a starting point; in the following workflow a DFT basis set fulfills this role. The first step is therefore a calculation of the ground state Kohn-Sham eigenstates and eigenvalues.

2. The accurate determination of the GW self-energy require a substantial number of empty orbitals (see section 2.1), which are calculated with a second DFT step. The number of bands employed *is determined by the complete basis set condition.*

| 1 | DFT : ground state calculation |

$$\left\{ E_{n\mathbf{k}}^{KS} \ , \ \psi_{n\mathbf{k}}^{KS} \right\}$$

| 2 | DFT : complete basis set |

$$\left\{ E_{n\mathbf{k}}^{KS} \ , \ \psi_{n\mathbf{k}}^{KS} \right\}$$

| 3 | perturbative one-shot   G0W0 |

$$E_{n\mathbf{k}}^{QP} = E_{n\mathbf{k}}^{KS} + Z_{n\mathbf{k}} < \Sigma(E_{n\mathbf{k}}^{KS}) - v_{xc} >$$
$$\psi_{n\mathbf{k}}^{QP} \approx \psi_{n\mathbf{k}}^{KS}$$

Figure 5.4:   Flowchart of a single G_0W_0 calculation in VASP.

In the same calculation the matrix elements of orbitals derivative with respect to $\mathbf{k}$ $\left\langle \psi_{n_1\mathbf{k}} \middle| \hat{S} \middle| \frac{\partial}{\partial \mathbf{k}} \psi_{n_2\mathbf{k}} \right\rangle$ are calculated (these elements are employed within the $\mathbf{k} \circ \mathbf{p}$ perturbation theory to build the head and wings of $\epsilon_{\mathbf{q}}(\mathbf{G}_1, \mathbf{G}_2, \omega)$, see reference [176]).
While in theory the first two steps could be performed in a single DFT run, splitting them in two separate calculations results in a more computationally efficient procedure.

3. The third step is the perturbative single-shot G_0W_0 calculation, which introduces a QP correction to the Kohn-Sham eigenvalues and adopts the wavefunctions retrieved from the second step as starting point.

To further clarify the computation details a brief review of the relevant VASP flags of each step is discussed below. First step (DFT calculation):

- Guassian smearing is selected, with a small σ value in order to avoid partial occupancies. (`SIGMA=0 ; SIGMA=0.05`). These values are employed also in the following steps.
- A very accurate break condition on the self-consistent electronic iteration is adopted (`EDIFF=1E-8`).

Second step:

- A direct optimization algorithm is adopted (`ALGO=All`).
- The flag `LOPTICS=.TRUE.` is introduced to print out the matrix elements $\left\langle \psi_{n_1\mathbf{k}} \middle| \hat{S} \middle| \frac{\partial}{\partial \mathbf{k}} \psi_{n_2\mathbf{k}} \right\rangle$ to file (called WAVEDER).
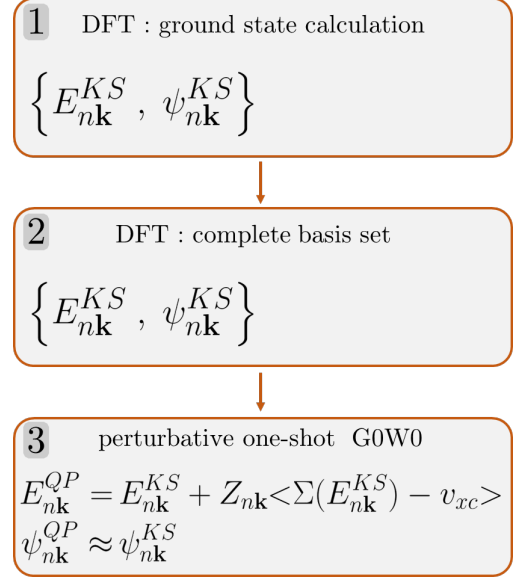
Third step:

- The spectral method for calculating $\chi^0_{\mathbf{q}}$ is activated (`LSPECTRAL = .TRUE.`), since it greatly reduces the computational workload.

- `Prec=Normal` is used instead of `Prec=Accurate` to reduce to memory requirements.

- The number of frequency points ω used to describe the response function $\chi^0_{\mathbf{q}}(\mathbf{G}_1, \mathbf{G}_2, \omega)$ is fixed at `NOMEGA=96`.

- `ENCUTGW` (E^{χ}_{cut} variable of section 2.1) is kept fixed at the default value of 2/3 `ENCUT` (E_{cut}).

- The main parallelization options included in VASP for GW routines are `MAXMEM` (which defines a threshold for the maximum allocated memory), `KPAR` (which defines the number of k-points calculated in parallel) and `NCSHMEM` (which activates memory sharing for response function routines).
  Version 6.x of VASP (unlike the previous versions) automatically tries to estimate an effective `MAXMEM` value for each calculation - and our tests indicate that the chosen values are usually close to the optimal ones.
  K-point parallelization is activated, while the shared memory option for the response routines is deactivated by setting `NCSHMEM=1` (since previous tests indicated that, depending on the MPI libraries used, this option might become a source of execution errors).

3.1   General workflow architecture

In this section an overview of the basis extrapolation workflow is given, starting from a description of its general architecture. The convergence scheme has a modular structure, composed by a main workflow and two secondary (lower-level) sub-workflows:

1. The sub-workflows `workchain_DFTgroundState` and `workchain_DFTvirtualBands_GW` encode the different steps listed above. they can be understood as a *wrapper* of the intermediate DFT and G_0W_0 steps: they provide a higher-level and *code-independent* interface to the upper level logic, requiring only generic AiiDA types input arguments such as the material structure, k-points mesh, bands number and cutoff values. The definition of the VASP INCAR parameters and the assembly of the necessary VASP inputs from these arguments are handled internally, as well as the outputs elaboration (including the extraction of gaps and bandstructures).

2. The upper level workflow `workchain_ExtrapolationScheme` implements the basis extrapolation scheme described in section 2.3. The workflow determines the $E_{cut} - N_b$ parameters under the complete basis hypothesis for each G_0W_0 calculation and submits them by calling `workchain_DFTvirtualBands_GW` (each call of `workchain_DFTvirtualBands_GW` corresponds to a single G_0W_0 simulation). The resulting bandgap energies are collected and extrapolated in order to determine $E^{\infty}_g(n_k, N^{\infty}_b)$.

The purpose of this modular organization is to have two lower-level classes that include code-specific implementations and internally handle VASP technical details (such as INCAR definition and automatic parameter tuning), while `workchain_ExtrapolationScheme` is an almost code-independent class which performs the convergence logic.

The main workflow and the sub-workflows introduced above will be now presented in more detail by discussing their inputs, outputs and internal routines, starting by the lower level `workchain_DFTgroundState` and `workchain_DFTvirtualBands_GW`.
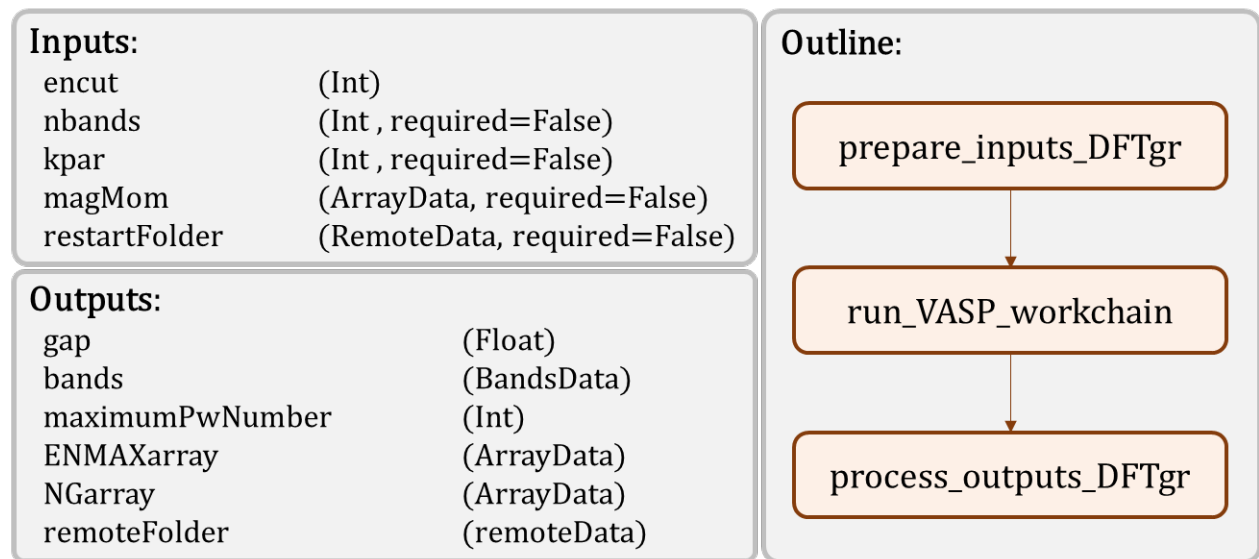
`workchain_DFTgroundState`

Inputs:	
encut	(Int)
nbands	(Int , required=False)
kpar	(Int , required=False)
magMom	(ArrayData, required=False)
restartFolder	(RemoteData, required=False)

Outputs:	
gap	(Float)
bands	(BandsData)
maximumPwNumber	(Int)
ENMAXarray	(ArrayData)
NGarray	(ArrayData)
remoteFolder	(remoteData)

Outline:
- prepare_inputs_DFTgr
- run_VASP_workchain
- process_outputs_DFTgr

Figure 5.5: Principal inputs, outputs and routines (as called inside `outline()`) of the sub-workflow `workchain_DFTgroundState`. `Int`, `Float`, `ArrayData`, `RemoteData` and `BandsData` are all native AiiDA types.

In addition to the inputs variables inherited from the AiiDA-VASP main workchain `VaspWorkChain` (parser and MPI settings, pseudopotentials and k-point mesh) the subworkflow has several supplementary inputs arguments which can be used to override the default INCAR parameters. More precisely, `kpar` can be used to specify a custom value for the k-point parallelization; if `magMom` is set a spin-polarized calculation is performed with the atoms' magnetic moments initialized from the array's values. If `magMom` is not passed, a non spin-polarized calculation is performed.

The workflow executes three different methods in sequence:

- The first routine defines the parameters required by the `INCAR`, specifies the parser settings and copy the WAVECAR from the input `restartFolder` path (if present) to the current calculation's folder.

- `run_VASP_workchain` submits the actual VASP calculation (by calling the `VaspWorkChain` workchain defined inside the AiiDA-VASP) using the parameters defined in the previous routine.

- The last routine checks for failures during the VASP run, extracts the bands and gap and returns the output variables.

The output arguments `ENMAXarray`, `NGarray` and `maximumPwNumber` (parsed from the OUT-CAR) will be used to determine $E_{cut}^1, E_{cut}^2, E_{cut}^3$ and the corresponding N_b^1, N_b^2, N_b^3 under the complete basis set hypothesis. More specifically, `ENMAXarray` contains the default `ENCUT`s of all species involved (as defined inside the pseudopotential files), `NGarray` the FFT mesh used by VASP and `maximumPwNumber` the number of plane waves contained in the complete basis for the cutoff value employed during the calculation.
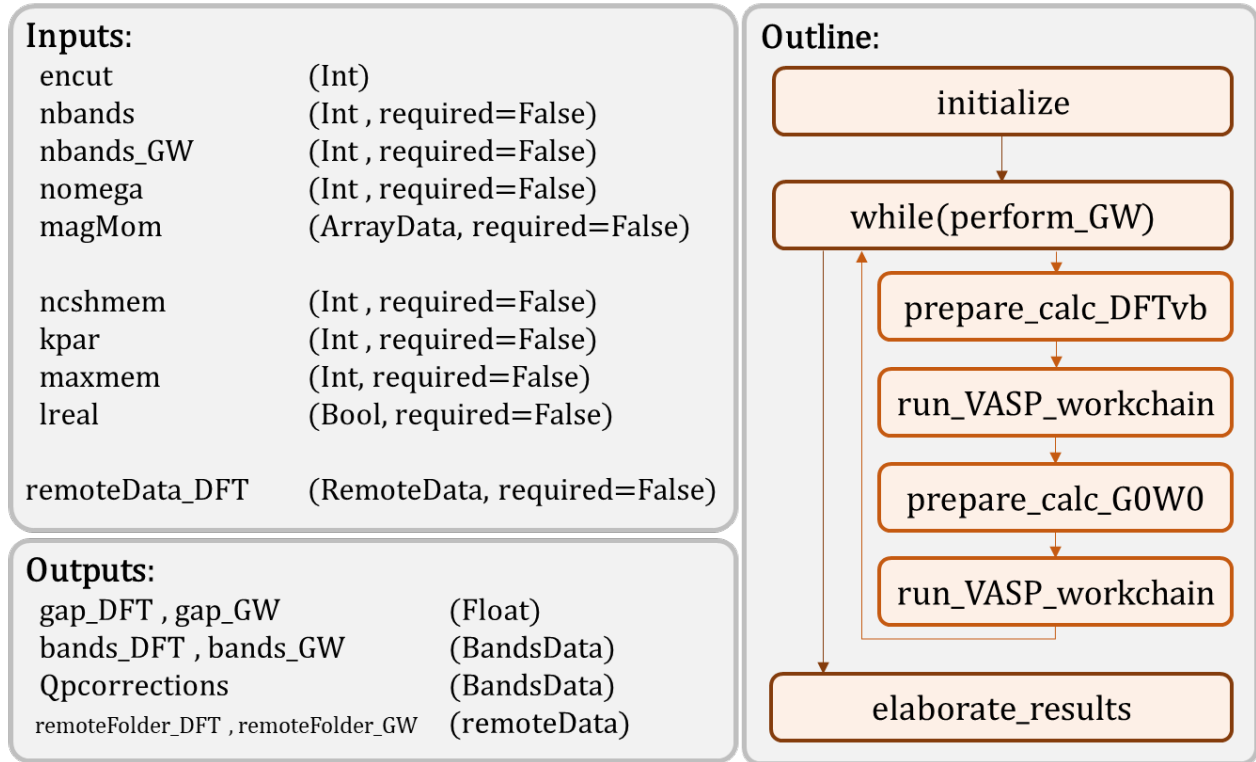
`workchain_DFTvirtualBands_GW`

Inputs:

encut	(Int)
nbands	(Int , required=False)
nbands_GW	(Int , required=False)
nomega	(Int , required=False)
magMom	(ArrayData, required=False)
ncshmem	(Int , required=False)
kpar	(Int , required=False)
maxmem	(Int, required=False)
lreal	(Bool, required=False)
remoteData_DFT	(RemoteData, required=False)

Outputs:

gap_DFT , gap_GW	(Float)
bands_DFT , bands_GW	(BandsData)
Qpcorrections	(BandsData)
remoteFolder_DFT , remoteFolder_GW	(remoteData)

Outline:

initialize

while(perform_GW)

prepare_calc_DFTvb

run_VASP_workchain

prepare_calc_G0W0

run_VASP_workchain

elaborate_results

Figure 5.6: Principal inputs, outputs and routines (as called inside `outline()`) of the subworkflow `workchain_DFTvirtualBands_GW`.

Each iteration of the while loop performs a sequence of two calculations: a DFT run (step 2 of the procedure described in section 3) plus G_0W_0 calculation. A first DFT + G_0W_0 iteration is always performed; after their execution the `perform_GW` routine inspects the resulting

calculation nodes in search of errors or crashes; in case of failure it modifies the parameters and restarts another sequence of DFT + G_0W_0 simulations.

`prepare_calc_DFTvb` and `prepare_calc_GOWO` set up the inputs of the respective calculations, including:

- The parser and MPI settings, pseudopotentials and k-point mesh inputs (inputs inherited from the AiiDA-VASP main VASP workchain).

- INCAR parameters using the cutoff and number of bands supplied through `encut` and `nbands`.

- The default values can be overridden using the optional input arguments. More specifically `ncshmem`, `kpar`, `maxmem` control the parallelization options and `lreal` determines the `LREAL` VASP flag (which defines the method for the projection operators evaluation; the real space optimization reduces the memory occupation for large cells). `nbands_GW` and `nomega` override the VASP INCAR `NBANDSGW` and `NOMEGA` parameters.

- If `magMom` is passed a spin-polarized calculation is performed with the atoms' magnetic moments initialized from the arrays' values (instead of the standard non-spin polarized setting).

`run_VASP_workchain` submits the actual VASP calculation (by calling the VASP standard workchain defined inside AiiDA-VASP) using the parameters defined in the previous `prepare_calc` routine.

The last method `elaborate_results` extracts the bands and gaps and returns the output variables. The variables `remoteFolder_DFT`, `remoteFolder_GW` represent the folders containing the calculations on the remote cluster.

workchain_Extrapolation_scheme

As a first step `workchain_Extrapolation_scheme` runs a single DFT ground state calculation (`workchain_DFTgroundstate`). This calculation has two purposes: providing the orbitals for the DFT continuation run and returning the FFT mesh employed by VASP for this structure.

Why the FFT mesh? the maximum orbitals number that a basis set with a given cutoff E_{cut} allows to calculate is defined as the total number of the (reciprocal) vectors $\{\mathbf{G}\}$ of the finite FFT grid satisfying $|\mathbf{q} + \mathbf{G}|^2 < E_{cut}$. The FFT mesh adopted must be therefore known in order to determine N_b^1, N_b^2 and N_b^3. VASP includes advanced routines that automatically choose the optimal FFT mesh for a given cell structure; the mesh is parsed from the DFT ground state calculation and taken into account in the workflow.

The role of the `determine_completeBasis_encutNband` routine is to compute the cutoffs-bands pairs under the complete basis hypothesis. Klimeš *et al.* proposed to adopt $E_{cut}^1, E_{cut}^2, E_{cut}^3$
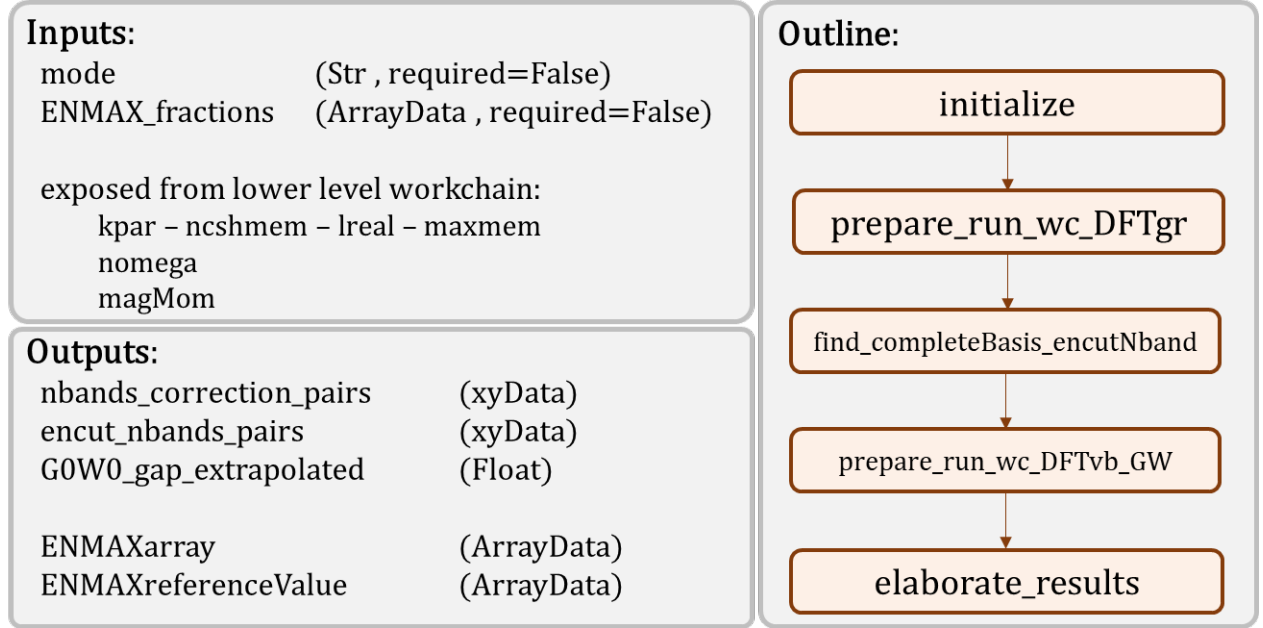
57

Figure 5.7: Principal inputs, outputs and routines (as called inside `outline()`) of the subworkflow `workchain_Extrapolation_scheme`.

equal to respectively $1.0\times, 1.25\times, 1.5\times$ the maximum energy cutoff provided in the pseudo-potentials, while Ellinger *et al.* introduces a memory conserving variant based on the $0.75\times$, $1.0\times$ and $1.25\times$ factors. Both versions are available in the current workflow and can be selected through the `mode` flag.

As cited above, the calculation of N_b for a given cutoff takes into account the finite FFT mesh. However it's of paramount importance to consider a parallelization constraint introduced by VASP: N_b has to be an integer multiple of (`total number of MPI threads`)/KPAR. If the supplied bands number breaks this condition, VASP forcibly increases the parameter to the closest multiple. If not correctly taken into account, this behavior breaks the correct E_{cut}-N_b relation, in the sense that the total number of bands does *not* coincide anymore with the complete basis defined by E_{cut}. The solution adopted here improves over the idea introduced by Ellinger *et al.*:

1. The standard pairs E^1_{cut}-N^1_b, E^2_{cut}-N^2_b, E^3_{cut}-N^3_b are computed. It's expected that *as-is* N^1_b, N^2_b and N^3_b might break the parallelization constraint.

2. A new set of $(N^1_b)^{corr}, (N^2_b)^{corr}$ and $(N^3_b)^{corr}$ are calculated as the values closest to the original N^1_b, N^2_b and N^3_b that satisfy the condition stated above.

3. The original $E_{cut} - N_b$ pairs are fitted using a polynomial function; the relation is inverted to determine the $(E^1_{cut})^{corr}, (E^2_{cut})^{corr}$ and $(E^3_{cut})^{corr}$ values associated to $(N^1_b)^{corr}$, $(N^2_b)^{corr}$ and $(N^3_b)^{corr}$.

Once the pairs $(E_{cut})^{corr} - (N_b)^{corr}$ are established, the `prepare_run_wc_DFTvb_GW` routine submits *in parallel* three instances of the subworkflow `workchain_DFTvirtualBands_GW`, one for each pair.

The last task of the workchain is to collect the G_0W_0 gaps and Quasiparticle corrections and perform the extrapolation; the resulting value is the output argument `GOWO_gap_extrapolated`. The `nbands_correction_pairs` and `encut_nbands_pairs` arguments contains the G_0W_0 gaps used for the $1/N_b$ fit alongside the $(E_{cut})^{corr} - (N_b)^{corr}$ pairs.

4 Implementation details: Contributions to the plugin development

AiiDA-VASP native core routines, parser and workchains allow the execution of DFT calculations only; therefore, as a part of this project, support for G_0W_0 and BSE calculations was added and tested. The AiiDA-VASP plugin delegates the parsing of the output files to an external python package, called Parsevasp, developed by the same community[6]. The package is composed by a main class and several specialized parser classes associated with specific output files (one for OUTCAR, one for vasprun.xml, etc.). The original parser classes do not include the possibility of beyond-DFT runs, and would therefore fail and return an error state if such calculations were submitted. An extension of Parsevasp in order to support GW and BSE calculations (and solve these errors) has been developed and implemented.

The specialized classes have also been expanded to parse additional quantities:

- Added support in the OUTCAR parser for extraction of the FFT mesh and of the maximum number of plane waves at DFT level; added support for G_0W_0 OUTCARs.

- Added support in the vasprun.xml parser for the BSE oscillator strengths and dielectric functions, using the library `xml.etree.ElementTree`.

- Modified the AiiDA-VASP main workchain to add the corresponding flags between the input settings.

- Modified the AiiDA-VASP core and error checking routines.

Both AiiDA-VASP core routines have been modified to add support for G0W0 calculations. Lastly, the AiiDA-VASP main workchain does not support the copy of arbitrary files from two different calculations. This feature is needed for `workchain_DFTvirtualBands_GW`, due to the WAVEDER file required by GW calculations, and has been developed. All modifications will be included in a future release of the plugin.

---

[6]The Parsevasp package can be found at `https://github.com/aiida-vasp/parsevasp`

5 Conclusions

In this chapter we presented the implementation of the convergence method derived by Klimeš *et al.* as an automated workflow based on the AiiDA and AiiDA-VASP plugins. The scheme defines a procedure to extrapolate Quasiparticle energies to the infinite-basis-set limit and was validated on molecules and bulk solids. Its main advantages are the reduced number of calculations required to achieve extrapolated results and the assumption of a complete basis set, which by design averts the risk of false convergences. In the second part of the chapter the general logic of the workflow, its various components and their technical aspects have been documented.

Chapter 6

Optical and excitonic properties of bulk transition metal oxide perovskites

The study of transition metal oxide (TMO) perovskites has brought to light a wide array of physical and chemical properties, including colossal magnetoresistance [177, 178], multiferroicity [179], metal-insulator transitions [180], superconductivity [181, 182], two dimensional electron gas [40] and spin and charge ordering [183]. In the last decades the $4d$ and $5d$ TMO perovskites have gained increasing interest due to the discovery of novel electronic and magnetic quantum states of matter arising from the coupling between spin-orbit interaction and other active degrees of freedom [184, 185, 186, 187].
Up to now, few theoretical studies have investigated the role of excitonic effects on the optical spectra of TMO perovskites [159, 188, 164, 189, 190]. These works have proved that the Independent Particle Approximation (IPA) is able to reproduce the experimental data only to a limited extent and that the inclusion of electron-hole (e-h) interaction is often pivotal to achieve a satisfying account of the optical transitions [188, 164, 189].

This work attempts to extend the study of excitonic effects from individual compounds towards a larger representative dataset, aiming to contribute to a comprehensive understanding of the role of the electron-hole interaction in TMO perovskites and perform a systematic investigation of its importance. Following the work of He et $al.$ [191] and Ergörenc et $al.$ [144], a representative dataset of fourteen TM perovskites is selected, including $3d$ ($SrTiO_3$, $LaScO_3$, $LaTiO_3$, $LaVO_3$, $LaCrO_3$, $LaMnO_3$, $LaFeO_3$ and $SrMnO_3$), $4d$ ($SrZrO_3$, $SrTcO_3$ and Ca_2RuO_4) and $5d$ ($SrHfO_3$, $KTaO_3$ and $NaOsO_3$) perovskites. The dataset includes compounds with different electronic, structural, magnetic and dielectric properties, as summarized in Table 6.1 and in Refs. [144]. Specifically: (i) insulating gaps ranging from 0.1 eV to 6 eV; (ii) $3d$, $4d$ and $5d$ TM-based perovskites with different orbital occupancy; (iii) non-magnetic and differently ordered AFM patterns; (iv) various crystal structures with different types of internal structural distortions (e.g. with and without Jahn-Teller instabilities); (v) macroscopic dielectric constant from 1 to 10.

An accurate estimation of the fundamental bandgap and of Quasiparticle energies are required in order to predict reliable interband optical transition energies. Density Functional Theory is usually considered not suitable in this regard; it commonly underestimates fundamental gaps and does not provide a reliable account of the excited state properties [70]. This task is instead successfully achieved by the G_0W_0 approximation [192, 193, 194], which provides a good description of the insulating gaps and band dispersions for the TMO perovskites [144, 165, 195, 161, 160].

In order to compute the optical properties, we solve the Bethe-Salpeter equation (BSE) [65, 108].

This chapter is extracted from a dedicated publication: **L. Varrassi**, P. Liu, Z. Ergönenc Yavas, M. Bokdam, G. Kresse and C. Franchini, Optical and excitonic properties of transition metal oxide perovskites by the Bethe-Salpeter equation, *Phys. Rev. Materials* 5, 074601 (2021)

	Crystal Structures	Electronic Configs.	Magnetic Orderings	E_{pw}	N_{pw}	N_ω	N_O	N_C
$SrTiO_3$	C-P$_{m\bar{3}m}$	$3d^0$	NM	600	512	96	12	10
$SrZrO_3$	C-P$_{m\bar{3}m}$	$4d^0$	NM	650	1972	64	12	12
$SrHfO_3$	C-P$_{m\bar{3}m}$	$5d^0$	NM	650	2304	96	12	13
$KTaO_3$	C-P$_{m\bar{3}m}$	$5d^0$	NM	500	896	96	12	12
$LaScO_3$	O-P$_{nma}$	$3d^0$	NM	500	1280	64	32	32
$LaTiO_3$	O-P$_{nma}$	$3t_{2g}^1$	G-AFM	500	448	64	34	34
$LaVO_3$	M-P$_{21/b}$	$3t_{2g}^2$	G-AFM	500	448	64	30	30
$LaCrO_3$	O-P$_{nma}$	$3t_{2g}^3$	G-AFM	500	448	64	32	32
$LaMnO_3$	O-P$_{nma}$	$3t_{2g}^3e_g^1$	A-AFM	500	448	64	26	26
$LaFeO_3$	O-P$_{nma}$	$3t_{2g}^3e_g^2$	G-AFM	500	448	96	34	34
$SrMnO_3$	C-P$_{m\bar{3}m}$	$3t_{2g}^3$	G-AFM	500	448	64	29	29
$SrTcO_3$	O-P$_{nma}$	$4t_{2g}^3$	G-AFM	500	512	64	30	30
Ca_2RuO_4	O-P$_{nma}$	$4t_{2g}^3e_g^1$	AFM	500	512	64	30	37
$NaOsO_3$	O-P$_{bca}$	$5t_{2g}^3$	G-AFM	500	448	64	30	30

Table 6.1: Material dataset and main computational parameters. The first column lists the considered compounds. The second set of columns collects the crystal structures (C=cubic, O=orthorombic, M=monoclinic), electronic configurations of the transition metal d shell and ground state magnetic orderings (NM=non-magnetic and different types of anti-ferromagnetic spin configurations [191]). The last set of columns lists the relevant computational parameters: plane-wave energy cutoff (E_{pw}, in eV), number of bands (N_{pw}), number of frequency points used for the G_0W_0 calculation (N_ω). N_O and N_C refer to the number of occupied and conduction bands included in the BSE.

1   Computational procedure and details

El.	PAW	r_s	r_p	r_d	r_f	E_{pw}
O	GW-US	1.2	1.5	1.6	1.4	434
	GW-NC	1.0	1.1	1.1		765
Na	GW-US	1.6	2.0	2.2		260
K	GW-US	1.7	2.0	2.5		249
Ca	GW-US	1.6	1.9	2.2		281
Sc	GW-US	1.7	1.7	1.9	2.0	379
Ti	GW-US	1.7	1.7	2.0	2.0	384
	GW-NC	0.9	1.4	1.9	1.9	785
V	GW-US	1.8	1.7	1.9	2.0	382
Cr	GW-US	2.8	2.5	2.5	2.8	219
Mn	GW-US	1.6	1.7	1.9	1.9	385
Fe	GW-US	1.5	1.7	1.9	2.0	388
Sr	GW-US	1.7	2.1	2.5	2.5	225
	GW-NC	1.1	2.0	2.3	2.1	543
Zr	GW-US	1.3	1.8	2.0	2.1	346
Tc	GW-US	1.5	1.8	2.2	2.3	318
Ru	GW-US	1.5	1.8	2.2	2.3	321
La	GW-US	1.6	1.8	2.2	2.5	314
Hf	GW-US	1.5	1.9	2.2	2.5	283
Ta	GW-US	1.5	1.9	2.2	2.5	286
Os	GW-US	1.5	1.8	2.2	2.3	319

Table 6.2: List of radial cutoff parameters (core radii, in atomic units) for each angular quantum number and default E_{pw} in eV for all potentials employed.

All *ab initio* calculations were performed using the Vienna *ab initio* Simulation Package (VASP) [17, 18] with the augmented wave method (PAW) [59]. The potential types are listed in Table 6.2; the GW versions of all PAW potentials were used. The ultra-soft (US) versions of the potentials were used for all materials except for Sr and Ti in $SrTiO_3$, for which the norm-conserving (NC) versions were used, consistently with Ergörenc *et al.* [144].

In order to determine the QP bandstucture we employ a G_0W_0 calculation from a DFT starting point. For $LaTiO_3$ and $LaVO_3$ PBE alone is not able to open the gap - therefore a small effective onsite Hubbard $U_{eff}= 2$ eV [144] was added, using the DFT+U formulation of Dudarev [196]. The spin-orbit coupling (SOC) is included for $NaOsO_3$ [197].

The convergence with respect to the number of bands and to the cutoff energy of the dataset is discussed in Ergönenc *et al.* [144]; their work also determines the basis-extrapolation corrections with respect to the number of bands/-cutoff energy for the dataset (employing the scheme described in section 2.3). Our results *include the basis set corrections determined through the extrapolation*: a scissor operator equal to the correction is applied to the unoccupied bands.

The Bethe-Salpeter equation is solved through a direct diagonalization scheme, which offers direct access to excitonic wavefunctions and allows for a more transparent interpretation of the main features of the optical spectra.

The exciton binding energies E_{xb} are computed as the difference between the first bright BSE transition and the fundamental G_0W_0 gap. The optical results will be interpreted in section

2.1 in terms of the joint density of states (JDOS) defined as:

$$\text{JDOS}(\omega) = 2 \sum_{v,c,\mathbf{k}} w_{\mathbf{k}} \delta \left(E_c(\mathbf{k}) - E_v(\mathbf{k}) - \hbar\omega \right),$$

where $E_c(\mathbf{k})$ and $E_v(\mathbf{k})$ are the G_0W_0 eigenvalues; the Dirac δ is approximated by a normalized Gaussian function with a broadening parameter of 0.10 eV.

The application of said G_0W_0+BSE procedure to TMO is computationally challenging: on the one hand, both G_0W_0 and BSE are notoriously computationally expensive, with an unfavorable scaling (The employed VASP implementations exhibit at least quartic scaling in the system size and quadratic in the number of k-points [198]). On the other hand to obtain reliable results *in particular with respect to the k-point mesh*, a precise convergence procedure is needed [108, 199]. In order to manage the computational cost associated to dense k-point mesh, alternative schemes have been proposed from shifted [198, 200] or hybrid k-point meshes [201] to interpolation schemes [202, 203, 200] or methods based on density matrix perturbation theory [204].

In order to mitigate these limitations and to achieve converged and reliable exciton binding energies for all compounds in the dataset, we adopted two different strategies: **(i)** a model-BSE approximation (which uses a parametrized model for the dielectric screening [205, 164]) and **(ii)** a k-averaging procedure.

	Converged k-mesh	k-point density $(kpts/\text{Å}^{-3})$
$SrTiO_3$	$20 \times 20 \times 20$	1920
$SrZrO_3$	$20 \times 20 \times 20$	2240
$SrHfO_3$	$20 \times 20 \times 20$	2240
$KTaO_3$	$20 \times 20 \times 20$	2040
$LaScO_3$	$10 \times 10 \times 6$	640
$LaTiO_3$	$10 \times 10 \times 6$	600
$LaVO_3$	$10 \times 10 \times 6$	580
$LaCrO_3$	$10 \times 10 \times 6$	570
$LaMnO_3$	$10 \times 10 \times 6$	590
$LaFeO_3$	$10 \times 10 \times 6$	590
$SrMnO_3$	$8 \times 8 \times 4$	230
$SrTcO_3$	$9 \times 9 \times 6$	480
Ca_2RuO_4	$8 \times 8 \times 4$	370
$NaOsO_3$	$9 \times 9 \times 6$	430

Table 6.3: Converged k-point grids and k-points densities for the listed materials. The k-point density is calculated as the total number of k-points divided by the Brillouin zone volume.

The mBSE scheme is used to perform the convergence tests and to determine the E_{xb} values, while the k-averaging technique (using the standard BSE scheme in the Tamm-Dancoff approximation [206]) is employed to calculate the optical conductivity spectra $\sigma(\omega)$.
In the next sections these strategies will be discussed in detail.

K-point convergence

It is well known that optical properties exhibit a strong dependence on k-point sampling and generally very dense k-point meshes are required to obtain well converged optical conductivities [199, 200, 201, 207, 208, 108, 199]. A too sparse k-point mesh may in fact introduce

spurious artifacts [209, 210] or incorrect estimations of the exciton binding energy [201, 205]. The criteria here employed for the k-point convergence is based on the accurate estimation of the first BSE eigenvalue E^Λ: a k-point mesh is considered converged when the first non-dark BSE eigenvalue is determined within an accuracy of 5 meV. The k-point grids that ensure the required E_{xb} accuracy are presented in Table 6.3 and range from $8 \times 8 \times 4$ to $20 \times 20 \times 20$, depending on the system.

We note that the cubic (C-P$_{m\bar{3}m}$) perovskites require considerably denser k-meshes than the magnetic compounds.

Nevertheless, even a $20 \times 20 \times 20$ mesh does not yield a fully converged $\sigma(\omega)$ over the entire energy range (see for example SrTiO$_3$ and KTaO$_3$ in Fig. 6.1).

In contrast, a fully converged $\sigma(\omega)$ has been obtained for all remaining perovskites, and even sparser k-point meshes are able to reproduce the spectra (see Fig. 6.1).

This behavior can be traced back to the different degree of localization of the first non-dark BSE eigenvectors $A_{cv\mathbf{k}}^\Lambda$, illustrated as contour-plots of the squared modulus $\sum_{v,c} \left| A_{cv\mathbf{k}}^\Lambda \right|^2$ in $\mathbf{k}$-space for selected examples in Fig. 6.2. The cubic compounds exhibit an excitonic wavefunction strongly localized around the Γ point in the BZ. This in turn imposes the necessity of very dense k-point meshes to correctly describe $A_{cv\mathbf{k}}^\Lambda$ [211, 209] and to avoid spurious artificial confinement effects [212]. The remaining perovskites show excitonic wavefunctions that span a larger portion of the BZ and thus require a less dense BZ sampling.
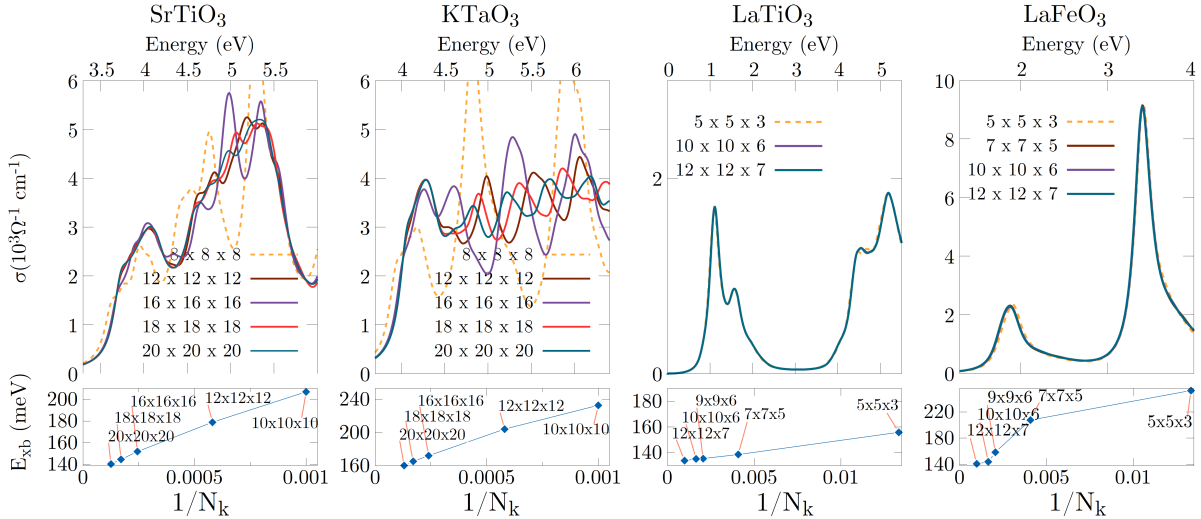
Figure 6.1: Convergence tests for the mBSE-derived $\sigma(\omega)$ (top panels) and exciton binding energies E_{xb} (lower panels) with respect to the number of k-points. The optical conductivities are expressed in $10^3\Omega^{-1}$cm^{-1}.
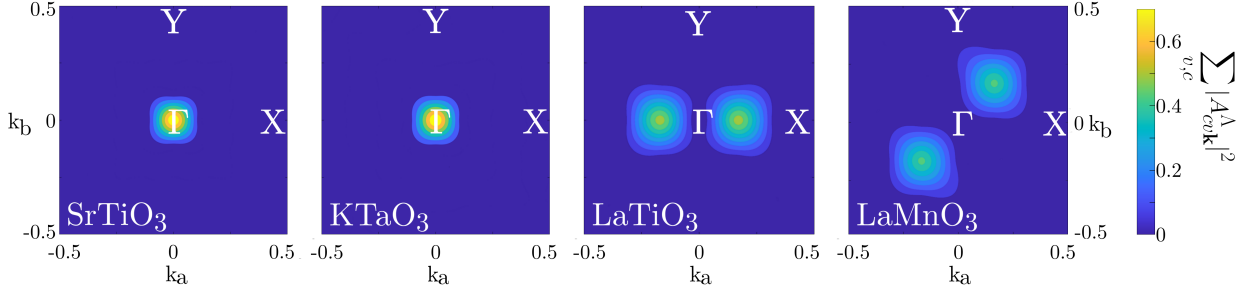
65

Figure 6.2: Contour plots of the squared modulus $\sum_{v,c} \left| A_{cv\mathbf{k}}^{\Lambda} \right|^2$ of the first non-dark exciton for $SrTiO_3$, $KTaO_3$, $LaTiO_3$ and $LaMnO_3$ along the $k_a - k_b$ plane (k_c=0) in the Brillouin zone. The eigenvectors are calculated with the BSE scheme on a $8 \times 8 \times 8$ k-mesh for $SrTiO_3$ and $KTaO3_3$ and on a $6 \times 6 \times 4$ for $LaTiO_3$ and $LaMnO_3$.

Model-BSE

The mBSE approach [201, 205] introduces two approximations to the standard BSE scheme:

1. Model dielectric screening approximation: the RPA dielectric function calculated in the G_0W_0 step is approximated by an analytic model [205]:

$$\epsilon_{\mathbf{G},\mathbf{G}}^{-1}(\mathbf{k}) = 1 - (1 - \epsilon_{\infty}^{-1})exp\left[-\frac{|\mathbf{k} + \mathbf{G}|^2}{4\lambda^2} \right], \tag{6.1}$$

where ϵ_{∞} is the static ion-clamped dielectric function and λ the range separation parameter, which is determined by fitting $\epsilon_{\mathbf{G},\mathbf{G}}^{-1}(\mathbf{k})$ to the RPA calculated one. The off-diagonal elements of the inverse dielectric function are neglected implying a diagonal ($\mathbf{G} = \mathbf{G}'$)screened Coulomb kernel. This analytical model has proven to be a good approximation to the full dielectric function [213].

2. The QP energies are approximated through the application of a scissor operator to the DFT one-electron energies (such that the resulting band gap matches the G_0W_0 one).

This approach reduces the overall computational cost and was successfully applied to halide perovskites [205, 214], iridates [164], 3d TMO [83, 189], and it has been shown to correctly reproduce the full BSE spectrum up to 6 eV for $SrTiO_3$ [189]. All scissor operators used, along with λ and ϵ_{∞}^{-1}, are detailed in Appendix C.

k-averaging

A k-averaging procedure was adopted to calculate the full BSE spectra [109, 164]. This averaging procedure includes two steps: in the first step all L irreducible k-points $\widetilde{\mathbf{k}}_{1,..,L}$ from a Γ-centered $n \times n \times n$ grid are generated; in the second step L independent G_0W_0+BSE

calculations are executed. Each calculation is based on a $m \times m \times m$ grid, shifted by the corresponding $\widetilde{\mathbf{k}}_{1,..,L}$. The final dielectric function is therefore attained by averaging over the previous results:

$$\epsilon(\omega) = \frac{1}{W} \sum_{p=1}^{L} w_{\widetilde{\mathbf{k}}_p} \epsilon_{\widetilde{\mathbf{k}}_p}(\omega), \qquad W = \sum_{p=1}^{L} w_{\widetilde{\mathbf{k}}_p}, \qquad (6.2)$$

where $\epsilon_{\widetilde{\mathbf{k}}}$ is the dielectric function calculated on the mesh shifted by $\widetilde{\mathbf{k}}$. The final result, which includes all k-points of a regular $(n \cdot m) \times (n \cdot m) \times (n \cdot m)$ calculation, is denoted by $m \times m \times m | n \times n \times n$.

This k-averaging scheme implicitly involves an approximation [109]: the long-range part of the Coulomb kernel is truncated at $\sim m$ times the unit cell size and consequently may cause spurious artifacts for extended real-space exciton wavefunctions. The cubic (C-P$_{m\bar{3}m}$) compounds, in particular, possess a (first non-dark) exciton wavefunction strongly localized around Γ, which corresponds to a delocalized real-space wavefunction and requires therefore careful testing. The magnetic TMO perovskites are instead less affected by the risk of spurious artifacts due to a more delocalized exciton wavefunction in reciprocal space.

The choice ($m = 4$, $n = 5$) does not introduce artificial artifacts in SrHfO$_3$, SrZrO$_3$ and KTaO$_3$; however to avoid a spurious peak suppression inside the SrTiO$_3$ optical spectrum, a larger $m = 7$ value is needed (see Appendix for more details B).

2 Electronic and optical properties

The discussion of the results is divided into three sections, each focusing on a specific subset of perovskites:

1. cubic non-magnetic perovskites (SrTiO$_3$, SrZrO$_3$, SrHfO$_3$ and KTaO$_3$)

2. Lanthanum series (LaScO$_3$, LaTiO$_3$, LaVO$_3$, LaCrO$_3$, LaMnO$_3$ and LaFeO$_3$)

3. Ca$_2$RuO$_4$, NaOsO$_3$, SrMnO$_3$, and SrTcO$_3$

2.1 Cubic Perovskites

Comparison between BSE and IPA spectra

The optical conductivity $\sigma(\omega)$ obtained through the k-averaging procedure for all cubic compounds is shown in Fig. 6.3. All spectra exhibit a similar lineshape characterized by two main structures (designated by their most intense peaks p_1 and p_2) caused by the crystal field splitting of the TM-d states into t_{2g} and e_g subsets.
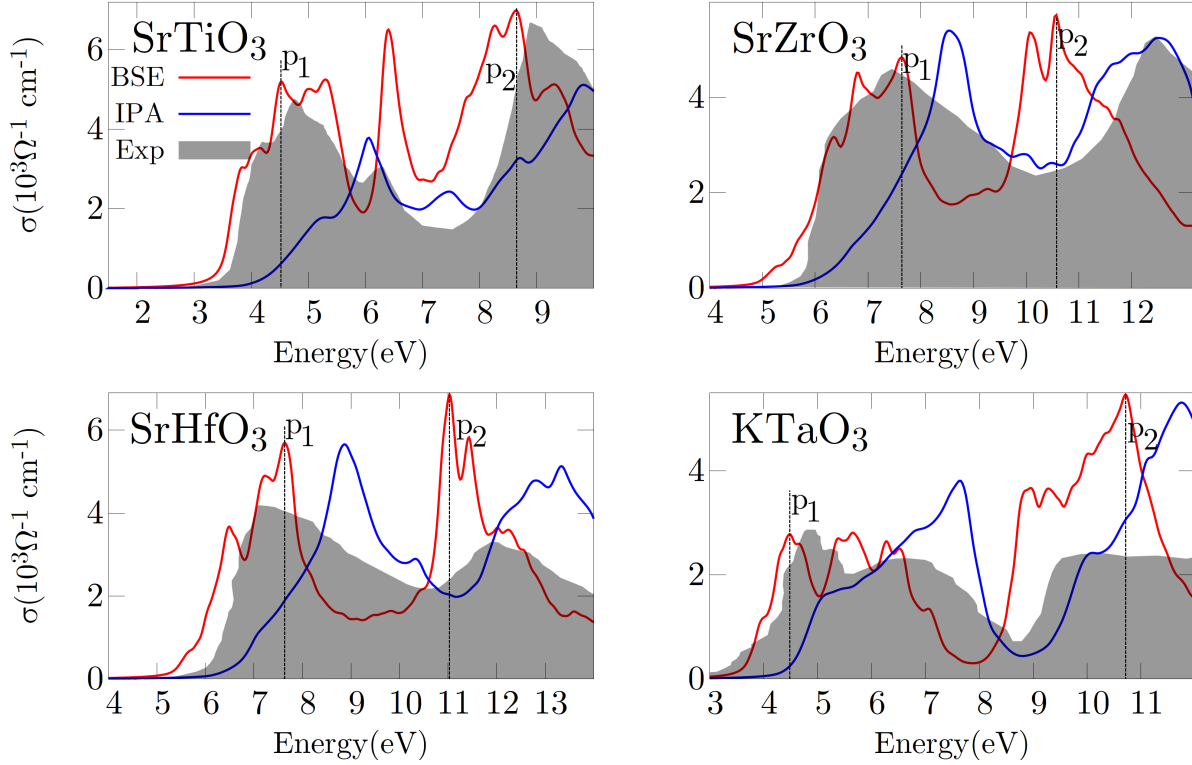
Figure 6.3: Optical conductivity $\sigma(\omega)$ calculated within the IPA (blue line), BSE approach (red line) and experimental data. All curves are obtained through a $5 \times 5 \times 5|4 \times 4 \times 4$ k-averaging, except for $SrTiO_3$ which employed a $7 \times 7 \times 7|4 \times 4 \times 4$. The main two peaks of the BSE spectra of each structure are labeled as p_1 and p_2.

We note that the very sharp peak observed in $SrTiO_3$ at ≈ 6.4 eV has no analogues in the other cubic materials. Its origin has been examined by Ref. [188, 189] and has been related to transitions to (low dispersing) localized Ti-e_g states along the Γ-X direction in the BZ. Sponza *et al.* [188] discussed the neglect of coupling terms (i.e. electron-phonon interaction or the dynamical screening) of the standard BSE approach as a possible reason behind the exceedingly strong intensity of the peak, which does not appear in the experimental data.

The BSE improves considerably upon IPA the quantitative agreement with the experimental data, in particular for what concern the intensities and energy positions of the first structures. The differences between the experimental centers of mass (CoM) of the p_1 structures and the BSE CoM are strongly reduced, with a mean absolute error of 0.24 eV compared to 1.00 eV for the IPA curves (see Fig. 6.4).

Small residual discrepancies between BSE and measured curves are visible at the onset, especially for $SrHfO_3$ and $SrZrO_3$. Significant contributions to these discrepancies originate from differences between the experimental and G_0W_0 predicted gaps [144], equal to 0.30 eV ($SrTiO_3$, $SrZrO_3$) and 0.40 eV ($SrHfO_3$). The BSE-induced redshift of the p_1

	k-mesh	SrTiO$_3$	SrZrO$_3$	SrHfO$_3$	KTaO$_3$
BSE	$11 \times 11 \times 11$	0.205	0.321	0.319	0.230
mBSE	$11 \times 11 \times 11$	0.195	0.308	0.293	0.215
% error		5	4	8	7
mBSE	$20 \times 20 \times 20$	0.149	0.275	0.258	0.160
ϵ_∞^{-1}		0.165	0.231	0.242	0.195
λ		1.463	1.457	1.448	1.420

Table 6.4: Exciton binding energies E_{xb} in eV for the cubic materials, calculated through the BSE and mBSE approaches. The third row summarizes the percentage errors between the BSE reference values and the mBSE ones. The employed k-point meshes are specified in the second column. The calculated inverse static dielectric constants and screening length parameters λ (Å^{-1}) used for the mBSE (Eq. (6.1)) are given.

structures (evaluated as the difference between the IPA and BSE spectra at the onset at $\sigma(\omega) \sim 1 \times 10^3 \Omega^{-1} \text{cm}^{-1}$) varies from 0.80 eV (KTaO$_3$) to 1.20 eV (SrTiO$_3$); significant spectral weight transfers are thus visible, signaling strong excitonic contributions for the considered cubic systems.

The onsets for the p_2 structure are instead systematically underestimated by about 1-2 eV; for SrTiO$_3$ this deviation was attributed to excessively strong excitonic effects [188]. The mean absolute error between the BSE CoM of the p_2 structures and the experimental ones (see Fig. 6.4) is equal to -0.75 eV.

The exciton binding energies E_{xb} for different k-meshes are listed in Table 6.4: the converged E_{xb} range between ≈ 150 and 250 meV. The use of mBSE for the E_{xb} estimation is justified by a direct comparison with the BSE prediction on a reduced $11 \times 11 \times 11$ mesh: the BSE reference values are very well reproduced by the mBSE, with an error varying from 4% (SrZrO$_3$) to 8% (SrHfO$_3$).

Our BSE calculated E_{xb} for SrTiO$_3$ (205 meV) is consistent with previous BSE predictions of Begum *et al.* [189] (246 meV, determined from a SCAN starting point) and Sponza *et al.* [188] (220 meV, determined from a LDA starting point).
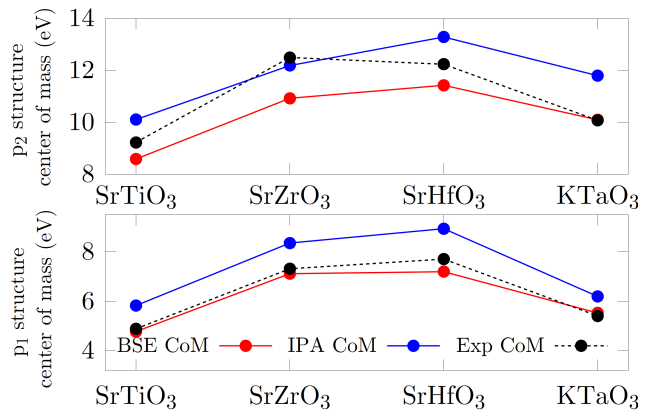
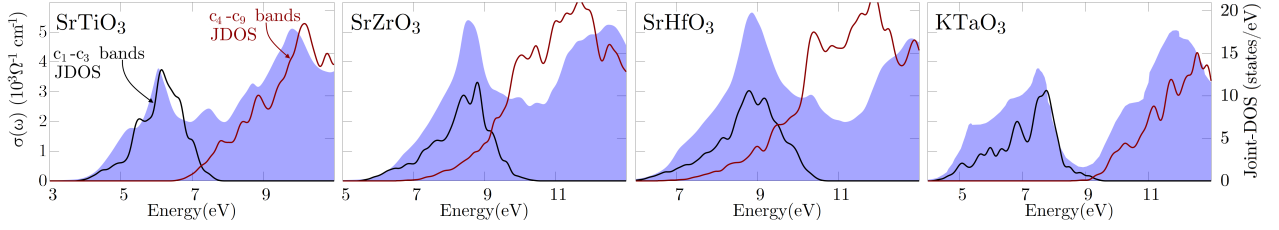**Figure 6.4:** Centers of mass (CoM) of the two main structures in the cubic compounds spectra.

69

Figure 6.5: Optical conductivity $\sigma(\omega)$ in the IPA (blue shadow background), along with the Joint Density of States associated with transitions to the first three conduction bands $c_1 - c_3$ (black lines) and to conduction bands $c_4 - c_9$ (red lines). All curves are obtained with a $11 \times 11 \times$ k-point mesh.

We note lastly that the choice of the k-point mesh has a paramount effect on the final values; the change of E_{xb} between the $11 \times 11 \times 11$ and the (converged) $20 \times 20 \times 20$ mesh is between 0.056 eV ($SrZrO_3$) and 0.088 eV ($KTaO_3$), see Table 6.4.

Origin and character of main optical transitions

We start the analysis of the transitions from the Joint Density of States (JDOS), visible in Fig. 6.5, which provides a measure of the number of allowed optical transitions between initial and final states. Here and in the following the discussion of the optical transitions is given in terms of the band labeling shown in Fig. 6.6, where the conduction bands are denoted as c_n with $n = 1$ for the first conduction band and so on.

The octahedral crystal field that causes the splitting of the d states is the dominant factor for the formation of the observed two-structure spectra. For $KTaO_3$ and $SrTiO_3$ the first structures (around peak p_1) are almost completely determined by transitions from the occupied oxygen manifold to the first three conduction bands (denoted as $c_1 - c_3$), i.e. $O\text{-}2p \rightarrow c_1 - c_3$ (the higher $c_4 - c_9$ conduction bands almost do not contribute to the first structures' JDOS). For these two compounds the $c_1 - c_3$ manifolds have a main $TM-t_{2g}$ character, with a limited $O-p$ hybridization away from the Γ point (between 5% and 15% for $SrTiO_3$ and between 2% and 20% for $KTaO_3$).

The analysis of $SrHfO_3$ and $SrZrO_3$ optical transitions is complicated by the presence of bands entanglement between the $c_1 - c_3$ manifold and the upper $c_4 - c_9$ manifold, not present in $KTaO_3$ and $SrTiO_3$ (where these two sets of bands are separated in energy, see Fig. 6.6). In fact the JDOS related to the two manifolds exhibit a significant overlap in Fig. 6.5. Similarly to $SrTiO_3$ and $KTaO_3$, the $c_1 - c_3$ bands possess a main $TM-t_{2g}$ character, which however is not uniform in the Brillouin zone and exhibits a significant hybridization with $O-p$ states (up to 27% for $SrZrO_3$ and 31% for $SrZrO_3$). Due to this bands entanglement the JDOS shows some contributions to the p_1 structures from transitions to bands $c_4 - c_9$ (see Fig. 6.5).

70

To ascertain the actual importance of these transitions and the relative significance of the $c_1 - c_3$ and $c_4 - c_9$ more quantitatively we list in Table 6.5 the BSE eigenvectors relative to the p_1 peak for each material in terms of the amplitude distribution (i.e. the total square amplitude) associated with transitions to bands $c_1 - c_3$ ($D^\Lambda_{c_1-c_3} = \sum_k \sum_{v \in O-2p} \sum_{c \in c_1-c_3} \left| A^\Lambda_{\mathbf{k}vc} \right|^2$) and bands $c_4 - c_9$ ($D^\Lambda_{c_1-49} = \sum_k \sum_{v \in O-2p} \sum_{c \in c_4-c_9} \left| A^\Lambda_{\mathbf{k}vc} \right|^2$). The eigenvalues listed in Table 6.5 are chosen as the transitions with the highest oscillator strength close to the p_1 peaks. Taking into account that $A^\Lambda_{\mathbf{k}vc}$ is normalized ($\sum_{\mathbf{k},v,c} \left| A^\Lambda_{\mathbf{k}vc} \right|^2 = 1$), the data in Table 6.5 indicate that transitions to $c_1 - c_3$ provide $\sim 90\%$ of the total spectral weight in $SrZrO_3$ and $SrHfO_3$, about 9% lower than the corresponding amplitudes in $SrTiO_3$ and $KTaO_3$.

	$SrTiO_3$	$SrZrO_3$	$SrHfO_3$	$KTaO_3$
$D^\Lambda_{c_1-c_3}$	0.99	0.89	0.88	0.99
$D^\Lambda_{c_4-c_9}$	0.01	0.11	0.12	0.01
E^Λ (eV)	4.400	7.178	7.513	4.883

Table 6.5: Comparison between BSE amplitude distributions D^Λ related to the final states c_1-c_3 ($D^\Lambda_{c_1-c_3} = \sum_k \sum_{v \in O-2p} \sum_{c \in c_1-c_3} \left| A^\Lambda_{\mathbf{k}vc} \right|^2$) and c_4-c_9 ($D^\Lambda_{c_1-49} = \sum_k \sum_{v \in O-2p} \sum_{c \in c_4-c_9} \left| A^\Lambda_{\mathbf{k}vc} \right|^2$). E^Λ represent the corresponding BSE eigenvalues: the analysed transitions are associated with the p_1 peaks. The data are obtained using a $11 \times 11 \times 11$ k-point mesh.

Additional insights on the character of the dominant optical transitions can be extracted by the fat band analysis of the BSE eigenvectors. This is displayed in Fig. 6.6 for the first non-dark excitons as well as for A^Λ_{vck} with the highest oscillator strength close to the p_1 peaks and p_2 peaks. As a general feature, common to all cubic materials, the contributions to $\left| A^\Lambda_{vck} \right|$ are predominantly localized at Γ (in particular for the first excitations, from the top of the valence band to the bottom of the conduction band) and, less intensively, along the $\Gamma-X$ direction. The fat band plots support the association of the p_1 peak with the transitions from the occupied $O-p$ bands (blue) to t_{2g} (red, $c_1 - c_3$).
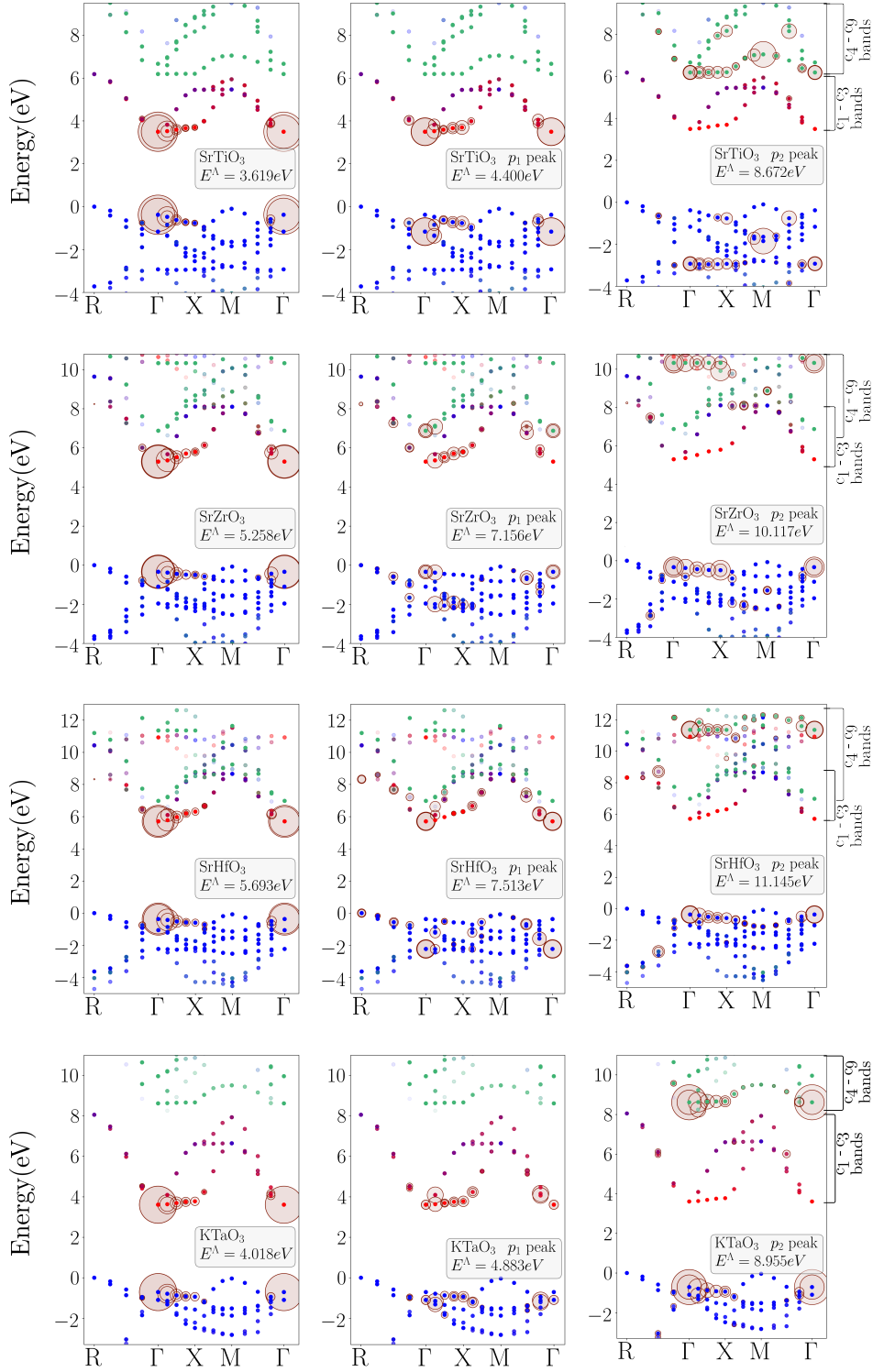
Figure 6.6: Fat band pictures: each circle radius corresponds to the contribution $\left| A^{\Lambda}_{\mathbf{k}vc} \right|^2$ at that k-point. The left panels refer to the *first* non-dark eigenvector of each material; the middle and right panels picture the $A^{\Lambda}_{\mathbf{k}vc}$ associated to the p_1 and p_2 peaks. The colors of the band-structures are associated with the orbital characters: blue for $O{-}p$, red for $TM{-}t_{2g}$ and green for $TM{-}e_g$.

2.2 La series

Comparison between BSE and IPA spectra
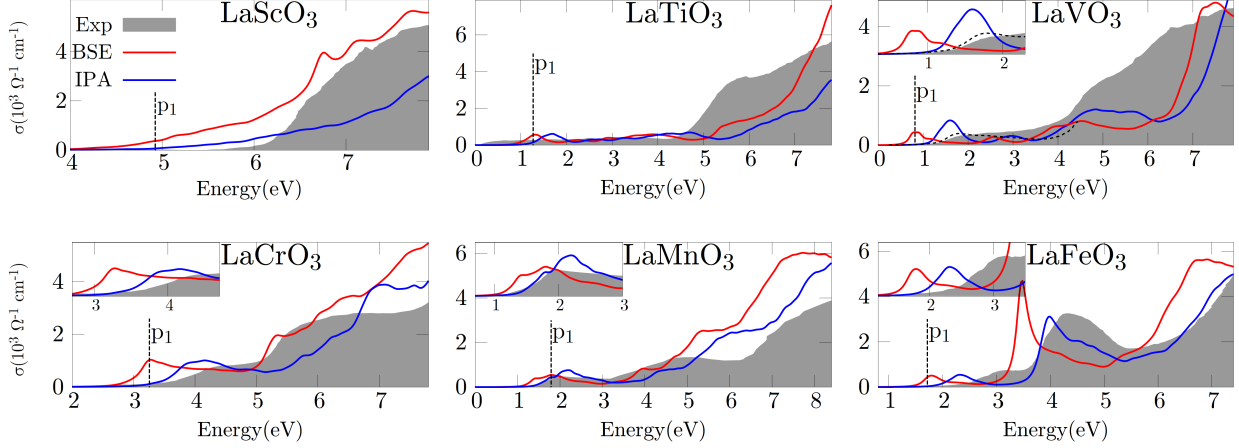
Figure 6.7: $\sigma(\omega)$ within the IPA (blue line), BSE approach (red line) and experimental data (from Arima *et al.* [215]; the dashed line for $LaVO_3$ represents the optical conductivity measurement from Miyasaka *et al.* [216]). All curves are obtained through a $5 \times 2 \times 5|2 \times 2 \times 2$ k-averaging, except for $LaScO_3$, for which a $5 \times 5 \times 3|2 \times 2 \times 2$ mesh was used. The p_1 labels denote the first (low intensity) BSE structures.

The optical conductivity spectra for the La-based perovskites are collected in Fig. 6.7. All members of the La series exhibit a qualitatively similar $\sigma(\omega)$ (with the exception of $LaScO_3$), characterized by two main different features: *a low intensity structure* at low energies and a *second* peak at higher energies, broader and more intense.
The low intensity peak is mainly associated with a Mott-Hubbard type (MH) *d-d* fundamental gap, while the second is typically associated with a charge-transfer (CT) type gap [215, 191, 144]. $LaCrO_3$ in particular can be better described by a mixed MH/CT state, where the first peak is essentially merged with the CT transitions [191]. The band insulator $LaScO_3$ does not obviously show any Mott-like $d - d$ transition.

The transition energies related to the first excitation are well reproduced already at the IPA level. The systematic redshifts produced by the excitonic effects (evaluated at $\sigma(\omega) \sim 0.3 \times 10^3 \Omega^{-1} cm^{-1}$) are reduced compared to the cubic compounds and vary from 0.3 eV (for $LaTiO_3$ and $LaMnO_3$) to 0.5 eV ($LaCrO_3$ and $LaFeO_3$) and 0.7 eV ($LaVO_3$). Therefore, when compared to the experimental curves, the BSE approach produces an underestimation of the first transition energies for almost all compounds. The only exception is $LaTiO_3$, where the optical gap is overestimated as a consequence of the corresponding overestimation of the experimental gap (0.1 eV) [215] obtained at G_0W_0 level (≈ 0.5 eV, as described by the non-extrapolated case of   [144]).

	k-point mesh	LaTMO$_3$					
		Sc	Ti	V	Cr	Mn	Fe
BSE	$6 \times 6 \times 4$	0.324	0.130	0.434	0.166	0.147	0.202
mBSE	$6 \times 6 \times 4$	0.292	0.145	0.273	0.200	0.181	0.162
% error		10	12	37	20	23	20
mBSE	$10 \times 10 \times 6$	0.189	0.134	0.263	0.171	0.160	0.116
ϵ_∞^{-1}		0.201	0.120	0.122	0.147	0.107	0.103
λ		1.462	1.349	1.420	1.393	1.335	1.336

Table 6.6: Exciton binding energies E_{xb} in eV for the La series compounds, calculated by mBSE and BSE approaches. Conventions used are the same as in Table 6.4.

The sources of the above deviations are discussed below for each compound. This involves both theoretical arguments and aspects of the experimental measurements (for instance, the available experimental data were obtained by different techniques at different temperatures, making a consistent comparison with computational data achieved at 0 K difficult, see Table S1 in the SM).

The second structure, located at $7 - 8$ eV, dominates the spectra and exhibits stronger excitonic effects, with redshifts (evaluated at $\sigma(\omega) \sim 3 \times 10^3 \Omega^{-1} \text{cm}^{-1}$) between 0.6 eV (LaCrO$_3$ and LaFeO$_3$) and 1.0 eV (LaVO$_3$). An improvement over the IPA is observed only for LaTiO$_3$, LaVO$_3$ and LaCrO$_3$; the quality of the agreement with the experimental curves is overall material dependent.

The ($p{\rightarrow}d$) band insulator LaScO$_3$ follows a trend dissimilar to the picture described above: it presents a single, wide and intense peak with a rather strong excitonic redshift of 0.9 eV (evaluated at $\sigma(\omega) \sim 0.3 \times 10^3 \Omega^{-1}\text{cm}^{-1}$). The disagreement between the measured and calculated spectrum should be traced back to the difference between the G$_0$W$_0$ and the experimental gap (≈ 1 eV [144]), which has been attributed to difficulties in measuring the long tail in the bottom part of the spectrum [144].
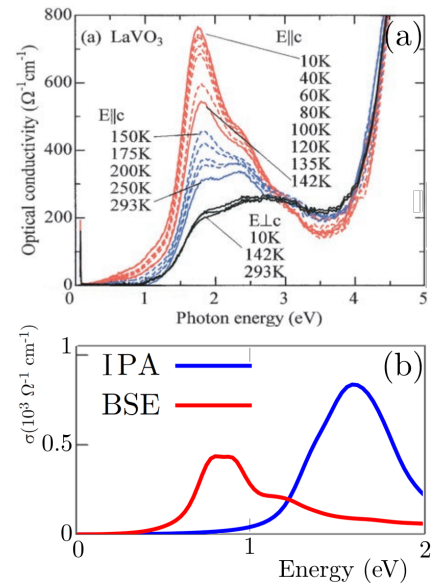
Figure 6.8: Comparison between the (a) experimental data for LaVO$_3$ reproduced from Miyasaka *et al.* J. Phys. Soc. Jpn., Vol. 71, No. 9,(2002) [216] and the ab-initio results (b).

The exciton binding energies (listed in Table 6.6) fall within the 120 meV - 190 meV range and are overall smaller than their cubic non-magnetic counterparts (with the exception of LaVO$_3$). The predicted higher E_{xb} for LaVO$_3$ is consistent with the larger experimental value of Lovinger *et al.* [217] ($\sim$ 0.6 eV). Recent experimental optical conductivity measurements [216] also highlight a splitting of the low-energy structure (visible as an additional shoulder at lower temperatures, see Figure 6.8) which has been related to excitonic effects [217, 218, 219] and is correctly reproduced by the BSE data - but completely absent in the IPA curve.

Compared to the full BSE, mBSE introduces an error ranging between 10% (LaScO$_3$) and 37% (LaVO$_3$), with a mean absolute error of 0.20 eV. The mBSE scheme therefore performs less satisfactorily for this subset than for the cubic non-magnetic perovskites; LaVO$_3$ exhibits the larger discrepancy both in absolute and percentage values of the whole set.

To gain insight on the cause of the larger error observed for LaVO$_3$, we completed a series of tests:

1. A mBSE calculation on top of the G$_0$W$_0$ band structure (while keeping the k-mesh, μ and λ fixed at the values of Table 6.6) was performed as a first step. In this manner the scissor operator is not required and we can isolate and gauge the effect of the model dielectric function approximation alone. The resulting mBSE@G$_0$W$_0$ exciton binding energy is only slightly increased with respect to the mBSE value (0.299 eV vs. 0.273 eV), and is still much smaller than $E_{xb}^{BSE} = 0.434$ eV. This in turn implies that the disagreement mostly arises from the model dielectric function approximation.
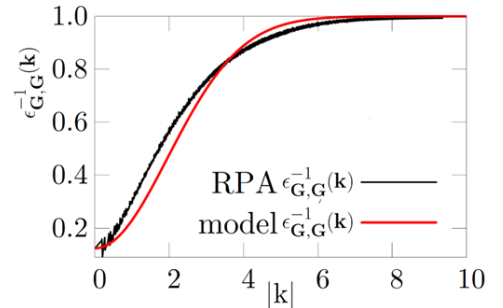
Figure 6.9: Comparison between the IPA $\epsilon_{\mathbf{G},\mathbf{G}}^{-1}(\mathbf{k})$ and the analytic expression determined from eq. 6.1.

2. The analytic expression for the *diagonal* terms $\mathbf{G} = \mathbf{G}'$ from eq. 6.1 reproduces satisfactorily the IPA curve as visible from Figure 6.9.

3. Is the neglect of non-diagonal terms the source of the error? To test this hypothesis an additional standard BSE@G$_0$W$_0$ calculation (within the Tamm-Dancoff approximation) retaining only the diagonal elements of the screened exchange kernel was performed. The resulting binding energy is $E_{xb}^{BSE-diag\,only} = 0.322$ eV, much closer to the mBSE@G$_0$W$_0$ value of 0.299 eV than to E_{xb}^{BSE} with the full (diagonal+off diagonal) screened exchange kernel (0.434 eV).

This proves that including off-diagonal elements in the inverse dielectric function and in the screened kernel is essential for accurately describing the excitonic properties of LaVO$_3$ and explains the limits of the model dielectric screening approximation for this material.

Origin and character of main optical transitions

We decode the character of the optical transition by analysing the excitonic eigenvectors also for this series of compounds. Fig. 6.12 presents the fat band pictures related to the first non-dark excitation and to the most intense oscillator strength of the p_1 peaks (as indicated in Fig. 2.2). The character of the excitonic wavefunction is closely connected to the electronic nature of the insulating state (band insulator, MH, CT and mixed MH/CT) [191, 215].

For the band-insulator $LaScO_3$ (top-left) the direct transitions at Γ dominate the excitonic wavefunctions (only minor contributions can be seen along the Γ-X direction) which involve $O - p$ to $Sc - d$ excitations.

The first (lowest) set of optical excitations for MH insulators $LaTiO_3$ (top-right), $LaVO_3$ (middle-left) and $LaMnO_3$ (bottom-left) are determined by d-d transitions exclusively involving the two MH sub-bands, whose states have a predominant $TM-d$ character [191, 165, 220, 221]. We note that contributions to eigenstates $A_{vc\mathbf{k}}^\Lambda$ at Γ are almost negligible. This can be explained by recalling that $d \to d$ transitions are dipole forbidden at k-points with a small point group equal to the full point group of the crystal, like the Γ point [222, 223]. However, the remaining region of the BZ has a small point group with a lowered symmetry, thus allowing the $d \to d$ transitions

Figure 6.10: Fat band picture for $A_{\mathbf{k}vc}$ associated with the third peak of $LaFeO_3$. The two main transition categories contributing to the eigenvector are distinguished by different colors.

determining the Mott peaks. The second main structures (for energies approximately larger than 4 eV) are instead determined by $p - d$ transitions from the valence $O-p$ bands (laying below the occupied MH subband) to the conduction MH subband; at higher energies transitions to $La-d$ states are also involved (not shown).

For $LaCrO_3$ and $LaFeO_3$ optical experiments reported the coexistence of MH/CT-type excitations at the fundamental gap [215]. This was later confirmed by first principles analyses which indicate a sizable admixture of O-p ($\approx 20\%/30\%$ for $LaCrO_3$ and $LaFeO_3$ respectively) and TM-d ($\approx 80\%/70\%$) [144, 165, 191, 224]. This mixed CT/MH nature of the optical excitations in $LaFeO_3$ is well captured by the BSE eigenvectors shown in the fat band plots of Fig. 6.12

Moreover, the optical spectrum of $LaFeO_3$ exhibits a peculiar third intense peak at $\sim 3-4eV$, whose contributions are analysed in Figure 6.10. Transitions from the mixed $O-p/Fe-d$ subband near the Fermi energy to the $Fe-d$ states located at ~ 4 eV provide the majority of the total square amplitude $\left(\sum_{\mathbf{k}}\sum_{v\in O\text{-}p/Fe\text{-}d}\sum_{c\in Fe\text{-}d\sim4eV}\left|A^\Lambda_{\mathbf{k}vc}\right|^2 \sim 0.59\right)$ and are particularly intense at the X and T points. A secondary contribution emerges from valence $O-p$ states at ~ -2 eV to the conduction bands at ~ 2 eV (with a $\sim 30\%$ total square amplitude).

For $LaCrO_3$ the coexistence of MH/CT-type transitions at the optical gap is associated with an overlapping of the Mott and CT excitations in the spectrum [215] and has been explained in terms of a significant mixing of Cr-t_{2g} and O-p at the valence band top [165, 191, 224]. The optical conductivity in Figure 6.7 only partially agrees with this picture: the energy separation between the p_1 peak and the CT structure is significantly overestimated and the optical gap possesses

Figure 6.11: Comparison between $LaCrO_3$ G_0W_0+BSE spectra and fat band pictures calculated from the PBE functional and from the hybrid functional (with an exchange fraction of 0.15). The p_1 peak of each spectra is labeled. The fat band pictures are associated with the first non-dark transitions.

a dominant $d-d$ character. This reduced mixed CT/MH character is due to a low O-p orbital character of the $LaCrO_3$ valence band maxima [144] (with an O-p percentage of $17\%-20\%$). Considering the perturbative nature of the G_0W_0 scheme, this apparent discrepancy could originate from the PBE starting point. To test this hypothesis we performed an additional G_0W_0+BSE calculation starting from hybrid functional orbitals (following the setup of Ref. [191], with an exchange fraction $\alpha = 0.15$). The results, shown in Figure 6.11, lead to an improved agreement with the experimental data. The oxygen character of the top of the valence band increases from $\sim 20\%$ to $\sim 30\%$, restoring the MH/CT mixed nature of the optical gap. The O-p valence bands below the MH subband are shifted towards higher energies, producing a reduction of the energy separation between the p_1 and CT peaks. However G_0W_0 on top of Heyd-Scuseria-Ernzerhof (HSE06) hybrid functional overestimates the experimental optical gap by ~ 0.6 eV (with BSE optical gap of 3.89 eV versus the experimental value of 3.30 eV [215]). Conversely, the calculations based on G_0W_0@PBE (on the same k-mesh) predicts a smaller optical gap of 2.74 eV.
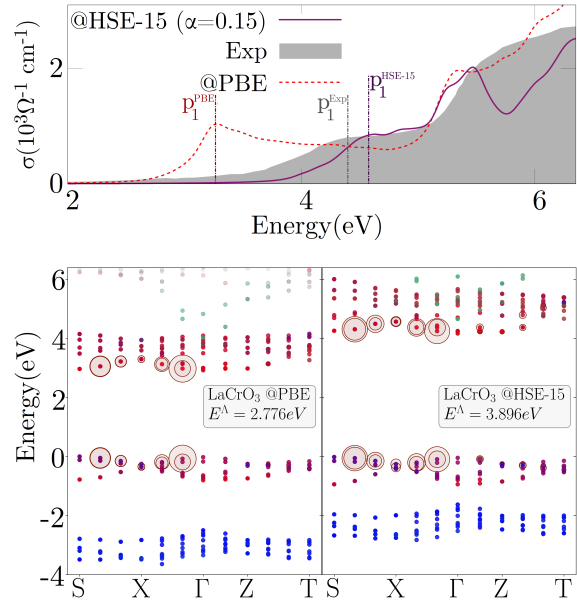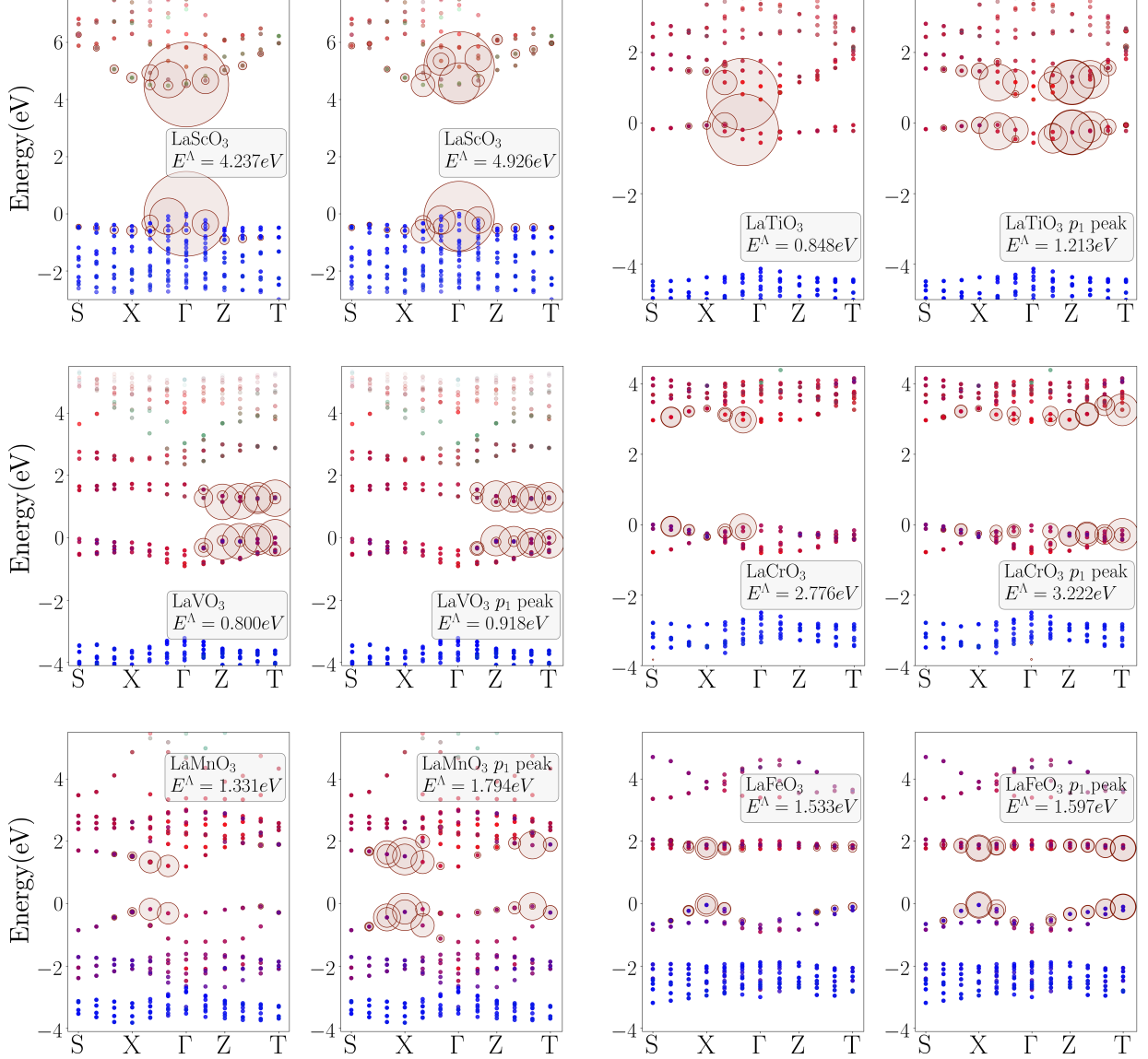
Figure 6.12: Fat band plots for members of the La series (LaTiO$_3$, LaVO$_3$, LaCrO$_3$, LaMnO$_3$, LaFeO$_3$ and LaScO$_3$). For each compound we show two panels: the left one refers to the *first* non-dark eigenvector whereas the right one is related to the eigenvector with the highest oscillator strength close to the p_1 BSE structures (see Fig. 6.7). Color codings and labelings are similar to those adopted in Fig. 6.6: blue for O$-p$, red for TM$-d$ and green for La$-d$.

2.3 Ca_2RuO_4, $NaOsO_3$ and $SrTMO_3$ (TM=Mn, Tc)

Comparison between BSE and IPA spectra
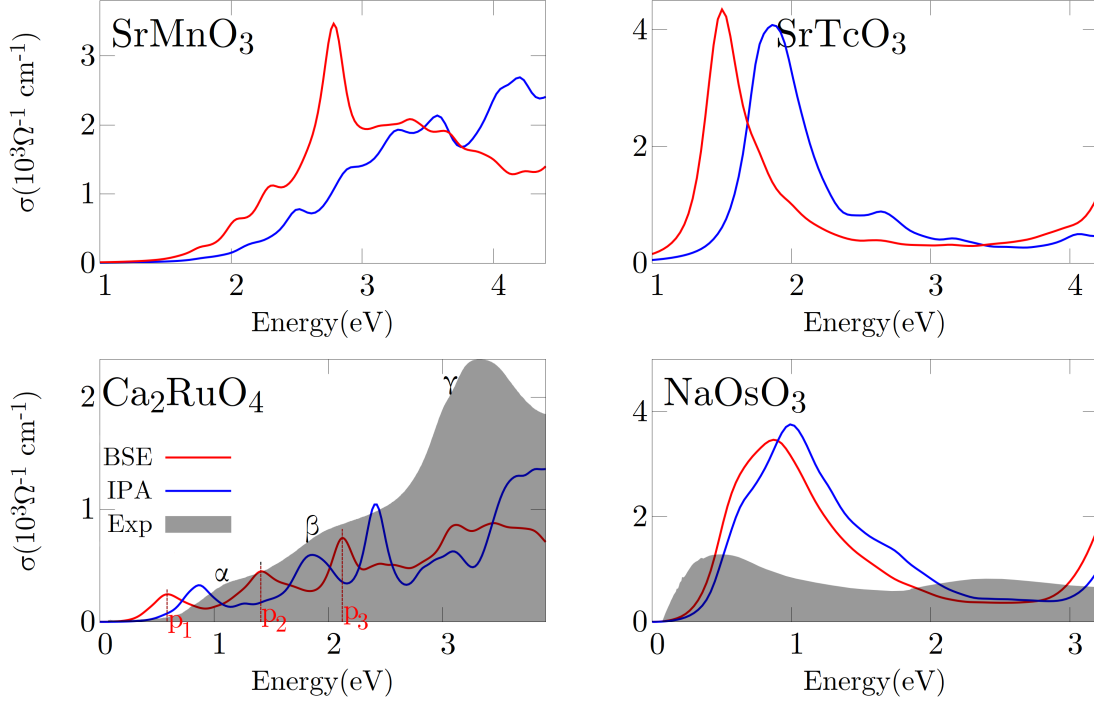
Figure 6.13: $\sigma(\omega)$ within the IPA (blue line), BSE approach (red line) and experimental data (from Arima *et al.* [215]; the dashed line for $LaVO_3$ represents the optical conductivity measurement from Miyasaka *et al.* [216]). All curves are obtained through a $5 \times 2 \times 5 | 2 \times 2 \times 2$ k-averaging, except for $LaScO_3$, for which a $5 \times 5 \times 3 | 2 \times 2 \times 2$ mesh was used. The p_1 labels denote the first (low intensity) BSE structures.

We complete the discussion of the results by reporting the analysis of the optical transitions for the remaining compounds: Ca_2RuO_4, $NaOsO_3$, $SrMnO_3$, and $SrTcO_3$ (the computed $\sigma(\omega)$ are collected in Fig. 6.13). For these compounds, a comparison with the measured optical conductivity is limited to $NaOsO_3$ [225] and Ca_2RuO_4 [226] (to the best of our knowledge, we are not aware of any experimental spectra for $SrMnO_3$ and $SrTcO_3$). For those materials only a qualitative agreement between theory and experiment is achieved.

The experimental spectrum of Ca_2RuO_4 exhibits three distinct peaks: 2 weak shoulders labeled α and β (following the nomenclature of Jung *et al.* [226]) and a third intense one at ~ 3 eV designated as γ. These peaks are correctly identified by both IPA and BSE approaches, despite the lower intensities. $\sigma^{IPA}(\omega)$ underestimates the experimental onset, and the BSE slightly aggravates this discrepancy with a redshift of ~ 0.2 eV. The α and β peaks

predicted by BSE exhibit a slightly more pronounced redshift (respectively ~ 0.3 eV and ~ 0.4 eV).

Despite retaining a transition metal of the same group, $SrMnO_3$ and $SrTcO_3$ exhibit rather different spectra. The $3d$ $SrMnO_3$ perovskite displays a wide and multi-peaked structure between 2 eV and 4 eV. The excitonic corrections are prominent, with a significant enhancement of the peak at 2.8 eV associated with a redshift of ~ 0.6 eV (evaluated at $\sigma \sim 2 \times 10^3 \Omega^{-1} cm^{-1}$). For the $4d$ perovskite $SrTcO_3$ BSE does not substantially modify the peaks intensity, but leads to a sizable redshift of about 0.4 eV for the first peak (evaluated at $\sigma \sim 2 \times 10^3 \Omega^{-1} cm^{-1}$). The $5d$ compound $NaOsO_3$ exhibits the highest ϵ_∞ within the dataset (suggesting a strong electronic screening) and the lowest excitonic redshift among all considered systems (~ 0.1 eV). This is reminiscent of the BSE prediction for other $5d$ systems (e.g. iridates [164, 187]), indicating relatively weak excitonic effects in extended $5d$ orbitals.

The calculated exciton binding energies, along with the parameters used for the constructing the model screening functions, are listed in Table 6.7. For this subset of materials, mBSE reproduces rather well the BSE binding energies E_{xb}.

	k-mesh	$SrMnO_3$	$SrTcO_3$	Ca_2RuO_4	$NaOsO_3$
	$4 \times 4 \times 2$			0.199	
BSE	$5 \times 5 \times 3$	0.081	0.104		0.059
	$4 \times 4 \times 2$			0.165	
mBSE	$5 \times 5 \times 3$	0.077	0.106		0.051
% error		5	2	17	14
	$8 \times 8 \times 4$	0.034		0.118	
mBSE	$9 \times 9 \times 6$		0.057		0.024
ϵ_∞^{-1}		0.088	0.071	0.087	0.031
λ		1.340	1.329	1.225	1.109

Table 6.7: Exciton binding energies E_{xb} in eV for Ca_2RuO_4, $NaOsO_3$ and $STMO_3$ (TM=Mn, Tc), calculated through the mBSE and BSE approaches. Conventions used are the same as in Table 6.4.

Origin and character of main optical transitions

We discuss the nature of the main transitions based on the fat bands analysis shown in Fig. 6.15. Similar to the previous cases, we focus our analysis on the first non-dark excitations and on the main peaks in the first part of the optical spectra.

For $SrTcO_3$ both the optical gap and the sharp peak at 1.4 eV exhibit a clear Mott char-

acter. Although the greater contributions to the $A^\Lambda_{\mathbf{k}vc}$ originate from the $Z - T$ direction, the excitonic wavefunctions themselves are delocalized in the BZ and their amplitudes are suppressed at the Γ point, as expected from Mott-type $d - d$ transitions (see discussion for the La series).

As already mentioned, SrMnO$_3$ displays marked differences: the uppermost valence bands exhibit a strong admixture of O$-p$ and Mn$-d$ (with a O$-p$ percentage varying between 18% along the Γ-X direction and 46% along M-R) indicating an intermediate CT/MH nature of the optical gap [144]. The associated wavefunction is more localized than the one calculated for SrTcO$_3$, with strong contributions only around the Γ-X direction.

The low-energy electronic structure of Ca$_2$RuO$_4$ has been widely studied and discussed [227, 226, 228, 229, 230, 231, 232, 233, 234, 231]. The $4d$ electrons occupy the t_{2g} orbitals, with the e_g states well separated in energy and completely empty. Our G$_0$W$_0$ data, in agreement with previous computational studies [226, 235], describes a t_{2g} manifold subjected to a further splitting, with the d_{xy} dominantly occupied and the d_{xz}/d_{yz} mixed and partially filled. The t_{2g} splitting has been associated with different mechanisms, including the rotation and tilting of the RuO$_6$ octahedra [228], spin-orbit interaction [229], c-axis contraction and crystal field stabilization [230, 231]. The O$-p$ percentage varies between 14% and 25% for the highest valence band and between 20% and 24% for the lowest conduction band, indicating an admixture of p and d states with a predominantly MH $d - d$ optical gap [144]. Our data suggest that the α peak is determined by transitions between filled and empty t_{2g} bands, more specifically between filled d_{xy} states and conduction d_{xz}/d_{yz} states. The β peak at ~ 1.5 eV can be assigned to transitions between the splitted d_{xz}/d_{yz} manifolds, whereas the γ peak at 2.2 eV is established by excitations from d_{xy} orbitals just below the Fermi energy
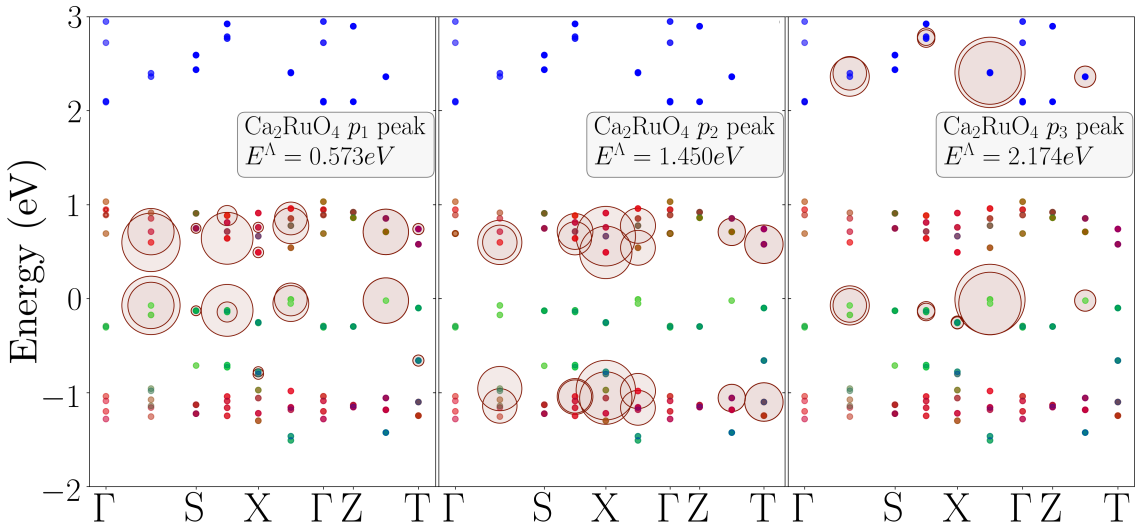
Figure 6.14: Fat band picture for $A_{\mathbf{k}vc}$ related to the first three BSE peaks of Ca$_2$RuO$_4$. Green color for Ru$-d_{xy}$, red for mixed Ru$-d_{xz}/d_{yz}$, blue for Ru$-e_g$.
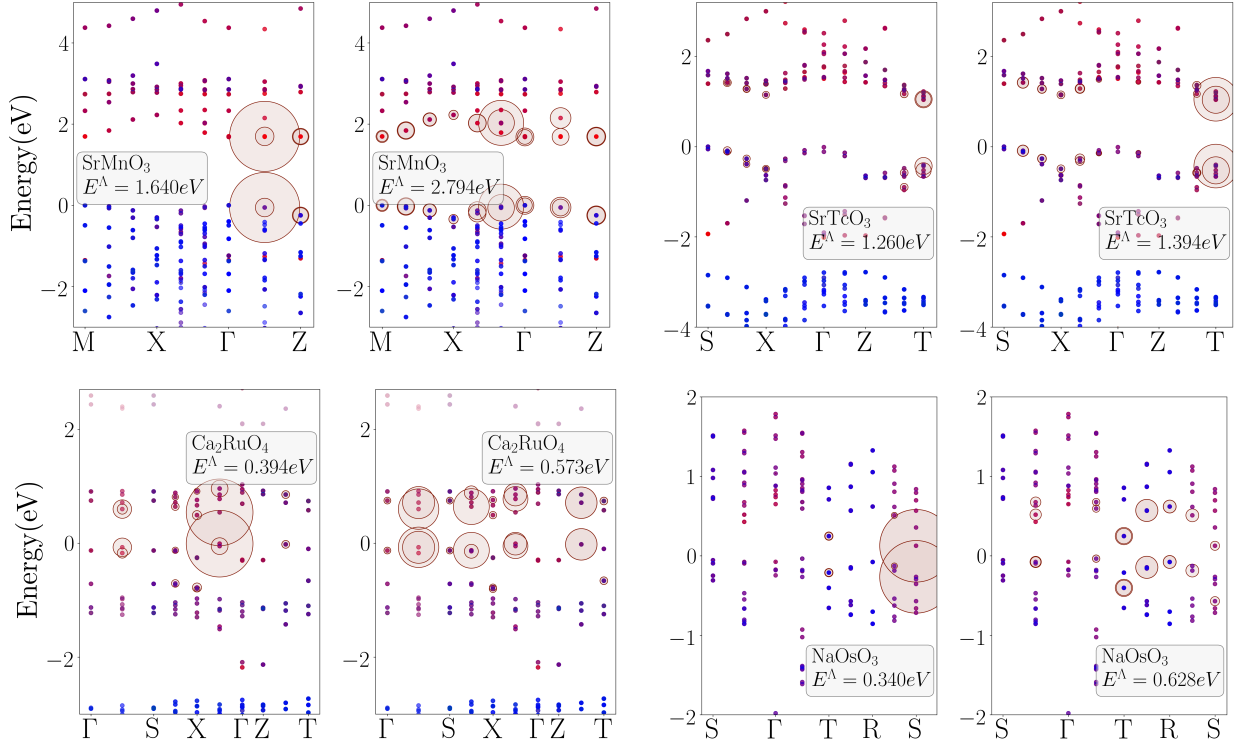
Figure 6.15: Fat band pictures for $SrMnO_3$, $SrTcO_3$, Ca_2RuO_4 and $NaOsO_3$. The left column refers to the *first* non-dark eigenvector of each material; the right column to the eigenvectors associated with the highest peaks in the first structures. Color codings and labelings are analogous to those adopted in Fig. 6.12: blue for $O-p$, red for $TM-t_{2g}$ and green for $Sr/Ca/Na-d$.

to Ru-e_g states > 2 eV above the Fermi energy (see Fig. 6.14). The wide structure around 3 eV in the BSE spectrum is determined by excitations from the $O-p$ bands near -3 eV under the Fermi energy towards the conduction d_{xz}/d_{yz} orbitals.

3 Conclusions

A systematic investigation of the optical and excitonic properties of a selected set of TMO perovskites was presented in this chapter by *ab-initio* G_0W_0 + BSE. The fourteen compounds were selected in order to constitute a minimal dataset representative of the variety of structural and electronic properties characteristic of this class of perovskites.

The solution of the Bethe Salpeter equation proves to be decisive to reach a quantitative agreement between the theoretical and experimental spectra for the cubic perovskites $SrTiO_3$, $SrHfO_3$, $SrZrO_3$ and $KTaO_3$. A pronounced spectral weight transfer is visible in their optical conductivity profiles (with an average redshift at the onset of 1.03 eV) due to excitonic ef-

fects. This confirms and extends the previous studies on $SrTiO_3$. To investigate the origin of the main structures of the spectra we analysed the e-h coupling coefficients associated with the most intense oscillator strengths. The contributions from transitions toward different conduction band manifolds are examined, and the role of band overlapping in $SrZrO_3$ and $SrHfO_3$ is discussed.

Comparisons with the reference experimental data have been discussed for the La series, $NaOsO_3$, and Ca_2RuO_4. The main features of the La series experimental spectra are correctly identified in both IPA and BSE approaches with similar line shapes. The excitonic corrections for this subset can be summarized as a redshift of the entire spectra, with an average value of 0.5 eV and reduced peak enhancements (with $LaFeO_3$ as partial exception). The BSE approach, however, consistently underestimates the experimental onset by 0.3˘1.0 eV. Furthermore the DFT results unable to account for the mixed MH/CT nature of $LaCrO_3$ optical gap, which can be instead correctly described by hybrid functionals.

A model-BSE (mBSE) approach was also employed to calculate the excitonic binding energies for this subset. The model-BSE scheme introduces two approximations: a scissor operator to mimic the Quasiparticle shifts and a model dielectric function to determine the dielectric screening. To assess the validity of this approach, we bench-marked the mBSE-calculated E_{xb} against the G_0W_0+BSE values obtained with the same k-point mesh. The BSE values are very well reproduced for the cubic subset [with a mean absolute percentage error (MAPE) of 6%] and for $SrMnO_3$, $SrTcO_3$, Ca_2RuO_4, and $NaOsO_3$ (with a MAPE of 9%). The discrepancies for the La series are larger, with a MAPE of 20%; the largest outlier is $LaVO_3$primarily due to the diagonal dielectric screening approximation. The overall agreement with experimental data is satisfactory, also considering the technical difficulties that hamper a precise measurement of optical spectra for TMO perovskites, and the tendency of this class of materials to be subjected to chemical defect (e.g., oxygen vacancies or presence of TM impurities).

Chapter 7

Excitonic and Quasiparticle properties of freestanding monolayer SrTiO$_3$

In the last decades low-dimensional materials have attracted increasing attention due to their remarkable physical properties resulting from quantum confinement and reduced dimensionality effects, which strongly differentiate them from bulk phases. In particular two-dimensional monolayer structures have been intensely studied due to their optical and excitonic physics: the enhanced electron-hole interaction results in strongly bound excitons which dominate the optical response and the charge transfer properties [113, 236, 237, 238, 239, 240, 241, 242, 243, 244, 245].

Recently an important advance has been achieved by Ji *et al.* [38] through the first experimental synthesis of freestanding perovskites SrTiO$_3$ and BiFeO$_3$ films with a thickness reaching the monolayer limit (see Figure 7.1). Their work constitutes a major breakthrough and represents an experimental evidence that TMO perovskites films can be realized with thicknesses below the critical limit previously proposed as necessary for crystalline order stability [39]. A year later freestanding PbTiO$_3$ films were fabricated with thicknesses down to four unit cells by Han *et al.* [246].

Recent theoretical works [112, 37, 188, 189] (as also discussed in section 6) analysed the role of electronic correlations and localized d states in the optical response of bulk SrTiO$_3$, and highlighted how including an explicit description of electron-hole interaction is necessary to achieve a satisfactory agreement with the experimental data. The experimental synthesis of freestanding TMO perovskites monolayers opens therefore the possibility of extending these analyses to the two-dimensional phase. To the best of our knowledge studies of excitonic effect on this compound have been confined to thin films, bulk phases or on heterostructures with other oxides and do not comprise structures near the monolayer limit.

In this chapter we present therefore a first principle study of the Quasiparticle and excitonic properties of freestanding monolayer SrTiO$_3$. The electronic structure is determined through the G$_0$W$_0$ approach; the role and effect of the inclusion of non-diagonal self energy
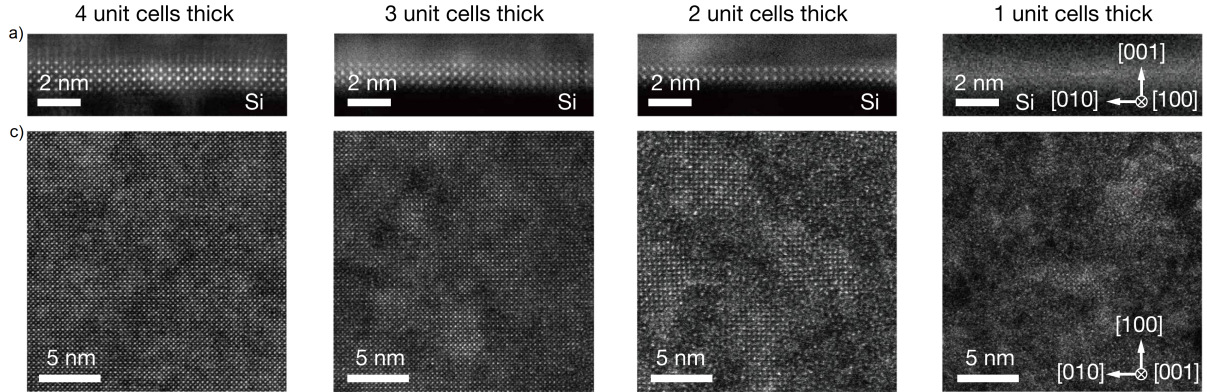
Figure 7.1: Figure reproduced from Ji *et al.* [38]. High-angle annular dark field (HAADF) image (**a**) and plan-view HAADFT images (**c**) of ultrathin freestanding SrTiO$_3$ films of various unit-cell thicknesses.

terms is discussed in section 3. The Bethe-Salpeter equation is solved in order to determine the optical properties (see section 4). Excitonic effects significantly alter the spectra, with the appearance of new bound exciton sharp peaks and a considerable enhancement of exciton binding energies. Through the analysis of the coupling components of the BSE eigenstates we show that the most intense peaks mix transitions to the Titanium localized d states in continuity to the bulk picture; however transitions to the *in plane* Ti$-d_{xy}$ orbitals and the remaining Ti$-d_{xz}/d_{yz}$ form separate excitation channels with different roles and contributions to the main features in the spectra. The exciton dispersion beyond the long wavelength limit is investigated by calculating the energy loss function at finite momentum.

This work is extracted from a paper currently ready for submission: **L. Varrassi**, P. Liu and C. Franchini, Quasiparticle and excitonic properties of freestanding monolayer SrTiO$_3$.

1 Computational procedure and details

Results from two different GW schemes are discussed in this chapter: in the first the QP energies are computed from a perturbative correction calculated with the diagonal approximation of the self energy - we label this scheme G$_0$W$_0$^{diag}. This method corresponds to the standard and most common GW scheme, which we employed in the other chapters of this Thesis. In the second approach the QP orbitals and eigenvalues are updated through the diagonalization of an Hamiltonian constructed from the full dynamic self-energy matrix Σ (which takes into account the off-diagonal terms) [73, 70, 71, 247], as described in section 5.3; we label this scheme as G$_0$W$_0$^{full} in order to distinguish it from the previous one. When required, we denote the starting point with the notation G$_0$W$_0$@starting point, as G$_0$W$_0$^{diag}@PBE or G$_0$W$_0$^{full}@PBE.

Unless otherwise stated, all GW calculations were carried with VASP version 6.2.1 and 6.3.1; the Yambo software (version 5.0.4) [19, 20], was employed for the bands number convergence, as discussed below. The norm conserving versions of the Sr, Ti and O VASP PAW PBE potentials [59] were adopted, as recommended by Ergönenc *et al.* [144]; more precisely the `Sr_sv_GW_nc 17Jun2013`, `Ti_sv_GW_nc 17Jun2013`, `O_h_GW 22May2013` POT-CARs were used for all GW results. For Yambo the Optimized Norm-Converving Vanderbilt pseudopotential of the `SG15` dataset were used [248], in particular `Sr_ONCV_PBE-1.2.upf`, `Ti_ONCV_PBE-1.2.upf` and `O_ONCV_PBE-1.2.upf`.

The GW production VASP simulations were performed with 96 frequency points ($N_\omega = 96$, `NOMEGA` flag), an energy cutoff of 600 eV and a cutoff of the response function (`ENCUTGW` flag) of 325 eV. To reduce the computational load a less dense FFT grid for the exact exchange part of the self-energy was used (`PRECFOCK=Fast`), after careful testing.

The basis extrapolation method was discarded for this 2D material due to computational constraints: due to the large vacuum required to prevent interactions between periodic images, the number of plane waves in the complete basis is exceedingly large (~ 22250 plane waves for a vacuum size of 40Å and a cutoff of 600 eV[1]).

The convergence study of the Quasiparticle (QP) direct and indirect gaps with respect to the vacuum size was carried out at $G_0W_0^{diag}$ level: a vacuum size of 40Å guarantees a convergence of 0.04 eV[2]. We point out a limitation of the employed setup: the current VASP implementation of the GW and BSE procedures does not provide the option of truncating the Coulomb interaction in low-dimensional materials. This feature has often played a very significant role in achieving accurate quantitative convergences [244, 239].

A k-mesh of $20 \times 20 \times 1$ guarantees a convergence of the QP gap and of the optical (direct) gap of 0.06 eV[3] (see Figure 7.2 (c)). The BSE matrix employed the Tamm-Dancoff approximation and included 6 conduction and 6 valence bands.

These two sets of convergence calculations were performed with the diagonal-only $G_0W_0^{diag}$ approximation, but the converged values were double-checked also for the G_0W_0 routines with the inclusion of the off-diagonal self-energy terms. The checkpointing feature described in section 5.5 was employed during the $G_0W_0^{diag}$ convergence studies.

The last step is the convergence study of the QP and optical gaps with respect to the energy cutoff and to the number of bands (which is often critical in GW calculations, see section 2.1). More than 1100 bands and a cutoff of 600 eV were required to reach a convergence threshold of 0.10 eV on the QP gaps, while ~ 2000 bands were required to achieve a convergence of

---

[1]The large vacuum size implies a unit cell with a sizable volume, which in turn implies a large FFT grid. The number of plane waves in a complete basis set depends on the FFT mesh, as described in section 4.

[2]The study was performed on a $8 \times 8 \times 1$ k-mesh, with 600 eV cutoff energy and 192 bands included; the vacuum size was increased during the convergence study at steps of 5Å.

[3]The calculations composing the convergence study with respect to the k-mesh were performed with a vacuum size of 40 Å, 600 eV energy cutoff and 192 bands.
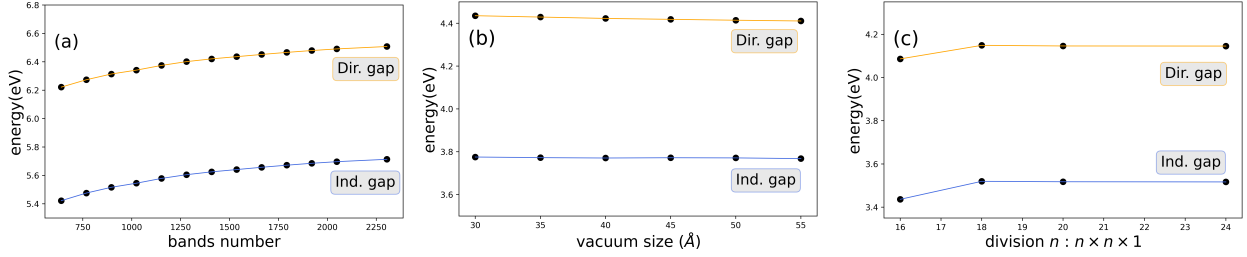
Figure 7.2: Convergence studies for the Quasiparticle gap with respect to (a) bands number, (b) vacuum size, (c) k-mesh divisions.

0.02 eV. The study was performed by running diagonal-only $G_0W_0^{diag}$ simulations on a very sparse k-mesh of $3 \times 3 \times 1$, which included the k-points determining the direct and indirect gaps (Figure 7.2 (a)).

Given the available resources, the computational cost of running a $G_0W_0^{full}$ simulation, (with the calculation of the full Σ matrix) with such converged parameters would have been prohibitive; we therefore adopted a different strategy:

1. In order to determine the QP gaps and bands a $G_0W_0^{full}$ calculation (with VASP) was performed with 192 bands, and the resulting bandstructure was corrected by a scissor operator which accounted for bands convergence. The scissor value was determined by subtracting the QP gap values obtained by performing two different $G_0W_0^{diag}$ calculations, one with the converged bands number and one with 192 bands. The GPU version of Yambo software was used for the calculations required for computing the scissor operator. The GPU acceleration of GW routines, available in Yambo but still in development for the VASP software, allowed a considerable speedup. hese calculations employed the Plasmon Pole model; in general the accuracy of the PPM can be strongly influenced and reduced for materials whose electronic properties are affected by transition metals' d level, such as ZnO or SnO_2 [249, 152]. Therefore as a first step we tested its validity for this particular material by comparing the PPM results with standard real axis integration ones within the Yambo code. The differences between the direct and indirect QP gaps from the two approaches are less than 0.04 eV. These tests were carried out on a reduced k-point mesh and a lower band number (respectively a $10 \times 10 \times 1$ k-mesh and 480 bands).

2. The scissor corrected $G_0W_0^{full}$ eigenvalues and orbitals were employed for the BSE step. However the RPA static screened kernels $W_\mathbf{q}(\omega = 0, \mathbf{G}_1, \mathbf{G}_2)$ were recalculated separately with the converged number of bands. The $\mathbf{q}$-point selection feature (part of the checkpointing feature described in section 5.5) was used for splitting the computational load in separate runs.

2 Relaxed structure and polarization

The one-unit-cell (001) for $SrTiO_3$ was determined through a structural optimization starting from the relaxed cubic bulk phase. The monolayer consists of two (nominally neutral) atom planes; the optimization results in a distortion along the z axis (see Figure 7.3), in agreement with previous works [250, 251]: The Ti and Sr atoms are displaced toward the inner side, with a larger displacement associated to the Sr atom (0.29 Å versus the 0.18 Å for Ti). The optimization has been carried out using the generalized gradient approximation of Perdew–Burke–Ernzerhof (PBE) as implemented in VASP, a cutoff of 900 eV, a k-point mesh of $10 \times 10 \times 1$ and a vacuum size of 40 Å.
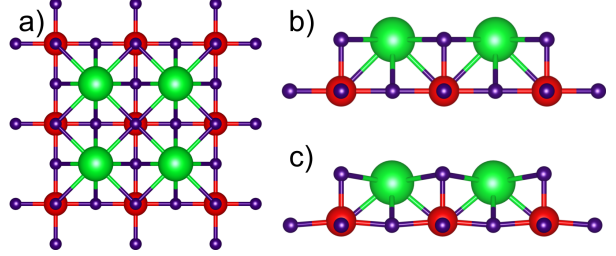
Figure 7.3: The lattice structures of monolayer $SrTiO_3$. a) describes the top view (identical for bot lattices), while b) and c) represent the non-relaxed and the relaxed structures respectively. green atoms are Sr, red Ti and blue Oxygens.

The distortion gives rise to a polarization perpendicular to the monolayer plane [251], which is equal to 0.069 |e|Å for the fully relaxed structure (determined through the evaluation of the Berry phase expressions). We note that the evaluation of the polarization using the approximated expression $P_{tot} = \sum_i \Delta R_i Z_i^*$ (where ΔR_i are the atomic displacements perpendicular to the monolayer plane and Z_i the Born effective charges) provides a value of 0.062 |e|Å close to the one determined by Berry phase formula.

3 Electronic properties: nonphysical dispersions

We start by examining the Quasiparticle bandstructures determined by the GW approaches for the relaxed and non-relaxed structures. The bandstructures at $G_0W_0{}^{diag}$ level for the relaxed structure are displayed in in Figure 7.4, while the different character contributions to the orbitals are visible in Figure 7.5. The GW schemes use a DFT (PBE) starting point.

Contrary to the bulk case, the QP corrections introduced by $G_0W_0{}^{diag}$ are not limited to a (almost constant) energy shift but are strongly band- and k-point dependent, and result in multiple band crossings and highly dispersive conduction bands at Γ-X and Γ-M (see Figure 7.4). The minima of the lowest conduction band at Γ and around Γ-X and Γ-M also possess a clear hybridization (with a reduced Ti-d contribution, between 55% and 65%, see Fig. 7.5). This is a clear difference from the PBE picture, where the lowest conduction bands are dominantly contributed by Ti-d. The valence band shapes are instead almost unchanged
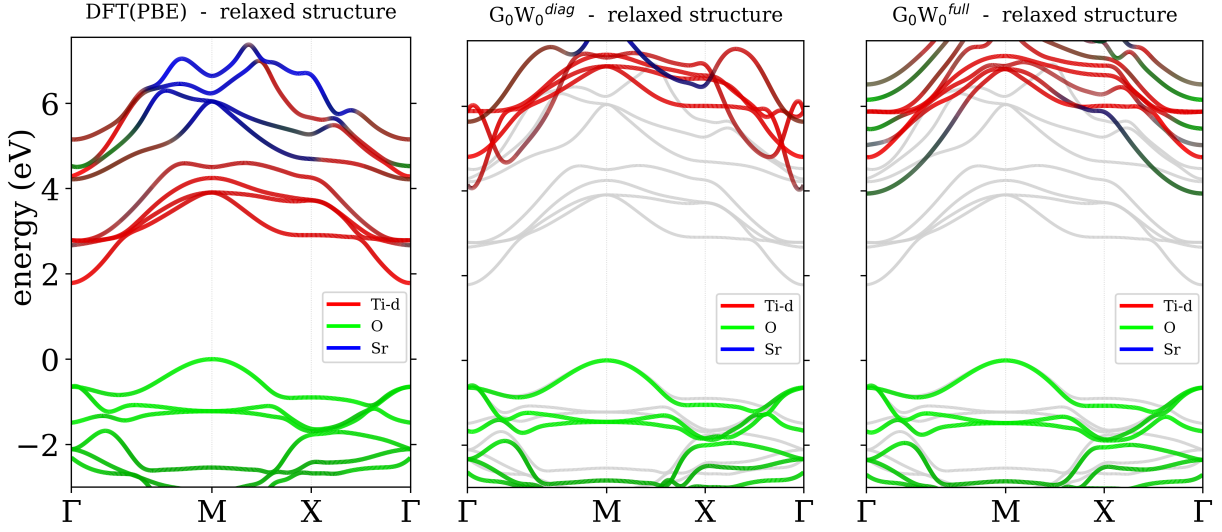
Figure 7.4: Orbital projected band structures for the *relaxed* structure. The zero of the energy scale is set at the top of the valence band for both PBE and G_0W_0 results. In the $G_0W_0{}^{diag}$ and $G_0W_0{}^{full}$ subfigures the DFT bandstucture is plotted for comparison as grey lines.
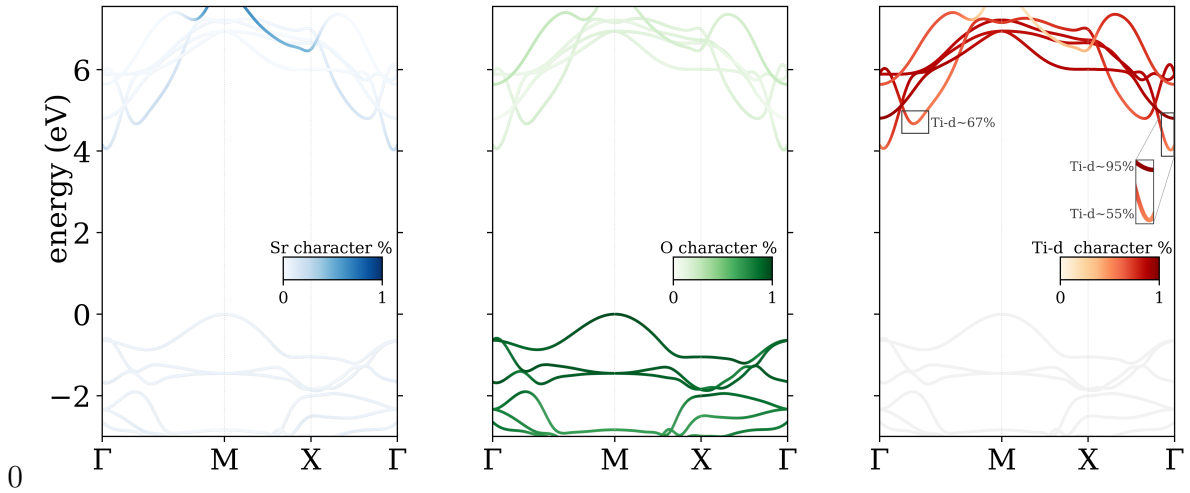

Figure 7.5: Orbital projected wavefunction character of the $G_0W_0{}^{diag}$ electronic bands for the *relaxed* monolayer. The character is determined as $\langle Y_{lm}^{\alpha} | \psi_{n\mathbf{k}} \rangle$, where Y_{lm}^{α} is the spherical harmonic centered on ion α with l, m angular and magnetic moments. For Ti only the contributions over the d states are displayed.

and the corrections are limited to a small stretching.

89

A comparable bandstructure for the relaxed structure was obtained from Yambo [19, 20] (see Appendix D), a different ab-initio software aimed at the study of excited state and Quasiparticle properties with many-body methods. The agreement between the two codes validates VASP data and suggests that this spurious behavior of the QP corrections is not imputable to the specific VASP implementation of the GW routines or to VASP pseudopotentials.

Yambo results were also employed to inspect the linear approximation of $\Sigma(\omega)$ close to the band crossings at Γ-X, in order to further validate the procedure. Figure 7.6 shows that for these states the linearization of the self-energy is very accurate: the feature described above cannot be therefore associated to a breakdown of this approximation.
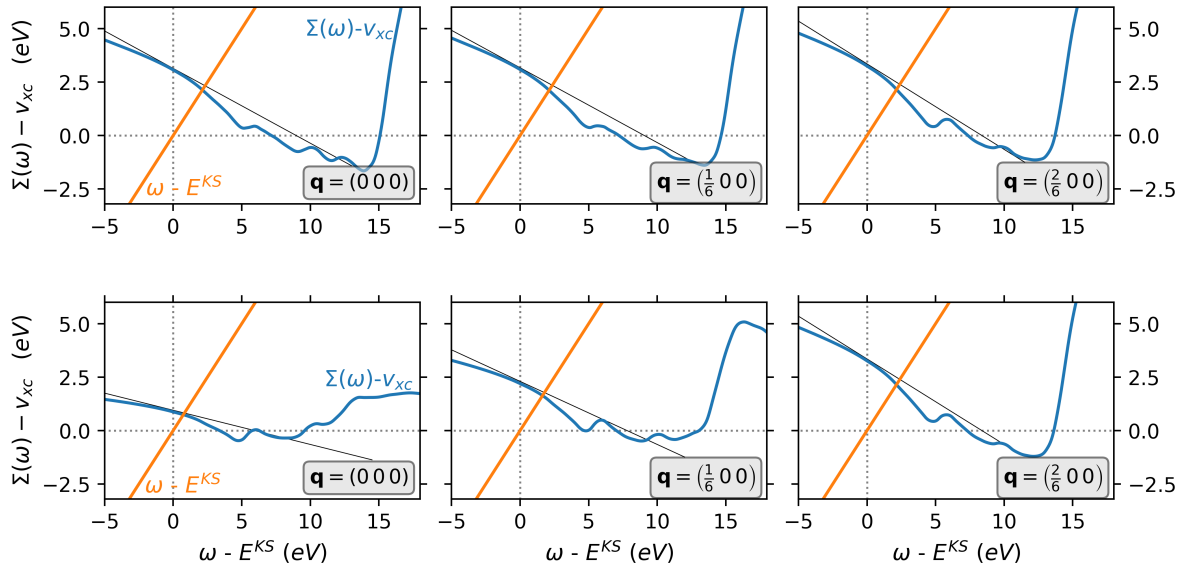
Figure 7.6: Graphical solution of the Quasiparticle equation for the first and second conduction bands near Γ-X. The orange line indicates $\omega - E^{KS}$, while the black line is the linear approximation. The intersection between the blue and orange line represents the solution to the QP equations, while the intersection between orange and black indicates the solution given by the linear approximation to the self energy.

Moreover, both VASP and Yambo allow to go beyond the linear approximation of the self-energy, either by using a non-linear iterative method based on the Secant scheme (Yambo, secant solver option) or through a Padé approximation of Σ and Brent method (as implemented in VASP for the low-scaling GW approach [29]). We compared the QP energies determined through the linerization and the non-linear iterative methods, and the differences for the first conduction bands are lower than 50 meV.

To clarify this subtle behavior it is instructive to compare the $G_0W_0^{diag}$ data with the QP energies produced by the $G_0W_0^{full}$ approach. The $G_0W_0^{full}$@PBE results

show markedly different conduction bands shapes with respect to the ones yielded by $G_0W_0{}^{diag}$@PBE: the bands crossings involving the lowest unoccupied bands and the unphysical bands dispersions around Γ-X and Γ-M are not visible anymore (see Fig. 7.4).

Moreover, the $G_0W_0{}^{full}$ conduction manifolds exhibit a more pronounced hybridization with respect to the $G_0W_0{}^{diag}$@PBE reference; in particular the lowest $G_0W_0{}^{full}$ conduction band possesses a sizable mixture with O states and secondarily Sr states at Γ. We note again that the conduction states character is completely different from the PBE description.

	Direct (eV)	Indirect (eV)
BSE@$G_0W_0^{full}(E_{xb})$	3.473 (1.04)	3.299 (0.59)
$G_0W_0^{full}$	4.514	3.888
$G_0W_0^{diag}$	4.774	4.114

Table 7.1: Direct and indirect quasiparticle (QP) and optical gaps for the relaxed monolayer, including the exciton binding energies E_{xb} of the first excitonic state. The QP gaps are displayed for both $G_0W_0^{full}$ and $G_0W_0^{diag}$ schemes; the optical gaps and E_{xb} are computed from the resolution of Bethe-Salpeter equation starting from $G_0W_0^{full}$ results. All energies are in eV.
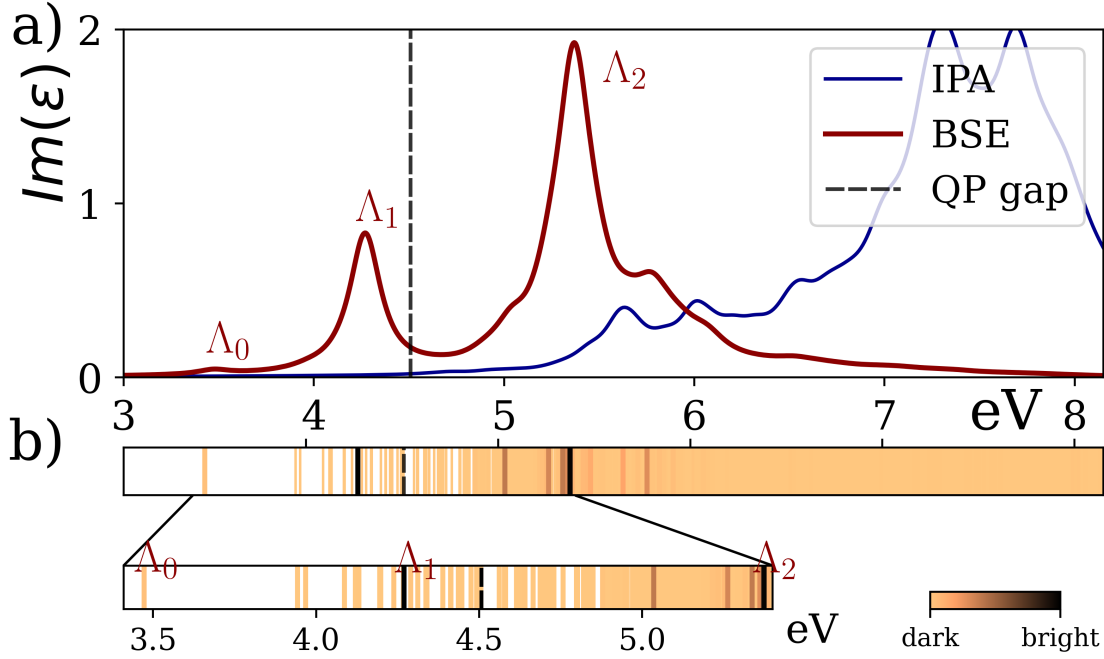
The unreliable description of $G_0W_0{}^{diag}$ is associated with two different factors: the first is the well known starting point dependence [65, 30, 252, 81, 253] of the diagonal G_0W_0 approximation. The incorrect orbital character description of the DFT calculations causes erroneous QP corrections and hence the $G_0W_0{}^{diag}$ unphysical band dispersions.

On the other hand, $G_0W_0{}^{diag}$ neglects non-diagonal self-energy elements: due to the absence of these terms the coupling that could *hybridize the single particle states is missing*. The inclusion of the off-diagonal Σ terms in the $G_0W_0{}^{full}$ scheme is in fact able to correctly *couple the single particle Kohn-Sham orbitals and restore the correct hybridization*. As cited in section 5.3, similar behaviors were also observed in topological insulators [87, 88, 89] and materials with strong p-d hybridization [90, 91, 92, 93].

We note moreover that a hybrid starting point is not able to correct the unphysical dispersions (see Appendix D): the $G_0W_0{}^{diag}$@HSE06 bandstructure exhibits partially similar band crossings and dispersions.

The fundamental Quasiparticle bandgaps are summarized in Table 7.1. The DFT bandgap for the relaxed structure is indirect, with the valence band maximum (VBM) at M and the Conduction Band minimum (CBm) at Γ, while the direct gap is defined at Γ. Despite the strong effect on orbitals of Quasiparticle corrections, the $G_0W_0{}^{full}$ indirect and direct gaps are opened between the same k-points ($\Gamma - M$ and Γ), and are equal to 3.888 eV and 4.514 eV respectively.

Figure 7.7: **a)** Imaginary dielectric function with excitonic effects (BSE) and in the Independent Particle Approximation (IPA) for the *relaxed* structure. The vertical dashed line represents the fundamental direct gap. The BSE eigenvalue spectrum is visible in **b)**, with an insert zooming over the bound exciton region. The colors indicate the associated oscillator strength; the maximum of the scale is related to Λ_2.

4 Optical and excitonic properties

The optical response of the monolayer is dominated by excitonic effects. The direct optical gap is associated to a large excitonic binding energy of ~ 1.0 eV (see Table 7.1). Previous studies on the bulk phase estimated a corresponding binding energy at $E_{xb}^{bulk} \sim 0.2$ eV [37, 188, 189]; the larger value compared to bulk is a typical consequence of the screening environment of 2D materials [245, 254, 244]. The indirect optical bandgap is located at M (as the fundamental QP bandgap), and we obtain a (indirect) binding energy of ~ 0.6 eV for the lowest-energy exciton.

The BSE imaginary dielectric function in Fig. 7.7 is dominated by two very intense and narrow peaks, in marked contrast with the long absorption tail of the Independent Particle curve. The first one is located in the bound exciton region and is determined by the excitonic state Λ_1. A low-intensity feature is also visible at the optical direct gap and can be associated to the lowest bound exciton Λ_0, with a considerable redshift at the onset at around ~ 1.8 eV. Λ_0 is related to a bright exciton, albeit with a very weak oscillator strength, less than 5% of Λ_1. The continuum region displays a single prominent structure, in the form of sharp
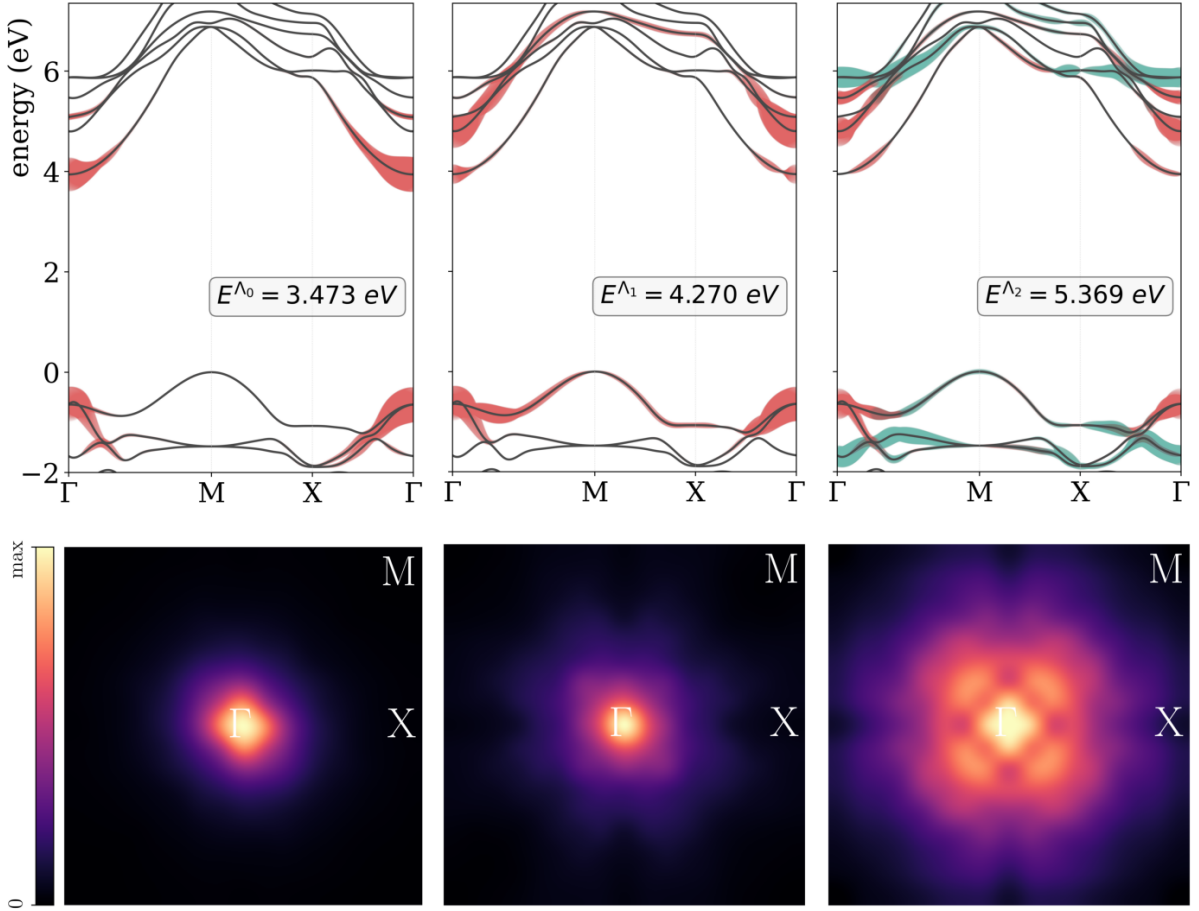
92

Figure 7.8: Upper panels: fatband pictures for the $|A^\Lambda_{\mathbf{k}vc}|^2$ of Λ_0, Λ_1 and Λ_2 states, associated to the optical gap and to the main spectra features. The fatbands are proportional to the square amplitude of the of the electron-hole coupling coefficients $|A^\Lambda_{\mathbf{k}vc}|^2$ relative to the marked transitions. For Λ_2 the O-p → Ti-d_{yz} – Ti-d_{xz} channel, discussed in the text, is highlighted with a different color. Lower panels: Distribution of the BSE eigenvectors in the Brillouin Zone for the corresponding excitons. The plotted values corresponds to $\sum_{v,c} |A^\Lambda_{\mathbf{k}vc}|^2$.

peak (determined by Λ_2 exciton eigenstate and related to strongest oscillator strength) plus a shoulder.

We turn now to the analysis of the bound excitons fine structure in Fig. 7.8. The lowest state Λ_0 is double-degenerate and weakly optically active, with a modest oscillator strength. The contributions to the excitonic wavefunction A^{Λ_0}, are predominantly localized at Γ and mix transitions from the valence O-p states the lowest conduction band. The low oscillator strength can be explained in terms of the character of the lowest conduction orbitals: as discussed in the previous section, the CBm retains a substantial O-p and Sr hybridization

(around 40% and 20% respectively) - in particular the Sr hybridization at Γ is mainly composed by Sr$-s$ and Sr$-p$ character. This in turn is associated to a partial suppression of the optical matrix elements between valence O-p states and the CBm.

The Λ_1 exciton is strongly bound, with an $E_{xb}^{\Lambda_1} \sim 1.2$ eV; the binding energies of Λ_1 and the following excitons are defined as the difference between the BSE eigenvalue and the interband transition with the strongest contribution in the excitonic eigenstate, as previously proposed in literature [255, 256]. The major $A_{\mathbf{k}vc}^{\Lambda_1}$ terms correspond to interband transitions localized near Γ from the two highest valence bands formed by O$-p_x/p_y$ states (twofold degenerate at Γ), to the second conduction band of Ti$-d_{xy}$ character.

The BSE eigenstate $A_{\mathbf{k}vc}^{\Lambda_2}$ in the continuum mixes the O-$p_x/p_y \to$ Ti-d_{xy} channel at Γ with a second channel (highlighted with a different color in Fig. 7.8), from the O-p_z valence states to the flat-non dispersive conduction bands in the two regions around $\Gamma - \mathrm{X}$ and $\Gamma - \mathrm{M}$ at $\sim$ 5.9 eV determined by Ti-d_{yz}/Ti-d_{xz} states (with negligible hybridization, less than 12%). The high intensity of the Λ_2 feature can be associated on one hand to the localization of the d states in the non-dispersive regions at $\sim$ 5.9 eV. We note moreover that all O-p valence orbitals involved in Λ_1 and Λ_2 originate from oxygen atoms situated in the Ti plane. Due to particular screening environment of 2D compounds we expect that orbitals perpendicular to the monolayer plane (as the ones involved in the O-$p_z \to$ Ti-d_{yz}/Ti-d_{xz} channel) experience a reduced screening with respect to plane confined ones [255]; this effect concurs to explain the large $\sim$ 2.4 eV redshift of the Λ_2 peak.

The investigation of the exciton band structure and dispersion at finite $\mathbf{q}$, beyond the optical limit, allows to further characterize and discriminate the excitonic properties in 2D systems [242, 129, 240, 257, 238]. The excitonic dispersion can be accessed experimentally by means of electron energy loss spectroscopy (EELS) or resonant inelastic x-ray spectroscopy (RIXS) [242]. In particular in the EELS technique the cross-section depends on the Loss function $L(\mathbf{q}, \omega) = -Im\left(\epsilon^{-1}(\mathbf{q}, \omega)\right)$.

The Loss functions for various $\mathbf{q}$ is plotted in Figure 7.9 along Γ-M direction (which corresponds to the indirect gap direction).

The double-degenerate lowest excitonic state Λ_0, which gives rise to a low-intensity feature for $\mathbf{q} \to 0$, becomes completely optically inactive along Γ-M. Furthermore, the analysis of its exciton dispersion (Fig 7.9) shows that the Λ_0 degeneracy is splitted away from Γ, and the two resulting excitonic bands reach their minimum at $\mathbf{q} = \mathrm{M}$, in correspondence of the indirect QP bandgap. The lowest (dark) exciton band shows a parabolic dispersion, with an associated binding energy at M equal to ~ 0.6 eV.

Upon increasing momentum transfer, the peak associated with the Λ_1 state disperses to higher energies and progressively merges with the high-intensity structure at ~ 5.5 eV (identifiable with the Λ_2 transition). At large $\mathbf{q}$ a new feature appears at transition energies ~ 4.1 eV, originating from interband transitions from the three highest valence bands to the lowest conduction band. In particular, for $\mathbf{q} = \mathrm{M}$ a non negligible contribution to its BSE eigenstate $A_{vc\mathbf{k}}(\mathbf{q} = \mathrm{M})$ (up to $\sim 30\%$ of the total spectral weight) is determined by transitions from
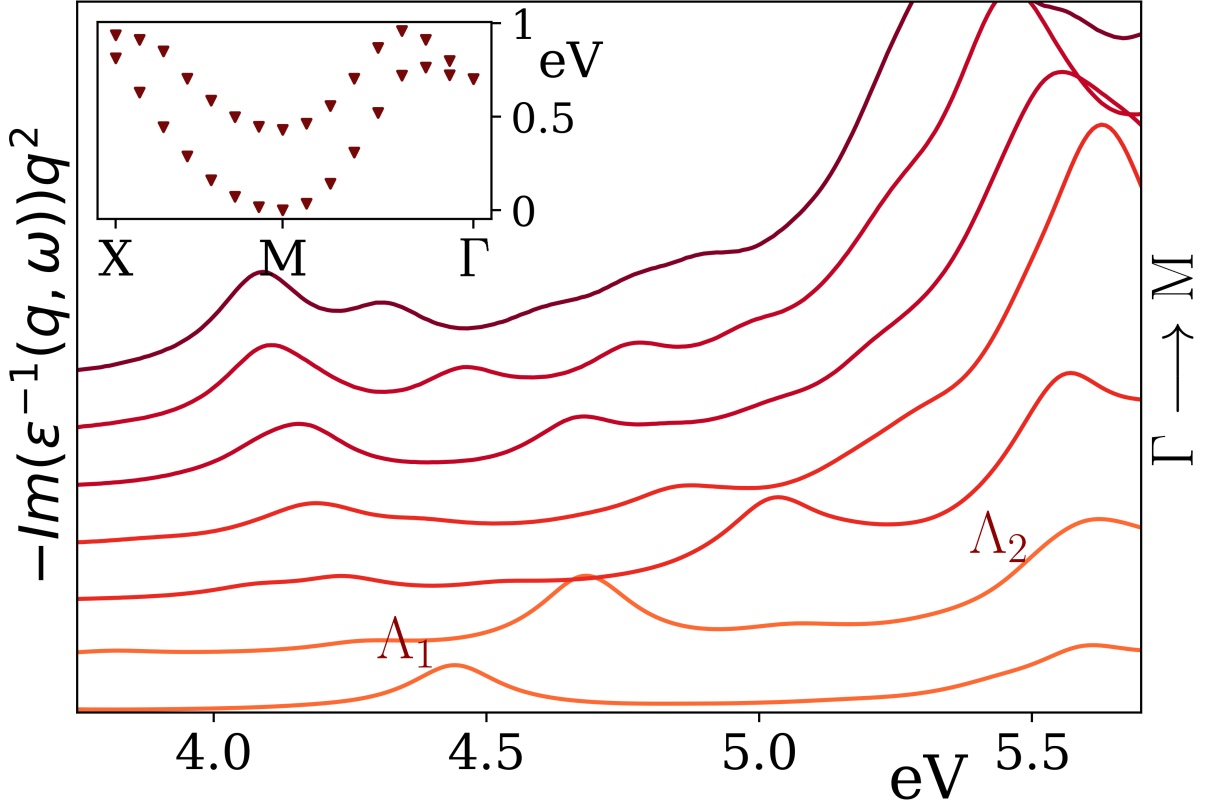
Figure 7.9: Loss function for transferred momenta along the symmetry direction Γ-M, from **q** = M/8 to **q** = M. Each curve is multiplied by q^2, following Cudazzo and coworkers [242, 129]. In the insert the excitonic bandstructures for the two lowest excitonic states along $X \to M \to \Gamma$ are displayed; the zero of the scale is set at the eigenvalues minimum at **q** =M.

valence O-p_z states (involved also in the Λ_2 excitonic transition).

5   Comparison with the non-relaxed structure

In order to understand the effect of the structural relaxation on the electronic and optical properties we briefly compare the previous results with the band-structure and the spectra determined on the non-relaxed structure.

The QP corrections display a strong variation along the BZ; the lowest conduction band near Γ is not pushed up as strongly as the other conduction states (which instead possess a reduced mixing and a higher Ti-d contribution, as visible from Fig. 7.10 and 7.11). The same band is involved in two band crossings near X and M, associated to an orbital character swap (from hybridized Ti$-d$/Sr character (with $\sim$ 55% Ti-d) to a prevalent Ti-d one).

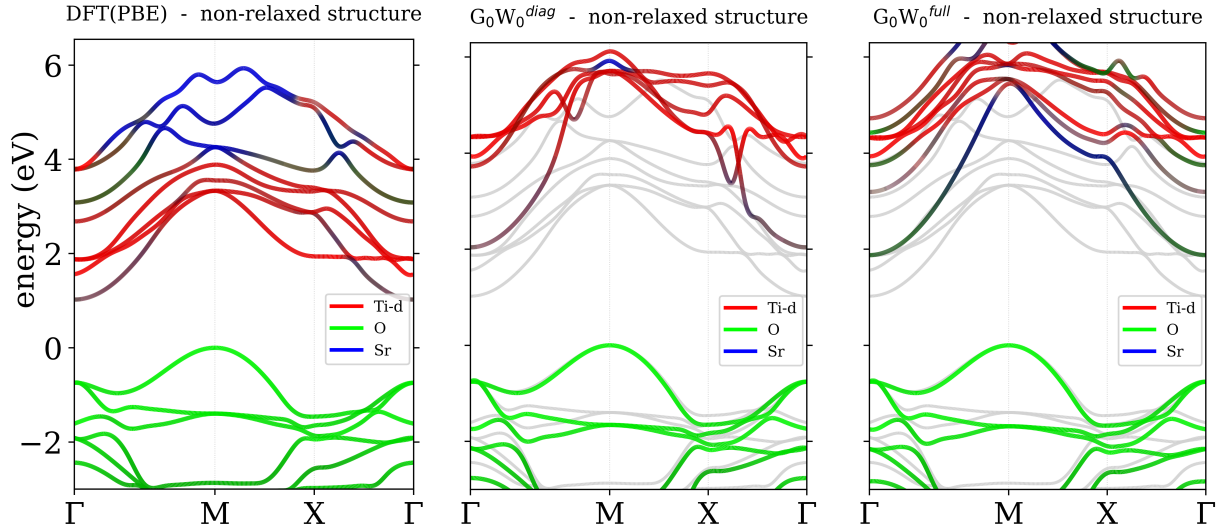In complete analogy con the relaxed structure picture, the inclusion of non-diagonal Σ el-

Figure 7.10: Orbital projected band structures for the *non-relaxed* structure. The zero of the energy scale is set at the top of the valence band for both PBE and G_0W_0 results. In the $G_0W_0{}^{diag}$ and $G_0W_0{}^{full}$ subfigures the DFT bandstructure is plotted for comparison as grey lines.
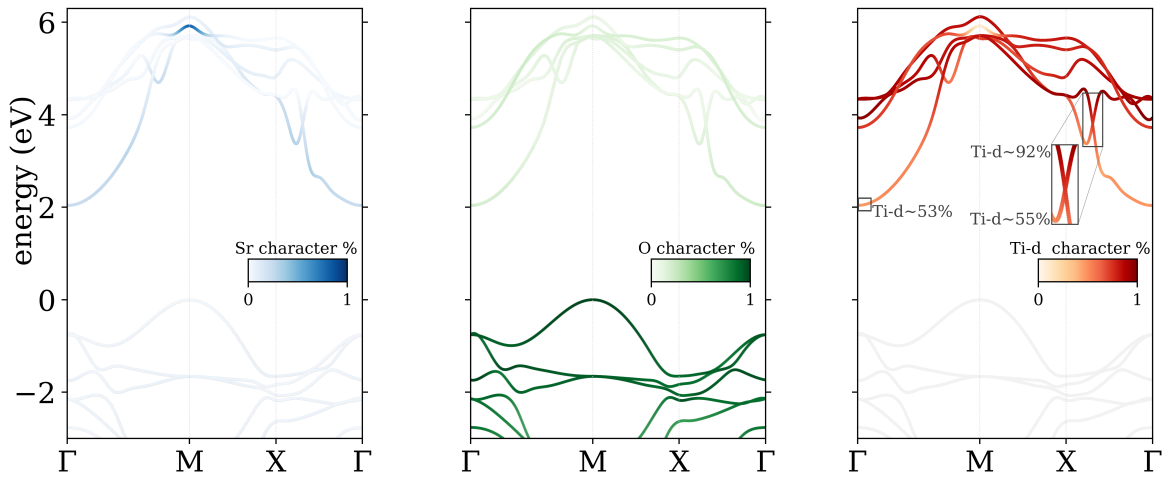

Figure 7.11: Calculated orbital projected wavefunction character of the electronic $G_0W_0{}^{diag}$ bands for the *non-relaxed* structure. The character is determined as $\langle Y_{lm}^{\alpha}|\psi_{n\mathbf{k}}\rangle$, where Y_{lm}^{α} is the spherical harmonic centered on ion α with l, m angular and magnetic moments. For Ti only the contributions over the d states are displayed.

ements restores the correct hybridization between single-particle orbitals and corrects the unphysical dispersions, removing the band crossing and character swap at Γ-X.
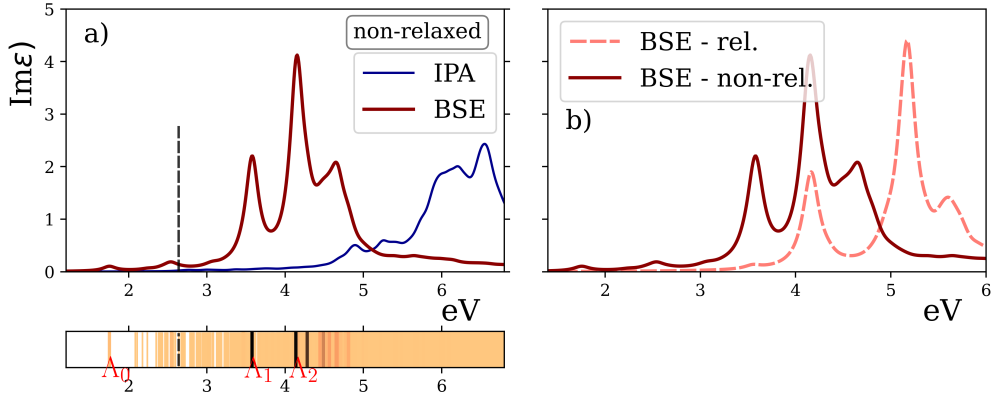
Figure 7.12: (a) Imaginary dielectric function with excitonic effects(BSE) and in the Independent Particle Approximation (IPA) for the *non-relaxed* structure, together with the BSE eigenvalue spectra. The colors indicate the associated oscillator strength; the maximum of the scale is related to Λ_2. (b) Comparison between the imaginary dielectric function between the two structures.

The BSE spectra of the non-relaxed structure (Figure 7.12) exhibits very similar features to the relaxed one: two main peaks plus a shoulder to the second one. In this sense, the relaxation of the structure introduces only slight changes to the main spectra features. The first peak (associated to transitions Λ_1), is redshifted from the relaxed Λ_1 analogue by 0.39 eV, while the Λ_2 BSE eigenvalue exhibits a larger shift of 0.82 eV.

6   Conclusions

In this chapter we have investigated the excitonic and Quasiparticle properties of freestanding monolayer $SrTiO_3$, using an ab-initio approach based on Many Body Perturbation Theory. Inclusion of off-diagonal self-energy elements in the G_0W_0 scheme has proved crucial to correctly describe the strong hybridization of the lower conduction bands (which is wrongly accounted for by DFT) and hence to prevent the appearance of unphysical dispersions.

The excitonic properties have been studied through the solution of the Bethe-Salpeter equation both in the optical limit $\mathbf{q} \to 0$ (by calculating the imaginary part of the dielectric function) and at finite momentum for the relaxed structure (by computing the electron energy loss spectra). The spectra of the relaxed structure at $\mathbf{q} \to 0$ is dominated by excitonic effects, with a binding energy of $\sim$ 1.04 eV at the direct optical gap. The analysis of the BSE coupling components has shown that the most intense peaks are determined by O-p $\to$ Ti-d interbands transitions, in continuity with the bulk description. In particular transitions between the in-plane O $\to$ Ti$-d_{xy}$ orbitals and between O-p_z $\to$ Ti-d_{xz}/d_{yz} form separate excitation channels, which allows us to distinguish and differentiate the two peaks. At finite $\mathbf{q}$ the lowest exciton state becomes inactive with a parabolic dispersion around the transition

minimum at $\mathbf{q}$ =M, located at lower energy than the direct optical gap.

Chapter 8

Pressure-Induced Excitations in the Out-of-Plane Optical Response of the Nodal-Line Semimetal ZrSiS

ZrSiS can be considered a paradigmatic example of the topological nodal-line semimetals (NLSM), a class of materials that has recently attracted increasing attention due to their very interesting physical properties [45]. The compound crystallizes in the PbFCl-type structure (see Fig. 8.1) with a tetragonal P4/nmm space group [258, 259]. A peculiar feature of the structure are the 2D square nets of Si atoms parallel to the a-b plane, with S and Zr layers sandwiched between nets of Si atoms. In short, the structure can be thought as square nets in the stacking sequence Si-Zr-S-S-Zr-Si.

The electronic structure of ZrSiS is characterized by linear dispersing bands crossing E_F *along specific lines* [45, 46]. The linear dispersion of these bands, which extends over an energy range of ~ 0.5 eV, has been associated to the square net structural motif cited above [45, 259, 46]. As a matter of fact the computed bandstructure of ZrSiS (see Figure 8.2) exhibits several Dirac crossings at the Fermi energy level located at Γ-X, Γ-M and slightly shifted from E_F along Z-R and Z-A. No other bands except these linear dispersing states cross the Fermi energy.

A second group of Dirac band crossings located away from the Fermi level (± 0.7 eV) is visible at the high symmetry k-points X and R.
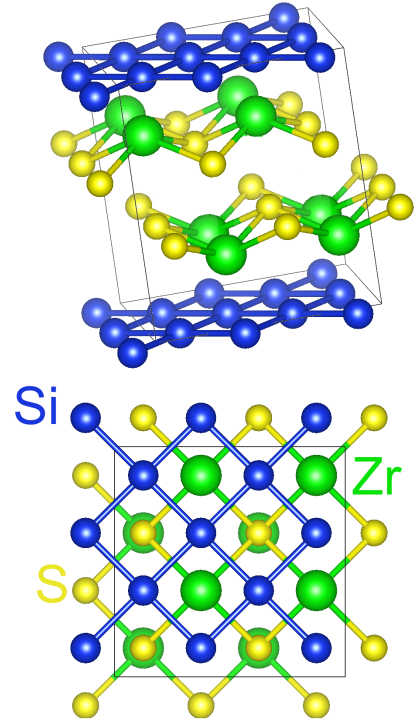

Figure 8.1: Crystal structure of ZrSiS (side and top views). The blue atoms are Si, the yellow S and the green Zr.
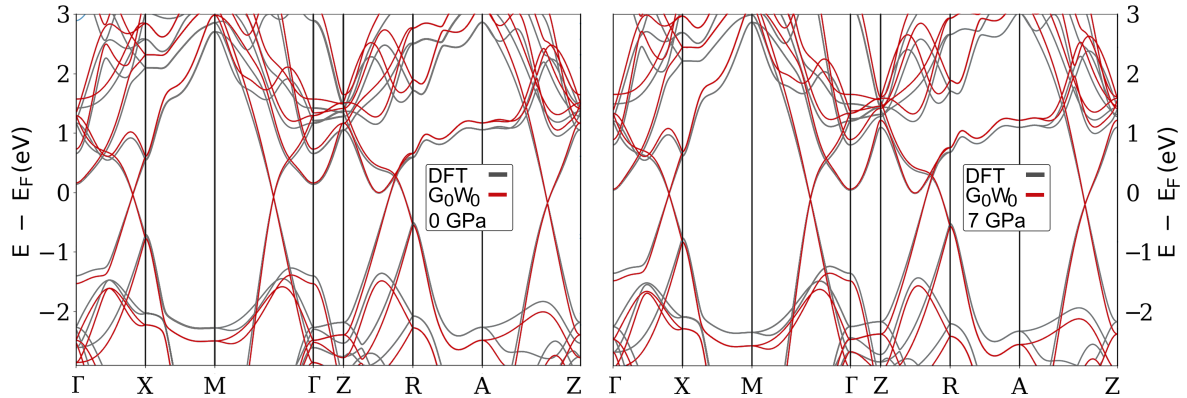
99

Figure 8.2: ZrSiS DFT and G_0W_0 band structures at ambient and high (7 GPa) pressures. The zero of the energy scale is set at Fermi energy.

The crossings create a diamond-shaped Fermi surface within the (k_x, k_y) plane which is strongly dispersive along k_z and overall *quasi 2D-dimensional* [260, 261, 262]. Intuitively, the electrons belonging to the nodal lines bands live in a two-dimensional space, despite ZrSiS being a bulk three-dimensional material. The nodal line features were also detected in the closely related compounds ZrGeS, ZrGeSe, ZrSiSe and ZrSiTe [260, 263, 264, 265, 266]; these materials also share the square-net layered PbFCl-structure. The Spin-Orbit Coupling (SOC) is able to open a small gap at the Dirac crossings at E_F; low-frequency optical measurements determined an experimental upper bound on the opening of 30 meV [267]. At the same time, SOC does not influence or play any role on the optical conductivity beyond the low frequency limit [260]. It should be noted that the crossings of the second group (at X and R) are protected by non-symmorphic symmetry [45, 263, 268] against gap opening due to SOC.

The peculiar features of ZrSiS electronic structure close to the Fermi energy offer an ideal platform to study nodal-line physics and explore the properties of Dirac electrons [269, 270, 271, 272]. This work, written in collaboration with the groups led by Prof. Dr. Kuntscher of the Augsburg University and Prof. J. Kunes of Technische Universität Wien, investigated (both experimentally and through ab-initio calculations) the in- and out-of-plane optical response at ambient and high pressures. The related publication is attached at the end of the chapter. My contribution, summarized below, concerned the calculations of the Quasiparticle bandstructure and of the optical properties (with the inclusion of excitonic effects) through the solution of the Bethe-Salpeter equation.

In Figure 8.2 the G_0W_0 and DFT bandstructures at ambient and high pressure (7 GPa) are compared. The effect of Quasiparticle corrections is limited to a stretching of the valence bands (see also Figure 8.3), and the band topology is conserved. Furthermore the corrections show a very limited band- or k-point- dependence in the $[-2, 3]$ eV energy window, with very small deviations from a linear dependence on the energy.

The G_0W_0 bandstructure was obtained using the ab-initio VASP software. An energy cutoff of 650 eV (plus a cutoff for the response function of 430 eV) was employed, with 512 total bands, a frequency grid composed by 96 points and a $10 \times 10 \times 8$ Gamma-centered k-point mesh.

Figure 8.3: DFT energies vs Quasi-particle G_0W_0 eigenvalues for the 7 GPa structure.

We now discuss the main properties of the in-plane and out-of-plane[1] optical conductivities at ambient pressure (see Figure 8.5). The Bethe-Salpeter results are calculated from the G_0W_0 bandstructure and RPA screened interaction, within the Tamm-Dancoff approximation and including 8 valence and 8 conduction bands. The validity of the Tamm-Dancoff approximation has been tested by comparing the spectra obtained within the approximation versus a full BSE calculation (the two simulations were run on a sparser k-point mesh $8 \times 8 \times 8$); the two $\sigma(\omega)$ curves coincide in the studied energy window. The converged k-mesh employed is equal to $25 \times 25 \times 15$; in order to reduce the computational weight, the averaging procedure described in chapter 1 has been employed. In brief, a set of independent calculations is performed on $m_1 \times m_2 \times m_3$ k-meshes shifted off Γ; the shifts are defined as the irreducible k-points of a $n_1 \times n_2 \times n_3$ mesh. The connection of all k-meshes reproduces the point of a regular $(n_1 \cdot m_1) \times (n_2 \cdot m_2) \times (n_3 \cdot m_3)$ k-mesh, and the dielectric function is thus calculated as:

$$\epsilon(\omega) = \frac{1}{W} \sum_p w_p \epsilon_p(\omega) \qquad W = \sum_p w_p$$

where w_p is the k-point weight. We employed $n_1 \times n_2 \times n_3 = 5 \times 5 \times 3$, $m_1 \times m_2 \times m_3 = 5 \times 5 \times 5$ through this work. The results at ambient pressure are in good agreement with previous experimental and theoretical works [267, 260, 261, 273]; we summarize below the main features of the spectra.

---

[1] The in-plane/out-of-plane definitions indicate an incident radiation **E** aligned parallel and perpendicularly to the ZrSiS layers.
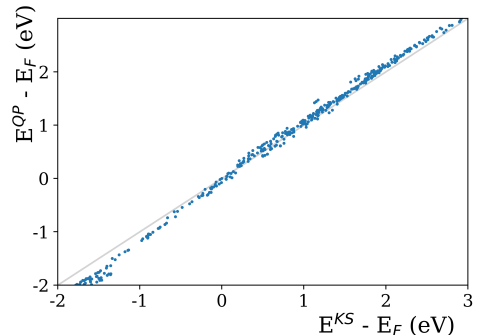
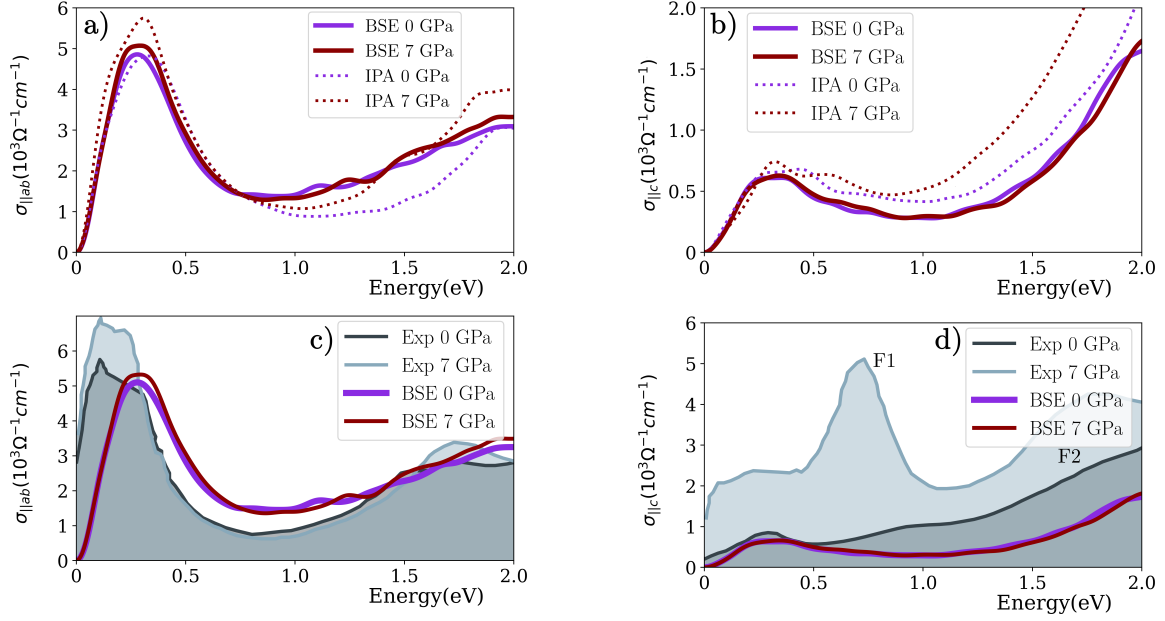**Figure 8.5:** Comparison between ambient and high pressures (7 GPa) interband optical conductivities for **a)** **E**||ab and **b)** **E**||c respectively. The filled curves are determined with the G_0W_0+BSE approach, while the dotted curves are computed within the Independent Particle Approximation (IPA). **c), d)** show the comparison between the BSE and experimental data for **E**||ab and **E**||c.
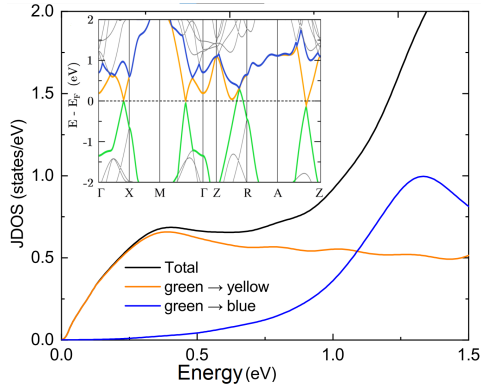

Figure 8.4: Contributions of different band combinations to the joint density of states JDOS for **E**||c at IPA level. Inset: electronic band structure at ambient pressure.

Both experimental and ab-initio results display a distinct anisotropy that has been associated to the layered structure of ZrSiS. At $\omega = 0$ the spectra is dominated by the Drude term, consistent with the metallic character of the material [274]. Beyond the Drude term $\sigma(\omega)$ is determined almost entirely by transitions between the linear dispersing band close to the Fermi energy, as clearly visible from the Joint Density of States (JDOS) (see Fig. 8.4). In particular, the linear dispersion of these bands gives origin to a characteristic broad and almost constant curve following an initial onset; this particular profile is visible also in the related nodal-line semimetal ZrSiTe [260]. For energies $\sim 0.7-0.8$ eV additional contributions to the JDOS and to the optical conductivity appear; these contributions have been associated to transitions between parallel bands close to the X and R Dirac crossings [260, 261, 275].

The in-plane optical response exhibits only limited changes under pressure. The main effect is a blueshift of the peak at 1.5 eV due to the compression of the crystal lattice. In marked contrast the experimental out-of-plane $\sigma(\omega)$ shows strong changes under pressure, with the appearance of two new pronounced peaks (labeled F1 and F2); in particular the F1 excitation at ~ 0.7 eV dominates the spectra at high pressure.

Several authors [276, 277, 278] suggested that ZrSiS undergoes a condensation of inter-layer (zero momentum) excitons due to moderately strong electronic correlations and high degree of electron-hole symmetry of the electronic bandstructure. This in turn could lead to the formation of a pseudogap and the appearance of distinct excitations in the conductivity spectrum. An ab-initio Bethe-Salpeter calculation was therefore performed in order to inspect the effect of electron-hole interaction on the spectra at high pressure (7 GPa) and test this hypothesis. However excitonic effects on $\sigma(\omega)$ are very limited and the curve is overall similar to the Independent Particle Approximation one. Therefore excitonic effects, as captured by the Bethe-Salpeter equation, cannot explain the emergence of the F1 peak.

We note that the ab-initio optical calculations were carried out only in the optical limit ($\mathbf{q} \to 0$); possible more complex mechanisms, which are not ruled out by the present calculation, might include the creation of finite-momentum excitons accompanied by other quasiparticles. The first step to investigate this scenario would be the mapping of the finite-momentum excitonic bandstructure and spectra.

Pressure-Induced Excitations in the Out-of-Plane Optical Response of the Nodal-Line Semimetal ZrSiS

J. Ebad-Allah,[1,2] S. Rojewski[1] M. Vöst,[3] G. Eickerling[3] W. Scherer[3] E. Uykur[4] Raman Sankar[5]
L. Varrassi,[6] C. Franchini[7,6] K.-H. Ahn[8,10] J. Kuneš[8,9] and C. A. Kuntscher[1,*]

[1]*Experimentalphysik II, University of Augsburg, 86159 Augsburg, Germany*
[2]*Department of Physics, Tanta University, 31527 Tanta, Egypt*
[3]*Chair of Chemical Physics and Materials Science, Institute of Physics, University of Augsburg, 86159 Augsburg, Germany*
[4]*1. Physikalisches Institut, Universität Stuttgart, 70569 Stuttgart, Germany*
[5]*Institute of Physics, Academia Sinica, Taipei 11529, Taiwan*
[6]*Department of Physics and Astronomy, Alma Mater Studiorum-Università di Bologna, Bologna 40127, Italy*
[7]*University of Vienna, Faculty of Physics and Center for Computational Materials Science, 1090 Vienna, Austria*
[8]*Institute of Solid State Physics, TU Wien, 1020 Vienna, Austria*
[9]*Institute of Physics, The Czech Academy of Sciences, 18221 Praha, Czechia*
[10]*Institute of Physics, The Czech Academy of Sciences, 16200 Praha, Czechia*

The anisotropic optical response of the layered, nodal-line semimetal ZrSiS at ambient and high pressure is investigated by frequency-dependent reflectivity measurements for the polarization along and perpendicular to the layers. The highly anisotropic optical conductivity is in very good agreement with results from density-functional theory calculations and confirms the anisotropic character of ZrSiS. Whereas the in-plane optical conductivity shows only modest pressure-induced changes, we found strong effects on the out-of-plane optical conductivity spectrum of ZrSiS, with the appearance of two prominent excitations. These pronounced pressure-induced effects can neither be attributed to a structural phase transition according to our single-crystal x-ray diffraction measurements, nor can they be explained by electronic correlation and electron-hole pairing effects, as revealed by theoretical calculations. Our findings are discussed in the context of the recently proposed excitonic insulator phase in ZrSiS.

Topological nodal-line semimetals (NLSMs) with linearly dispersing electronic bands, which cross along a line in reciprocal space, host two-dimensional (2D) Dirac fermions and are currently extensively investigated due to their exotic and highly interesting physical properties [1,2]. The layered material ZrSiS is considered as the prototype NLSM, where the linearly dispersing bands extend over a large energy range ~ 2 eV around the Fermi energy E_F, without the presence of topologically trivial bands in the vicinity of E_F, and the corresponding nodal lines form a three-dimensional cagelike structure [3–6]. There are additional Dirac crossings at the X and R point of the Brillouin zone located ~ 0.5 eV above and below E_F, which are protected by nonsymmorphic symmetry against gapping due to the spin-orbit coupling. The unconventional mass enhancement of quasiparticles in ZrSiS [6] suggests the importance of electronic correlations, which could potentially drive the material toward an excitonic insulator phase or a quantum critical region close to it [7–9].

The exceptional electronic band structure of ZrSiS and related materials ZrXY, where X is a carbon group element ($X =$ Si, Ge, Sn) and Y is a chalcogen element ($Y =$ S, Se, Te) [10], is mainly due to the 2D square nets of Si atoms

parallel to the ab plane, which are the main structural motif besides the square nets of Zr and chalcogen atoms, stacked perpendicular to the ab plane [see inset of Fig. 1(b)]. Further interesting properties of ZrSiS include high charge carrier mobility and exceptionally large magnetoresistance due to electron-hole symmetry [11–13]. Also, the electrodynamic properties of ZrSiS are unusual, with a nearly frequency-independent optical conductivity σ_1 for frequencies from 250 to 2500 cm^{-1} (30–300 meV) [14]. This rather flat behavior of σ_1 is followed by a U-shaped profile between 3000 and 10 000 cm^{-1} (0.37–1.24 eV), which was ascribed to transitions between the linearly crossing bands of the nodal line close to E_F, and a peak located at $\sim 11\,800$ cm^{-1} (~ 1.46 eV), associated with transitions between parallel bands of the Dirac crossings protected by nonsymmorphic symmetry [15].

All previous experimental studies on the electrodynamic properties of ZrSiS focused on the in-plane optical response, i.e., for the polarization **E** of the incident electromagnetic radiation aligned along the layers in the ab plane [see inset of Fig. 1(b)]. In this Letter, we report on the out-of-plane optical conductivity of ZrSiS, as obtained by frequency-dependent reflectivity measurements for **E**
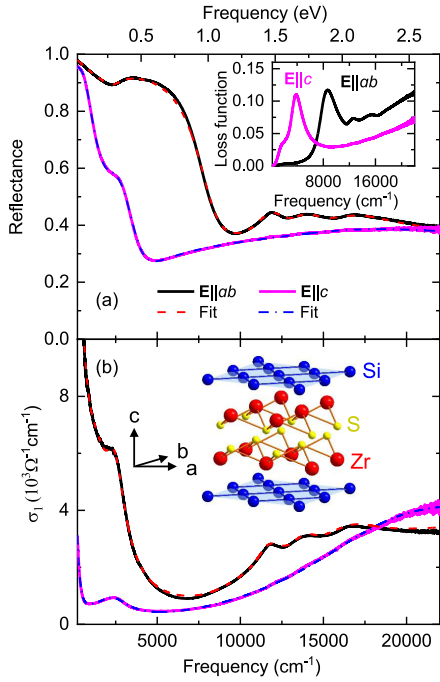
FIG. 1. Optical response functions of ZrSiS at ambient conditions for polarization directions $\mathbf{E}\|ab$ and $\mathbf{E}\|c$: (a) reflectivity spectra and (b) real part of the optical conductivity σ_1. Inset of (a): loss function $-\mathrm{Im}(1/\hat{\epsilon})$, where $\hat{\epsilon}$ is the complex dielectric function. Inset of (b): crystal structure of ZrSiS with Si square nets parallel to the ab plane.

directed perpendicular to the layers, i.e., $\mathbf{E}\|c$. Furthermore, we studied the in-plane and out-of-plane optical conductivity of ZrSiS under external, quasihydrostatic pressure, combined with pressure-dependent single-crystal x-ray diffraction (XRD) measurements. In the out-of-plane optical response, two new excitations appear under pressure, which cannot be reproduced by density-functional theory (DFT) calculations at the generalized gradient approximation [16] level or even by including electronic correlations at GW level and electron-hole pairing effects. Our findings add yet another interesting facet to the exceptional properties of ZrSiS.

Ambient-pressure reflectivity spectra of ZrSiS for the polarization along ($\mathbf{E}\|ab$) and perpendicular ($\mathbf{E}\|c$) to the layers are depicted in Fig. 1(a). (See the Supplemental Material [17] for a description of sample preparation, experimental details, and analysis of reflectivity data.) For both polarization directions, the reflectivity is high at low energies and shows a distinct plasma edge, indicating the metallic character consistent with recent resistivity measurements [38,39]. The anisotropic character of ZrSiS is manifested by the polarization-dependent energy position of the plasma edge, which is shifted toward lower energies for $\mathbf{E}\|c$ compared to $\mathbf{E}\|ab$. Consistently, the intraband plasmon peak in the loss function defined as $-\mathrm{Im}(1/\hat{\epsilon})$, where $\hat{\epsilon}$ is the complex dielectric function,

appears at lower energy, ≈ 0.47 eV, for $\mathbf{E}\|c$ as compared to ≈ 1.07 eV for $\mathbf{E}\|ab$ [inset of Fig. 1(a)]. The anisotropic optical response is also seen in the real part of the optical conductivity spectrum σ_1, displayed in Fig. 1(b). For both directions, σ_1 consists of a Drude term at low energies due to itinerant charge carriers. From the spectral weight analysis of the Drude contribution, we obtain a plasma frequency ω_p of 3.17 eV for $\mathbf{E}\|ab$ and 1.08 eV for $\mathbf{E}\|c$, in agreement with the results of first-principles calculations [40]. The ratio of dc conductivities σ_{ab}/σ_c amounts to ~ 16, i.e., it falls in the 8–30 range reported in previous studies [38,39], respectively. Obviously, the intra-layer charge transport dominates over the inter-layer one.

Also, the profile of the optical conductivity spectrum is strongly polarization dependent [Fig. 1(b)], in very good agreement with the theoretical results of Refs. [39,41]. For $\mathbf{E}\|ab$, the low-energy σ_1 spectrum consists of a Drude term and a rather flat region up to ~ 3000 cm^{-1} followed by a U-shape frequency dependence, which is bounded by a rather sharp peak at high frequencies [14,15]. This sharp peak (called $L4$ in the following) is associated with transitions between parallel bands of the Dirac crossings, which are protected by nonsymmorphic symmetry against gapping [15]. The profile of the $\mathbf{E}\|c$ optical conductivity is markedly different: It is rather featureless, namely, besides the Drude peak it shows only an absorption peak at ~ 2400 cm^{-1} and a monotonic increase above ~ 6000 cm^{-1}, which originates from transitions between Dirac bands and states further away from E_F. Compared to $\mathbf{E}\|ab$, the out-of plane momentum matrix elements exhibit substantially weaker $k-$ and band dependence, and thus the $\mathbf{E}\|c$ optical conductivity reflects the behavior of the particle-hole (joint) density of states (divided by frequency) [15]. For both directions, the optical conductivity and reflectivity spectra can be well fitted with the Drude-Lorentz model (see Fig. 1). The obtained Drude and Lorentz contributions at ambient pressure are shown in Figs. 2(a) and 2(b) for $\mathbf{E}\|ab$ and $\mathbf{E}\|c$, respectively. For comparison with the results of DFT calculations (see the Supplemental Material [17] for details), we subtracted the Drude term from the total σ_1 spectrum and obtained the contributions from the interband transitions $\sigma_{1,\mathrm{interband}}$. The interband conductivity spectra agree well with the corresponding theoretical spectra [see inset of Fig. 2(a)].

In the following, the main focus will be on the optical response of ZrSiS under external pressure. The experimental in-plane and out-of-plane σ_1 spectra are depicted for selected pressures in Figs. 2(a) and 2(b), respectively. First, we discuss the results for the in-plane optical response. One notices that the induced changes for $\mathbf{E}\|ab$ are only modest, and the characteristic profile of the optical conductivity with its U-shape is unchanged up to 7 GPa. A detailed analysis reveals a slight increase of σ_1 below ~ 3000 cm^{-1} and a shift of the $L4$ peak to higher energies with increasing pressure. A comparison between the experimental and
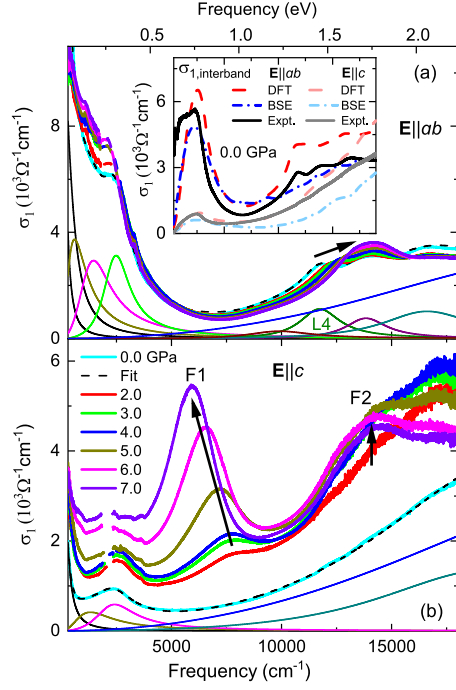
FIG. 2. Pressure-dependent optical conductivity σ_1 with the Drude-Lorentz fitting and the corresponding contributions at 0 GPa for (a) $\mathbf{E}\|ab$ and (b) $\mathbf{E}\|c$. Arrows mark the most pronounced pressure-induced changes in the spectra. Inset of (a): comparison between the experimental and both DFT and BSE calculated interband conductivity $\sigma_{1,\text{interband}}$ at 0 GPa.

theoretical interband optical conductivity from DFT calculations for $\mathbf{E}\|ab$ is given in Fig. 3(a) for two selected pressures (2.0 and 7.0 GPa). Similar to the experimental spectra, the ∪-shape of the theoretical spectrum is retained up to the highest measured pressure and the $L4$ peak at the high-energy bound of the ∪-shape is blueshifted. According to the behavior of the $L4$ peak, pressure induces a shift of the nonsymmorphic symmetry protected Dirac crossings *away* from E_F, as a result of the compression of the crystal lattice.

Consistently, the thermal contraction of the crystal lattice during cooling causes a blueshift of the $L4$ peak [see Fig. 3(c)] [42]. A comparison between the effect of cooling and pressure on the energy position of the $L4$ peak is given in Fig. 3(d), whereby for the latter both experimental and DFT results are displayed [43]. To conclude, tensile strain, instead of compressive strain, would be needed to push the nonsymmorphic symmetry protected Dirac nodes in ZrSiS *toward* E_F, in order to study the expected distinct physics related to these 2D Dirac fermions [45].

Next, we will discuss the pressure-induced effects on the out-of-plane optical conductivity [see Fig. 2(b)]. Starting from the lowest applied pressure (2 GPa), drastic changes occur in the profile of the $\mathbf{E}\|c$ σ_1 spectrum: in addition to the pressure-induced increase below ~5000 cm^{-1}, two new

excitations labeled $F1$ and $F2$ appear, which gain spectral weight with increasing pressure [46]. Similar to the in-plane optical response, a Drude-Lorentz model was applied for fitting the experimental spectra. As an example, we depict in Fig. 3(b) the experimental interband conductivity $\sigma_{1,\text{interband}}$ at 7 GPa, where the Drude term was subtracted from the total σ_1, together with the Lorentz contributions. Each of the two new excitations $F1$ and $F2$ can be well described by one Lorentzian term. With increasing pressure, the energy position of excitation $F2$ is almost unchanged, whereas $F1$ first shifts slightly to lower energies for pressures up to ~4 GPa, and for pressures above 4 GPa, this redshift gets more pronounced [Fig. 3(e)]. The oscillator strength of $F1$ and $F2$ slightly increases with increasing pressure up to 4 GPa and increases strongly above ~4 GPa [inset of Fig. 3(e)] due to a transfer of spectral weight from the energy range above ~1.9 eV. In Fig. 3(b), we compare the experimental $\mathbf{E}\|c$ $\sigma_{1,\text{interband}}$ spectrum for two selected pressures, 2.0 and 7.0 GPa, with the corresponding DFT results. Interestingly, the theoretical interband conductivity for $\mathbf{E}\|c$ is basically unchanged upon pressure application, in strong contrast to the experimental results. In particular, the two excitations $F1$ and $F2$ are *not* reproduced in the pressure-dependent theoretical spectra. Thus, the excitations $F1$ and $F2$ should be attributed to effects that are not included in the band structure calculations, and hence the role of beyond-DFT effects might be relevant, as discussed below.

For an interpretation of our findings, we performed a high-pressure XRD study on a ZrSiS single crystal (see the Supplemental Material [17] for details). With increasing pressure, the lattice parameters a and c monotonically decrease, resulting in a monotonic volume decrease [see Fig. 3(f)]. Further investigation of the reciprocal space up to maximum measured pressure (6.9 GPa) does not reveal the formation of additional or superstructural Bragg reflections [17]. Hence, our diffraction data do not provide any hint for a structural phase transition up to at least ~7 GPa, in agreement with Refs. [47,48]. This finding is in contradiction with results of powder XRD experiments, which suggested a structural phase transition at elevated pressures [44]. We fitted the volume V with the second-order Murnaghan equation of state (EOS) [49] according to $V(p) = V_0 \cdot [(B_0'/B_0) \cdot p + 1]^{-1/B_0'}$, where B_0 is the bulk modulus, B_0' is its pressure derivative, which is fixed to 4, and V_0 is the volume, all at $P = 0$ GPa. From the fitting, we obtain the value $B_0 = 144 \pm 5$ GPa, consistent with earlier reports [44,50].

Based on the results of our high-pressure XRD study, we can discuss the optical data in more detail. First, it has been proposed that the distance of the nonsymmorphic Dirac crossings from E_F is inversely proportional to the distance between the Si atoms in the Si-Si square nets [51] and hence inversely proportional to the lattice parameter a. Accordingly, the energy position of the related $L4$ peak in
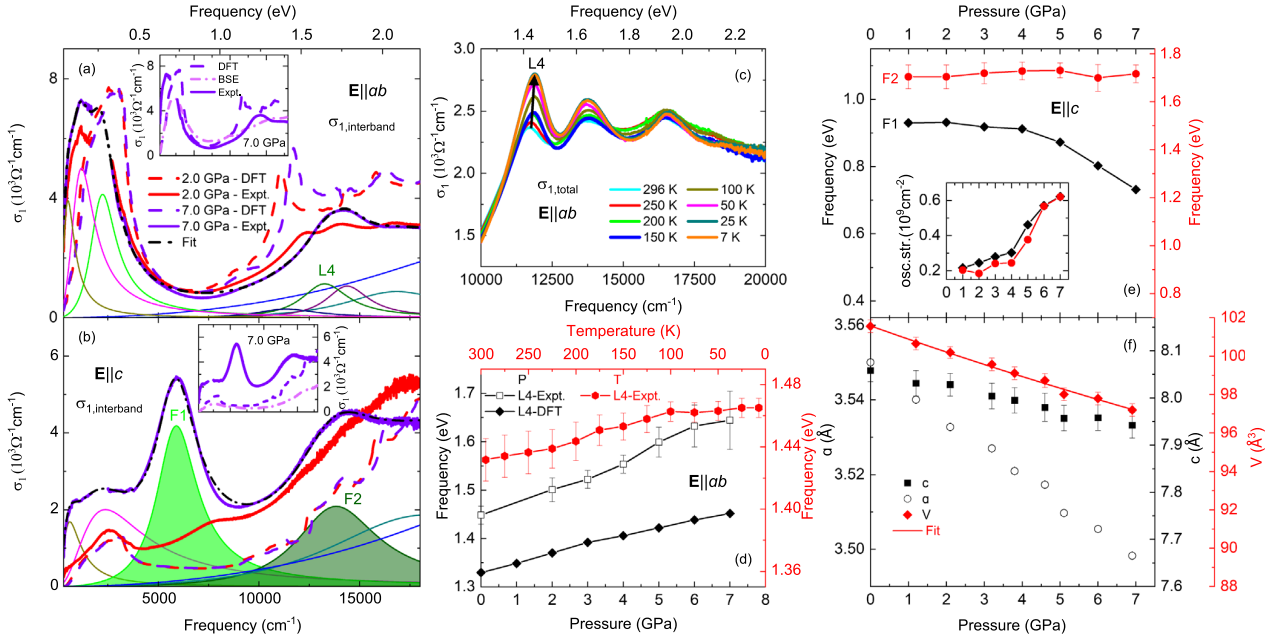
FIG. 3. (a),(b) Comparison between the experimental and DFT interband conductivity $\sigma_{1,\text{interband}}$ at 2.0 and 7.0 GPa, with the total fitting curve and the fitting contributions for the experimental $\sigma_{1,\text{interband}}$ at 7.0 GPa, for $\mathbf{E}\|ab$ and $\mathbf{E}\|c$, respectively. Insets of (a),(b): comparison between DFT and BSE theoretical results and experimental interband conductivity σ_1 at 7.0 GPa for $\mathbf{E}\|ab$ and $\mathbf{E}\|c$, respectively. (c) Temperature-dependent high-energy optical conductivity for $\mathbf{E}\|ab$. The arrow marks the temperature-induced shift of the $L4$ peak. (d) Comparison between the temperature (T) and pressure (P) dependence (both experimental and theoretical) of the frequency position of the $L4$ peak. (e) Pressure-dependent frequency position and oscillator strength (osc. str., inset) of the peaks $F1$ and $F2$. (f) Volume V of the unit cell and lattice parameters a and b as a function of pressure. The error bars represent three times the estimated standard deviation. The solid line is a fit with a Murnaghan-type EOS (see text).

the $\mathbf{E}\|ab$ σ_1 spectrum should scale with $1/a$. However, based on our pressure-dependent optical data, we cannot confirm such a behavior. Second, the experimental optical data show an anomaly at ≈ 4 GPa in the shift of the $F1$ excitation and in the oscillator strength of the $F1$ and $F2$ excitations. Since our pressure-dependent XRD results do not provide any evidence for a structural phase transition, this anomaly arises from purely electronic behavior, like in pressurized ZrSiTe [52,53]. The origin of the excitations $F1$ and $F2$, which appear under pressure in the experimental $\mathbf{E}\|c$ optical conductivity, remains, however, unclear.

It is interesting to note that, based on calculations for a bilayer square lattice model, Rudenko *et al.* [7] suggested that ZrSiS undergoes a condensation of interlayer zero-momentum excitons due to electronic correlations and a high degree of electron-hole symmetry of the electronic band structure, which gives rise to an excitonic insulator state at low temperature. In this weak-coupling scenario (formally similar to BCS superconductivity), a gap opens at E_F in the excitonic insulator state, which leads to a spectral weight transfer and appearance of Hebel-Slichter–like peaks [7,54]. Transitions between these peaks could, in principle, lead to distinct excitations in the conductivity spectrum [55]. However, the signatures of the exciton instability have not been experimentally observed in

ZrSiS until now, in particular, no pseudogap was observed in photoemission spectra. The observation that the $F1$ peak draws its spectral weight from the high- rather than the low-energy part of the spectrum also contradicts this scenario.

To inspect the role of zero-momentum excitons in the formation of the $F1$ and $F2$ peaks, we have computed the interband optical spectra by solving the Bethe-Salpeter equation (BSE) with quasiparticle energies calculated at GW level, also testing the impact of the coupling between the resonant and antiresonant excitations. The results, depicted in the insets of Figs. 2(a), 3(a), and 3(b), show that the optical conductivity is only marginally affected by the electronic correlation and excitonic effects: the BSE σ_1 spectra are very similar to the DFT spectra and do not exhibit any evident pressure dependence. Formation of a single exciton thus cannot explain our experimental results. A more complex possibility would be the creation of a finite-momentum exciton accompanied by a phonon or another exciton, in order to ensure the momentum conservation. A first step in analysis of such a scenario would be extending the BSE analysis to finite-momentum transfer.

Another scenario was proposed recently [9], suggesting that ZrSiS should be located in a quantum critical region between the NLSM and excitonic insulator phases, which could explain the observed quasiparticle mass

enhancement [6] in the absence of a pseudogap, consistent with reported photoemission spectra and our optical data. Nevertheless, both the excitonic insulator and quantum critical scenarios are at odds with our observation of pressure-insensitive in-plane response σ_{ab} and with our theoretical predictions. We note that a purely electronic excitonic insulator phase with permanent out-of-plane electric dipole moments arranged in an antiferroelectric pattern was recently proposed in bulk MoS_2 under pressure [56], which might be relevant for pressurized ZrSiS as well.

In conclusion, according to our reflectivity study, the optical response of the NLSM ZrSiS is highly anisotropic. The polarization-dependent optical conductivity at ambient pressure is in very good agreement with the results of DFT calculations. The in-plane optical response shows only modest changes under pressure, consistent with theoretical predictions. In stark contrast, the out-of-plane optical conductivity undergoes strong changes under pressure, with the appearance of two pronounced peaks. The observed pressure-induced changes can neither be attributed to a structural phase transition according to our single-crystal XRD data, nor can they be explained by electronic correlation effects and single exciton formation according to our theoretical calculations.

[*]christine.kuntscher@physik.uni-augsburg.de

[1] A. A. Burkov and L. Balents, Weyl Semimetal in a Topological Insulator Multilayer, Phys. Rev. Lett. **107**, 127205 (2011).

[2] C. Fang, Y. Chen, H.-Y. Kee, and L. Fu, Topological nodal line semimetals with and without spin-orbital coupling, Phys. Rev. B **92**, 081201(R) (2015).

[3] L. M. Schoop, M. N. Ali, C. Strasser, V. Duppel, S. S. P. Parkin, B. V. Lotsch, and C. R. Ast, Dirac cone protected by non-symmorphic symmetry and three-dimensional Dirac line node in ZrSiS, Nat. Commun. **7**, 11696 (2016).

[4] M. Neupane, I. Belopolski, M. M. Hosen, D. S. Sanchez, R. Sankar, M. Szlawska, S.-Y. Xu, K. Dimitri, N. Dhakal, P. Maldonado, P. M. Oppeneer, D. Kaczorowski, F. Chou, M. Z. Hasan, and T. Durakiewicz, Observation of topological nodal fermion semimetal phase in ZrSiS, Phys. Rev. B **93**, 201104(R) (2016).

[5] C. Chen et al., Dirac line nodes and effect of spin-orbit coupling in the nonsymmorphic critical semimetals MSiS (M = Hf, Zr), Phys. Rev. B **95**, 125126 (2017).

[6] S. Pezzini, M. R. van Delft, L. Schoop, B. Lotsch, A. Carrington, M. I. Katsnelson, N. E. Husse, and S. Wiedmann, Unconventional mass enhancement around the Dirac nodal loop in ZrSiS, Nat. Phys. **14**, 178 (2018).

[7] A. N. Rudenko, E. A. Stepanov, A. I. Lichtenstein, and M. I. Katsnelson, Excitonic Instability and Pseudogap Formation in Nodal Line Semimetal ZrSiS, Phys. Rev. Lett. **120**, 216401 (2018).

[8] M. M. Scherer, C. Honerkamp, A. N. Rudenko, E. A. Stepanov, A. I. Lichtenstein, and M. I. Katsnelson, Excitonic instability and unconventional pairing in the nodal-line materials ZrSiS and ZrSiSe, Phys. Rev. B **98**, 241112(R) (2018).

[9] J.-R. Wang, G.-Z. Liu, X. Wan, and C. Zhang, Quantum criticality of the excitonic insulating transition in the nodal-line semimetal ZrSiS, Phys. Rev. B **101**, 245151 (2020).

[10] C. Wang and T. Hughbanks, Main group element size and substitution effects on the structural dimensionality of zirconium tellurides of the ZrSiS type, Inorg. Chem. **34**, 5524 (1995).

[11] R. Sankar, G. Peramaiyan, I. P. Muthuselvam, C. J. Butler, K. Dimitri, M. Neupane, G. N. Rao, M.-T. Lin, and F. C. Chou, Crystal growth of Dirac semimetal ZrSiS with high magnetoresistance and mobility, Sci. Rep. **7**, 40603 (2017).

[12] Y.-Y. Lv, B.-B. Zhang, X. Li, S.-H. Yao, Y. B. Chen, J. Zhou, S.-T. Zhang, M.-H. Lu, and Y.-F. Chen, Extremely large and significantly anisotropic magnetoresistance in ZrSiS single crystals, Appl. Phys. Lett. **108**, 244101 (2016).

[13] R. Singha, A. K. Pariari, B. Satpati, and P. Mandal, Large nonsaturating magnetoresistance and signature of nondegenerate Dirac nodes in ZrSiS, Proc. Natl. Acad. Sci. U.S.A. **114**, 2468 (2017).

[14] M. B. Schilling, L. M. Schoop, B. V. Lotsch, M. Dressel, and A. V. Pronin, Flat Optical Conductivity in ZrSiS Due to Two-Dimensional Dirac Bands, Phys. Rev. Lett. **119**, 187401 (2017).

[15] J. Ebad-Allah, J. F. Afonso, M. Krottenmüller, J. Hu, Y. L. Zhu, Z. Q. Mao, J. Kuneš, and C. A. Kuntscher, Chemical pressure effect on the optical conductivity of the nodal-line semimetals ZrSiY (Y = S, Se, Te) and ZrGeY (Y = S, Te), Phys. Rev. B **99**, 125154 (2019).

[16] J. P. Perdew, K. Burke, and M. Ernzerhof, Generalized Gradient Approximation Made Simple, Phys. Rev. Lett. **77**, 3865 (1996).

[17] See Supplemental Material at http://link.aps.org/supplemental/10.1103/PhysRevLett.127.076402 for details about sample preparation, polarization-dependent reflectivity measurements at ambient and high pressure, analysis of reflectivity and optical conductivity spectra, XRD measurements under pressure, and theoretical calculations, which includes Refs. [18–37].

[18] W. Bensch, O. Helmer, M. Muhler, H. Ebert, and M. Knecht, Experimental and theoretical bandstructure of the layer compound ZrSiTe, J. Phys. Chem. **99**, 3326 (1995).

[19] H. K. Mao, J. Xu, and P. M. Bell, Calibration of the ruby pressure gauge to 800 kbar under quasi-hydrostatic conditions, J. Geophys. Res. **91**, 4673 (1986).

[20] K. Syassen, Ruby under pressure, High Press. Res. **28**, 75 (2008).

[21] M. I. Eremets and Y. A. Timofeev, Miniature diamond anvil cell: Incorporating a new design for anvil alignment, Rev. Sci. Instrum. **63**, 3123 (1992).

[22] L. Merrill and W. A. Bassett, Miniature diamond anvil pressure cell for single crystal x-ray diffraction studies, Rev. Sci. Instrum. **45**, 290 (1974).

[23] R. Boehler and K. De Hantsetters, New anvil designs in diamond-cells, High Press. Res. **24**, 391 (2004).

[24] S. A. Moggach, D. R. Allan, S. Parsons, and J. E. Warren, Incorporation of a new design of backing seat and anvil in a Merrill-Bassett diamond anvil cell, J. Appl. Crystallogr. **41**, 249 (2008).

[25] G. J. Piermarini, S. Block, J. D. Barnett, and R. A. Forman, Calibration of the pressure dependence of the R1 ruby fluorescence line to 195 kbar, J. Appl. Phys. **46**, 2774 (1975).

[26] A. Dewaele, M. Torrent, P. Loubeyre, and M. Mezouar, Compression curves of transition metals in the Mbar range: Experiments and projector augmented-wave calculations, Phys. Rev. B **78**, 104102 (2008).

[27] I. Kantor, Fluorescense pressure calculation and thermocouple tools, https://millenia.cars.aps.anl.gov/gsecars/ruby/ruby.htm, accessed August 13, 2020.

[28] G. J. Piermarini, S. Block, and J. D. Barnett, Hydrostatic limits in liquids and solids to 100 kbar, J. Appl. Phys. **44**, 5377 (1973).

[29] CrysAlisPro 1.171.38.46, Rigaku oxford diffraction (2017).

[30] G. Kresse and J. Hafner, Ab initio molecular dynamics for liquid metals, Phys. Rev. B **47**, 558 (1993).

[31] G. Kresse and J. Furthmüller, Efficient iterative schemes for ab initio total-energy calculations using a plane-wave basis set, Phys. Rev. B **54**, 11169 (1996).

[32] P. E. Blöchl, Projector augmented-wave method, Phys. Rev. B **50**, 17953 (1994).

[33] L. Hedin, New method for calculating the one-particle Green's function with application to the electron-gas problem, Phys. Rev. **139**, A796 (1965).

[34] M. S. Hybertsen and S. G. Louie, Electron correlation in semiconductors and insulators: Band gaps and quasiparticle energies, Phys. Rev. B **34**, 5390 (1986).

[35] M. Shishkin and G. Kresse, Implementation and performance of the frequency-dependent GW method within the PAW framework, Phys. Rev. B **74**, 035101 (2006).

[36] S. M. Dancoff, Non-adiabatic meson theory of nuclear forces, Phys. Rev. **78**, 382 (1950).

[37] J. Paier, M. Marsman, and G. Kresse, Dielectric properties and excitons for extended systems from hybrid functionals, Phys. Rev. B **78**, 121201(R) (2008).

[38] M. Novak, S. N. Zhang, F. Orbanić, N. Biliškov, G. Eguchi, S. Paschen, A. Kimura, X. X. Wang, T. Osada, K. Uchida, M. Sato, Q. S. Wu, O. V. Yazyev, and I Kokanović, Highly anisotropic interlayer magnetoresistance in ZrSiS nodal-line Dirac semimetal, Phys. Rev. B **100**, 085137 (2019).

[39] K. R. Shirer, K. A. Modic, T. Zimmerling, M. D. Bachmann, M. König, P. J. W. Moll, L. Schoop, and A. P. Mackenzie, Out-of-plane transport in ZrSiS and ZrSiSe microstructures, APL Mater. **7**, 101116 (2019).

[40] W. Zhou, A. N. Rudenko, and S. Yuan, Effect of mechanical strain on the optical properties of nodal-line semimetal ZrSiS, Adv. Electron. Mater. **6**, 1900860 (2019).

[41] T. Habe and M. Koshino, Dynamical conductivity in the topological nodal-line semimetal ZrSiS, Phys. Rev. B **98**, 125201 (2018).

[42] Please note that we concentrate here on the high-energy range, since the temperature dependence of the low-energy optical conductivity for $\mathbf{E}\|ab$ has been discussed in detail in Ref. [14].

[43] It is interesting to note that the temperature-dependent shift of the $L4$ peak slightly changes its slope between 150 and 100 K. In the same temperature range, the temperature dependence of the dc resistivity changes [13] and several Raman modes show an anomaly in their position and width [44], which was attributed to an interplay between electronic and phononic degrees of freedom.

[44] R. Singha, S. Samanta, S. Chatterjee, A. Pariari, D. Majumdar, B. Satpati, L. Wang, A. Singha, and P. Mandal, Probing lattice dynamics and electron-phonon coupling in the topological nodal-line semimetal ZrSiS, Phys. Rev. B **97**, 094112 (2018).

[45] S. M. Young and C. L. Kane, Dirac Semimetals in Two Dimensions, Phys. Rev. Lett. **115**, 126803 (2015).

[46] We cannot completely rule out that the $F2$ peak already exists at ambient pressure, but cannot be resolved due to small oscillator strength and overlap with higher-energy interband transitions.

[47] C. C. Gu et al., Experimental evidence of crystal symmetry protection for the topological nodal line semimetal state in ZrSiS, Phys. Rev. B **100**, 205124 (2019).

[48] D. VanGennep, T. A. Paul, C. W. Yerger, S. T. Weir, Y. K. Vohra, and J. J. Hamlin, Possible pressure-induced topological quantum phase transition in the nodal line semimetal ZrSiS, Phys. Rev. B **99**, 085204 (2019).

[49] F. D. Murnaghan, The compressibility of media under extreme pressures, Proc. Natl. Acad. Sci. U.S.A. **30**, 244 (1944).

[50] B. Salmankurt and S. Duman, First-principles study of structural, mechanical, lattice dynamical and thermal properties of nodal-line semimetals ZrXY ($X = $ Si,Ge; $Y = $ S, Se), Phil. Mag. **97**, 175 (2016).

[51] R. J. Kirby, A. Ferrenti, C. Weinberg, S. Klemenz, M. Oudah, S. Lei, C. P. Weber, D. Fausti, G. D. Scholes, and L. M. Schoop, Transient Drude response dominates near-infrared pump-probe reflectivity in nodal-line semimetals ZrSiS and ZrSiSe, J. Phys. Chem. Lett. **11**, 6105 (2020).

[52] J. Ebad-Allah, M. Krottenmüller, J. Hu, Y. L. Zhu, Z. Q. Mao, and C. A. Kuntscher, Infrared spectroscopy study of the nodal-line semimetal candidate ZrSiTe under pressure: Hints for pressure-induced phase transitions, Phys. Rev. B **99**, 245133 (2019).

[53] M. Krottenmüller, M. Vöst, N. Unglert, J. Ebad-Allah, G. Eickerling, D. Volkmer, J. Hu, Y. L. Zhu, Z. Q. Mao, W. Scherer, and C. A. Kuntscher, Indications for Lifshitz transitions in the nodal-line semimetal ZrSiTe induced by interlayer interaction, Phys. Rev. B **101**, 081108(R) (2020).

[54] L. C. Hebel and C. P. Slichter, Nuclear spin relaxation in normal and superconducting aluminum, Phys. Rev. **113**, 1504 (1959).

[55] We note that the $F1$ peak derives its spectral weight from the high-energy rather than low-energy region. This is opposite to the excitonic insulator scenario, where the spectral weight comes from the Drude peak or low-energy region, in general.

[56] S. Samaneh Ataei, D. Varsano, E. Molinari, and M. Rontani, Evidence of ideal excitonic insulator in bulk MoS_2 under pressure, Proc. Natl. Acad. Sci. U.S.A. **118**, e2010110118 (2021).

Conclusions

The present thesis investigated the Quasiparticle properties and optical responses of a series of bulk and two-dimensional structures, with a particular focus on the class of Transition Metal Oxide (TMO) perovskites.

The optical and excitonic properties of a perovskite dataset containing 3d, 4d, and 5d transition metals have been described with the ab-initio G_0W_0+BSE approach. A special emphasis was placed on the evolution of the spectra and excitonic properties along the $LaTMO_3$ $3d^1 \rightarrow 3d^6$ series and along the $3d^0 \rightarrow 5d^0$ cubic non-magnetic series ($SrTiO_3$, $SrHfO_3$, $SrZrO_3$ and $KTaO_3$). The main features of the spectra have been discussed through the analysis of the BSE coupling coefficients in terms of transitions between the Quasiparticle electronic bands. The theoretical predictions are systematically compared with the available experimental data and an overall satisfactory agreement is reached. An approximation of the standard BSE scheme (model-BSE) is bench-marked on the dataset, resulting in a very accurate performance for the cubic series and providing larger deviations for the La Series and the remaining materials.

For what regards two-dimensional systems, an in-depth study of the freestanding monolayer structure of $SrTiO_3$ has been performed. The inclusion of the off-diagonal self-energy elements in the G_0W_0 schemes has proved to be essential to reach a correct description of the strong hybridization of the conduction bands. The excitonic properties have been characterized in the optical limit and for finite momentum: the spectra is dominated by electron-hole effects, with intense peaks associated to bound excitons.

The G_0W_0 +BSE approach has been also employed to study the optical response of the topological nodal line semimetal ZrSiS. These results are part of a combined experimental and computational study of the in-plane and out-of-plane optical conductivity under pressure. The agreement with experimental data is satisfactory for what regards the optical response at ambient pressure; moreover the anisotropy between the in-plane and out-of-plane profiles is correctly reproduced. However experimental out-of-plane data at high pressure indicates the emergence of an intense peak which cannot be accounted by the electron-hole interaction in the optical limit as described by the Bethe-Salpeter Equation.

Lastly, a section of the thesis has been dedicated to the development of a workflow to perform in an automated way the basis-set extrapolation scheme for G_0W_0 calculations with VASP. The scheme performs an extrapolation of the QP-energies to the infinite-basis-set limit and it's specifically designed in order to avoid false convergences. Its implementation relies

on the AiiDA framework and the AiiDA-VASP plugin, which I extended in order to support GW and BSE simulations. The workflow includes error detection/handling features for the most common problems and automatically tunes the optimization flags.

Appendices

Appendix A

Proof of $\langle n \sim occ.|\mathbf{G}|m \sim E_F\rangle \approx 0$

Let's start by summarizing the different approximations:

1. we assume large $\mathbf{G}$ reciprocal lattice vectors.

2. n states are occupied orbitals, m states are assumed close to the Fermi energy.

Therefore:

$$\langle n|\mathbf{G}|m\rangle = \int_\Omega d\mathbf{r} \left[\frac{1}{\sqrt{\Omega}} \sum_{\mathbf{G}_n} C_{\mathbf{G}_n n} e^{i(\mathbf{G}_n+\mathbf{k})\mathbf{r}}\right]^* e^{i\mathbf{G}\mathbf{r}} \left[\frac{1}{\sqrt{\Omega}} \sum_{\mathbf{G}_m} C_{\mathbf{G}_m m} e^{i(\mathbf{G}_m+\mathbf{k})\mathbf{r}}\right]$$

$$= \frac{1}{\Omega} \sum_{\mathbf{G}_n} \sum_{\mathbf{G}_m} C^*_{\mathbf{G}_n n} C_{\mathbf{G}_m m} \int_\Omega d\mathbf{r} e^{-i(\mathbf{G}_n+\mathbf{k})\mathbf{r}} e^{i\mathbf{G}\mathbf{r}} e^{i(\mathbf{G}_m+\mathbf{k})\mathbf{r}}$$

$$\approx [\text{approx.2}] \approx \frac{1}{\Omega} \sum_{\mathbf{G}_n} \sum_{\mathbf{G}_m} C^*_{\mathbf{G}_n n} C_{\mathbf{G}_m m} \int_\Omega d\mathbf{r} e^{-i\mathbf{G}_n\mathbf{r}} e^{i\mathbf{G}\mathbf{r}} e^{i\mathbf{G}_m\mathbf{r}}$$

$$= \sum_{\mathbf{G}_n} \sum_{\mathbf{G}_m} C^*_{\mathbf{G}_n n} C_{\mathbf{G}_m m} \delta_{(\mathbf{G}_m-\mathbf{G}_n)+\mathbf{G}}$$

Only the terms satisfying the condition $(\mathbf{G}_m - \mathbf{G}_n) + \mathbf{G} = 0$ contributes to the sum; the condition implies that only states containing significant components $C_{\mathbf{G}_n n}$ at high frequency plane waves $\mathbf{G}_n = \mathbf{G}_m + \mathbf{G} \approx \mathbf{G}$ contributes to the sum. However occupied orbitals or states close to the Fermi energy have negligible component at $\mathbf{G} >> 0$.

Appendix B

k-averaging for bulk $SrTiO_3$

In Fig. B.1 we compare the spectra associated with two different k-averaging specifications to standard (single) BSE one to illustrate the presence of spurious peak artifacts (associated to the Coulomb kernel truncation approximation discussed in [109]). The $m = 5$, $n = 4$ exhibits a clear suppression of the 6.4 eV sharp and narrow peak with respect to the standard BSE calculation, which is restored by the $m = 7$, $n = 4$ curve.
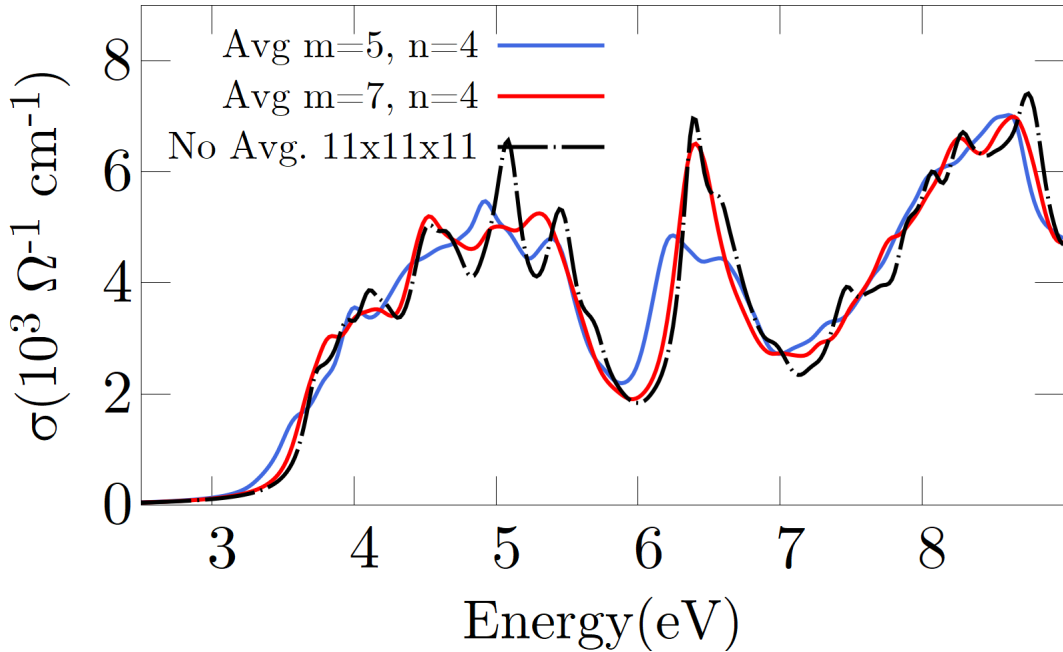

Figure B.1: $SrTiO_3$ BSE spectra calculated for different k-averaging parameters n, m of $m \times m \times m | n \times n \times n$ and compared with a standard BSE calculation on a $11 \times 11 \times 11$ k-mesh.

Appendix C

Model-BSE parameters for bulk perovskites dataset

In this section the parameters and the k-point meshes used for the model-BSE calculations of the exciton binding energies E_{xb} are collected:

	k-mesh	ϵ_∞^{-1}	λ	Scissor.op
SrTiO$_3$	$20 \times 20 \times 20$	0.1654	1.4629	1.645
SrZrO$_3$	$20 \times 20 \times 20$	0.2309	1.4573	0.9439
SrHfO$_3$	$20 \times 20 \times 20$	0.2419	1.4478	1.9131
KTaO$_3$	$20 \times 20 \times 20$	0.1946	1.4200	1.3946
LaScO$_3$	$10 \times 10 \times 6$	0.2013	1.4621	1.7000
LaTiO$_3$	$10 \times 10 \times 6$	0.1202	1.3491	0.3674
LaVO$_3$	$10 \times 10 \times 6$	0.1220	1.4201	0.3275
LaCrO$_3$	$10 \times 10 \times 6$	0.1468	1.3931	1.6057
LaMnO$_3$	$10 \times 10 \times 6$	0.1068	1.3353	0.8497
LaFeO$_3$	$10 \times 10 \times 6$	0.1031	1.3362	1.0644
SrMnO$_3$	$8 \times 8 \times 4$	0.0875	1.3404	1.2873
SrTcO$_3$	$9 \times 9 \times 6$	0.0713	1.3292	0.6018
Ca$_2$RuO$_4$	$8 \times 8 \times 4$	0.0870	1.2247	0.4796
NaOsO$_3$	$9 \times 9 \times 6$	0.0308	1.1092	0.2601

Table C.1: Parameters for the model-BSE calculations of the converged exciton binding energies. The inverse static dielectric constants and screening lengths λ (Å^{-1}) used for the model dielectric function are given; Scissor.op stands for the scissor operator needed to approximate the G_0W_0 band structures.

Appendix D

Additional results for monolayer SrTiO$_3$

We report two additional results regarding the bandstructure of SrTiO$_3$ monolayer. In Figure D.1 the G$_0$W$_0^{diag}$@HSE06 bandstructure is presented; the calculation employed a $10 \times 10 \times 1$ k-mesh, a wavefunction cutoff of 650 eV, $N_\omega = 96$, 192 bands and a vacuum size of 24 Å.

The calculation in Figure D.2 uses the Yambo code, with different parameters: a $10 \times 10 \times 1$ k-point mesh, 480 bands (with terminators for χ and G), a cutoff of 800 eV and a vacuum size of 20 Å. A Plasmon Pole Model is used for in the G$_0$W$_0$ algorithm, together with the Coulomb Truncation and the RIM integration method. Both calculations show the DFT bands as a grey background.
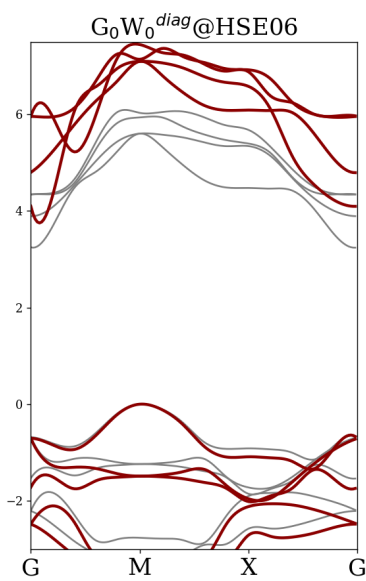
Figure D.1: $G_0W_0{}^{diag}$ bandstructure of the relaxed $SrTiO_3$ structure determined from a hybrid HSE06 starting point.
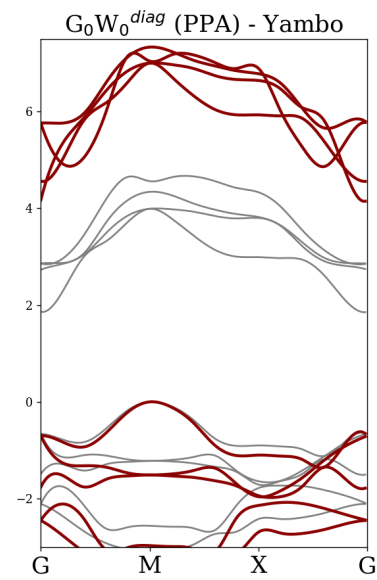

Figure D.2: $G_0W_0{}^{diag}$ bandstructure of the relaxed $SrTiO_3$ structure determined from a DFT (PBE) starting point using the Yambo code [19, 20].

Bibliography

[1] J. Frenkel. On the transformation of light into Heat in Solids. I. *Phys. Rev.*, 37:17–44, Jan 1931.

[2] J. Frenkel. On the transformation of light into Heat in Solids. II. *Phys. Rev.*, 37:1276–1294, May 1931.

[3] Gregory H. Wannier. The structure of electronic excitation levels in insulating crystals. *Phys. Rev.*, 52:191–197, Aug 1937.

[4] Nevill Francis Mott. On the absorption of light by crystals. *Proceedings of the Royal Society of London. Series A. Mathematical and Physical Sciences*, 167(930):384–391, 1938.

[5] E. F. Gross. Optical spectrum of excitons in the crystal lattice. *Il Nuovo Cimento (1955-1965)*, 3(4):672–701, Apr 1956.

[6] Richard M. Martin, Lucia Reining, and David M. Ceperley. *Interacting Electrons: Theory and Computational Approaches*. Cambridge University Press, 2016.

[7] P. Nozieres. *Theory Of Interacting Fermi Systems*. Advanced Books Classics. Avalon Publishing, 1997.

[8] D. Pines and P. Nozieres. *The Theory of Quantum Liquids, Vol. 1, Normal Fermi Liquids*. W. A. Benjamin, New York, 1966.

[9] Landau L. D. Theory of Fermi-liquids. *Soviet Physics JETP-USSR*, 3:920–925, 1956.

[10] E.M. LIFSHITZ and L.P. PITAEVSKI. Statistical Physics: Theory of the Condensed State. pages 1–27. Butterworth-Heinemann, Oxford, 1980.

[11] Lars Hedin. New Method for Calculating the One-Particle Green's Function with Application to the Electron-Gas Problem. *Phys. Rev.*, 139:A796–A823, Aug 1965.

[12] P. Hohenberg and W. Kohn. Inhomogeneous Electron gas. *Phys. Rev.*, 136:B864–B871, Nov 1964.

[13] W. Kohn and L. J. Sham. Self-Consistent equations including Exchange and Correlation effects. *Phys. Rev.*, 140:A1133–A1138, Nov 1965.

[14] G. Strinati, H. J. Mattausch, and W. Hanke. Dynamical aspects of correlation corrections in a covalent crystal. *Phys. Rev. B*, 25:2867–2888, Feb 1982.

[15] Mark S. Hybertsen and Steven G. Louie. First-Principles Theory of Quasiparticles: Calculation of band gaps in semiconductors and insulators. *Phys. Rev. Lett.*, 55:1418–1421, Sep 1985.

[16] Mark S. Hybertsen and Steven G. Louie. Electron correlation in semiconductors and insulators: Band gaps and quasiparticle energies. *Phys. Rev. B*, 34:5390–5413, Oct 1986.

[17] G. Kresse and J. Hafner. Ab initio molecular dynamics for liquid metals. *Phys. Rev. B*, 47:558–561, Jan 1993.

[18] G. Kresse and J. Furthmüller. Efficient iterative schemes for ab initio total-energy calculations using a plane-wave basis set. *Phys. Rev. B*, 54:11169–11186, Oct 1996.

[19] D Sangalli, A Ferretti, H Miranda, C Attaccalite, I Marri, E Cannuccia, P Melo, M Marsili, F Paleari, A Marrazzo, G Prandini, P Bonfà, M O Atambo, F Affinito, M Palummo, A Molina-Sánchez, C Hogan, M Grüning, D Varsano, and A Marini. Many-Body perturbation theory calculations using the Yambo code. *Journal of Physics: Condensed Matter*, 31(32):325902, may 2019.

[20] Andrea Marini, Conor Hogan, Myrta Grüning, and Daniele Varsano. yambo: An ab initio tool for excited state calculations. *Computer Physics Communications*, 180(8):1392–1403, 2009.

[21] Xavier Gonze, Bernard Amadon, Gabriel Antonius, Frédéric Arnardi, Lucas Baguet, Jean-Michel Beuken, Jordan Bieder, François Bottin, Johann Bouchet, Eric Bousquet, Nils Brouwer, Fabien Bruneval, Guillaume Brunin, Théo Cavignac, Jean-Baptiste Charraud, Wei Chen, Michel Côté, Stefaan Cottenier, Jules Denier, Grégory Geneste, Philippe Ghosez, Matteo Giantomassi, Yannick Gillet, Olivier Gingras, Donald R. Hamann, Geoffroy Hautier, Xu He, Nicole Helbig, Natalie Holzwarth, Yongchao Jia, François Jollet, William Lafargue-Dit-Hauret, Kurt Lejaeghere, Miguel A. L. Marques, Alexandre Martin, Cyril Martins, Henrique P. C. Miranda, Francesco Naccarato, Kristin Persson, Guido Petretto, Valentin Planes, Yann Pouillon, Sergei Prokhorenko, Fabio Ricci, Gian-Marco Rignanese, Aldo H. Romero, Michael Marcus Schmitt, Marc Torrent, Michiel J. van Setten, Benoit Van Troeye, Matthieu J. Verstraete, Gilles Zérah, and Josef W. Zwanziger. The Abinit project: Impact, environment and recent developments. *Comput. Phys. Commun.*, 248:107042, 2020.

[22] Marco Govoni and Giulia Galli. Large scale GW calculations. *Journal of Chemical Theory and Computation*, 11(6):2680–2696, Jun 2015.

[23] Jack Deslippe, Georgy Samsonidze, David A. Strubbe, Manish Jain, Marvin L. Cohen, and Steven G. Louie. Berkeleygw: A massively parallel computer package for the calculation of

the quasiparticle and optical properties of materials and nanostructures. *Computer Physics Communications*, 183(6):1269–1289, 2012.

[24] R. W. Godby, M. Schlüter, and L. J. Sham. Accurate Exchange-Correlation potential for Silicon and its discontinuity on addition of an electron. *Phys. Rev. Lett.*, 56:2415–2418, Jun 1986.

[25] R. W. Godby, M. Schlüter, and L. J. Sham. Quasiparticle energies in GaAs and AlAs. *Phys. Rev. B*, 35:4170–4171, Mar 1987.

[26] R. W. Godby, M. Schlüter, and L. J. Sham. Trends in self-energy operators and their corresponding exchange-correlation potentials. *Phys. Rev. B*, 36:6497–6500, Oct 1987.

[27] X. Blase, Angel Rubio, Steven G. Louie, and Marvin L. Cohen. Quasiparticle band structure of bulk hexagonal boron nitride and related systems. *Phys. Rev. B*, 51:6868–6875, Mar 1995.

[28] M. J. van Setten, M. Giantomassi, X. Gonze, G.-M. Rignanese, and G. Hautier. Automation methodologies and large-scale validation for GW: Towards High-Throughput GW calculations. *Phys. Rev. B*, 96:155207, Oct 2017.

[29] Peitao Liu, Merzuk Kaltak, Ji ří Klimeš, and Georg Kresse. Cubic scaling GW: Towards fast Quasiparticle calculations. *Phys. Rev. B*, 94:165109, Oct 2016.

[30] Dorothea Golze, Marc Dvorak, and Patrick Rinke. The GW Compendium: A practical guide to Theoretical Photoemission Spectroscopy. *Frontiers in Chemistry*, 7, 2019.

[31] Asbjørn Rasmussen, Thorsten Deilmann, and Kristian S. Thygesen. Towards fully automated GW band structure calculations: What we can learn from 60.000 self-energy evaluations. *npj Computational Materials*, 7(1):22, Jan 2021.

[32] Miki Bonacci, Junfeng Qiao, Nicola Spallanzani, Antimo Marrazzo, Giovanni Pizzi, Elisa Molinari, Daniele Varsano, Andrea Ferretti, and Deborah Prezzi. Towards high-throughput Many-Body perturbation theory: efficient algorithms and automated workflows, 2023.

[33] Ji ří Klimeš, Merzuk Kaltak, and Georg Kresse. Predictive GW calculations using plane waves and pseudopotentials. *Phys. Rev. B*, 90:075125, Aug 2014.

[34] Emanuele Maggio, Peitao Liu, Michiel J. van Setten, and Georg Kresse. GW100: A plane wave perspective for small molecules. *Journal of Chemical Theory and Computation*, 13(2):635–648, Feb 2017.

[35] Florian Ellinger and Cesare Franchini. High-Throughput GW calculations. In preparation, 2023.

[36] Florian Ellinger. High-Throughput GW calculations. Master's thesis.

[37] Lorenzo Varrassi, Peitao Liu, Zeynep Ergönenc Yavas, Menno Bokdam, Georg Kresse, and Cesare Franchini. Optical and excitonic properties of transition metal oxide perovskites by the Bethe-Salpeter equation. *Phys. Rev. Materials*, 5:074601, Jul 2021.

[38] Dianxiang Ji, Songhua Cai, Tula R. Paudel, Haoying Sun, Chunchen Zhang, Lu Han, Yifan Wei, Yipeng Zang, Min Gu, Yi Zhang, Wenpei Gao, Huaixun Huyan, Wei Guo, Di Wu, Zhengbin Gu, Evgeny Y. Tsymbal, Peng Wang, Yuefeng Nie, and Xiaoqing Pan. Freestanding crystalline oxide perovskites down to the monolayer limit. *Nature*, 570(7759):87–90, Jun 2019.

[39] Seung Sae Hong, Jung Ho Yu, Di Lu, Ann F. Marshall, Yasuyuki Hikita, Yi Cui, and Harold Y. Hwang. Two-dimensional limit of crystalline order in perovskite membrane films. *Science Advances*, 3(11):eaao5173, 2017.

[40] A. Ohtomo and H. Y. Hwang. A high-mobility electron gas at the $LaAlO_3/SrTiO_3$ heterointerface. *Nature*, 427(6973):423–426, Jan 2004.

[41] J. G. Bednorz and K. A. Müller. $Sr_{1-x}Ca_xTiO_3$: An XY Quantum Ferroelectric with transition to randomness. *Phys. Rev. Lett.*, 52:2289–2292, Jun 1984.

[42] Fran çois Bottin and Fabio Finocchi. $SrTiO_3$ substrates capped with a GaAs monolayer: An ab initio study. *Phys. Rev. B*, 76:165427, Oct 2007.

[43] Robert Evarestov, Evgeny Blokhin, Denis Gryaznov, Eugene A. Kotomin, Rotraut Merkle, and Joachim Maier. Jahn-Teller effect in the phonon properties of defective $SrTiO_3$ from first principles. *Phys. Rev. B*, 85:174303, May 2012.

[44] J. Inaba and T. Katsufuji. Large magnetoresistance in spin- and carrier-doped $SrTiO_3$. *Phys. Rev. B*, 72:052408, Aug 2005.

[45] Leslie M. Schoop, Mazhar N. Ali, Carola Straßer, Andreas Topp, Andrei Varykhalov, Dmitry Marchenko, Viola Duppel, Stuart S. P. Parkin, Bettina V. Lotsch, and Christian R. Ast. Dirac cone protected by non-symmorphic symmetry and three-dimensional Dirac line node in ZrSiS. *Nature Communications*, 7(1):11696, May 2016.

[46] Steve M. Young and Charles L. Kane. Dirac semimetals in Two Dimensions. *Phys. Rev. Lett.*, 115:126803, Sep 2015.

[47] Sebastiaan P. Huber, Spyros Zoupanos, Martin Uhrin, Leopold Talirz, Leonid Kahle, Rico Häuselmann, Dominik Gresch, Tiziano Müller, Aliaksandr V. Yakutovich, Casper W. Andersen, Francisco F. Ramirez, Carl S. Adorf, Fernando Gargiulo, Snehal Kumbhar, Elsa Passaro, Conrad Johnston, Andrius Merkys, Andrea Cepellotti, Nicolas Mounet, Nicola Marzari, Boris Kozinsky, and Giovanni Pizzi. AiiDA 1.0, a scalable computational infrastructure for automated reproducible workflows and data provenance. *Scientific Data*, 7(1):300, Sep 2020.

[48] Martin Uhrin, Sebastiaan P. Huber, Jusong Yu, Nicola Marzari, and Giovanni Pizzi. Workflows in AiiDA: Engineering a High-Throughput, event-based engine for robust and modular computational workflows. *Computational Materials Science*, 187:110086, 2021.

[49] R.G. Parr and Y. Weitao. *Density-Functional Theory of Atoms and Molecules*. International Series of Monographs on Chemistry. Oxford University Press, 1994.

[50] H. Eschrig. *The fundamentals of Density Functional Theory*. Teubner-Texte zur Physik. Teubner, 1996.

[51] R.M. Dreizler and J. da Providência. *Density Functional Methods In Physics*. Nato ASI Subseries B:. Springer US, 1985.

[52] M. Ferrario, G. Ciccotti, and K. Binder. *Computer Simulations in Condensed Matter: From Materials to Chemical Biology*. Number v. 1 in Lecture Notes in Physics. Springer Berlin Heidelberg, 2007.

[53] John P. Perdew, Kieron Burke, and Matthias Ernzerhof. Generalized Gradient Approximation Made Simple. *Phys. Rev. Lett.*, 78:1396–1396, Feb 1997.

[54] A. D. Becke. Density-functional exchange-energy approximation with correct asymptotic behavior. *Phys. Rev. A*, 38:3098–3100, Sep 1988.

[55] Chengteh Lee, Weitao Yang, and Robert G. Parr. Development of the Colle-Salvetti correlation-energy formula into a functional of the electron density. *Phys. Rev. B*, 37:785–789, Jan 1988.

[56] James C. Phillips and Leonard Kleinman. New method for calculating wave functions in crystals and molecules. *Phys. Rev.*, 116:287–294, Oct 1959.

[57] Leonard Kleinman and James C. Phillips. Crystal potential and energy bands of semiconductors. III. self-consistent calculations for silicon. *Phys. Rev.*, 118:1153–1167, Jun 1960.

[58] D. R. Hamann, M. Schlüter, and C. Chiang. Norm-conserving pseudopotentials. *Phys. Rev. Lett.*, 43:1494–1497, Nov 1979.

[59] G. Kresse and D. Joubert. From ultrasoft pseudopotentials to the projector augmented-wave method. *Phys. Rev. B*, 59:1758–1775, Jan 1999.

[60] O. Krogh Andersen. Linear methods in band theory. *Phys. Rev. B*, 12:3060–3083, Oct 1975.

[61] A. L. Fetter and J. D. Walecka. *Quantum Theory of Many-Particle Systems*. McGraw-Hill, 1971.

[62] E. K. U. Gross, E. Runge, and O. Heinonen. *Many-particle theory / E.K.U. Gross, E. Runge, O. Heinonen*. A. Hilger Bristol ; Philadelphia, 1991.

[63] F. Bechstedt. *Many-Body Approach to Electronic Excitations: Concepts and Applications*. Springer Series in Solid-State Sciences. Springer Berlin Heidelberg, 2014.

[64] W. Nolting and W.D. Brewer. *Fundamentals of Many-body Physics: Principles and Methods*. Springer Berlin Heidelberg, 2009.

[65] Giovanni Onida, Lucia Reining, and Angel Rubio. Electronic excitations: density-functional versus many-body Green's-function approaches. *Rev. Mod. Phys.*, 74:601–659, Jun 2002.

[66] Lars Hedin and Stig O. Lundqvist. *Effects of Electron-Electron and Electron-Phonon Interactions on the One-Electron States of Solids*, volume 23, pages 1–181. Academic Press, 1969.

[67] Tobias Sander. *Ab-initio description of optical properties of semiconductors and nanocrystals*. PhD thesis, Universität Wien, Wien, 2017.

[68] M. Shishkin and G. Kresse. Implementation and performance of the frequency-dependent GW method within the PAW framework. *Phys. Rev. B*, 74:035101, Jul 2006.

[69] T. Miyake and F. Aryasetiawan. Efficient algorithm for calculating noninteracting frequency-dependent linear response functions. *Phys. Rev. B*, 61:7172–7175, Mar 2000.

[70] M. van Schilfgaarde, Takao Kotani, and S. Faleev. Quasiparticle self-consistent GW theory. *Phys. Rev. Lett.*, 96:226402, Jun 2006.

[71] Sergey V. Faleev, Mark van Schilfgaarde, and Takao Kotani. All-electron self-consistent GW approximation: Application to Si, MnO, and NiO. *Phys. Rev. Lett.*, 93:126406, Sep 2004.

[72] Fabien Bruneval and Matteo Gatti. *Quasiparticle Self-Consistent GW Method for the Spectral Properties of Complex Materials*, pages 99–135. Springer Berlin Heidelberg, Berlin, Heidelberg, 2014.

[73] M. Shishkin, M. Marsman, and G. Kresse. Accurate quasiparticle spectra from self-consistent GW calculations with Vertex Corrections. *Phys. Rev. Lett.*, 99:246403, Dec 2007.

[74] Nora Salas-Illanes, Dmitrii Nabok, and Claudia Draxl. Electronic structure of representative band-gap materials by all-electron quasiparticle self-consistent GW calculations. *Phys. Rev. B*, 106:045143, Jul 2022.

[75] Fabien Bruneval, Nathalie Vast, and Lucia Reining. Effect of self-consistency on quasiparticles in solids. *Phys. Rev. B*, 74:045102, Jul 2006.

[76] Takao Kotani, Mark van Schilfgaarde, and Sergey V. Faleev. Quasiparticle self-consistent GW method: A basis for the independent-particle approximation. *Phys. Rev. B*, 76:165106, Oct 2007.

[77] M. Shishkin and G. Kresse. Self-consistent GW calculations for semiconductors and insulators. *Phys. Rev. B*, 75:235102, Jun 2007.

[78] Wolf-Dieter Schöne and Adolfo G. Eguiluz. Self-Consistent calculations of Quasiparticle states in metals and semiconductors. *Phys. Rev. Lett.*, 81:1662–1665, Aug 1998.

[79] B. Holm and U. von Barth. Fully self-consistent GW self-energy of the electron gas. *Phys. Rev. B*, 57:2108–2117, Jan 1998.

[80] Fabien Bruneval, Francesco Sottile, Valerio Olevano, Rodolfo Del Sole, and Lucia Reining. Many-Body Perturbation Theory using the Density-Functional Concept: Beyond the GW Approximation. *Phys. Rev. Lett.*, 94:186402, May 2005.

[81] F. Fuchs, J. Furthmüller, F. Bechstedt, M. Shishkin, and G. Kresse. Quasiparticle band structure based on a generalized Kohn-Sham scheme. *Phys. Rev. B*, 76:115109, Sep 2007.

[82] Joachim Paier, Martijn Marsman, and Georg Kresse. Dielectric properties and excitons for extended systems from hybrid functionals. *Phys. Rev. B*, 78:121201, Sep 2008.

[83] Peitao Liu, Cesare Franchini, Martijn Marsman, and Georg Kresse. Assessing model-dielectric-dependent hybrid functionals on the antiferromagnetic transition-metal monoxides MnO, FeO, CoO, and NiO. *Journal of Physics: Condensed Matter*, 32(1):015502, oct 2019.

[84] A. Svane, N. E. Christensen, M. Cardona, A. N. Chantis, M. van Schilfgaarde, and T. Kotani. Quasiparticle band structures of β-HgS, HgSe, and HgTe. *Phys. Rev. B*, 84:205205, Nov 2011.

[85] A. Svane, N. E. Christensen, M. Cardona, A. N. Chantis, M. van Schilfgaarde, and T. Kotani. Quasiparticle self-consistent GW calculations for PbS, PbSe, and PbTe: Band structure and pressure coefficients. *Phys. Rev. B*, 81:245120, Jun 2010.

[86] Andreas Grüneis, Georg Kresse, Yoyo Hinuma, and Fumiyasu Oba. Ionization potentials of solids: The importance of Vertex Corrections. *Phys. Rev. Lett.*, 112:096401, Mar 2014.

[87] Irene Aguilera, Christoph Friedrich, Gustav Bihlmayer, and Stefan Blügel. GW study of topological insulators bi_2se_3, bi_2te_3, and sb_2te_3: Beyond the perturbative one-shot approach. *Phys. Rev. B*, 88:045206, Jul 2013.

[88] Pablo Aguado-Puente, Stephen Fahy, and Myrta Grüning. GW study of pressure-induced topological insulator transition in group-IV tellurides. *Phys. Rev. Research*, 2:043105, Oct 2020.

[89] Irene Aguilera, Christoph Friedrich, and Stefan Blügel. Many-body corrected tight-binding hamiltonians for an accurate quasiparticle description of topological insulators of the $Bi_2 Se_3$ family. *Phys. Rev. B*, 100:155147, Oct 2019.

[90] Dmitrii Nabok, Stefan Blügel, and Christoph Friedrich. Electron–plasmon and electron–magnon scattering in ferromagnets from first principles by combining GW and GT self-energies. *npj Computational Materials*, 7(1):178, Nov 2021.

[91] Mark van Schilfgaarde, Takao Kotani, and Sergey V. Faleev. Adequacy of approximations in GW theory. *Phys. Rev. B*, 74:245125, Dec 2006.

[92] I. Aguilera, Pablo Palacios, and P. Wahnón. Understanding Ti intermediate-band formation in partially inverse thiospinel $MgIn_2S_4$ through Many-Body approaches. *Phys. Rev. B*, 84:115106, Sep 2011.

[93] Matteo Gatti, Fabien Bruneval, Valerio Olevano, and Lucia Reining. Understanding correlations in vanadium dioxide from first principles. *Phys. Rev. Lett.*, 99:266402, Dec 2007.

[94] Dario A. Leon, Claudia Cardoso, Tommaso Chiarotti, Daniele Varsano, Elisa Molinari, and Andrea Ferretti. Frequency dependence in GW made simple using a multipole approximation. *Phys. Rev. B*, 104:115157, Sep 2021.

[95] Paul Larson, Marc Dvorak, and Zhigang Wu. Role of the plasmon-pole model in the GW approximation. *Phys. Rev. B*, 88:125205, Sep 2013.

[96] R. W. Godby and R. J. Needs. Metal-insulator transition in Kohn-Sham theory and quasi-particle theory. *Phys. Rev. Lett.*, 62:1169–1172, Mar 1989.

[97] A. Oschlies, R. W. Godby, and R. J. Needs. GW self-energy calculations of carrier-induced band-gap narrowing in n-type silicon. *Phys. Rev. B*, 51:1527–1535, Jan 1995.

[98] Mark S. Hybertsen and Steven G. Louie. Electron correlation in semiconductors and insulators: Band gaps and quasiparticle energies. *Phys. Rev. B*, 34:5390–5413, Oct 1986.

[99] Wolfgang von der Linden and Peter Horsch. Precise quasiparticle energies and *hartree-fock* bands of semiconductors and insulators. *Phys. Rev. B*, 37:8351–8362, May 1988.

[100] G. E. Engel and Behnam Farid. Generalized plasmon-pole model and plasmon band structures of crystals. *Phys. Rev. B*, 47:15931–15934, Jun 1993.

[101] Lucia Reining, Giovanni Onida, and R. W. Godby. Elimination of unoccupied-state summations in ab initio self-energy calculations for large supercells. *Phys. Rev. B*, 56:R4301–R4304, Aug 1997.

[102] G. Strinati. Application of the Green's functions method to the study of the optical properties of semiconductors. *La Rivista del Nuovo Cimento (1978-1999)*, 11(12):1–86, Dec 1988.

[103] Mark E. Casida. *Time-Dependent Density Functional Response Theory for Molecules*, pages 155–192. Recent Advances in Computational Chemistry, 1995.

[104] D.J. Thouless and J.G. Valatin. Time-dependent Hartree-Fock equations and rotational states of nuclei. *Nuclear Physics*, 31:211–230, 1962.

[105] G. Strinati. Effects of dynamical screening on resonances at inner-shell thresholds in semiconductors. *Phys. Rev. B*, 29:5718–5726, May 1984.

[106] Arno Schindlmayr and R. W. Godby. Systematic vertex corrections through iterative solution of Hedin's Equations beyond the GW approximation. *Phys. Rev. Lett.*, 80:1702–1705, Feb 1998.

[107] F. Bechstedt, c. Rödl, l. E. Ramos, f. Fuchs, p. H. Hahn, and j. Furthmüller. *Parameter free calculations of optical properties for systems with magnetic ordering or three-dimensional confinement*, pages 28–40. The Science and Culture Series — Physics, 2008.

[108] Stefan Albrecht, Lucia Reining, Rodolfo Del Sole, and Giovanni Onida. Ab Initio Calculation of Excitonic Effects in the Optical Spectra of Semiconductors. *Phys. Rev. Lett.*, 80:4510–4513, May 1998.

[109] Tobias Sander, Emanuele Maggio, and Georg Kresse. Beyond the Tamm-Dancoff approximation for extended systems using exact diagonalization. *Phys. Rev. B*, 92:045209, Jul 2015.

[110] S. M. Dancoff. Non-adiabatic meson theory of nuclear forces. *Phys. Rev.*, 78:382–385, May 1950.

[111] Myrta Grüning, Andrea Marini, and Xavier Gonze. Exciton-plasmon states in nanoscale materials: Breakdown of the Tamm-Dancoff approximation. *Nano Letters*, 9(8):2820–2824, Aug 2009.

[112] Pranjal Kumar Gogoi, Lorenzo Sponza, Daniel Schmidt, Teguh Citra Asmara, Caozheng Diao, Jason C. W. Lim, Sock Mui Poh, Shin-ichi Kimura, Paolo E. Trevisanutto, Valerio Olevano, and Andrivo Rusydi. Anomalous excitons and screenings unveiling strong electronic correlations in $SrTi_xNb_xO_3$ ($0 \leq x \leq 0.005$). *Phys. Rev. B*, 92:035119, Jul 2015.

[113] Li Yang, Jack Deslippe, Cheol-Hwan Park, Marvin L. Cohen, and Steven G. Louie. Excitonic effects on the optical response of Graphene and Bilayer Graphene. *Phys. Rev. Lett.*, 103:186802, Oct 2009.

[114] H J Kulik, T Hammerschmidt, J Schmidt, S Botti, M A L Marques, M Boley, M Scheffler, M Todorović, P Rinke, C Oses, A Smolyanyuk, S Curtarolo, A Tkatchenko, A P Bartók, S Manzhos, M Ihara, T Carrington, J Behler, O Isayev, M Veit, A Grisafi, J Nigam, M Ceriotti, K T Schütt, J Westermayr, M Gastegger, R J Maurer, B Kalita, K Burke, R Nagai, R Akashi, O Sugino, J Hermann, F Noé, S Pilati, C Draxl, M Kuban, S Rigamonti, M Scheidgen, M Esters, D Hicks, C Toher, P V Balachandran, I Tamblyn, S Whitelam,

C Bellinger, and L M Ghiringhelli. Roadmap on Machine Learning in electronic structure. *Electronic Structure*, 4(2):023004, aug 2022.

[115] Michele Ceriotti, Cecilia Clementi, and O. Anatole von Lilienfeld. Introduction: Machine Learning at the atomic scale. *Chemical Reviews*, 121(16):9719–9721, Aug 2021.

[116] Edwin Bedolla, Luis Carlos Padierna, and Ramón Castañeda-Priego. Machine Learning for condensed matter physics. *Journal of Physics: Condensed Matter*, 33(5):053001, nov 2020.

[117] Anubhav Jain, Shyue Ping Ong, Geoffroy Hautier, Wei Chen, William Davidson Richards, Stephen Dacek, Shreyas Cholia, Dan Gunter, David Skinner, Gerbrand Ceder, and Kristin A. Persson. Commentary: The Materials Project: A materials genome approach to accelerating materials innovation. *APL Materials*, 1(1):011002, 2013.

[118] Stefano Curtarolo, Gus L. W. Hart, Marco Buongiorno Nardelli, Natalio Mingo, Stefano Sanvito, and Ohad Levy. The High-Throughput highway to computational materials design. *Nature Materials*, 12(3):191–201, Mar 2013.

[119] Stefano Curtarolo, Wahyu Setyawan, Gus L.W. Hart, Michal Jahnatek, Roman V. Chepulskii, Richard H. Taylor, Shidong Wang, Junkai Xue, Kesong Yang, Ohad Levy, Michael J. Mehl, Harold T. Stokes, Denis O. Demchenko, and Dane Morgan. *aflow*: An automatic framework for high-throughput materials discovery. *Computational Materials Science*, 58:218–226, 2012.

[120] Leopold Talirz, Snehal Kumbhar, Elsa Passaro, Aliaksandr V. Yakutovich, Valeria Granata, Fernando Gargiulo, Marco Borelli, Martin Uhrin, Sebastiaan P. Huber, Spyros Zoupanos, Carl S. Adorf, Casper Welzel Andersen, Ole Schütt, Carlo A. Pignedoli, Daniele Passerone, Joost VandeVondele, Thomas C. Schulthess, Berend Smit, Giovanni Pizzi, and Nicola Marzari. Materials Cloud, a platform for open computational science. *Scientific Data*, 7(1):299, Sep 2020.

[121] Mark D. Wilkinson, Michel Dumontier, IJsbrand Jan Aalbersberg, Gabrielle Appleton, Myles Axton, Arie Baak, Niklas Blomberg, Jan-Willem Boiten, Luiz Bonino da Silva Santos, Philip E. Bourne, Jildau Bouwman, Anthony J. Brookes, Tim Clark, Mercè Crosas, Ingrid Dillo, Olivier Dumon, Scott Edmunds, Chris T. Evelo, Richard Finkers, Alejandra Gonzalez-Beltran, Alasdair J.G. Gray, Paul Groth, Carole Goble, Jeffrey S. Grethe, Jaap Heringa, Peter A.C 't Hoen, Rob Hooft, Tobias Kuhn, Ruben Kok, Joost Kok, Scott J. Lusher, Maryann E. Martone, Albert Mons, Abel L. Packer, Bengt Persson, Philippe Rocca-Serra, Marco Roos, Rene van Schaik, Susanna-Assunta Sansone, Erik Schultes, Thierry Sengstag, Ted Slater, George Strawn, Morris A. Swertz, Mark Thompson, Johan van der Lei, Erik van Mulligen, Jan Velterop, Andra Waagmeester, Peter Wittenburg, Katherine Wolstencroft, Jun Zhao, and Barend Mons. The FAIR guiding principles for scientific data management and stewardship. *Scientific Data*, 3(1):160018, Mar 2016.

[122] Gregor von Laszewski, Mihael Hategan, and Deepti Kodeboyina. *Java CoG Kit Workflow*, pages 340–356. Springer London, London, 2007.

[123] Valerio Vitale, Giovanni Pizzi, Antimo Marrazzo, Jonathan R. Yates, Nicola Marzari, and Arash A. Mostofi. Automated High-Throughput Wannierisation. *npj Computational Materials*, 6(1):66, Jun 2020.

[124] Gianluca Prandini, Antimo Marrazzo, Ivano E. Castelli, Nicolas Mounet, and Nicola Marzari. Precision and efficiency in solid-state pseudopotential calculations. *npj Computational Materials*, 4(1):72, Dec 2018.

[125] Rocío Mercado, Rueih-Sheng Fu, Aliaksandr V. Yakutovich, Leopold Talirz, Maciej Haranczyk, and Berend Smit. In Silico Design of 2D and 3D covalent organic frameworks for methane storage applications. *Chemistry of Materials*, 30(15):5069–5086, Aug 2018.

[126] Leonid Kahle, Aris Marcolongo, and Nicola Marzari. High-Throughput computational screening for solid-state Li-ion conductors. *Energy Environ. Sci.*, 13:928–948, 2020.

[127] Nicolas Mounet, Marco Gibertini, Philippe Schwaller, Davide Campi, Andrius Merkys, Antimo Marrazzo, Thibault Sohier, Ivano Eligio Castelli, Andrea Cepellotti, Giovanni Pizzi, and Nicola Marzari. Two-Dimensional materials from high-throughput computational exfoliation of experimentally known compounds. *Nature Nanotechnology*, 13(3):246–252, Mar 2018.

[128] Michael O. Atambo, Daniele Varsano, Andrea Ferretti, S. Samaneh Ataei, Marilia J. Caldas, Elisa Molinari, and Annabella Selloni. Electronic and optical properties of doped TiO_2 by Many-Body Perturbation Theory. *Phys. Rev. Materials*, 3:045401, Apr 2019.

[129] Miki Bonacci, Matteo Zanfrognini, Elisa Molinari, Alice Ruini, Marilia J. Caldas, Andrea Ferretti, and Daniele Varsano. Excitonic effects in graphene-like C_3N. *Phys. Rev. Mater.*, 6:034009, Mar 2022.

[130] Feliciano Giustino, Marvin L. Cohen, and Steven G. Louie. GW method with the self-consistent Sternheimer equation. *Phys. Rev. B*, 81:115105, Mar 2010.

[131] P. Umari, Geoffrey Stenuit, and Stefano Baroni. Optimal representation of the polarization propagator for large-scale GW calculations. *Phys. Rev. B*, 79:201104, May 2009.

[132] Fabien Bruneval and Xavier Gonze. Accurate GW self-energies in a plane-wave basis using only a few empty states: Towards large systems. *Phys. Rev. B*, 78:085125, Aug 2008.

[133] J. A. Berger, Lucia Reining, and Francesco Sottile. Efficient GW calculations for SnOThe effective-energy technique. *Phys. Rev. B*, 85:085126, Feb 2012.

[134] Jack Deslippe, Georgy Samsonidze, Manish Jain, Marvin L. Cohen, and Steven G. Louie. Coulomb-hole summations and energies for GW calculations with limited number of empty orbitals: A modified static remainder approach. *Phys. Rev. B*, 87:165124, Apr 2013.

[135] Weiwei Gao, Weiyi Xia, Xiang Gao, and Peihong Zhang. Speeding up GW calculations to meet the challenge of large scale quasiparticle predictions. *Scientific Reports*, 6(1):36849, Nov 2016.

[136] Dario Rocca, Ralph Gebauer, Yousef Saad, and Stefano Baroni. Turbo charging time-dependent density-functional theory with Lanczos chains. *The Journal of Chemical Physics*, 128(15):154105, 2008.

[137] Sten Haastrup, Mikkel Strange, Mohnish Pandey, Thorsten Deilmann, Per S Schmidt, Nicki F Hinsche, Morten N Gjerding, Daniele Torelli, Peter M Larsen, Anders C Riis-Jensen, Jakob Gath, Karsten W Jacobsen, Jens Jørgen Mortensen, Thomas Olsen, and Kristian S Thygesen. The Computational 2D Materials Database: High-Throughput modeling and discovery of atomically thin crystals. *2D Materials*, 5(4):042002, sep 2018.

[138] AiiDA Quantum Espresso plugin. `https://github.com/aiidateam/aiida-quantumespresso`. Accessed: 2023-01-21.

[139] AiiDA Yambo plugin. `https://github.com/yambo-code/aiida-yambo`. Accessed: 2023-01-21.

[140] AiiDA Abinit plugin. `https://github.com/sponce24/aiida-abinit`. Accessed: 2023-01-21.

[141] AiiDA VASP plugin. `https://aiida-vasp.readthedocs.io/en/latest/`. Accessed: 2023-01-21.

[142] Murilo L. Tiago, Sohrab Ismail-Beigi, and Steven G. Louie. Effect of semicore orbitals on the electronic band gaps of Si, Ge, and GaAs within the GW approximation. *Phys. Rev. B*, 69:125212, Mar 2004.

[143] Bi-Ching Shih, Yu Xue, Peihong Zhang, Marvin L. Cohen, and Steven G. Louie. Quasiparticle band gap of ZnO: High accuracy from the conventional G0W0 approach. *Phys. Rev. Lett.*, 105:146401, Sep 2010.

[144] Zeynep Ergönenc, Bongjae Kim, Peitao Liu, Georg Kresse, and Cesare Franchini. Converged GW quasiparticle energies for transition metal oxide perovskites. *Phys. Rev. Materials*, 2:024601, Feb 2018.

[145] Gabriel Lopez-Candales, Zhao Tang, Weiyi Xia, Fanhao Jia, and Peihong Zhang. Quasiparticle band structure of $SrTiO_3$ and $BaTiO_3$: A combined LDA+U and G0W0 approach. *Phys. Rev. B*, 103:035128, Jan 2021.

[146] Weiwei Gao, Weiyi Xia, Yabei Wu, Wei Ren, Xiang Gao, and Peihong Zhang. Quasiparticle band structures of CuCl, CuBr, AgCl, and AgBr: The extreme case. *Phys. Rev. B*, 98:045108, Jul 2018.

[147] A. Fleszar and W. Hanke. Spectral properties of quasiparticles in a semiconductor. *Phys. Rev. B*, 56:10228–10232, Oct 1997.

[148] Min-Ye Zhang and Hong Jiang. Electronic band structure of cuprous and silver halides: An all-electron GW study. *Phys. Rev. B*, 100:205123, Nov 2019.

[149] Christoph Friedrich, Mathias C. Müller, and Stefan Blügel. Band convergence and linearization error correction of all-electron GW calculations: The extreme case of zinc oxide. *Phys. Rev. B*, 83:081101, Feb 2011.

[150] Fabien Bruneval. Ionization energy of atoms obtained from GW self-energy or from Random Phase Approximation total energies. *The Journal of Chemical Physics*, 136(19):194107, 2012.

[151] Fabien Bruneval and Miguel A. L. Marques. Benchmarking the starting points of the GW approximation for molecules. *Journal of Chemical Theory and Computation*, 9(1):324–329, Jan 2013.

[152] M. Stankovski, G. Antonius, D. Waroquiers, A. Miglio, H. Dixit, K. Sankaran, M. Giantomassi, X. Gonze, M. Côté, and G.-M. Rignanese. G0W0 band gap of ZnO: Effects of plasmon-pole models. *Phys. Rev. B*, 84:241201, Dec 2011.

[153] Gijae Kang, Youngho Kang, and Seungwu Han. Influence of wave-function updates in GW calculations on titanates. *Phys. Rev. B*, 91:155141, Apr 2015.

[154] Minjung Kim, Glenn J. Martyna, and Sohrab Ismail-Beigi. Complex-time shredded propagator method for large-scale GW calculations. *Phys. Rev. B*, 101:035139, Jan 2020.

[155] Marco Govoni and Giulia Galli. Large Scale GW calculations. *Journal of Chemical Theory and Computation*, 11(6):2680–2696, Jun 2015.

[156] Ivan Duchemin and Xavier Blase. Cubic-Scaling all-electron GW calculations with a separable density-fitting space–time approach. *Journal of Chemical Theory and Computation*, 17(4):2383–2393, Apr 2021.

[157] Jan Wilhelm, Dorothea Golze, Leopold Talirz, Jürg Hutter, and Carlo A. Pignedoli. Toward GW calculations on thousands of atoms. *The Journal of Physical Chemistry Letters*, 9(2):306–312, Jan 2018.

[158] Arno Förster and Lucas Visscher. Low-Order scaling G0W0 by pair atomic density fitting. *Journal of Chemical Theory and Computation*, 16(12):7381–7399, Dec 2020.

[159] Jiangang He and Cesare Franchini. Structural determination and electronic properties of the $4d$ perovskite $SrPdO_3$. *Phys. Rev. B*, 89:045104, Jan 2014.

[160] Siheon Ryee, Seung Woo Jang, Hiori Kino, Takao Kotani, and Myung Joon Han. Quasiparticle self-consistent GW calculation of Sr_2RuO_4 and $SrRuO_3$. *Phys. Rev. B*, 93:075125, Feb 2016.

[161] C Franchini, R Ková čik, M Marsman, S Sathyanarayana Murthy, J He, C Ederer, and G Kresse. Maximally localized Wannier functions in $LaMnO_3$within PBE +U, hybrid functionals and partially self-consistent GW: an efficient route to construct ab initio tight-binding parameters for e_g perovskites. *Journal of Physics: Condensed Matter*, 24(23):235602, may 2012.

[162] Gabriel Lopez-Candales, Zhao Tang, Greis J. Cruz, Weiyi Xia, Fanhao Jia, and Peihong Zhang. Quasiparticle band structures of the 4d perovskite oxides $SrZrO_3$ and $BaZrO_3$. *Phys. Rev. B*, 104:195129, Nov 2021.

[163] Chia-Nan Yeh, Sergei Iskakov, Dominika Zgid, and Emanuel Gull. Electron correlations in the cubic paramagnetic perovskite $Sr(V,Mn)O_3$: Results from fully self-consistent self-energy embedding calculations. *Phys. Rev. B*, 103:195149, May 2021.

[164] Peitao Liu, Bongjae Kim, Xing-Qiu Chen, D. D. Sarma, Georg Kresse, and Cesare Franchini. Relativistic GW+BSE study of the optical properties of Ruddlesden-Popper iridates. *Phys. Rev. Materials*, 2:075003, Jul 2018.

[165] Yoshiro Nohara, Susumu Yamamoto, and Takeo Fujiwara. Electronic structure of perovskite-type transition metal oxides $LaMO_3$ ($M = Ti \sim Cu$) by U + GW approximation. *Phys. Rev. B*, 79:195110, May 2009.

[166] Jack Deslippe, Georgy Samsonidze, Manish Jain, Marvin L. Cohen, and Steven G. Louie. Coulomb-hole summations and energies for GW calculations with limited number of empty orbitals: A modified static remainder approach. *Phys. Rev. B*, 87:165124, Apr 2013.

[167] Rick A. Kendall, Thom H. Dunning, and Robert J. Harrison. Electron affinities of the first row atoms revisited. systematic basis sets and wave functions. *The Journal of Chemical Physics*, 96(9):6796–6806, 1992.

[168] Wim Klopper, Keld L Bak, Poul Jørgensen, Jeppe Olsen, and Trygve Helgaker. Highly accurate calculations of molecular electronic structure. *Journal of Physics B: Atomic, Molecular and Optical Physics*, 32(13):R103, jul 1999.

[169] Werner Kutzelnigg and John D. Morgan. Rates of convergence of the partial wave expansions of atomic correlation energies. *The Journal of Chemical Physics*, 96(6):4484–4508, 1992.

[170] Xinguo Ren, Patrick Rinke, Christian Joas, and Matthias Scheffler. Random-Phase Approximation and its applications in computational chemistry and materials science. *Journal of Materials Science*, 47(21):7447–7471, Nov 2012.

[171] Andris Gulans. Towards numerically accurate Many-Body Perturbation Theory: Short-range correlation effects. *The Journal of Chemical Physics*, 141(16):164127, 2014.

[172] Wei Kang and Mark S. Hybertsen. Quasiparticle and optical properties of rutile and anatase TiO_2. *Phys. Rev. B*, 82:085203, Aug 2010.

[173] Christoph Friedrich, Stefan Blügel, and Arno Schindlmayr. Efficient implementation of the GW approximation within the all-electron FLAPW method. *Phys. Rev. B*, 81:125102, Mar 2010.

[174] Marco Govoni and Giulia Galli. GW100: Comparison of methods and accuracy of results obtained with the WEST code. *Journal of Chemical Theory and Computation*, 14(4):1895–1909, Apr 2018.

[175] Xinguo Ren, Patrick Rinke, Volker Blum, Jürgen Wieferink, Alexandre Tkatchenko, Andrea Sanfilippo, Karsten Reuter, and Matthias Scheffler. Resolution-of-identity approach to Hartree–Fock, hybrid density functionals, RPA, MP2 and GW with numeric atom-centered orbital basis functions. *New Journal of Physics*, 14(5):053020, may 2012.

[176] M. Gajdoš, K. Hummer, G. Kresse, J. Furthmüller, and F. Bechstedt. Linear optical properties in the projector-augmented wave methodology. *Phys. Rev. B*, 73:045112, Jan 2006.

[177] R. von Helmolt, J. Wecker, B. Holzapfel, L. Schultz, and K. Samwer. Giant negative magnetoresistance in perovskite like $La_{2/3}Ba_{1/3}MnO_x$ ferromagnetic films. *Phys. Rev. Lett.*, 71:2331–2333, Oct 1993.

[178] Myron B. Salamon and Marcelo Jaime. The physics of manganites: Structure and transport. *Rev. Mod. Phys.*, 73:583–628, Aug 2001.

[179] K.F. Wang, J.-M. Liu, and Z.F. Ren. Multiferroicity: the coupling between magnetic and polarization orders. *Advances in Physics*, 58(4):321–448, 2009.

[180] Masatoshi Imada, Atsushi Fujimori, and Yoshinori Tokura. Metal-insulator transitions. *Rev. Mod. Phys.*, 70:1039–1263, Oct 1998.

[181] J. G. Bednorz and K. A. Müller. Possible high T_c superconductivity in the Ba-La-Cu-O system. *Zeitschrift für Physik B Condensed Matter*, 64(2):189–193, Jun 1986.

[182] Yoshinori Tokura. Correlated-Electron Physics in Transition-Metal Oxides. *Physics Today*, 56(7):50–55, 2003.

[183] C. N. R. Rao. Charge, Spin, and Orbital Ordering in the Perovskite Manganates, $Ln_{1-x}A_xMnO_3$ (Ln = Rare Earth, A = Ca or Sr). *The Journal of Physical Chemistry B*, 104(25):5877–5889, Jun 2000.

[184] William Witczak-Krempa, Gang Chen, Yong Baek Kim, and Leon Balents. Correlated Quantum Phenomena in the Strong Spin-Orbit Regime. *Annual Review of Condensed Matter Physics*, 5(1):57–82, 2014.

[185] Cyril Martins, Markus Aichhorn, and Silke Biermann. Coulomb correlations in 4d and 5d oxides from first principles—or how spin–orbit materials choose their effective orbital degeneracies. *Journal of physics / Condensed matter*, 29:263001, 2017.

[186] Peitao Liu, Jiangang He, Bongjae Kim, Sergii Khmelevskyi, Alessandro Toschi, Georg Kresse, and Cesare Franchini. Comparative ab initio study of the structural, electronic, magnetic, and dynamical properties of $LiOsO_3$ and $NaOsO_3$. *Phys. Rev. Materials*, 4:045001, Apr 2020.

[187] Peitao Liu and Cesare Franchini. Advanced first-principle modeling of relativistic Ruddlesden—Popper strontium iridates. *Applied Sciences*, 11(6), 2021.

[188] Lorenzo Sponza, Valérie Véniard, Francesco Sottile, Christine Giorgetti, and Lucia Reining. Role of localized electrons in electron-hole interaction: The case of $SrTiO_3$. *Phys. Rev. B*, 87:235102, Jun 2013.

[189] Vijaya Begum, Markus Ernst Gruner, and Rossitza Pentcheva. Role of the exchange-correlation functional on the structural, electronic, and optical properties of cubic and tetragonal $SrTiO_3$including many-body effects. *Phys. Rev. Materials*, 3:065004, Jun 2019.

[190] Christopher Lane and Jian-Xin Zhu. Landscape of coexisting excitonic states in the insulating single-layer cuprates and nickelates. *Phys. Rev. B*, 101:155135, Apr 2020.

[191] Jiangang He and Cesare Franchini. Screened hybrid functional applied to $3d^0 \rightarrow 3d^8$ transition-metal perovskites $LaMO_3$ (M = Sc-Cu): Influence of the exchange mixing parameter on the structural, electronic, and magnetic properties. *Phys. Rev. B*, 86:235117, Dec 2012.

[192] Lars Hedin. New Method for Calculating the One-particle Green's Function with Application to the Electron-Gas Problem. *Phys. Rev.*, 139:A796–A823, Aug 1965.

[193] G. Strinati, H. J. Mattausch, and W. Hanke. Dynamical aspects of correlation corrections in a covalent crystal. *Phys. Rev. B*, 25:2867–2888, Feb 1982.

[194] Mark S. Hybertsen and Steven G. Louie. First-Principles Theory of Quasiparticles: Calculation of Band Gaps in Semiconductors and Insulators. *Phys. Rev. Lett.*, 55:1418–1421, Sep 1985.

[195] Stephan Lany. Band-structure calculations for the $3d$ transition metal oxides in GW. *Phys. Rev. B*, 87:085112, Feb 2013.

[196] S. L. Dudarev, G. A. Botton, S. Y. Savrasov, C. J. Humphreys, and A. P. Sutton. Electron-energy-loss spectra and the structural stability of nickel oxide: An LSDA+U study. *Phys. Rev. B*, 57:1505–1509, Jan 1998.

[197] Soner Steiner, Sergii Khmelevskyi, Martijn Marsmann, and Georg Kresse. Calculation of the magnetic anisotropy with projected-augmented-wave methodology and the case study of disordered $Fe_{1-x}Co_x$ alloys. *Phys. Rev. B*, 93:224425, Jun 2016.

[198] Lorin X. Benedict and Eric L. Shirley. Ab initio calculation of $\epsilon_2(\omega)$ including the electron-hole interaction: Application to GaN and CaF_2. *Phys. Rev. B*, 59:5441–5451, Feb 1999.

[199] Stefan Albrecht, Lucia Reining, Giovanni Onida, Valerio Olevano, and Rodolfo Del Sole. Albrecht et al. Reply:. *Phys. Rev. Lett.*, 83:3971–3971, Nov 1999.

[200] David Kammerlander, Silvana Botti, Miguel A. L Marques, Andrea Marini, and Claudio Attaccalite. Speeding up the solution of the Bethe-Salpeter equation by a double-grid method and Wannier interpolation. *Phys. Rev. B*, 86:125203, Sep 2012.

[201] F. Fuchs, C. Rödl, A. Schleife, and F. Bechstedt. Efficient $\mathcal{O}(N^2)$ approach to solve the Bethe-Salpeter equation for excitonic bound states. *Phys. Rev. B*, 78:085103, Aug 2008.

[202] Michael Rohlfing and Steven G. Louie. Electron-hole excitations and optical spectra from first principles. *Phys. Rev. B*, 62:4927–4944, Aug 2000.

[203] Ignacio M. Alliati, Davide Sangalli, and Myrta Grüning. Double k-grid method for solving the Bethe-Salpeter equation via Lanczos approaches. *Frontiers in Chemistry*, 9, 2022.

[204] Dario Rocca, Yuan Ping, Ralph Gebauer, and Giulia Galli. Solution of the Bethe-Salpeter equation without empty electronic states: Application to the absorption spectra of bulk systems. *Phys. Rev. B*, 85:045116, Jan 2012.

[205] Menno Bokdam, Tobias Sander, Alessandro Stroppa, Silvia Picozzi, D. D. Sarma, Cesare Franchini, and Georg Kresse. Role of Polar Phonons in the Photo Excited State of Metal Halide Perovskites. *Scientific Reports*, 6:28618, Jun 2016.

[206] S. M. Dancoff. Non-Adiabatic Meson Theory of Nuclear Forces. *Phys. Rev.*, 78:382–385, May 1950.

[207] P. H. Hahn, K. Seino, W. G. Schmidt, J. Furthmüller, and F. Bechstedt. Quasiparticle and excitonic effects in the optical spectra of diamond, SiC, Si, GaP, GaAs, InP, and AlN. *physica status solidi (b)*, 242(13):2720–2728, Nov 2005.

[208] Lyudmyla Adamska and Paolo Umari. Bethe-Salpeter equation approach with electron-phonon coupling for exciton binding energies. *Phys. Rev. B*, 103:075201, Feb 2021.

[209] Robert Laskowski, Niels Egede Christensen, Gilles Santi, and Claudia Ambrosch-Draxl. Ab Initio calculations of excitons in GaN. *Phys. Rev. B*, 72:035204, Jul 2005.

[210] Irene Aguilera, Julien Vidal, Perla Wahnón, Lucia Reining, and Silvana Botti. First-principles study of the band structure and optical absorption of $CuGaS_2$. *Phys. Rev. B*, 84:085145, Aug 2011.

[211] Francesco Sottile. *Response functions of semiconductors and insulators : from the Bethe-Salpeter equation to time-dependent density functional theory*. Theses, Ecole Polytechnique X, September 2003.

[212] Alejandro Molina-Sánchez, Davide Sangalli, Kerstin Hummer, Andrea Marini, and Ludger Wirtz. Effect of spin-orbit interaction on the optical spectra of single-layer, double-layer, and bulk MoS_2. *Phys. Rev. B*, 88:045412, Jul 2013.

[213] Alexey Tal, Peitao Liu, Georg Kresse, and Alfredo Pasquarello. Accurate optical spectra through time-dependent density functional theory based on screening-dependent hybrid functionals. *Phys. Rev. Research*, 2:032019, Jul 2020.

[214] Zeeshan Muhammad, Peitao Liu, Rashid Ahmad, Saeid Jalali Asadabadi, Cesare Franchini, and Iftikhar Ahmad. Tunable relativistic quasiparticle electronic and excitonic behavior of the $FAPb(I_{1-x}Br_x)_3$ alloy. *Phys. Chem. Chem. Phys.*, 22:11943–11955, 2020.

[215] T. Arima, Y. Tokura, and J. B. Torrance. Variation of optical gaps in perovskite-type 3d transition-metal oxides. *Phys. Rev. B*, 48:17006–17009, Dec 1993.

[216] Shigeki Miyasaka, Yoichi Okimoto, and Yoshinori Tokura. Anisotropy of Mott–Hubbard Gap Transitions due to Spin and Orbital Ordering in $LaVO_3$ and YVO_3. *Journal of the Physical Society of Japan*, 71(9):2086–2089, 2002.

[217] D. J. Lovinger, M. Brahlek, P. Kissin, D. M. Kennes, A. J. Millis, R. Engel-Herbert, and R. D. Averitt. Influence of spin and orbital fluctuations on Mott-Hubbard exciton dynamics in $LaVO_3$ thin films. *Phys. Rev. B*, 102:115143, Sep 2020.

[218] Minjae Kim. Signatures of spin-orbital states of t_{2g}^2 system in optical conductivity: RVO_3 (R=Y and La). *Phys. Rev. B*, 97:155141, Apr 2018.

[219] J. Reul, A. A. Nugroho, T. T. M. Palstra, and M. Grüninger. Probing orbital fluctuations in RVO_3 (R=Y, Gd, or Ce) by ellipsometry. *Phys. Rev. B*, 86:125128, Sep 2012.

[220] Julien Varignon, Manuel Bibes, and Alex Zunger. Origin of band gaps in 3d perovskite oxides. *Nature Communications*, 10(1):1658, Apr 2019.

[221] Bongjae Kim, Peitao Liu, Jan M. Tomczak, and Cesare Franchini. Strain-induced tuning of the electronic Coulomb interaction in $3d$ transition metal oxide perovskites. *Phys. Rev. B*, 98:075130, Aug 2018.

[222] Claudia Rödl and Friedhelm Bechstedt. Optical and energy-loss spectra of the antiferromagnetic transition metal oxides MnO, FeO, CoO, and NiO including quasiparticle and excitonic effects. *Phys. Rev. B*, 86:235122, Dec 2012.

[223] Bechstedt Friedhelm. *Many-Body Approach to Electronic Excitations : Concepts and Applications.* Springer Series in Solid-State Sciences. Springer, Berlin, Heidelberg, 2015.

[224] Zhongqin Yang, Zhong Huang, Ling Ye, and Xide Xie. Influence of parameters u and j in the LSDA+U method on electronic structure of the perovskites $LaMO_3(M = Cr, Mn, Fe, Co, Ni)$. *Phys. Rev. B*, 60:15674–15682, Dec 1999.

[225] I. Lo Vecchio, A. Perucchi, P. Di Pietro, O. Limaj, U. Schade, Y. Sun, M. Arai, K. Yamaura, and S. Lupi. Infrared evidence of a slater metal-insulator transition in $NaOsO_3$. *Scientific Reports*, 3(1):2990, Oct 2013.

[226] J. H. Jung, Z. Fang, J. P. He, Y. Kaneko, Y. Okimoto, and Y. Tokura. Change of Electronic Structure in Ca_2RuO_4 induced by Orbital Ordering. *Phys. Rev. Lett.*, 91:056403, Jul 2003.

[227] D. Sutter, C. G. Fatuzzo, S. Moser, M. Kim, R. Fittipaldi, A. Vecchione, V. Granata, Y. Sassa, F. Cossalter, G. Gatti, M. Grioni, H. M. Rønnow, N. C. Plumb, C. E. Matt, M. Shi, M. Hoesch, T. K. Kim, T.-R. Chang, H.-T. Jeng, C. Jozwiak, A. Bostwick, E. Rotenberg, A. Georges, T. Neupert, and J. Chang. Hallmarks of Hunds coupling in the Mott insulator Ca_2RuO_4. *Nature Communications*, 8(1):15176, May 2017.

[228] T. Mizokawa, L. H. Tjeng, G. A. Sawatzky, G. Ghiringhelli, O. Tjernberg, N. B. Brookes, H. Fukazawa, S. Nakatsuji, and Y. Maeno. Spin-orbit coupling in the mott insulator Ca_2RuO_4. *Phys. Rev. Lett.*, 87:077202, Jul 2001.

[229] C. G. Fatuzzo, M. Dantz, S. Fatale, P. Olalde-Velasco, N. E. Shaik, B. Dalla Piazza, S. Toth, J. Pelliciari, R. Fittipaldi, A. Vecchione, N. Kikugawa, J. S. Brooks, H. M. Rønnow, M. Grioni, Ch. Rüegg, T. Schmitt, and J. Chang. Spin-orbit-induced orbital excitations in Sr_2RuO_4 and Ca_2RuO_4: A resonant inelastic x-ray scattering study. *Phys. Rev. B*, 91:155104, Apr 2015.

[230] E. Gorelov, M. Karolak, T. O. Wehling, F. Lechermann, A. I. Lichtenstein, and E. Pavarini. Nature of the Mott Transition in Ca_2RuO_4. *Phys. Rev. Lett.*, 104:226401, Jun 2010.

[231] Guoren Zhang and Eva Pavarini. Mott transition, spin-orbit effects, and magnetism in Ca_2RuO_4. *Phys. Rev. B*, 95:075145, Feb 2017.

[232] Guoren Zhang and Eva Pavarini. Higgs mode and stability of xy-orbital ordering in Ca_2RuO_4. *Phys. Rev. B*, 101:205128, May 2020.

[233] Guo-Qiang Liu. Competition between spin-orbit coupling and magnetic exchange splitting in Ca_2RuO_4. *Phys. Rev. B*, 88:104428, Sep 2013.

[234] Takashi Hotta and Elbio Dagotto. Prediction of Orbital Ordering in Single-Layered Ruthenates. *Phys. Rev. Lett.*, 88:017201, Dec 2001.

[235] Zhong Fang, Naoto Nagaosa, and Kiyoyuki Terakura. Orbital-dependent phase control in $Ca_{2-x}Sr_xRuO_4$ ($0 \leq x \leq 0.5$). *Phys. Rev. B*, 69:045116, Jan 2004.

[236] Hartmut Haug and Stephan W Koch. *Quantum Theory of the Optical and Electronic Properties of Semiconductors*. WORLD SCIENTIFIC, 5th edition, 2009.

[237] Diana Y. Qiu, Felipe H. da Jornada, and Steven G. Louie. Optical spectrum of MoS_2: Many-Body effects and diversity of exciton states. *Phys. Rev. Lett.*, 111:216805, Nov 2013.

[238] Lorenzo Sponza, Hakim Amara, Claudio Attaccalite, Sylvain Latil, Thomas Galvani, Fulvio Paleari, Ludger Wirtz, and Fran çois Ducastelle. Direct and indirect excitons in boron nitride polymorphs: A story of atomic configuration and electronic correlation. *Phys. Rev. B*, 98:125206, Sep 2018.

[239] Diana Y. Qiu, Felipe H. da Jornada, and Steven G. Louie. Screening and Many-Body effects in two-dimensional crystals: Monolayer MoS_2. *Phys. Rev. B*, 93:235435, Jun 2016.

[240] Giorgia Fugallo, Pierluigi Cudazzo, Matteo Gatti, and Francesco Sottile. Exciton band structure of molybdenum disulfide: from monolayer to bulk. *Electronic Structure*, 3(1):014005, apr 2021.

[241] C. E. Ekuma. Optical absorption in monolayer SnO_2. *Phys. Rev. B*, 99:075421, Feb 2019.

[242] Pierluigi Cudazzo, Lorenzo Sponza, Christine Giorgetti, Lucia Reining, Francesco Sottile, and Matteo Gatti. Exciton band structure in Two-Dimensional materials. *Phys. Rev. Lett.*, 116:066803, Feb 2016.

[243] Gang Wang, Alexey Chernikov, Mikhail M. Glazov, Tony F. Heinz, Xavier Marie, Thierry Amand, and Bernhard Urbaszek. Colloquium: Excitons in atomically thin transition metal dichalcogenides. *Rev. Mod. Phys.*, 90:021001, Apr 2018.

[244] Falco Hüser, Thomas Olsen, and Kristian S. Thygesen. How dielectric screening in two-dimensional crystals affects the convergence of excited-state calculations: Monolayer MoS_2. *Phys. Rev. B*, 88:245309, Dec 2013.

[245] Alexey Chernikov, Timothy C. Berkelbach, Heather M. Hill, Albert Rigosi, Yilei Li, Burak Aslan, David R. Reichman, Mark S. Hybertsen, and Tony F. Heinz. Exciton binding energy and nonhydrogenic Rydberg series in Monolayer WS_2. *Phys. Rev. Lett.*, 113:076802, Aug 2014.

[246] Lu Han, Yanhan Fang, Yunqi Zhao, Yipeng Zang, Zhengbin Gu, Yuefeng Nie, and Xiao-qing Pan. Giant uniaxial strain ferroelectric domain tuning in Freestanding PbTiO$_3$ films. *Advanced Materials Interfaces*, 7(7):1901604, 2020.

[247] Lucia Reining. The GW approximation: content, successes and limitations. *WIREs Computational Molecular Science*, 8(3):e1344, 2018.

[248] Martin Schlipf and François Gygi. Optimization algorithm for the generation of ONCV pseudopotentials. *Computer Physics Communications*, 196:36–44, 2015.

[249] A. Miglio, D. Waroquiers, G. Antonius, M. Giantomassi, M. Stankovski, M. Côté, X. Gonze, and G.-M. Rignanese. Effects of plasmon pole models on the G0W0 electronic structure of various oxides. *The European Physical Journal B*, 85(9):322, Sep 2012.

[250] Hong Pan, Yongjia Zhang, Hui Jia, Ensi Cao, and Zhi Yang. Electronic structures, stabilities, and magnetism of SrTiO$_3$ Monolayer and Ultrathin Nanotubes. *Journal of Superconductivity and Novel Magnetism*, 34(8):2093–2104, Aug 2021.

[251] Xiang-Bo Xiao and Bang-Gui Liu. Freestanding perovskite oxide monolayers as two-dimensional semiconductors. *Nanotechnology*, 32(14):145705, jan 2021.

[252] Kris Delaney, P. García-González, Angel Rubio, Patrick Rinke, and R. W. Godby. Comment on "band-gap problem in semiconductors revisited: Effects of core states and Many-Body Self-Consistency". *Phys. Rev. Lett.*, 93:249701, Dec 2004.

[253] Jiří Klimeš and Georg Kresse. Kohn-Sham band gaps and potentials of solids from the optimised effective potential method within the Random Phase Approximation. *The Journal of Chemical Physics*, 140(5):054516, 2014.

[254] Pierluigi Cudazzo, Ilya V. Tokatly, and Angel Rubio. Dielectric screening in two-dimensional insulators: Implications for excitonic and impurity states in graphane. *Phys. Rev. B*, 84:085406, Aug 2011.

[255] Hongyu Yu, Magdalena Laurien, Zhenpeng Hu, and Oleg Rubel. Exploration of the bright and dark exciton landscape and fine structure of MoS$_2$ using G$_0$W$_0$-BSE. *Phys. Rev. B*, 100:125413, Sep 2019.

[256] Gabriel Antonius, Diana Y. Qiu, and Steven G. Louie. Orbital Symmetry and the optical response of Single-Layer MX Monochalcogenides. *Nano Letters*, 18(3):1925–1929, Mar 2018.

[257] Diana Y. Qiu, Ting Cao, and Steven G. Louie. Nonanalyticity, valley quantum phases, and lightlike exciton dispersion in Monolayer Transition Metal Dichalcogenides: Theory and First-Principles calculations. *Phys. Rev. Lett.*, 115:176801, Oct 2015.

[258] Chwanchin Wang and Timothy Hughbanks. Main group element size and substitution effects on the structural dimensionality of Zirconium Tellurides of the ZrSiS type. *Inorganic Chemistry*, 34(22):5524–5529, Oct 1995.

[259] Sebastian Klemenz, Shiming Lei, and Leslie M. Schoop. Topological semimetals in square-net materials. *Annual Review of Materials Research*, 49(1):185–206, 2019.

[260] J. Ebad-Allah, J. Fernández Afonso, M. Krottenmüller, J. Hu, Y. L. Zhu, Z. Q. Mao, J. Kuneš, and C. A. Kuntscher. Chemical pressure effect on the optical conductivity of the nodal-line semimetals ZrSiY(Y=S,Se,Te) and ZrGeY(Y=S,Te). *Phys. Rev. B*, 99:125154, Mar 2019.

[261] Artem V. Pronin and Martin Dressel. Nodal semimetals: A survey on optical conductivity. *physica status solidi (b)*, 258(1):2000027, 2021.

[262] S. Pezzini, M. R. van Delft, L. M. Schoop, B. V. Lotsch, A. Carrington, M. I. Katsnelson, N. E. Hussey, and S. Wiedmann. Unconventional mass enhancement around the Dirac nodal loop in ZrSiS. *Nature Physics*, 14(2):178–183, Feb 2018.

[263] Andreas Topp, Judith M Lippmann, Andrei Varykhalov, Viola Duppel, Bettina V Lotsch, Christian R Ast, and Leslie M Schoop. Non-symmorphic band degeneracy at the Fermi level in ZrSiTe. *New Journal of Physics*, 18(12):125014, dec 2016.

[264] F. C. Chen, Y. Fei, S. J. Li, Q. Wang, X. Luo, J. Yan, W. J. Lu, P. Tong, W. H. Song, X. B. Zhu, L. Zhang, H. B. Zhou, F. W. Zheng, P. Zhang, A. L. Lichtenstein, M. I. Katsnelson, Y. Yin, Ning Hao, and Y. P. Sun. Temperature-induced Lsifshitz transition and possible excitonic instability in ZrSiSe. *Phys. Rev. Lett.*, 124:236601, Jun 2020.

[265] Jin Hu, Zhijie Tang, Jinyu Liu, Xue Liu, Yanglin Zhu, David Graf, Kevin Myhro, Son Tran, Chun Ning Lau, Jiang Wei, and Zhiqiang Mao. Evidence of topological nodal-line fermions in ZrSiSe and ZrSiTe. *Phys. Rev. Lett.*, 117:016602, Jun 2016.

[266] M. Mofazzel Hosen, Klauss Dimitri, Ilya Belopolski, Pablo Maldonado, Raman Sankar, Nagendra Dhakal, Gyanendra Dhakal, Taiason Cole, Peter M. Oppeneer, Dariusz Kaczorowski, Fangcheng Chou, M. Zahid Hasan, Tomasz Durakiewicz, and Madhab Neupane. Tunability of the topological nodal-line semimetal phase in ZrSix-type materials ($x =$ S, Se, Te). *Phys. Rev. B*, 95:161101, Apr 2017.

[267] M. B. Schilling, L. M. Schoop, B. V. Lotsch, M. Dressel, and A. V. Pronin. Flat optical conductivity in ZrSiS due to Two-Dimensional Dirac bands. *Phys. Rev. Lett.*, 119:187401, Nov 2017.

[268] Madhab Neupane, Ilya Belopolski, M. Mofazzel Hosen, Daniel S. Sanchez, Raman Sankar, Maria Szlawska, Su-Yang Xu, Klauss Dimitri, Nagendra Dhakal, Pablo Maldonado, Peter M. Oppeneer, Dariusz Kaczorowski, Fangcheng Chou, M. Zahid Hasan, and Tomasz

Durakiewicz. Observation of topological nodal fermion semimetal phase in ZrSiS. *Phys. Rev. B*, 93:201104, May 2016.

[269] Yang-Yang Lv, Bin-Bin Zhang, Xiao Li, Shu-Hua Yao, Y. B. Chen, Jian Zhou, Shan-Tao Zhang, Ming-Hui Lu, and Yan-Feng Chen. Extremely large and significantly anisotropic magnetoresistance in ZrSiS single crystals. *Applied Physics Letters*, 108(24):244101, 2016.

[270] Junran Zhang, Ming Gao, Jinglei Zhang, Xuefeng Wang, Xiaoqian Zhang, Minhao Zhang, Wei Niu, Rong Zhang, and Yongbing Xu. Transport evidence of 3d topological nodal-line semimetal phase in ZrSiS. *Frontiers of Physics*, 13(1):137201, Jul 2017.

[271] Mazhar N. Ali, Leslie M. Schoop, Chirag Garg, Judith M. Lippmann, Erik Lara, Bettina Lotsch, and Stuart S. P. Parkin. Butterfly magnetoresistance, quasi-2D Dirac Fermi surface and topological phase transition in ZrSiS. *Science Advances*, 2(12):e1601742, 2016.

[272] Marcin Matusiak, J. R. Cooper, and Dariusz Kaczorowski. Thermoelectric quantum oscillations in ZrSiS. *Nature Communications*, 8(1):15219, May 2017.

[273] Weiqing Zhou, Alexander N. Rudenko, and Shengjun Yuan. Effect of mechanical strain on the optical properties of Nodal-Line semimetal ZrSiS. *Advanced Electronic Materials*, 6(1):1900860, 2020.

[274] Kent R. Shirer, Kimberly A. Modic, Tino Zimmerling, Maja D. Bachmann, Markus König, Philip J. W. Moll, Leslie Schoop, and Andrew P. Mackenzie. Out-of-plane transport in ZrSiS and ZrSiSe microstructures. *APL Materials*, 7(10):101116, 2019.

[275] Tetsuro Habe and Mikito Koshino. Dynamical conductivity in the topological nodal-line semimetal ZrSiS. *Phys. Rev. B*, 98:125201, Sep 2018.

[276] A. N. Rudenko, E. A. Stepanov, A. I. Lichtenstein, and M. I. Katsnelson. Excitonic instability and pseudogap formation in Nodal Line Semimetal ZrSiS. *Phys. Rev. Lett.*, 120:216401, May 2018.

[277] M. M. Scherer, C. Honerkamp, A. N. Rudenko, E. A. Stepanov, A. I. Lichtenstein, and M. I. Katsnelson. Excitonic instability and unconventional pairing in the nodal-line materials ZrSiS and ZrSiSe. *Phys. Rev. B*, 98:241112, Dec 2018.

[278] Jing-Rong Wang, Guo-Zhu Liu, Xiangang Wan, and Changjin Zhang. Quantum criticality of the excitonic insulating transition in the nodal-line semimetal ZrSiS. *Phys. Rev. B*, 101:245151, Jun 2020.